Virtual prototyping of grabs
Co-simulations of discrete element and rigid body models

Lommen, Stef

DOI
10.4233/uuid:418996d9-9b48-4349-823e-b78d8349af25

Important note
To cite this publication, please use the final published version (if applicable).
Please check the document version above.

Virtual Prototyping of Grabs

Co-simulations of Discrete Element and Rigid Body Models

Proefschrift

ter verkrijging van de graad van doctor
aan de Technische Universiteit Delft,
op gezag van de Rector Magnificus prof. ir. K. C. A. M. Luyben,
voorzitter van het College voor Promoties,
in het openbaar te verdedigen op donderdag 26 mei 2016 om 12:30 uur

door
Stef Willem LOMMEN,

werktuigkundig ingenieur,
geboren te Utrecht.

Dit proefschrift is goedgekeurd door de
promotor: Prof. dr. ir. G. Lodewijks en
copromotor: Dr. ir. D.L. Schott.

Samenstelling promotiecommissie:

Rector Magnificus	voorzitter
Prof. dr. ir. G. Lodewijks	Technische Universiteit Delft, promotor
Dr. ir. D.L. Schott	Technische Universiteit Delft, copromotor

onafhankelijke leden:

|	
Prof. dr. ir. P. Breedveld	Technische Universiteit Delft
Prof. dr. ir. H.J. Glass	University of Exeter (United Kingdom)
Prof. dr. C. Jommi	Technische Universiteit Delft
Prof. Dr.-Ing. A. Katterfeld	Otto-von-Guericke-Universität Magdeburg (Germany)
Prof. dr. ir. C. van Rhee	Technische Universiteit Delft

Printed in the Netherlands.

Summary

Grabs are a type of equipment used for unloading dry bulk cargo vessels, grabbing dry bulk material such as iron ore or coal from the vessel and transfer the grabbed material to a hopper on the quay. Development of grabs and other types of bulk handling equipment is still a complicated process as predicting the performance of a new design is hard. The current design process is based on years of experience and consists of designing a prototype, building it in the factory and evaluating it at a test site. This is expensive, time consuming, and testing the prototypes requires a bulk terminal with a crane and bulk material. Last but not least, the output of physical tests is rather limited; the tests are capable of determining whether the performance of the prototypes lives up to the expectations but it is hard to look inside the grab and understand why a prototype is working or, in a less desirable situation, to determine why it is underperforming.

An attractive way to evaluate grab prototype performance is by testing a virtual grab in a virtual test environment where bulk material and a crane are modelled. A combination of the Discrete Element Method (DEM) and MultiBody Dynamics (MBD) could capture both material behaviour and grab behaviour and predict the grab performance. An approach for creating and validating an accurate co-simulation does not exist yet, caused by the absence of grab model and the lack of a material model for bulk materials such as iron ore. Additionally, today's computational power is still insufficient to simulate all the particles, therefore techniques for speeding up DEM simulations need to be developed, while both models also need to be coupled.

This thesis investigates whether a co-simulation of Multibody Dynamics and the Discrete Element Method can establish a reliable and accurate environment for the virtual prototyping of grabs for iron ore. To create such an environment, a scissors grab has been modelled. The developed Multibody Dynamics model compares well to an analytic approach and measurements on a bulk terminal. Material characteristics of iron ore are measured and iron ore pellets are selected. Two material models are calibrated to the measured characteristics, one where angular motion of particles is restricted and another where rolling is allowed. A complete match between model and
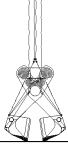
material characteristics turned out to be impossible, therefore making it necessary to prioritize penetration and density characteristics.

Large scale DEM simulations using original stiffness properties and particle size distributions require prohibitive amounts of time, thus two promising options for reducing computational time have been investigated: a particle stiffness reduction and a coarse grain system. A particle stiffness reduction can result in undesired effects and therefore should be treated with care. For the iron ore pellet models, the particle stiffness reduction resulted in cost reduction factor of 7.3, while the calibrated behaviour of the material model is not affected.

The developed coarse grain system has identical amounts of potential, kinetic, rotational and dissipated energy as the original system. This has been confirmed in angle of repose and sliding tests, however penetration resistance increased 16% when grain size doubled. This increase caused by the coarser grain could be compensated by lowering the sliding friction of the penetrating tip, bringing the resistance back to normal levels. The coarse graining technique resulted in a reduction of 10^4 hours to just under 18 hours for the iron ore pellet grab simulation while the calibrated behaviour including penetration resistance remained constant.

The MultiBody Dynamics and Discrete Element Method have been coupled into a co-simulation, exchanging loads and positions of the equipment. This coupling has been tested extensively and verified in a series of particle equipment interaction tests. This has resulted in a verified coupling between the two methods and a guideline for obtaining reliable results.

The grab model has been coupled to the large scale material models and compared to validation tests of a scissors grab with iron ore pellets on a bulk terminal. Predictions made by the coupled models matched the outcome of bulk terminal tests excellently, both in flat and sloped situations. Crane loads were predicted at an average of 27.5 ton while experiments showed an average filling of a grab at 27.8 ton. Coefficients of determination for the load comparion exceeded 0.922 on a flat surface and even 0.958 on a sloped surface. Vertical motion of the grab during closing has been predicted, achieving $R^2 > 0.975$ for flat surface and 0.964 for the sloped surface. The observed comparisons validate that the developed coupled models are capable of accurately predicting grab performance.

A demonstration of virtual prototyping of grabs using the validated model showed that an improved grab can be achieved through virtual prototyping. In a comparison of selected grab prototypes, performance increases in grabbed material of up to 15 percent have been achieved. Larger improvements should be feasible when the prototype design variables are extended to all possible parameters. It is recommended to implement the developed virtual prototyping into the grab design process, as this offers rapid assessment of a prototypes performance. Instead of the traditional ways of evaluating grab performance, virtual prototyping can now be used as an accurate and affordable alternative.

Samenvatting

Een grijper is een type werktuig dat wordt gebruikt om bulkschepen te lossen door het materiaal, bijvoorbeeld ijzererts of kolen uit het ruim te grijpen en naar de silo op de kade te transporteren. Het ontwikkelen van grijpers en andere machines voor de overslag van stortgoed is nog altijd een ingewikkeld proces omdat het lastig is de prestaties accuraat te voorspellen. Het huidige ontwerpproces is gebaseerd op jarenlange ervaring en bestaat uit het ontwerpen van een prototype, het bouwen in de fabriek en het testen op een proefterminal voor stortgoedoverslag. Dit is een lang en kostbaar traject, maar het grootste bezwaar is dat het resultaat van deze fysieke testen beperkt is. Het is weliswaar mogelijk om te beoordelen of de verwachte prestaties worden waargemaakt, maar het is lastig de processen in de grijper te bestuderen en te begrijpen waarom een prototype werkt of, in een minder ideaal scenario, te bepalen waarom de prestatie van een prototype tegenvalt.

Een aantrekkelijk alternatief om de prestaties van grijperprototypes te evalueren is het testen van een virtuele grijper in een virtuele omgeving waarin kraan en materiaal zijn gemodelleerd. Een simulatie waarbij de Discrete Elementen Methode (DEM) en MultiBody Dynamica (MBD) worden gecombineerd, zou zowel het gedrag van het materiaal als dat van de grijper kunnen vastleggen en zo de prestatie van de grijper kunnen voorspellen. Er bestaat echter nog geen aanpak voor het creëren en valideren van een accurate co-simulatie, onder andere door het ontbreken van een grijpermodel en een geschikt materiaalmodel voor bulkmaterialen zoals ijzererts. Bovendien is de huidige rekenkracht nog onvoldoende om alle deeltjes te simuleren; er moeten dus technieken voor het versnellen van DEM-simulaties worden ontwikkeld, terwijl beide modellen ook aan elkaar moeten worden gekoppeld.

In dit proefschrift wordt onderzocht of een co-simulatie van MBD en de DEM een betrouwbare en nauwkeurige omgeving vormt voor virtual prototyping van ijzererts-grijpers. Om een dergelijke omgeving te creëren, is een schaargrijper geselecteerd en gemodelleerd; dit model was geschikt voor een analytische aanpak en metingen op een bulkterminal. De eigenschappen van ijzerertsen zijn gemeten en vervolgens zijn ijzerertspellets geselecteerd. Er zijn twee materiaalmodellen afgestemd op de

gemeten karakteristieken: één waarin de rotatie van deeltjes wordt beperkt en één waarin rotaties zijn toegestaan. Het bleek niet mogelijk om volledige overeenkomst tussen model en materiaaleigenschappen vast te stellen, waardoor het noodzakelijk was de penetratieweerstand en dichtheid te prioriteren.

Grootschalige DEM-simulaties met originele stijfheid en deeltjesgrootte vereisen enorme hoeveelheden rekentijd. Om de kosten die daarmee zijn gemoeid te verminderen, zijn twee veelbelovende opties onderzocht: Reductie van deeltjesstijfheid en een grovedeeltjessysteem. Reductie van deeltjesstijfheid kan leiden tot ongewenste effecten en moet daarom met zorg worden toegepast. Voor de ijzerertspelletsmodellen heeft de vermindering van deeltjesstijfheid geleid tot een kostenreductiefactor van 7.3, terwijl het gekalibreerde gedrag van het materiaalmodel niet werd beïnvloed.

Het ontwikkelde grovedeeltjessysteem heeft dezelfde hoeveelheden potentiële, kinetische, rotatie- en gedissipeerde energie als het oorspronkelijke systeem. Dit werd bevestigd door storthoek- en wandwrijvingsproeven, hoewel de penetratieweerstand met 16% toenam wanneer de korrelgrootte verdubbelde. Deze toename is gecompenseerd door de wandwrijving van de indringende punt te verlagen, waardoor de indringingsweerstand weer op normaal niveau komt. Met dit grovedeeltjessysteem werd de rekentijd gereduceerd van 10^4 uur tot 18 uur voor een simulatie terwijl het geijkte gedrag, met inbegrip van de penetratieweerstand, constant bleef.

De MBD en DEM zijn gekoppeld in een co-simulatie waarbij de last en posities van de schelpen worden uitgewisseld. Deze koppeling is uitgebreid gecontroleerd in een reeks proeven van interactie tussen deeltjes en werktuig. Dit heeft geresulteerd in een geverifieerde koppeling tussen de twee methoden, waarbij ook een richtlijn voor stabiele resultaten is opgesteld.
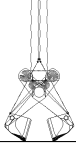
Het gekoppelde grijper-materiaalmodel is getoetst aan validatiemetingen met een schaargrijper met ijzererts pellets op een bulkterminal. Voorspellingen van de gekoppelde modellen kwamen uitstekend overeen met de gemeten praktijk, zowel in vlakke als in hellende situaties. De vulling van de grijper werd voorspeld op een gemiddelde van 27.5 ton terwijl experimenten een gemiddelde van 27.8 ton opleverden. De lastvergelijking had een $R^2 > 0.922$ op een vlakke ondergrond en op een hellend oppervlak zelfs 0.958. De verticale beweging van de grijper tijdens het sluiten is ook correct voorspeld: een $R^2 > 0.975$ voor de vlakke ondergrond en 0.964 voor het schuine oppervlak. Deze vergelijkingen bevestigen dat de ontwikkelde gekoppelde modellen in staat zijn om grijperprestaties nauwkeurig te voorspellen.

Een demonstratie met het gevalideerde model heeft aangetoond dat een verbeterd grijperontwerp kan worden bereikt door virtual prototyping. Een vergelijking van geselecteerde grijperprototypes leverde prestatieverbeteringen op tot 15 procent (in termen van gegrepen materiaal). Grotere verbeteringen moeten haalbaar zijn als de prototypevariabelen worden uitgebreid tot alle mogelijke variaties. Aanbevolen wordt om de ontwikkelde virtual prototyping in het grijperontwerpproces te implementeren. In plaats van de traditionele prestatie-evaluatie van grijperprototypes kan nu virtual prototyping als een accuraat en betaalbaar alternatief worden gebruikt.

Contents

"Science is the captain, practice the soldiers."

Leonardo da Vinci (1452 – 1519)

1

Introduction*

Bulk materials such as coal, iron ore and grain are consumed all over the world in all kinds of processes. They are used for energy production, as raw materials in factories or by end users. Very often supply and demand of bulk materials are not located at the same place and therefore the bulk materials require transportation. Especially bulk materials such as coal and iron ore are being transported over long distances, as some continents have very large deposits while other continents lack deposits while having a high demand. Other reasons for transporting bulk materials could be a difference in bulk material quality or in price, making it attractive to use imported bulk materials. Large trade flows of bulk materials exist in the world, for example 1142 Mt for coal in 2011 (World Coal Association, 2015) and 1260 Mt for iron ore in 2013 (International Steel Statistics Bureau, 2015). When bulk materials are transported overseas, large vessels of up to 400,000 tonnes deadweight are used, sailing between terminals as shown in Figure 1.1. On these terminals different types of equipment are used for the unloading and handling of bulk materials and their performance is essential to the efficiency of the total mining, shipping and handling operation.

A dry bulk vessel needs to be unloaded swiftly and reliably, minimizing the mooring time of the vessel. This can be done with different types of equipment, such as grab unloaders and continuous unloaders. While grab unloaders produce a discontinuous material flow, a hopper on the quay can be used to buffer the material and produce a continuous output for the conveying system. Grab unloaders and continuous unloaders

---

*This chapter is partially based on Lommen et al. (2012b)

each have their advantages and disadvantages (Sepling, 1985; Spanke, 2000), making it impossible to use a universal unloader for all unloading tasks. For heavy bulk materials such as iron ore, grab unloaders offer the lowest cost per ton, also due to the abrasive nature of the material.

Figure 1.1: Arrival of a dry bulk vessel at EMO terminal, Rotterdam (2012). Courtesy of EMO B.V.

1.1   Grabs, for Unloading Bulk Materials

Grabs are a type of equipment used for unloading dry bulk cargo vessels as displayed in Figure 1.2. They grab dry bulk material such as iron ore or coal from the vessel and transfer the grabbed material to a hopper on the quay. The grab is hoisted by a quay crane and its opening and closing can be controlled by wire ropes or hydraulically. Grabs are made in a wide spectrum of sizes, ranging from about $4\,\mathrm{m}^3$ up to $60\,\mathrm{m}^3$, depending on the density of the bulk material and the hoisting capacity of the crane. Each cycle takes a minute or less and consists of four steps: First, positioning the open grab above the cargo hold and lowering the grab until the grab is resting on the surface of the bulk material. Next, the closing of the grab, moving both shells towards each other and enclosing a part of the bulk material in the grab. After the grab has been closed and filled with bulk material, the crane starts hoisting the grab towards the hopper on the quay. The last step of the cycle is the emptying of the grab and the unloading of the bulk material above the hopper. Since the availability of steam power,

grabs have developed into reliable equipment that can swiftly unload a bulk cargo vessel moored at a quay crane. Vessels grew larger which resulted in the request of customers for higher capacities, shorter cycle times and longer lifetime of grabs.

Figure 1.2: Unloading a vessel with a grab at TATA Steel, IJmuiden. Courtesy of Nemag B.V.

Minimizing the mooring time of the vessel means that the grab should carry as much material each cycle as the crane limit allows, otherwise the hourly production is not as high as it could be. Cycle times should ideally be less than a minute, thereby increasing the cycles per hour and the hourly throughput. Spillage of bulk material is undesirable, not only because of the loss of product but also because of the environmental impact. Designing a grab that satisfies these demands is not an easy task, especially as each type of bulk material requires a different design.

Development of grabs and other types of bulk handling equipment is still a complicated process as predicting the performance of a new design is hard. The particular nature of bulk materials has made it difficult for scientists to develop continuum models describing the behaviour of bulk materials. When also the interaction with equipment has to be taken into account, often empirical investigation was the best option for the development of bulk handling equipment as demonstrated by Gebhardt (1972). For a few applications, such as silo design (Janssen, 1895) and cutting (Miedema, 1987), continuum models have proven to be helpful in the design process of these equipment types. However, due to the complex interaction between grab and material, no applicable models exist for the design of grabs. The current design process of bulk

handling equipment such as grabs is based on years of experience and consists of designing a prototype, building it in the factory and evaluating it at a test site.

Constructing a prototype is expensive and time consuming due to the material costs and man hours. Moreover, building a prototype is a high risk investment as the costs cannot be recovered: if the prototype fails, the prototype can then only be sold as scrap. Another drawback of physical prototypes is the testing. Testing the prototypes is not easy as it requires a large crane equipped with four wire ropes which can only be found on a bulk terminal. Also required is a sufficient amount of bulk material and the time to test. Last but not least, the output of physical tests is rather limited; the tests are capable of determining whether the prototypes live up to their expectations but it is hard to look inside the grab and understand why a prototype is working, or in a less desirable situation, to determine why it is underperforming.

1.2   Virtual Prototyping by Simulating Grab and Material Behaviour

An attractive alternative to the traditional ways of evaluating grab performance could be the use of virtual prototypes. Instead of building and testing a physical prototype, a virtual model of a grab could be adjusted and its effect on the performance could be simulated. This would eliminate the resources and time involved in the construction of a prototype as well as the need for a testing site, reducing the development costs of bulk handling equipment. The virtual model would need to take into account the behaviour of the grab and the nature of the bulk material.

Virtual prototypes are cheap to construct and based on its predicted behaviour it is possible to research whether a design change has a positive or negative effect on the performance. The low price of virtual prototypes allows for a large number of tests, each investigating the effect of a single variable. It would also be possible to examine the interaction of bulk material and certain sections of the grab, allowing for isolating local effects inside the grab. These benefits would increase the knowledge of grabs and help in improving the equipment. For the simulation of virtual grab prototypes, different computational methods have been developed in the last decades which could help to predict grab performance.

One method to simulate the behaviour of a mechanism such as a grab is called Multi Body Dynamics (MBD) simulation. This method numerically simulates systems composed of multiple bodies each having mass, inertia and degrees of freedom (Whittaker, 1970; Wittenburg, 2007; Meijers, 1997). The bodies are connected with each other by means of joints, cables, contacts or other kinematic or force constraints. The bodies and constraints lead to the equations of motion of the system which can then be solved. For example, a pendulum can be modelled by creating a body for the pendulum, a revolute joint, add some friction and connect the pendulum to the joint. The results of a multibody simulation of such a system would be the exact pendulum movement over

time as well as the forces acting on the joint. Overall, the multibody dynamics method has proven to be a useful tool for motion analysis of multibody systems (Langerholc et al., 2012).

The Discrete Element Method (DEM) is a particle-based method that can be used to simulate the behaviour of bulk material. The method computes the individual behaviour of each particle, studying its interactions with neighbouring particles and walls (Cundall and Strack, 1979). By calculating the interaction forces, the resulting motion can be computed with the help of the equations of motion. After collecting all the information of the particles it is possible to study the behaviour and flow of a bulk material. For example, a box of containing iron ore pellets can be simulated by modelling each particle as a discrete element. By computing all the interactions of each element the movements of each particle can be derived. When the box is tilted, a flow of iron ore pellets will be pouring out of the box, all of this based on the interactions of the pellets. This is obviously a computationally intensive method, which has only recently become applicable for large scale problems with the recent increase in computational power.

A combination of both methods could capture both material behaviour and grab behaviour and predict the grab performance as presented in Figure 1.3 (Coetzee et al., 2010). The Discrete Element Method could compute the loads from the bulk material on the grab geometry and feed these values to the Multi Body Dynamics. This method takes these loads and calculates the corresponding movements of the geometries. These movements are send back to the Discrete Element Method program which then can start computing behaviour of the discrete elements and the loads on the geometries again.
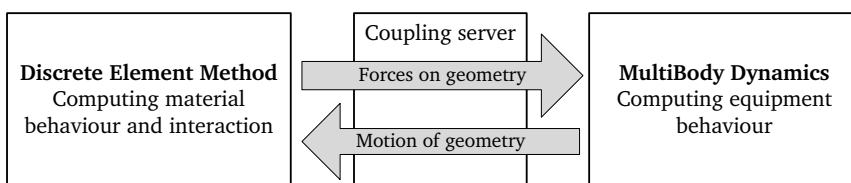
Figure 1.3: A co-simulation using Multibody Dynamics and Discrete Element Method.

By repeating those steps repeatedly over time, both equipment and bulk material behaviour are captured by the co-simulation. For example, a grab mechanism could be modelled using multibody dynamics and the iron ore particles with the Discrete Element Method. Such a coupled model could simulate both grab behaviour and the iron ore pellets behaviour, including their interaction. This would allow for investigating which grab design grabs as much iron ore as possible while not wasting energy.

While a co-simulation of these two methods looks promising, an approach for

creating and validating an accurate co-simulation does not exist. This is caused by the absence of a grab model. Another cause is the lack of a material model for bulk materials such as iron ore. Material models exists for simple materials such as spherical glass beads, however models for complex materials which can be rocky and pointy are not widely available. Additionally, today's computational power is still insufficient to simulate all the particles and techniques for speeding up DEM simulations still need to be developed.

1.3   Research Objective

This research investigates whether a co-simulation of Multibody Dynamics and the Discrete Element Method can establish a reliable and accurate environment for the virtual prototyping of grabs for iron ore. This is achieved by studying the nature of iron ore and translating this into a material model. A Multi Body Dynamics model of a grab is created, taking into account all relevant aspects of grab operation. These models are joined into one co-simulation which will be compared against grab experiments conducted with iron ore pellets on a terminal. This research continues with a demonstration of virtual prototyping based on grab performance indicators, showing that the developed simulation environment opens new possibilities for evaluating and improving grab performance.

1.4   Outline of this Dissertation

The outline of this dissertation can be viewed in Figure 1.4. Chapter 2 presents a validated model of scissors grab based on an overview of state of the art grabs. Such a model needs to include the mechanism of the grab, the crane and its operator. Chapter 3 investigates the material characteristics of bulk materials such as iron ore pellets, preferably in conditions similar to unloading conditions in the cargo hold of the vessel. Chapter 4 uses these characteristics to establish a material model for iron ore pellets. In Chapter 5 different ways of reducing computational costs are examined, including their effects on the model. Chapter 6 examines the coupling of both models into a co-simulation and the challenges associated with this operation. Chapter 7 compares the combined model to reality, therefore establishing the accuracy of the model. Chapter 8 demonstrates the benefits of the validated model in a case study of different grab prototypes. Testing these new virtual prototypes of grabs and analysing their performance leads to a proposal for a new grab design, evidently proving the advantages of the new approach for grab development. Chapter 9 concludes and provides recommendations for further research.
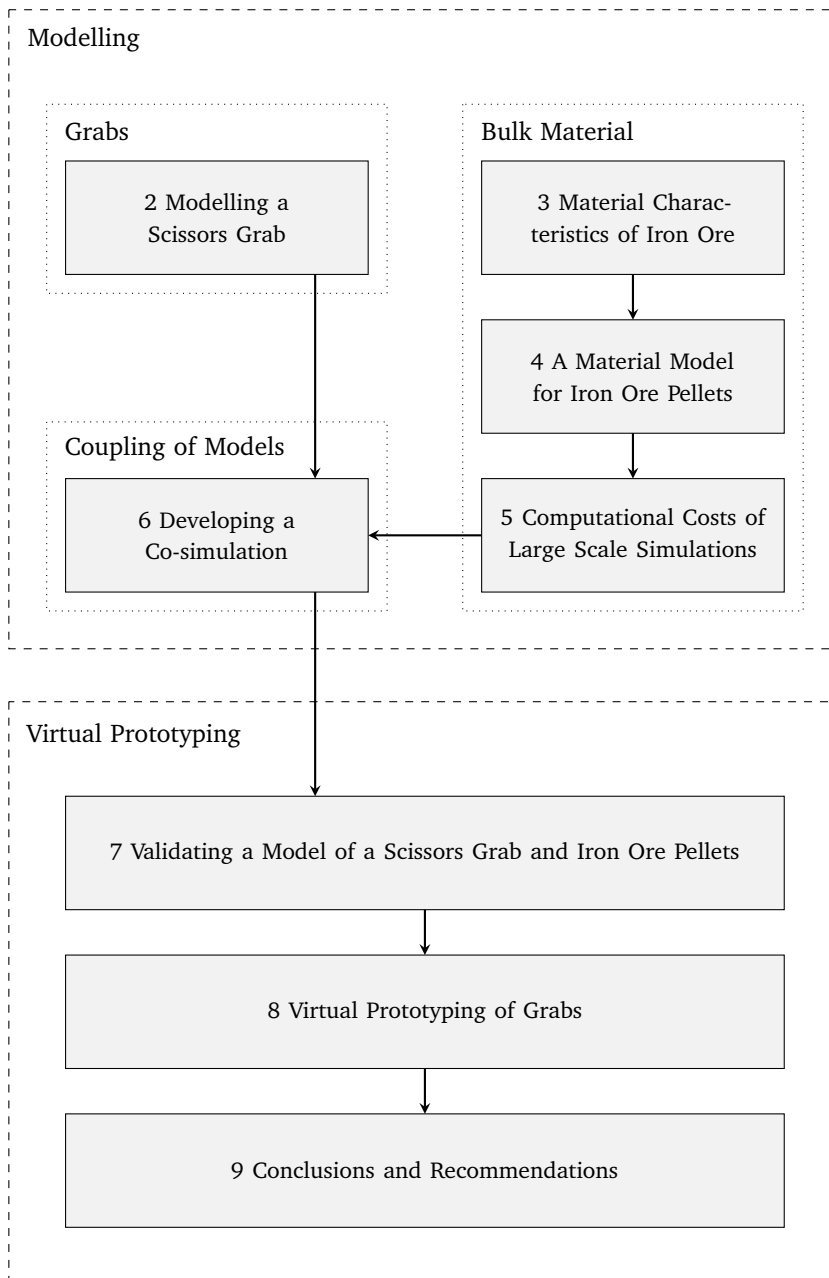
Figure 1.4: Visual outline of this dissertation.

"The machine does not isolate man from the great problems of nature but plunges him more deeply into them."

Antoine de Saint Exupéry (1900 – 1944)

2

Modelling a Scissors Grab[*]

This chapter leads to a validated model of a grab which can be used in combination with a material model for the virtual prototyping of grabs. A validation of a grab model is important to obtain a reliable solution for virtual prototyping of grabs. Although many different grab designs have existed over the years, it is not required to develop a model for each design. For now, a single grab will be selected from a comparison of state of the art grabs, other grab types can be modelled at a later stage. Modelling of the grab occurs with Multibody Dynamics software, including all the winches, cables and required contacts between different parts. After modelling the selected grab, the accuracy of the model is established in a validation with experiments of an empty grab.

Section 2.1 defines grabs and their operation by examining the different classes of grabs. Section 2.2 compares a selection of state of the art rope grab designs such as the clamshell grab and the scissors grab. In Section 2.3.2 a scissors grab is modelled with multibody dynamics, including the crane and the operator. Section 2.4 validates the scissors grab model with experiments conducted with a similar grab at a bulk terminal.

2.1 Grabs and Their Operation

Grabs for handling bulk materials have been around for a considerable amount of time, and have evolved from dredging grabs design for the removal of materials under water.

---

[*]This chapter is partially based on Lommen et al. (2012c,d).

According to Priestman (1946) the grab shown in Figure 2.1 was designed by Leonardo da Vinci (1452 - 1519) which is considered to be first grab designed, however it is not certain whether this design was ever made. Certain elements of this design are still widely seen in today's grab designs, such as two opposing buckets as well as the use of cables for the operation of the grab. Gower (1967) mentions that a working grab was seen in Venice about 1500 which could have been inspired by Da Vinci. Gower also reports of a grab dredging crane in Kampen, The Netherlands in 1562 and credits both Faust Vrančić or Fausto Veranzio of Venice and Lorini of Italy with serviceable grab machines around 1590. These are the first grabs that have been reported and since then, grab development has continued and grab designs have slowly evolved into high performance unloaders for bulk materials.
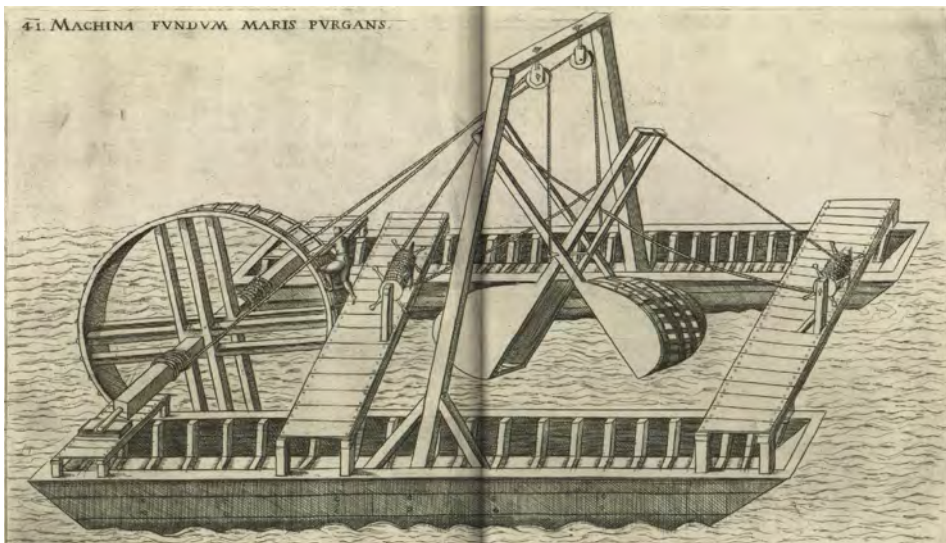
Figure 2.1: Primitive grab design by Leonardo da Vinci drawn by Vrančić (1615).

2.1.1   Definition and Classification of Grabs

A grab can be defined as a type of hoisting equipment designed for picking up a specific type of bulk material that can be attached to a crane. Grabs exists in various sizes, from small ones designed to pick up not more than a handful of material up to grabs that can grab $60\,m^3$ of bulk material. After the bulk material has been picked, the crane moves the grab and material to the drop zone, the grab acting as a temporary container for the bulk material. At the drop zone, the grab opens and unloads the bulk material. When the grab has completely been emptied, it moves to a new pick-up location ready for a new unloading cycle.

Grab performance is not just a matter of grabbing as much material as possible, the capabilities of the crane should also be considered, consequently the combination

of crane and grab needs to be assessed. The crane controls the operation of the grab and needs to have sufficient capacity to close the grab and hoist the load. The hoisting capacity of a crane is the design capacity and can go up to 85 ton for the largest bulk gantry unloading cranes in the world (marinelink.com, 2013). The hoisted load which consists of the cargo m_{material} and the hoisting equipment m_{grab} has to remain below the load limit $m_{\text{load limit}}$ (Equation 2.1) as overloading the crane triggers automatic shutdowns to prevent unsafe operation and possible damages to the crane. Equation 2.2 shows the load limit thresholds of a crane with a design capacity of 45 ton (Vermeer et al., 2012).

$$m_{\text{material}} + m_{\text{grab}} \leq m_{\text{load limit}} \tag{2.1}$$

$$m_{\text{load limit}} = \begin{cases} 48\,\text{ton} & t \geq 3\,\text{s} \\ 65\,\text{ton} & t \geq 1\,\text{s} \end{cases} \tag{2.2}$$

The mechanism that closes and opens the grab is called the *closing mechanism* and different categories of closing mechanism exist. A classification by closing mechanism provided by Scheffler et al. (1998) is a common way to classify grabs into three main categories:

Rope grabs (Figure 2.2a) have a closing mechanism that is operated and powered by the cables of the crane. Rope grabs are preferably equipped with four ropes, as these have separate hoisting and closing rope sets that allow for a balanced and separated closing and hoisting operation. Other rope configuration exist such as single rope grabs for simple cranes such as single winch cranes on-board ships. Single ropes often have a set of two wireropes to prevent twisting of the grab, however, these grabs still have a single winch and are therefore considered single-rope grabs. In fact, a more sensible distinction between single rope and multi-rope grabs would be single-winch and dual-winch grabs as mentioned by Verhoeven (1949). For large scale applications multi-rope grabs are preferred, as this type can be constructed lighter and closes faster than motor grabs (Champion, 1989).

Motor grabs (Figure 2.2b) have a motorized closing mechanism installed on the grab and therefore do not need a closing winch to be installed on the crane (Zemmrich, 1965). The motor can be controlled by the crane operator while powered with a diesel or electrical power source. A disadvantage of motor grabs is that the added motor to the grab increases the dead weight of the grab m_{grab} and therefore reduces the maximum allowed mass of material m_{material} to stay below the hoisting capacity of the crane $m_{\text{cranecapacity}}$ (Equation 2.1). Motor grabs can be electro-mechanical, electro-hydraulic or diesel-hydraulic.

Hydraulic and pneumatic grabs (Figure 2.2c) are powered by a drive unit such as a hydraulic or pneumatic pump located on the crane (Zemmrich, 1965). Hydraulic

or pneumatic lines from crane to the grab are required to supply the closing mechanism of energy required for closing. This is not a problem when the grab is attached directly to a boom, however this can be challenging when the grab is suspended from the crane through wireropes due to the possible swinging of the grab and the large distances between the grab and the boom.
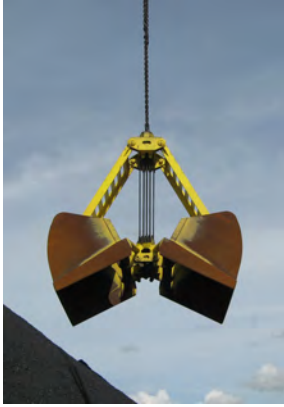
(a) Rope grab. Image courtesy of Nemag B.V.

(b) Motor grab. Copyright of Kinshofer GmbH.

(c) Hydraulic grab. Copyright Strominski.

Figure 2.2: Closing mechanism categories.

Another way of classifying grabs is the shape of the buckets in correlation with the type of material to handle, such as proposed by Conrad (1969):

Dual scoop grabs have two opposing buckets and this grab is most often used for the grabbing of bulk materials. Examples of this type of grab are the clamshell grab, the scissors grab and the trimming grab. They can have either an open or closed structure depending on the risk of material spillage.

Multi scoop grabs have more than two scoops and can be used for bulk materials as well as for the handling of large pieces of material such as scrap. An example of such a grab is the orange peel grab.

Special grabs that have specialized scoops adapted to handle specific cargo, for example tree trunks.

This research focuses on the operation of dual winch rope grabs that have two scoops. This class of grab is currently the most popular for unloading bulk material in the bulk handling industry.

2.1.2 Operation by the Crane and its Operator

Figure 2.3 shows a schematic drawing of a grab, vessel, crane and bulk terminal. Grab operation can be described as a cyclic process, where each cycle unloads one grab from vessel to shore. It consists of four phases:
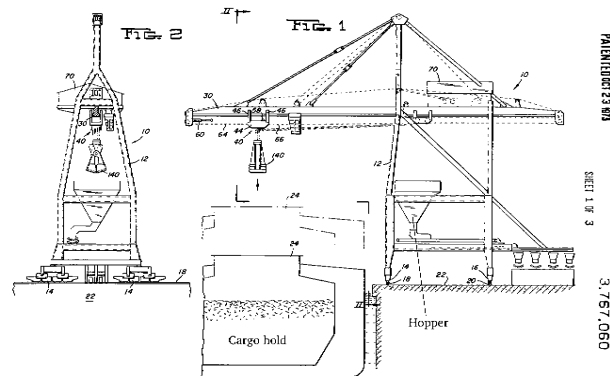
Figure 2.3: Schematic drawing of grab unloader (Briggs, 1973).

1. Picking up of the bulk material from the cargo hold by closing the grab. This is done by placing the opened grab on the bulk material which causes the knives of the buckets to penetrate the bulk material. When touchdown is completed and the grab has come to a standstill, the hoisting winch is stopped and the closing winch is reversed, causing the grab to close. After the grab has closed the hoisting winch is activated and together with the closing winch it starts hoisting the grab and the grabbed material.

2. Transferring the grab from the cargo hold to the hopper on the quay. This transfer can be a combination of vertical movement (hoisting) and horizontal movement (trolley travelling).

3. Release of the bulk material. By releasing the closing wireropes the grab will open itself due to the mass of the bulk material in the grab. The grab is constructed in such a way that no external force is required to open the grab. After releasing the material, the grab closes and is ready to be moved to a new pick-up location.

4. Transfer of the empty grab to a new pick-up location in the cargo hold.

The total amount of time required for a complete cycle is known as the cycle time t_{cycle} has been investigated by Kirincic (1983). The cycle time can be as short as 45 seconds (Drenth and Cool, 2000), although the depth of the cargo hold can increase the cycle

time significantly. Figure 2.4 shows an example of two cycles and the time required to complete each segment of the cycle. The closing takes place from $t = 678\,\text{s}$ until $t = 683.5\,\text{s}$, consuming 5.5 seconds of the cycle between 678 and 730 s. Improving the closing time will therefore have a small effect as 80% of the cycle time is determined by the hoisting and travelling speeds and distance of the grab.
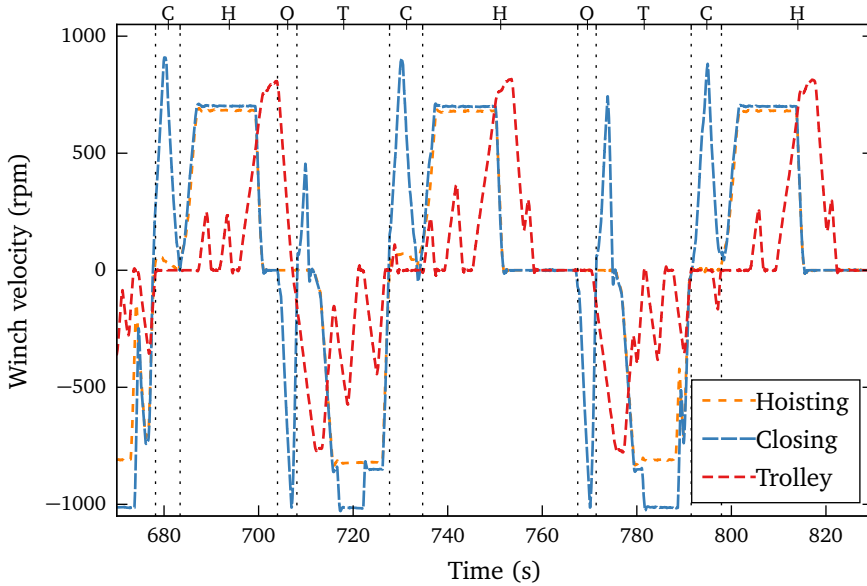
Figure 2.4: Grab unloading cycles, consisting of closing (C), hoisting to the quay (H), opening above the hopper (O) and transferring the empty grab back to the cargo hold (T).

2.2   Rope Grabs

Rope grabs have been selected for the grab model as this type of grab is most common for the handling of bulk material (Champion, 1989). Before a rope grab can be modelled, a type has to be selected. Several types of rope grabs exists, each having their own characteristics leading to benefits and drawbacks of each type.

All types of dual winch rope grabs have in common that they use both closing and hoisting cables to operate a grab.

- The grab is completely opened when the grab is hanging solely on the hoisting cables and the closing cables are tensionless. The most open position, from here on defined as the *maximum opening angle*, is mechanically limited by an angle limiter. In order to close the grab, reducing the opening angle to zero, the closing cables are tensioned and winched up.

- The grab is completely closed when the hoisting cables become tensionless and the closing cables are fully tensioned. This is, however, not a common practice as crane operators prefer to split the load between the closing and hoisting cables, causing the load to be equally divided on the cables and the winches and therefore reducing the required torque per winch.

The total amount of closing cable required to go from the maximum opening angle is called the rope pull-out length $l_{\text{pull-out}}$. The rope pull-out length determines the closing and opening times of a rope grab. Grabs with a short $l_{\text{pull-out}}$ close faster than grabs with a longer pull out length as the required length can be reached quicker by the crane's winch.

The amount of winched up closing cable is related to the opening angle θ through the closing mechanism. The closing mechanism consists of a number of pulleys and sheaves, creating several tackles to amplify the force of the closing cable F_c into torque for closing the buckets T_{closing}. Equation 2.3 shows that the characteristics of closing mechanism can be defined as the mechanism ratio $M(\theta)$. Each type of rope grab has its characteristic mechanism ratio $M(\theta)$ which affects its grabbing behaviour.

$$M(\theta) = \frac{v_c}{\dot{\theta}} = \frac{T_{\text{closing}}(\theta)}{F_c(\theta)} \tag{2.3}$$
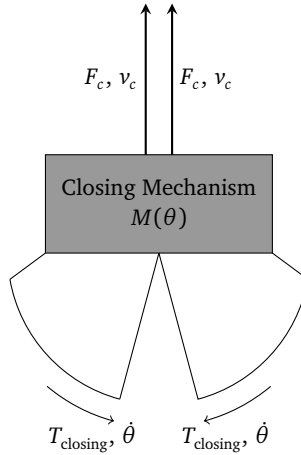
Figure 2.5: Closing mechanism.

The trajectory of both knives of the bucket during closing is called the *closing trajectory*, for example displayed in Figure 2.6. The closing trajectory is the result of the available closing torque T_{closing} and the resistance met by the knives and buckets. Because T_{closing} depends on the mechanism ratio $M(\theta)$ (Equation 2.3), the closing trajectory is determined by the configuration of the closing mechanism.
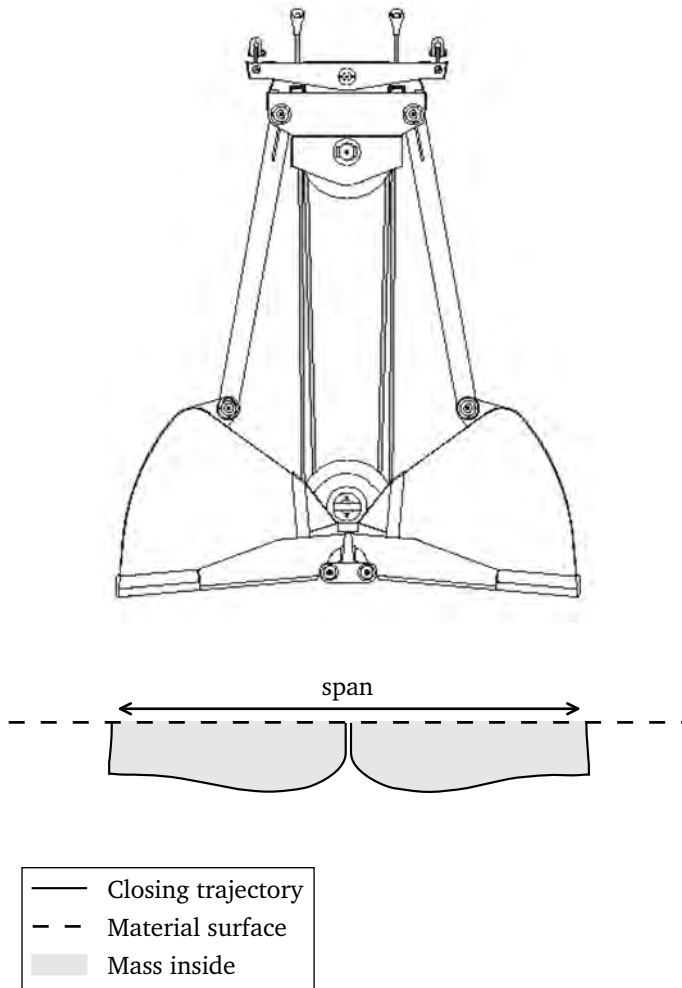
Figure 2.6: Span and closing trajectory.

The three main dimensions of a grab bucket are shown in Figure 2.7. Another important dimension is the distance between both knives at the maximum opening angle, which is called the *span* and displayed in Figure 2.6. Grabs with a large span are at an advantage during the final stage of unloading because the large span allows them to gather the remaining material with more ease. The clean-up qualities of a grab are also affected by its closing trajectory, where a more horizontal closing trajectory is beneficial to the clean-up as well.

Currently two grab designs dominate the market for large scale bulk handling, the clamshell grab and the scissors grab. These two designs are presented in detail while other grab types are reviewed briefly.
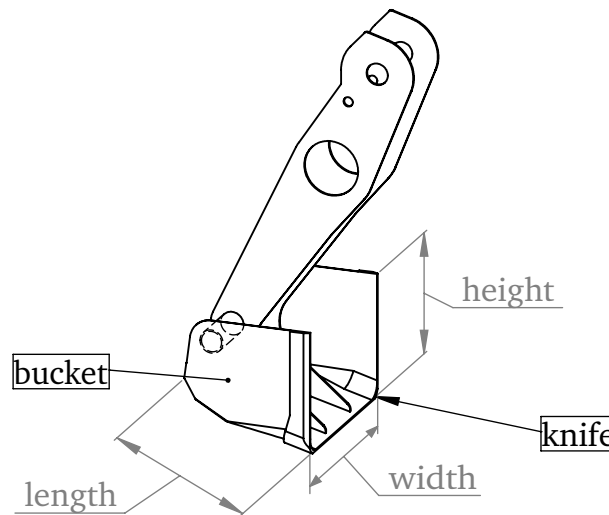
Figure 2.7: Grab parameters.

2.2.1   Clamshell Grab

The clamshell grab shown in Figure 2.8 is a common type of grab and its principles and performance have been investigated by several researchers. A clamshell grab consists of 4 different types of parts, being the buckets, the arms and the upper and lower sheave block. For the closing mechanism a vertical tackle is used, reefing the closing cable several times between the lower and upper sheave block to increase the closing force. The number of tackle blocks depends on the characteristics of the bulk material to be grabbed; ranging from three for materials with a low digging resistance to five tackle blocks for materials with a high digging resistance. The mechanism ratio of a clamshell grab reduces when the grab closes, resulting in less leverage in transferring of the closing force to closing moment.

Early research on clamshell grabs includes the work of Pfahl (1912); Ninnelt (1924); Nieman (1935). A literature review by Miedema (2008) provides insight into the content of these papers as the original publications are hard to obtain. Pfahl investigated the influence of the dead weight, clamshell dimensions and the bulk material characteristics. He concluded that payload is proportional to the dead weight and that the payload is influenced negatively by the increased penetration resistance for larger grain sizes. Ninnelt (1924) performed similar research as Pfahl by testing motorized clamshell grabs and confirmed Pfahl's findings. Ninnelt also gave some recommendations for the shape of the buckets depending on the grain size of the material. Nieman (1935) was the first researcher to use model testing of grabs, using

a scale of 1:15. He examined the effects of grab width, dead weight and bucket shape on the filling process of his model grabs. The main conclusion of his work was that the payload of a grab can be increased simply by enlarging the grab width without the changing the dead weight of the grab.

1. Hoisting cable

2. Closing cable

3. Upper sheave block

4. Arm

5. Closing tackle

6. Lower sheave block

7. Bucket

8. Bucket knife
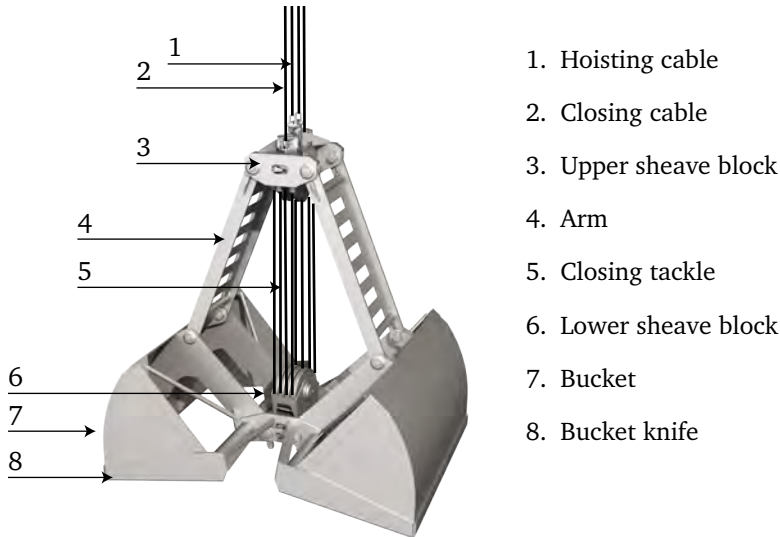
Figure 2.8: Clamshell grab. Courtesy of Nemag B.V.

Tauber (1959) investigated both prototypes and scale models. According to Miedema (2008), Tauber confirmed the findings of Pfahl and Ninnelt but also discovered that the the payload does not always increase with the bucket volume, contrary to the findings of Nieman (1935). Indeed, Tauber wrote that increasing the size of grab does not always lead to an increase in payload. He suggested that an optimum payload exists for a span / width ratio between 0.6 and 0.75. This was later confirmed by Dietrich (1971a,b,c). Later work of Tauber (1967) included a theoretical prediction of the filling process of the buckets. Other research on clamshell grabs in the twentieth century was performed by Conrad (1969); Wilkinson (1963); Dietrich (1969); Torke (1962); Leikert (1963); Hellkotter (1975) and Bauerschlag (1979).

More research on clamshell grabs was carried out by several students and research-ers of TU Delft. Reports written by Aberkrom (1982a); Janszen (1967); Pronk (1999) give an overview of different grab types including clamshells. Wittekoek (1991a,b,c) studied the behaviour of a clamshell grab in saturated sand and this work was contin-ued by Miedema et al. (1992); Miedema and Becker (1993); Miedema and Vlasblom (2006). Together they developed a model for predicting cutting forces of a clamshell grab in saturated sand using the cutting theory of Miedema (1987). It is not clear whether these models are applicable to unsaturated bulk materials. Brans (2000)

created a multibody model of a clamshell grab, allowing for insight on the closing curve of a clamshell grab and the outcome of his work resembled the measurements made by Tauber (1959).

Overall, quite some research has been performed on clamshell grabs in the twentieth century, however the last two decades did not show many advances, with the exception of the work on clamshells cutting in water saturated sands. It is unclear why research ceased on clamshell grabs, although Thomas (2002) suggest that users and producers did not feel a need to investigate clamshell grabs further and were satisfied with the performance of the grab.

2.2.2 Scissors Grab

The scissors grab is developed to combine the advantages of having a large span and a short closing time. The closing mechanism of a scissors grab is similar to a pair of scissors and shown in Figure 2.9.

Figure 2.9: A Nemag Scissors grab releasing iron ore.

The mechanism ratio of a scissors is almost inverse to a clamshell grab and starts with a low ratio at the maximum opening angle and increases during the closing of the grab, resulting in a lot of closing moment available to close the grab. The grab drawn by Leonardo da Vinci might be the first scissors grab (Figure 2.1). His design included the main hinge point still seen in scissor grabs today, however the suspension and closing mechanism differed. One of the first scissors grabs with a closing mechanism that uses

a horizontal tackle is a grab designed for well excavation by Gale (1892). In 1969, Nemag B.V. developed a scissors grab suitable for the handling of bulk material which can be observed in Figure 2.9. Since that date the scissors grab has been gradually improved by Nemag B.V. (Grootveld, 1977), e.g. increase payload and reduce unit costs. Research on scissors grabs has been carried out by Brouwer (1986); Aberkrom (1982b,a); Aberkrom and Aberkrom (1988), although most of their work focuses on a scissors grab with a single tackle block instead of the currently more common two tackle blocks. Compared to the clamshell grab, little scientific research has been performed on the scissors grab, although some conclusions of the research on clamshell grabs might be applicable to scissors grabs.

Figure 2.10 shows the parts of a scissors grab. The scissors grab consists of two scissor arms, hinged together in the main hinge point. The scissors are suspended by sets of chains attaching the buckets to the suspension that connects to the hoisting cables. Each scissor has a bucket attached on the lower side and the closing tackle on the upper side. The grab is operated with two closing wireropes which go through two pulleys each. The closing tackle is positioned horizontally between the upper parts of the arms, compared to the vertical closing tackle of the clamshell grab. The closing tackles each consist of two pulleys and an endpoint located on the scissor. The first pulley leads the vertical segment connected to the crane into the horizontal tackle. The second pulley on the other scissor then leads the closing cable back to the end point located on the original scissor.
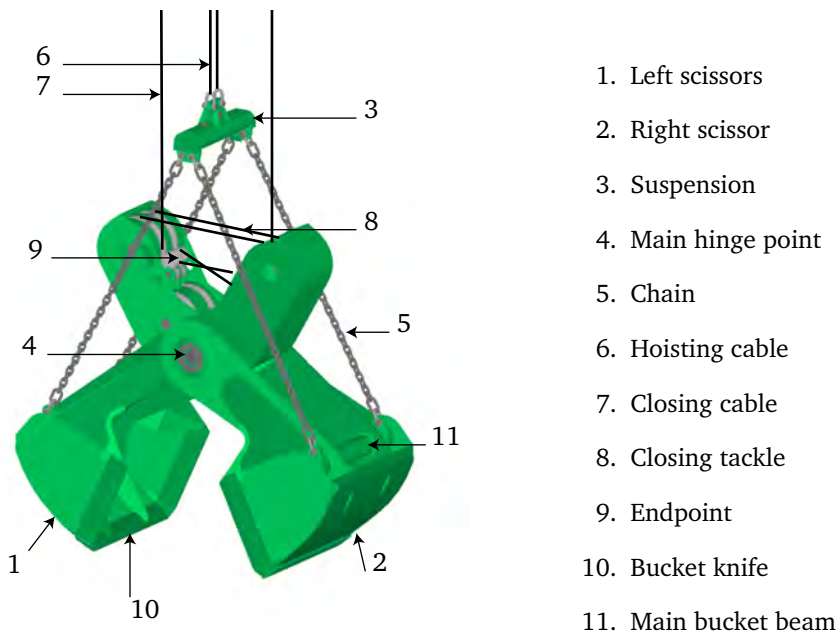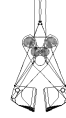

1. Left scissors
2. Right scissor
3. Suspension
4. Main hinge point
5. Chain
6. Hoisting cable
7. Closing cable
8. Closing tackle
9. Endpoint
10. Bucket knife
11. Main bucket beam

Figure 2.10: Parts of a scissors grab. Image courtesy of Nemag.

2.2.3 Other Grab Types

Numerous grab types existed besides the clamshell and scissors grab, however most of these types were found inferior compared to the clamshell and scissors grab and their development stalled. This could be due to unfavourable payload ratios or a complex construction of the closing mechanism. In the book of Priestman (1946) an overview is given of different types of grabs, although most of these grabs are no longer in use. A grab that is still used today is the trimming grab, also known as the Voorwinde grab. The trimming grab has a very large span which makes it ideal for unloading barges and rail cars. The trimming grab has a main hinge point as well, similar to the scissors grab, however the suspension of the trimming grab differs. The closing tackle is located below the main hinge point instead of above the hinge point. A drawback is that the wireropes come in contact with the bulk material when the grab is positioned on the bulk material, causing excessive wear to the wireropes and sheaves. Another drawback of the trimming grab is its stability, which is less compared to the clamshell and scissors grab due to the suspension of the grab. The trimming grab has been a topic of research for Verhoeven (1949); Wilkinson (1963); Alting (1967).

2.3 A Multibody Dynamics Model for Scissors Grab Operation

A suitable technique to develop a grab model is the Multibody Dynamics described by Whittaker (1970); Meijaard (1991); Wittenburg (2007). According to Wittenburg, Multibody Dynamics deals with systems composed of rigid bodies that are interconnected to each other by joints and force elements. The technique allows the behaviour of these systems to be described in mass-, damping- and stiffness matrices, offering the possibility to numerically solve complex systems with a large number of bodies. Research of Brans (2000); Park et al. (2004); Yoo et al. (2007) and Langerholc et al. (2012) show that Multibody Dynamics is a capable tool for the modelling of complex large scale rigid body mechanisms such as a scissors grab. Several software packages exist for this purpose, and in this research the package Adams® from MSC Software was used for the modelling of a scissors grab.

2.3.1 Multibody Dynamics

The dynamics of mechanical systems consisting of multiple bodies are based on with the dynamics of the individual bodies. For each of the individual bodies, Newton-Euler equations of motion describe the motions of the body (Equation 2.4 and 2.5)

$$\sum \mathbf{F} - m\ddot{\mathbf{x}} = \mathbf{0} \tag{2.4}$$
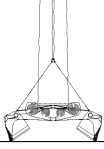
$$\sum \mathbf{T} - I\ddot{\boldsymbol{\theta}} = \mathbf{0} \tag{2.5}$$

where **F** is a vector containing the net forces in three directions, m is the mass of the body, $\ddot{\mathbf{x}}$ the second derivative of the position of the body. In the Euler equation T denotes the moments acting on the body, I denotes the matrix containing the principal moments of inertia and $\ddot{\boldsymbol{\theta}}$ denotes the angular accelerations around the centre of mass of the body.

The constraints of the mechanical system, linking the bodies together, can also be formulated in equations. For example, a coincident point on two bodies i and j can be described with Equation 2.6, leading to a spherical joint restricting all translational motions. Here **x** is the position of the body's centre of mass in the global coordinate system and **d** the vector from the centre of mass to the location of the joint. An overview of Adams®' constraint equations covering all types of standard joints can be found in the work of Blundell and Harty (2015).

$$(\mathbf{x}_i + \mathbf{d}_i) - (\mathbf{x}_j + \mathbf{d}_j) = \mathbf{0} \tag{2.6}$$

Besides continuous motions captured in the equations of motion and the constraints also discontinuous changes can occur in a mechanical system of bodies. Impact collisions are an example of a discontinuous change, such as the collision of two bodies. Impact energy can be transferred from body i to body j according to the law of conservation of momentum in Equation 2.7.

$$m_i v_i + m_j v_j - m_i v_i' + m_j v_j' = 0 \tag{2.7}$$

During impact of two bodies, energy is lost in the contact area. The amount of energy dissipated is depending on the restitution coefficient C_R defined as the ratio between restoration and deformation impulses (Equation 2.8). For $C_R = 1$ a completely elastic collision occurs and energy is preserved while for $C_R = 0$ all energy is dissipated resulting in a plastic collision.

$$C_R = \frac{\int F_r dt}{\int F_d dt} = \frac{v_i' - v_j'}{v_i - v_j} \tag{2.8}$$

The equations of motion, constraints and impact can then be written in the form of Equation 2.9, where B is a set of implicit equations depending on the variables **y**. By solving these equations the results of the model can be obtained.

$$B\mathbf{y} = \mathbf{0} \tag{2.9}$$

Several methods of obtaining and solving these equations exist, for example based on virtual work, Langrangian or Hamiltonian dynamics. However, selecting a reliable and computational efficient method is not part of this study and instead the build-in
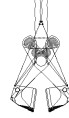
solver WSTIFF was used. Further insight on Adams®' solver can be found in MSC Software (2013); Blundell and Harty (2015), while an investigation into the stability of the solver is presented in Chapter 6.

2.3.2 A Model for Scissors Grab Operation

A four rope scissors grab for iron ores as displayed in Figure 2.9 is used to create the grab model displayed in Figure 2.11. CAD geometry and dimensions were supplied by the grab manufacturer Nemag. Both scissor parts and the suspension were modelled as bodies with their respective masses and moments of inertia, based on a calculation in a 3D CAD program.
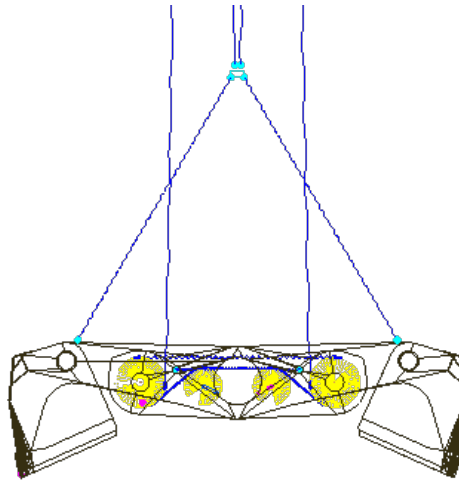
Figure 2.11: Multibody Dynamics model of a scissors grab.

Cables, sheaves and winches were modelled with the help of the TKC toolkit provided by SayField International (Verheul, 1996). The cables were modelled using Equation 2.10 (Feyrer, 2007):

$$F_{cable} = \frac{EA}{l}((\delta + \delta_{init}) + c_d \Delta v) \tag{2.10}$$

Where δ is the elongation, δ_{init} the initial elongation to adjust the natural length to the initial load, c_d the damping coefficient and Δv the difference in velocity between the two endpoints of the cable. The stiffness of the cables is based on the elasticity modulus E, metallic area A and length of the cable l.

However, the elasticity of a wire rope is non-linear and dependent on the tensile stresses present in the wire rope according to Feyrer. Feyrer states that for stranded
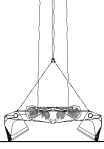
wireropes used in grab operation, the elasticity modules cannot be calculated analytically but can only be evaluated by measurements, and – due to the non-linearity – will only be valid for the given definition of loading. Wiek (1986) writes that Equation 2.10 is unfit to calculate the stresses in the strands, however it can be used for the calculation of the elongation of the wireropes if an elasticity modulus for cables is used.

An investigation on the effect of cable stiffness on grab behaviour showed an influence during opening and closing, as forces and therefore elongation shift from hoisting cables to closing cables and back. The elasticity modulus was determined based on data of CASAR's stratoplast , a commonly used cable in the bulk handling industry, resulting in $EA = 1.6e7\,\text{N}$ for the linear cable model. A suitable value for the damping coefficient was chosen based on empirically realistic values and set at $c = 0.1$. The chains between the shells and the suspension have been modelled in a similar fashion, only using $EA = 3e7\,\text{N}$.

The pulleys have been modelled to connect both cable ends, minus frictional torque caused by bearings as defined by Equation 2.11:

$$T_{bearing} = \omega\left(\mu_b F_n\right) \tag{2.11}$$

using the rotational speed ω, friction coefficient μ_b, and bearing force F_n. The bearings in the main hinge point have been modelled in a similar fashion. Friction coefficients are set to $\mu_b = 2e-3$, based on specifications provided by the bearing manufacturer FAG Germany (2012).

Modelling the aiding pulleys was challenging due to the on and off contact between cable and aiding pulleys. This was resolved by modelling the aiding pulleys on auxiliary bodies and adding a sliding constraint between the auxiliary body and the scissor and a contact where the auxiliary body would reach its position. The contacts were modelled using two identical spheres, a penalty coefficient of 1e8 and a restitution coefficient of $C_R = 0$. This solution enabled the cable to connect the pulley to the endpoint while redirecting the cable over the aiding pulley in case the cable would intersect with the main hinge point.

Additional contacts were configured in the knives of both buckets to limit the minimum opening angle to 0 degrees. This contact prevents the two shells from overlapping during closing. The restitution coefficient was set to $C_R = 0.8$, a value typical for steel to steel contacts (MSC Software, 2013). The maximum opening angle was limited as well with a contact to meet the specifications of the actual design.

2.3.3   Grab Control

For the control of the grab, in practice provided by the crane and its operator, a virtual crane operator was modelled. Four winches were created, using velocity input data obtained from measurements on a crane at a bulk terminal. These winches represent both the electric drives and gearboxes. The gearboxes were eliminated by scaling the
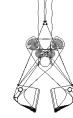
moments of inertia of the drives. The gearbox factor was retrieved by comparing the cable length required to close the grab to the number of rotations during one cycle.

In order to prevent cable slack during lowering of the grab towards the surface of the bulk material, a detection mechanism was implemented to stop crane winches when cable forces dropped to zero. The detection mechanism is activated the moment the maximum angle limiter contact is detected. This occurs when the knives penetrate the bulk material, forcing the buckets to open until the maximum angle is reached. This detection mechanism enables the winches to start the closing curve without the need to wind up excessive cable length and is very useful when comparing virtual prototypes in Chapter 8.

2.4   Validation of Grab Model

This section validates the developed multibody dynamics model of grab and crane. The model needs to have the same kinematics and statics as an analytical calculation would give. In addition, dynamical behaviour of the model is compared to a measurement on the terminal to prove the model's behaviour is realistic and comparable to its physical counterpart.

2.4.1   Kinetics and Statics

The kinematics and statics of the MBD model are validated by comparing the forces in the closing cables at different opening angles. Such a comparison can be achieved by analytically formulating the closing force F_c, based on the equations of equilibrium of the bodies of a scissors grab.

A free body diagram of a scissors grab is shown in Figure 2.12, where the scissors grab is hanging on both the closing cables and hoisting cables. Assuming all forces act in the same plane, the equations of equilibrium can be derived. Equations 2.12 through 2.17 show that the equilibrium depends on the force in the hoisting cables F_h, the forces in the closing cables F_c, the mass of the suspension m_s and the mass of the scissors m. The main hinge point H is considered the origin of the torque equilibriums.
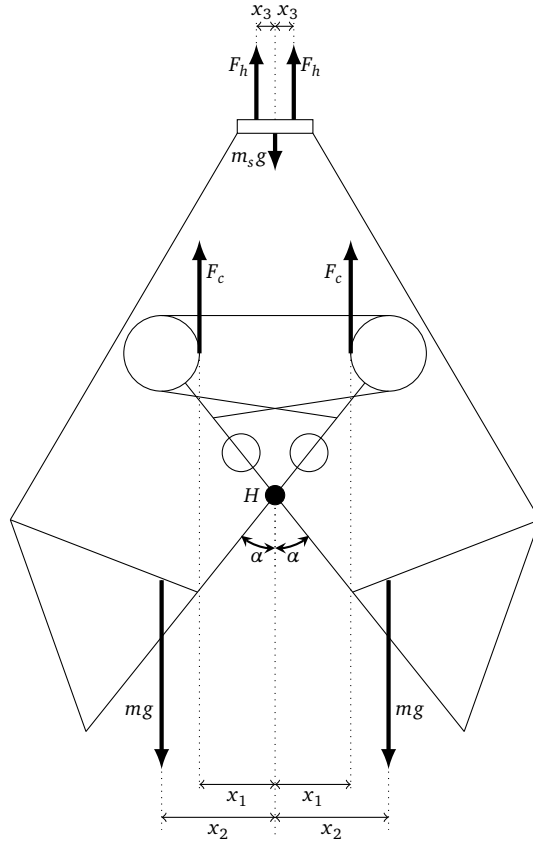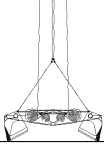
Figure 2.12: Free body diagram of a scissors grab.

$$\sum F_x \quad = \quad 0 \tag{2.12}$$

$$\sum F_y \quad = \quad 0 \tag{2.13}$$

$$= \quad 2F_h + 2F_c - (m_l + m_r + m_s)\,g$$

$$\sum F_z \quad = \quad 0 \tag{2.14}$$

$$\sum T_x \quad = \quad 0 \tag{2.15}$$

$$\sum T_y \quad = \quad 0 \tag{2.16}$$

$$\sum T_z \quad = \quad 0 \tag{2.17}$$

$$= \quad x_1 F_c - x_1 F_c + x_2 mg - x_2 mg + x_3 F_h - x_3 F_h$$

The suspension is the top body of a scissor grab, connecting the hoisting cables to the scissors through four chains. Isolating the suspension results in the free body diagram of Figure 2.13 and Newton equations can be derived. Here F_{ch} is the force in each chain, z_{ch} the arm between the chain and the centre of mass of the suspension. and ϕ_{ch} is the angle of the chain. (2.19, 2.18):
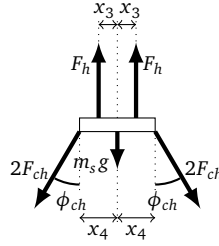

Figure 2.13: Free body diagram of suspension.

$$\sum F_x \quad = \quad 0 \qquad (2.18)$$
$$= \quad 2\sin\phi_{ch}F_{ch} - 2\sin\phi_{ch}F_{ch}$$
$$\sum F_y \quad = \quad 0 \qquad (2.19)$$
$$= \quad 2F_h - m_s g - 4\cos\phi_{ch}F_{ch}$$
$$\sum F_z \quad = \quad 0 \qquad (2.20)$$
$$\sum T_x \quad = \quad 0 \qquad (2.21)$$
$$= \quad 2\cos\phi_{ch}F_{ch}z_{ch} - 2\cos\phi_{ch}F_{ch}z_{ch}$$
$$\sum T_y \quad = \quad 0 \qquad (2.22)$$
$$\sum T_z \quad = \quad 0 \qquad (2.23)$$
$$= \quad 2\cos\phi_{ch}F_{ch}x_4 - 2\cos\phi_{ch}F_{ch}x_4 + x_3 F_h - x_3 F_h$$

Isolating the right scissor results in the free body diagram shown in Figure 2.14. Based on this diagram the equations of equilibrium for a scissor are derived in Equation 2.24 through 2.29.
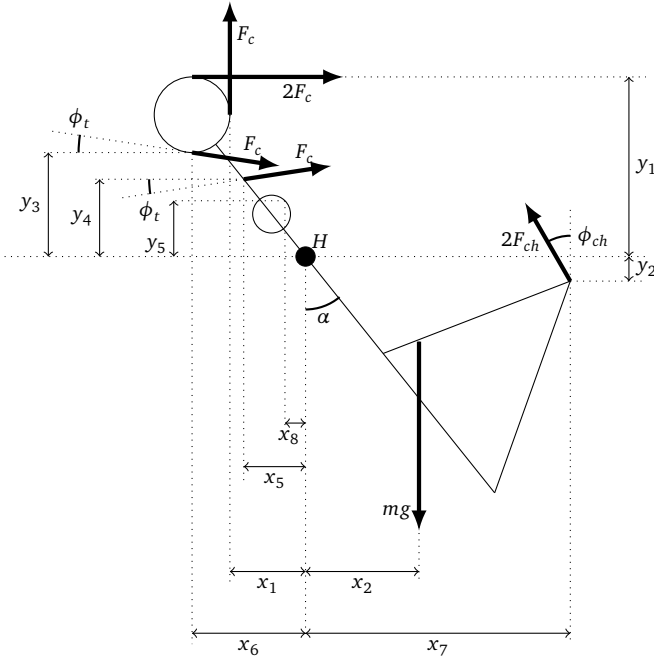
Figure 2.14: Free body diagram of a scissors arm.

$$\sum F_x = 0 \tag{2.24}$$
$$= -2\sin\phi_{ch}F_{ch} + 2\cos\phi_t F_c + 2F_c$$
$$\sum F_y = 0 \tag{2.25}$$
$$= -2\sin\phi_t F_c + F_c + 2\cos\phi_{ch}F_{ch} - mg$$
$$\sum F_z = 0 \tag{2.26}$$
$$\sum T_x = 0 \tag{2.27}$$
$$= 2\cos\phi_{ch}F_{ch}z_{ch} - 2\cos\phi_{ch}F_{ch}z_{ch}$$
$$\sum T_y = 0 \tag{2.28}$$
$$\sum T_z = 0 \tag{2.29}$$
$$= 2F_{ch}x_7\cos\phi_{ch} - 2F_{ch}y_2\sin\phi_{ch} - mgx_2 - F_c\left(\sum r_c\right)$$

Here is F_{ch} the force in the chain, Σr_c is defined according Equation 2.30 while the remaining dimensions can be found in Figure 2.14. At a certain opening angle α_a the closing cable in the tackle touches the aiding pulleys which lead the cable around the main hinge point. The aiding pulley is located at $(x_{8,}, y_5)$ from the main hinge point and the direction of the closing cable to the endpoint located on the other scissors is identicated by the angle ϕ_a.

$$\sum r_c = \begin{cases} x_1 + 2y_1 + (y_3 + y_4)\cos\phi_t + (x_5 - x_6)\sin\phi_t & \alpha < \alpha_a \\ x_1 + 2y_1 + y_4\cos\phi_t - x_6\sin\phi_t + y_5\cos\phi_a - x_8\cos\phi_a & \alpha \geq \alpha_a \end{cases} \tag{2.30}$$

The closing force F_c required for the kinematic and static validation can be obtained by combining these equations of equilibrium and rewriting them. First, the force in two chains $2F_{ch}$ can be obtained through rewriting Equation 2.19 into Equation 2.31:

$$2F_{ch} = \left(F_h - \frac{m_s g}{2}\right)\frac{1}{\cos\phi_{ch}} \tag{2.31}$$

The force in the hoisting cables F_h can be obtained by rewriting Equation 2.13, resulting in Equation 2.32:

$$F_h = -F_c + \left(m + \frac{m_s}{2}\right)g \tag{2.32}$$

Inserting Equation 2.32 into Equation 2.31 leads to Equation 2.33:

$$2F_{ch} = (-F_c + mg)\frac{1}{\cos\phi_{ch}} \tag{2.33}$$

Next, the new equation for the force in the chains (Equation 2.33) can be combined with Equation 2.29 into Equation 2.34:

$$F_c \sum r_c = (-F_c + mg)\frac{1}{\cos\phi_{ch}}(x_7\cos\phi_{ch} - y_2\sin\phi_{ch}) - mg x_2 \tag{2.34}$$

Rewriting Equation 2.34 leads to the equation for the closing force F_c (Equation 2.35), depending solely on the mass of the scissors and the kinematics of the grab.

$$F_c = mg\frac{(x_7 - y_2\tan\phi_{ch} - x_2)}{\left(\sum r_c + x_7 - y_2\tan\sin\phi_{ch}\right)} \tag{2.35}$$

Figure 2.15 shows the comparison between Equation 2.35 and the results of the MBD scissors grab model. It can be observed that the forces calculated analytically and by simulation match well, confirming the static and kinematic validity of the model. In addition, the rope pule-out length $l_{\text{pull-out}}$ of the model compared well with the specification of the grab.
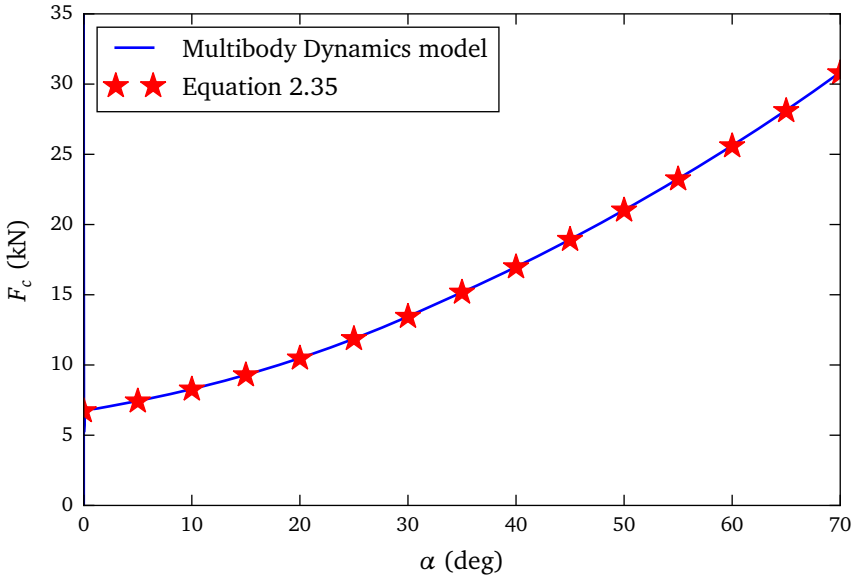
Figure 2.15: Force of the closing cable.

2.4.2 Dynamics

For the dynamic validation, torques computed in the winches are compared with motor torques recorded during full scale experiments with a scissors grab on a bulk handling terminal in the Netherlands. An extensive description of these experiments is presented in Chapter 7. The torques in the winches are related to the closing forces in the wireropes according to Equation 2.36.

$$T_c = I_w \ddot{\phi}_w + F_c r_w \tag{2.36}$$

Here I_w is the inertia of the winch, F_c the cable force and r_{winch} the radius of the winch.

Figure 2.16 shows how the dynamic validation is set up. The cable velocities recorded during the experiment are used as input for the model. In order to achieve these cable velocities, the winches in the model have to exert certain torques, exactly like the winches in the crane. Comparing the torque of the model to the experiment gives the opportunity to validate the model and therefore to establish the accuracy of the model. In the comparison, the coefficient of determination R^2 described in Weisberg (2005) is used to establish the correlation between both signals. A coefficient of determination of $R^2 > 0.8$ is considered to be sufficient during closing, as this means that less than 20% of the variance can be attributed to unknown variables such as modelling errors, measurement errors and variability caused by wind, swinging of the grab and other external factors.
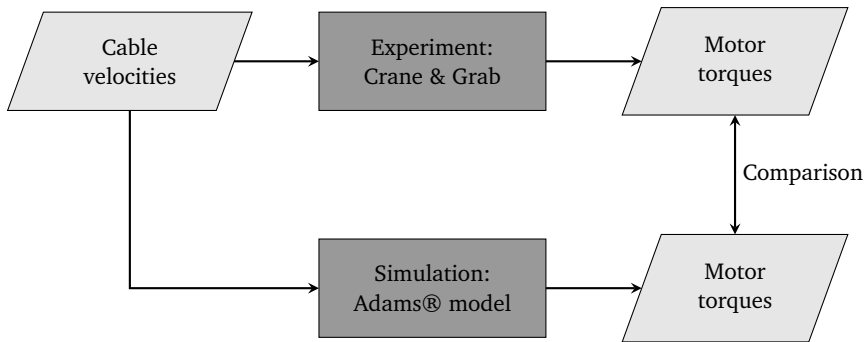
Figure 2.16: Comparison used during validation.

In these experiments, motor rotational velocity and torques were measured during the opening and closing of an empty grab. Two experiments were conducted:

1. An experiment with normal winch operating velocities. Opening and closing occurs in 12 seconds.

2. An experiment with reduced winch velocities. Here openings and closing occurs in 20 seconds.

Figure 2.17 shows the winch velocities of the slow measurement. The result of these winch velocities is that the grab opens and closes, as can be seen in Figure 2.18. It can also be seen that the position of the suspension does not change during opening, but lowers during closing due to movement of the hoisting cable.
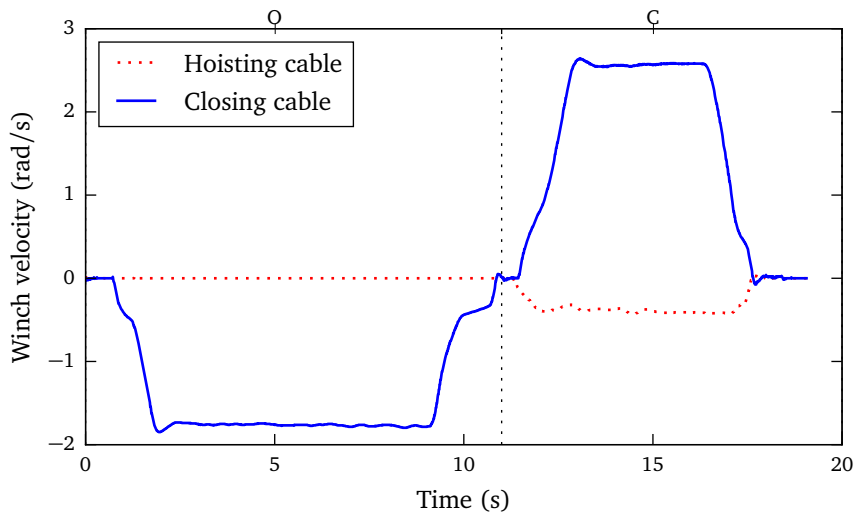

Figure 2.17: Input signal of opening (O) and closing (C).

(a) $t = 0$ s.   (b) $t = 11$ s.   (c) $t = 20$ s.
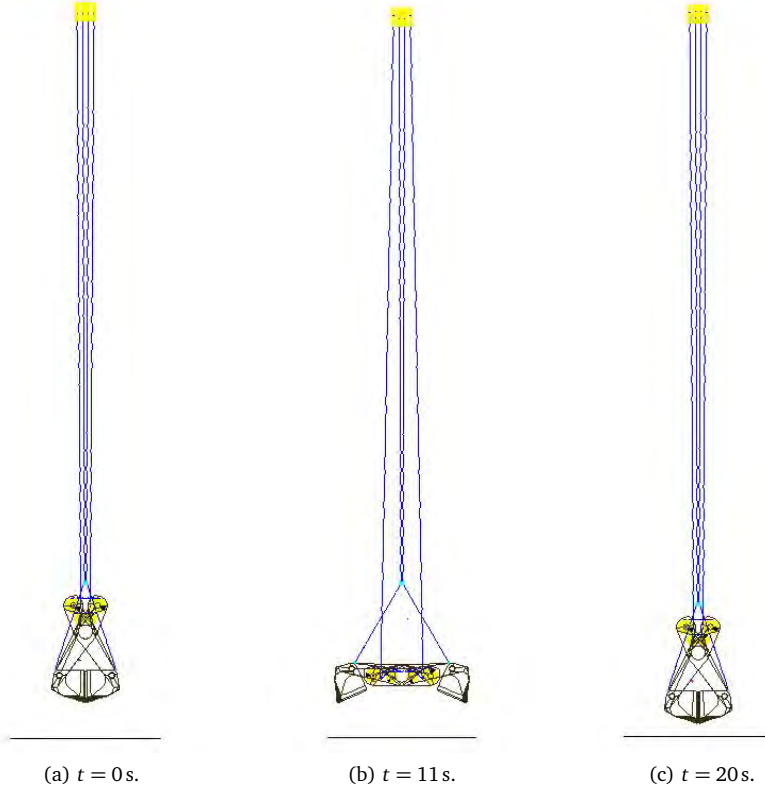
Figure 2.18: Position of the grab at different moments.

The original measurement data of winch velocities turned out to be heavily discretized, resulting output of the model using the unfiltered input is shown in Figure 2.19 with a R^2 of 0.32. The noise in the output is caused due to the strong influence of the very erratic winch accelerations. An analysis comparing the original signal to a filtered signal was performed, using different spans and both the moving average smoothing technique and the Savitzky-Golay filter. A cubic spline interpolation algorithm was used in Adams® to create the continuous input signal required. Compared to the Akima algorithm, this cubic spline has smoother derivatives, which result in smoother torques in the winches as winch acceleration $\ddot{\phi}_w$ has an effect on winch torque (Equation 2.36). Based on inspection of the filtered signal and its derivative the Savitizky-Golay filter with a span of 17 ($\Delta t = 0.17$ s) was chosen.

When this filter was applied to the cable velocities, the R-squared increases to 0.91, as can be seen in Figure 2.20. The difference at the end of the simulation is caused by the not completely closing of the grab and the absence of a load balancer in the model. This results in high forces on the hoisting cables instead of balancing the load between the closing and hoisting cables. Also normal operation, e.g. opening and closing in
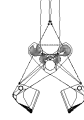
12 seconds was examined as well. The model predicted the outcome very well, with $R^2 = 0.97$ for the closing cable.
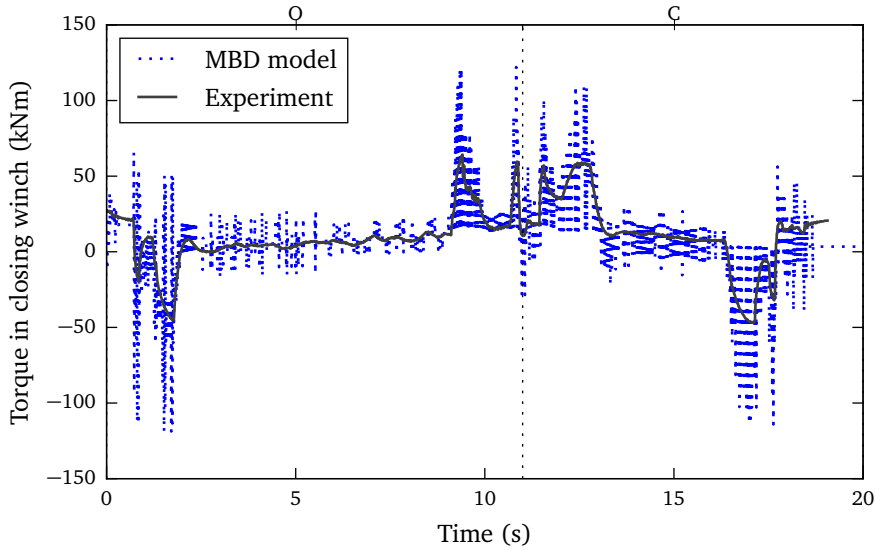

Figure 2.19: Model output using unfiltered input compared to measured signal from experiment during opening (O) and closing (C). $R^2 = 0.32$.
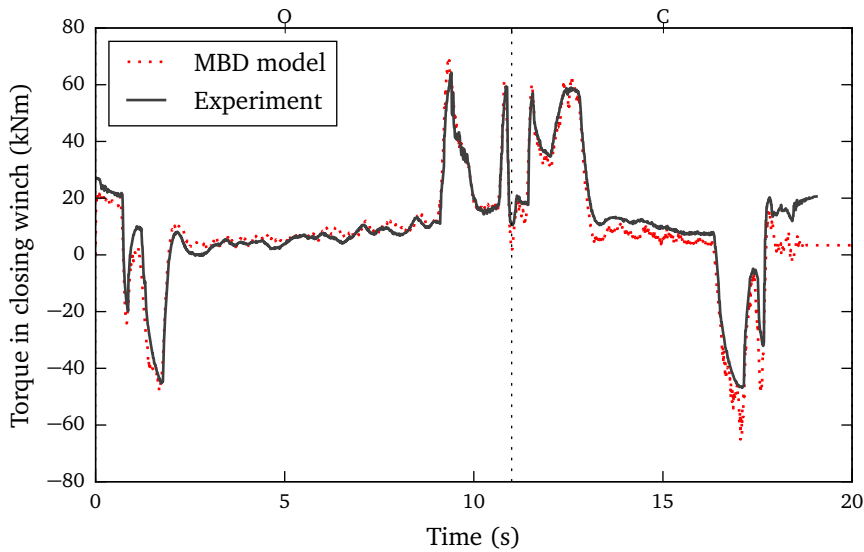

Figure 2.20: Model output using filtered input compared to measured signal during opening (O) and closing (C). $R^2 = 0.91$.
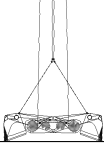
Figure 2.21 shows the torque of the hoisting winch, both the output predicted by the model as well as the measured output. During opening, the hoisting winches do not move and the physical drives can engage their brakes. The modelled winches do not have a brake and have to hold the drum in position by exerting a torque, which explains the difference in the opening stage. At the end the model predicts higher torques than measured; this is also caused by the grab not completely closing. The R-squared between $t = 11.4\,\mathrm{s}$ and $t = 18\,\mathrm{s}$ reaches 0.71. In the scenario with normal operation, similar agreement was reached with R^2 of 0.76. This is slightly lower than the requested 0.8 and likely caused by the absence of a load balancer in the model. However, considering the fact that the hoisting cables will be tensionless during the grabbing of the bulk material, this variance is not conceived as too high for a co-simulation of a closing grab.
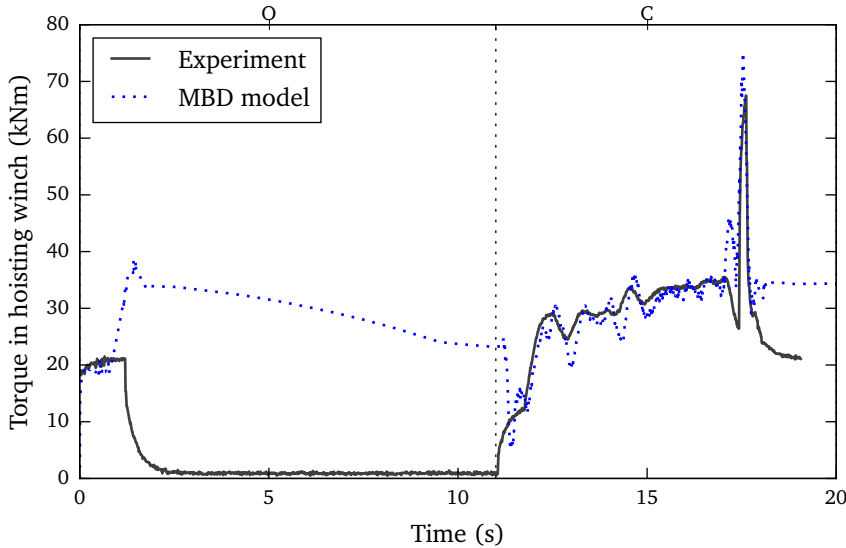
Figure 2.21: Model output of hoisting torque compared to measurements during opening (O) and closing (C). $R^2 = 0.71$ for $11.4 < t < 18\,\mathrm{s}$.

This validation proves that the scissors grab model presented in Section 2.3.2 can be used for the prediction of grab behaviour. Kinematic, static and dynamic behaviour of the model matched theory and experiments, demonstrating the model's readiness for a co-simulation with a material model.
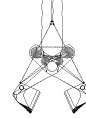
2.5 Conclusions

This chapter has shown that MultiBody Dynamics is a suitable method for simulation the behaviour of a scissors grab. The developed model was compared to an analytical solution as well as measurements conducted with an empty scissors grab on a bulk terminal. The closing cable forces of the model matched with the analytical solution showing an increasing an increasing closing cable force for larger a opening angle of the grab. In the comparison with measurements on the bulk terminal, closing winch torques were predicted with an R^2 of 0.91, demonstrating the accuracy of the model. In brief, these comparisons confirm that MultiBody Dynamics can predict the behaviour of complex mechanisms such as a grab.

The scissors grab model developed in this chapter has been validated and is ready to be coupled to a material model for the virtual prototyping. In the next chapter, iron ore tests will be conducted, the results will serve as the basis for the material model developed in Chapter 4.

Material Characteristics of Iron Ore[*]
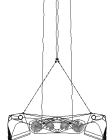
"You know, sometimes the world seems like a pretty mean place. That's why animals are so soft and huggy."

Bill Watterson (1958 – present)

In this chapter the material characteristics of iron ore are determined, which can then be used to develop a material model. The behaviour of the bulk material depends on material and interaction properties such as particle size, particle size distribution, particle shape, dry density, bulk modulus and inter-particle friction (Iwashita and Oda, 1999; Rhodes, 2008). Besides material properties and the interaction with equipment, loading conditions and transport effects such as vibrations due to stormy seas determine the actual material behaviour (Laue, 1997). All these properties and effects need to be considered before a material model can be developed.

Section 3.1 discusses iron ores in general and the tested ores in more detail. Section 3.2 presents the experimental set-ups, resulting in the characteristics of the tested iron ores. Based on these results, Section 3.3 selects the most suitable material to develop into a material model fit for DEM simulation.

3.1 Iron Ore

This research focusses on iron ores, as iron ore is a bulk material that is shipped in very large quantities and is vital to the global economy. Iron ore is required for steelmaking, and steel represents almost 95 percent of all metal used each year (Blas, 2009). In fact, it is argued by Christopher LaFemina, mining analyst at Barclays Capital, that "Iron

---

[*]This chapter is partially based on Lommen et al. (2011); Miszewski et al. (2012); Lommen et al. (2013)
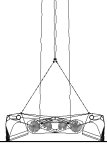
ore may be more integral to the global economy than any other commodity, except perhaps oil" (Blas, 2009). Shipments of iron ore in 2013 totalled to an amount 1260 Mt being shipped worldwide (International Steel Statistics Bureau, 2015), and these shipments are essential for the operation of numerous blast furnaces in Europe which do not have access to domestic iron ore deposits.

Another reason for focussing on iron ore is that it is one of the most challenging materials to unload due to its high weight and its abrasive nature. The bulk density of iron ores ranges from 2000 $^{kg}/m^3$ for iron ore pellets to up to 3200 $^{kg}/m^3$ for MAF sinter fines from LKAB in Malmberget, which is more than three times as heavy as coal (Vermeer, 2011). The abrasive nature of iron ore causes high amounts of wear on the unloading equipment, calling for a considerable amount of maintenance and possible downtime of the equipment. These properties make grabs the ideal type of unloading equipment compared to continuous unloading systems, since high material weight of iron ore is not an issue and maintenance due to its abrasive nature can be performed when a second grab is taking care of unloading, hence minimizing the disruption to the unloading process. The high closing forces at near closing of the scissors grab are also beneficial as the grab has sufficient force to compress and push the heavy material up to close the grab.

Iron ore pellets are marble-sized, heat hardened balls of iron ore mixed with limestone (1%) and bentonite (0.8%), which are used for steelmaking. The direct use of low grade iron ore concentrates is undesirable since it restricts the air flow in the blast furnace or the iron content is insufficient. Pelletizing is an agglomeration process to achieve uniform-sized pellets with an iron ore content of at least 90 percent (Mbele, 2012). Shipments of iron ore pellets have increased over the years and are expected to continue to increase. This is caused by shifting the production of pellets from the steelmaking location to the mining location (Mukherji, 2014). The bulk density of iron ore pellets is usually lower than iron ore concentrates, particle diameter ranges between 8 and 18 mm. Although iron ore pellets have been characterized, for example by Gustafsson et al. (2009); Barrios et al. (2013), this data is insufficient to develop a material model as the amount of force required for penetrating remains unknown.

3.1.1   Effect of Moisture on Iron Ore Characteristics

Iron ores with a high iron content are ideal for the steelmaking process but often also come with a drawback: the high moisture content. Handling of highly moisturised iron ore on bulk terminals causes a lot of inconvenience. It affects handling equipment such as unloading systems, belt conveyors and stacker reclaimers, for example excessive material build-up occurring at transfer points. Storage piles of the highly moisturised ore have collapsed more often than dry ores, this might be the result of the moisture level reaching the flow moisture point and affecting the angle of repose. The biggest risks are during shipment as cargo liquefaction can result in the shifting of cargo, leading to a loss of the stability of the ship (Maitland, 2012). Grab operation is also
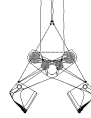
affected by the moisture content of the bulk material, for example resulting in severe overloading of the grab.

One of the causes in these handling difficulties is perhaps the resulting changes in bulk density. A literature study on the effect of moisture on the bulk material behaviour shows that there are four main mechanisms that were shown to affect the bulk density of bulk materials: particle size distribution tightening, agglomerate deformation, inter-agglomerate friction, and agglomerate density (Sohn and Moreland, 1968; Hinkley et al., 1994; Yu et al., 1995; Feng and Yu, 1998; Xu et al., 2006). All these mechanisms rely on agglomeration of the material. The literature study showed that increasing the moisture content of a bulk material tightens the particle size distribution due to agglomeration, which reduces the bulk density. Also, agglomerate deformation increases the bulk density of a bulk material; this effect is most significant at high moisture contents. Increasing the moisture content was also shown to increase the inter-agglomerate friction on the materials tested which has the effect of decreasing the bulk density. When the moisture content is increased further, the density of the agglomerates decreases and results in a decrease the bulk density of the material. Overall, the bulk density has been shown to decrease with increasing moisture content until it reaches a minimum and begins to increase again. This minimum represents the point when agglomerate deformation begins to overcome the other three mechanisms.

Another cause for the handling difficulties of highly moisturised ores is a change in the angle of repose. The angle of repose increased steadily with moisture content for iron ore (Xu et al., 2006) and for coal (Standish et al., 1991). Using the angle of repose, inter-agglomerate friction was shown to increase with increasing moisture content, as mentioned in the previous paragraph. When selecting a suitable material, these effects of moisture content on the angle of repose and bulk density in relation to the particle size distributions of the tested materials should be investigated.

3.1.2 Test Materials

Figure 3.1 and Table 3.1 show the four materials tested in this research, three being iron ores concentrates and one type of iron ore pellets. The d_{50} of the three concentrates is displayed in Table 3.1, as well as the origin, moisture content and particle density of the materials. The moisture content is dry based, calculated according to the definition given in Equation 3.1.

$$\text{Moisture content} = \frac{m_{wet} - m_{dry}}{m_{dry}} \times 100 \tag{3.1}$$

The particle density was measured using a Quantachrome Ultrapycnometer 1000 using the medium sized sample container and ten runs, resulting in an average coefficient of variation of 0.05%.

The particle size distributions of the three materials are displayed in Figure 3.2 and it can be seen that SSFG and Carajas share very similar particle size distributions. The
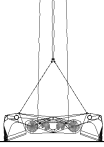
Figure 3.1: Test materials. Clockwise, starting top left: iron ore pellets, Sishen , Carajas and SSFG.

Ore	Origin	d_{50}	Moisture Content	Particle Density
Carajas	Brazil	1 mm	6.3 %	4.89 ton/m³
Guaiba (SSFG)	Brazil	2 mm	5.3 %	4.78 ton/m³
Sishen fine	South Africa	3 mm	1.0 %	4.93 ton/m³

Table 3.1: Iron ores and their d_{50}, dry based moisture content and particle density.

iron ore from the Carajas region is known for its high moisture content and difficulties during handling. This ore is compared to other ores such as Sinter Feed Guaiba (SSFG) and Sishen ore. By comparing the three materials it should be possible to see how different particle size distributions affect the relationships seen in previous research as described in Section 3.1.1. Due to the similar particle size distribution of SSFG and Carajas it is expected that they would behave in a similar way. The tighter size distribution coupled with the very low proportion of fines relative to the amount of larger particles indicates that Sishen ore will have difficulties forming agglomerates and thus have a minimal effect of moisture on its behaviour.

The iron ore pellets used in this research consist of spherically shaped particles with a diameter between 8 and 14 mm. The particle size distribution of the material is measured using manual sieving as this provided more accurate results than sieving with the help of a vibration table. The vibration table was not able to provide the large excitation required to rotate and move the relatively large particles. The particle
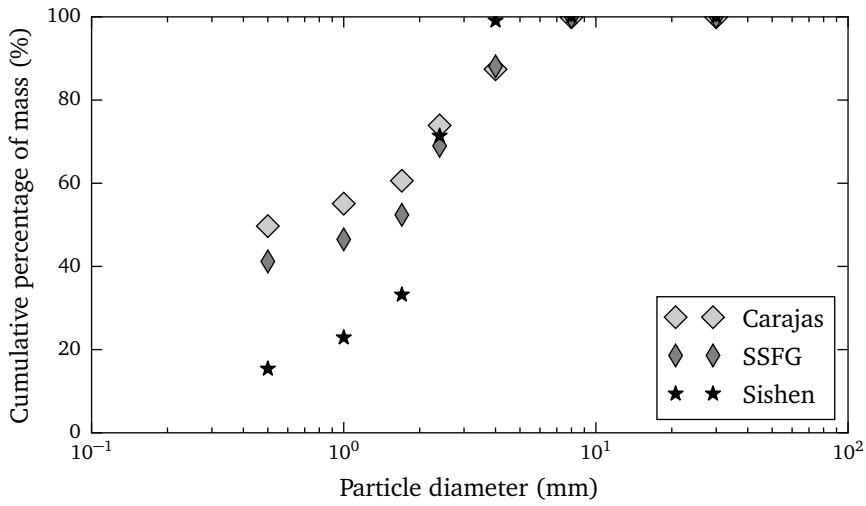
Figure 3.2: Particle size distribution of the three iron ore concentrates.

size distribution is displayed in Figure 3.3 and can be approximated with a normal distribution with a average diameter of 11 mm and a normalized standard deviation of 0.1. This approximation had a R^2 of 0.9997. The particle density of the iron ore pellets was measured at 4260 $\mathrm{kg/m^3}$ with a coefficient of variation of 0.0475 %.

Figure 3.3: Particle size distribution of iron ore pellets.

3.2 Experiments to Characterize Iron Ore Behaviour

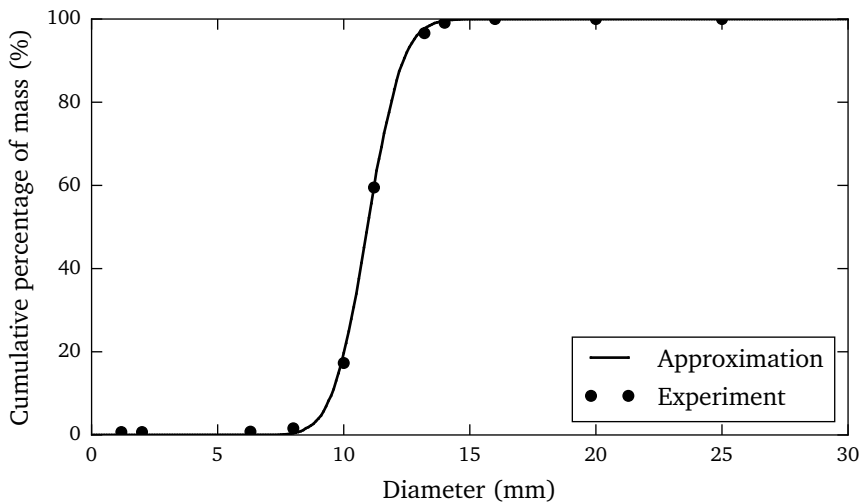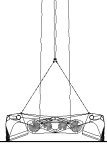Several experiments were conducted to characterise the iron ore: A bulk density test, two angle of repose tests, penetration tests, flow moisture point tests and tests for determining wall and rolling friction. With the help of these tests, the material characteristics relevant to the filling process of a grab can be acquired. All tests were conducted more than once in order to establish a 95% confidence interval of the mean, whose definition can be found in F.M. Dekking et al. (2004).

For changing the moisture content, the materials were dried in an oven at 120 °C for 19 hours similar to previous research (Hinkley et al., 1994; Yu et al., 1995; Xu et al., 2006). The moisture content of the materials was raised approximately two percent (dry mass based) for each increment. The moisture content was raised until either the material could hold no more liquid or the particles became suspended in the liquid. For each increment, water was added before using a mixing attachment and power drill to mix the material for 90 seconds. To ensure the actual moisture content of the material was known, five 10 gram samples were taken after mixing and analysed using a moisture content analyser.

3.2.1 Bulk Density Tests

Bulk densities are important to the grab process as they determine the relation between the volume of a grab and the weight of the material carried in the grab. Bulk materials with a lower bulk density require a large grab in order to fill the grab to its designed load capacity, while higher density materials benefit from a smaller grab since these weigh less. The bulk density is also likely to influence the filling process of a grab, determining the amount of material to be pushed inside the grab.

The bulk density of the materials was measured using a cylindrical container with a diameter of 125 mm and depth of 200 mm and volume of 2.46E-3 m^3. The bulk density was measured after each of the four types of consolidation carried out on the material. The four consolidation types were: loose, vibrated only, compacted without vibration and compacted while vibrated. The loose measurement was the bulk density of the material before vibration or compaction. The vibrated only measurement was taken after the sample had been vibrated for 120 seconds at 10 m/s^2. The compacted without vibration measurement used 60 kg placed on the lid. Finally, the compacted and vibrated measurement was taken after the sample had been compressed using the 60 kg from the previous measurement and then vibrated at 5 m/s^2 at 120 seconds. The bulk density could then be found from the volume and the mass of the sample. Unfortunately it was not possible to relate the consolidation conditions to grab unloading conditions at a bulk terminal.

For Carajas and SSFG iron ore, Figure 3.4 clearly show the bulk density decreases with increasing moisture content to a minimum before increasing again. The bulk density of the Carajas and SSFG at more than 8% dry mass based moisture content

actually exceeds that of the dry material after vibration. It can also be seen that the minimum bulk density occurs at a lower moisture content when the sample is vibrated than the loose condition. This means that care must be taken in using laboratory density measurements if they are made with only a loose sample.

The second point of note about Figure 3.4 is that the end point of the experiment was at a moisture content around 2% lower for SSFG than for Carajas. This may have happened earlier for SSFG than for Carajas due to the higher proportion of large particles and lower proportion of fines which would mean that there would be a smaller number of liquid bridges or particles to bond with thereby meaning that less water was required to overwhelm the liquid bridges. When the material is in this condition all the voids have been saturated with liquid or it is possible that particles are held in suspension in the liquid.
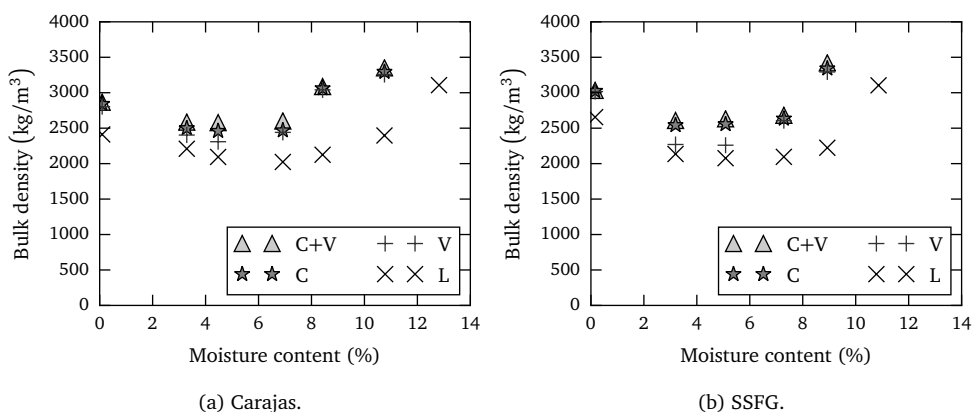

(a) Carajas.

(b) SSFG.

Figure 3.4: Bulk density of iron ore concentrates for loose (L), compacted (C), vibrated (V) and combined compacted and vibrated (C+V) condition.

Sishen ore showed a different behaviour than the Carajas and SSFG ore. It was impossible to increase the moisture content over 3%, as this completely oversaturated the sample and the water level raised above the material level. Bulk densities at 1% dry based moisture content are 2466 kg/m^3 for the loose condition, 2635 kg/m^3 for the vibrated condition and 2682 kg/m^3 for the condition with both vibration and compaction. At 2.7%, the bulk densities were 2229 kg/m^3, 2597 kg/m^3 and 2630 kg/m^3 respectively. As Sishen contains a low proportion of fines and a high proportion of large particles agglomeration cannot occur sufficiently for a large quantity of moisture to be added, which requires lots of individual liquid bridges to form between particles. This lack of agglomeration also means that agglomerate deformation never becomes significant enough to raise the bulk density. Comparing Carajas and SSFG to the results for Sishen ore it can be concluded that the particle size distribution plays a key role in determining the effect of moisture content on iron ore.

The bulk densities of iron ore pellets are tested for the same three different loading conditions, however, the effect of moisture content was not examined, since agglomerates are completely absent in the material. Bulk densities for these three conditions are 2067 kg/m³ for the loose condition, 2135 kg/m³ for the vibrated condition and 2146 kg/m³ for the condition with vibration and compaction, each with a 95% confidence interval of less than 7 kg/m³. This shows that the bulk density of iron ore pellets is relatively insensitive to the loading conditions as the increase from loose condition to the most dense condition is less than four percent.

3.2.2   Angle of Repose Tests

The angle of repose of a bulk material is expected to be an important characteristic for the grabbing process. Figure 3.5 shows a grab filled to its maximum, determined by the angle of repose of the material since excess material rolls down the slope and falls out of the grab. Another aspect of the shearing behaviour of a bulk material on the grabbing process is during the cutting, where the bulk material is sheared and the angle of internal friction affects this as well. A complicating factor of measuring the angle of repose is the manner in which the angle is created. Duran (2000) describes that angles created by pouring are less steep than angles created by shearing of the material. Since the manner in which the angle is created in the grab process, both measuring techniques are utilized to characterize the test materials.

Figure 3.5: Angle of repose on top of a grab.

Two angle of repose set ups were used: a ledge method set up (Figure 3.6a) and a free cone set up (Figure 3.6b):

- The ledge method set up consisted of a rectangular box with acrylic sides for visual observation and image analysis. The container is dimensioned at 250 mm in height, 215 mm in length and 180 mm in width. There was a 200 mm high flap opening on the front of the container and an edge of 20 mm creating a ledge at the opening. The container was filled with material and then the flap opened to release the material and allow the angle of repose to form. An image was then taken from both sides and image analysis carried out to determine the angle of repose.

- The free cone method used two buckets. One bucket was placed above the other and filled with material. To undertake the test a set of trap doors in the bottom of the top bucket were opened and the material was allowed to flow through the hole with the aid of a flow promoting device. Images were then taken of the cone from three equally spaced positions around the bottom bucket and image analysis was carried out to determine the angle of repose from the cone. The angle of repose was found from the images by taking the coordinates of ten equally spaced points on the slope of the material. Linear regression was then used to fit a straight line to the data points and the angle of the line with the horizontal represented the angle of repose.

For both set ups, every experiment was repeated seven times.
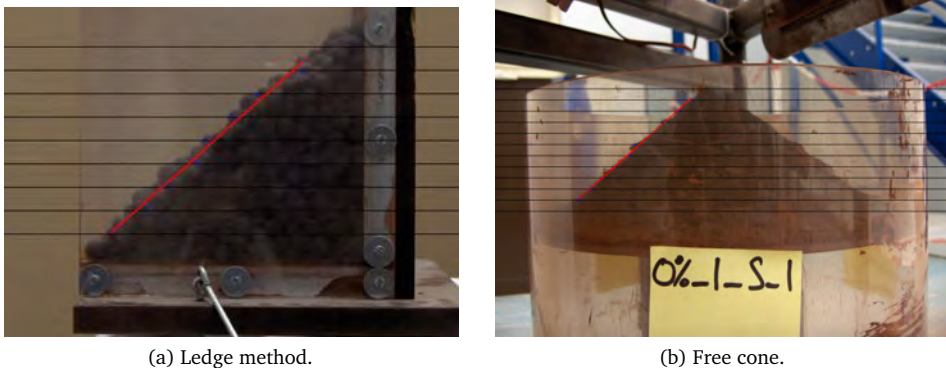

(a) Ledge method.   (b) Free cone.

Figure 3.6: Two angle of repose set-ups.

Both Carajas and SSFG showed a negligible increase in angle of repose with moisture content other than at the very highest moisture content reached before liquefaction (Figure 3.7). This would suggest that inter-agglomerate friction does not play a large role in reducing the bulk density of the material. The sudden increase in the angle of repose is most probably down to agglomerates deforming as the container is loaded with a sample. The deformation, which can occur easily without vibration at high moisture contents, causes the particles to interlock and the increased surface contact between the
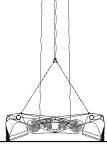
agglomerates allows for more bonding and thereby increasing the inter-agglomerate friction.

The sudden increase in angle of repose at the highest moisture content for both materials is not shown by the free cone method as shown in Figure 3.7. This is most likely to be because the angle of repose increased to nearly 90° which is very difficult to pick up using the free cone method as the particles just roll away rather than stack up. There is also a substantial difference in the results between the two methods, clearly demonstrating the difference between the angle of repose and the angle of movement known from literature (Duran, 2000). When the moisture content was increased even further, the bulk material would fail as liquefaction occurred and an angle of repose would no longer be sustainable.

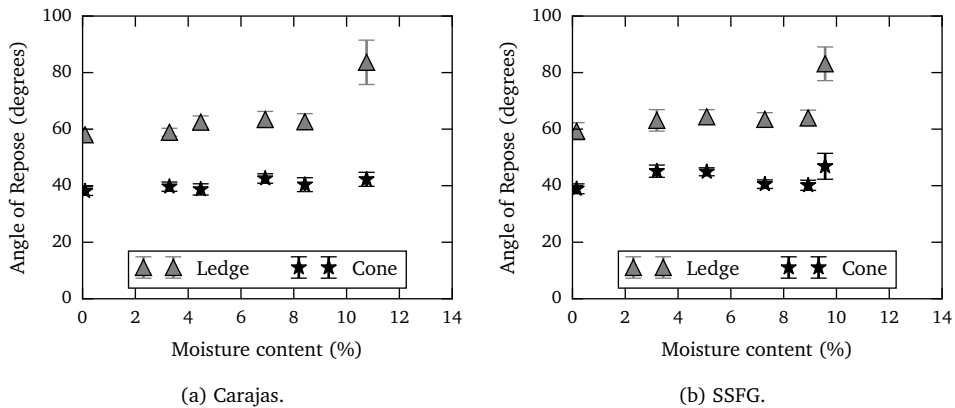(a) Carajas.   (b) SSFG.

Figure 3.7: Angle of repose of iron ore concentrates.

For Sishen ore, angle of repose values were 36.5 degrees for the free cone method and 45.6 degrees for the ledge method as shown in Table 3.2. Completely dry Sishen ore resulted in an increase of 1 degree for the free cone method and 2 degrees for the ledge method. Completely saturated Sishen ore produced a free cone angle of 45.4 degrees and a ledge method angle of 54.8 degrees, with a 95% confidence interval of up to two degrees.

	Dry (0%)	Normal (1%)	Saturated (2.7%)	CI
Free cone method	37.7	36.5	45.4	$1.5-2.0$
Ledge method	47.6	45.6	54.8	$0.8-2.0$

Table 3.2: Angle of repose for Sishen.

Table 3.3 shows the results of iron ore pellets for the two angle of repose test methods. The pellets tended to roll much more than the other materials in the free
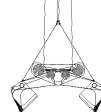
cone test, significantly reducing the angle of repose of the free cone method to 26.0 degrees with a 95% confidence interval of 0.9 degrees. Similar to the other materials, the angle of movement tested by the ledge method showed a large increase compared to the free cone method. The ledge method test of iron ore pellets resulted in an average angle of movement of 40.8 degrees with a confidence interval of 0.5 degrees and can be viewed in Figure 3.6a.

	Angle	CI
Free cone method	26.0	0.9
Ledge method	40.8	0.5

Table 3.3: Angle of repose of iron ore pellets.

3.2.3 Penetration Tests

When a grab is lowered into the bulk material and touches the surface, the knives of the grab penetrate the bulk material. The penetration resistance affects the initial penetration depth and then the closing trajectory of the knifes. Penetration resistance is therefore expected to be a significant material property to the performance of a grab and consequently included in the material characterisation tests. The penetration test determines the amount of resistance met when the bulk material is penetrated with a steel object similar to the knives of a grab. This test should comprehend the resistance met at a certain penetration depth for different ores and penetrating tool shapes. The influence of material properties to the penetration resistance has been investigated by a number of researchers (Ayers and Perumpral, 1982; Muthuswamy and Tordesillas, 2006; Asaf et al., 2007; Fowkes et al., 1973; Gebhardt, 1972). They identified bulk density, moisture content, internal friction and particle size as properties influencing the penetration resistance.

The object that penetrates the bulk material, also called a *tool*, also influences the penetration resistance. Tool related factors are the size, shape, roughness and penetration velocity of the tool (Fowkes et al., 1973; Jiang et al., 2006; Gebhardt, 1972; Kim et al., 2008). Most (soil) research focuses on the angle of the tool using a sharp tip, as blunt tips produce more resistance, making them unattractive in soil research. However, in bulk handling equipment a sharp tip is undesired: due to high wear of iron ore cutting a sharp tip will quickly buckle and fail. Therefore the effect of a blunt tip in the penetration of iron ore pellets will be investigated in this research, by experiments.

A universal tester equipped with a wedge penetrating a container filled with pellets located in the laboratory was selected as the experimental set-up. A Zwick universal tester as seen in Figure 3.8, equipped with a loadcell with a maximum load of 10 kN and a resolution of 0.1 N was used. Tests are conducted with a constant penetration rate, using three different rates: 1, 8 and 32 mm/s. Here the 32 mm/s is determined by the
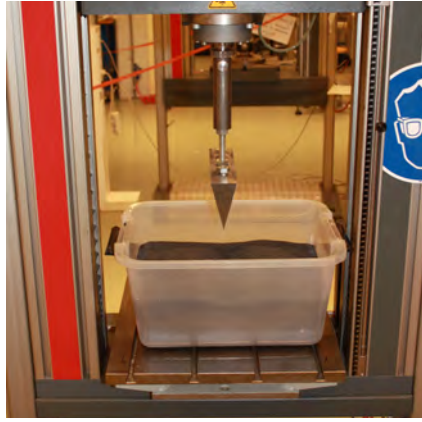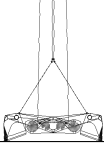
Figure 3.8: Penetration test.

maximum attainable velocity of the universal tester and the $1\,\mathrm{mm/s}$ has been selected to include a pseudo-static penetration. Three tools (Figure 3.9) have been manufactured, each having a length of 200 mm. The size and shape of tool A is similar to the tool used by Asaf et al. (2007)), while the two other tools B and C are of equal length and same angle, only both tools have a blunt tip. Due to the blunt tip they are expected to have a larger penetration resistance than tool A.
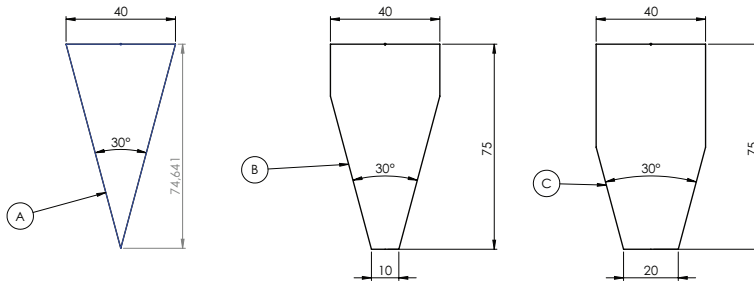

Figure 3.9: Three tools for the penetration test.

The measurement procedure consisted of preparing the sample of iron ore pellets and the actual measurement, this preparation consisted of emptying and refilling the container with pellets. After the bulk material has been prepared, the container is placed under the tool, the measured force is set to zero and the tool starts moving towards the bulk solid. When the tool touches the surface of the soil and a force of 0.5 N is measured, the current position is marked as the beginning of the measurement. From this point, the tool accelerates to the desired penetration rate and starts recording the time, force and depth data every 0.1 seconds seconds. Noise was reduced by performing five measurements, ensuring the detection of possible high variation in measurements.
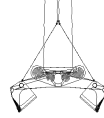
In case of high variation more measurements are performed to minimize the margin of error and reduce the confidence interval to a maximum of 10 of the mean resistance. By integrating the resulting force F over the depth s, the penetration resistance in Joules is obtained.

For iron ore pellets, experiments with blunt tools showed an increase up to a factor of three in penetration resistance compared to the tool with a sharp tip as can be seen in Figure 3.10.
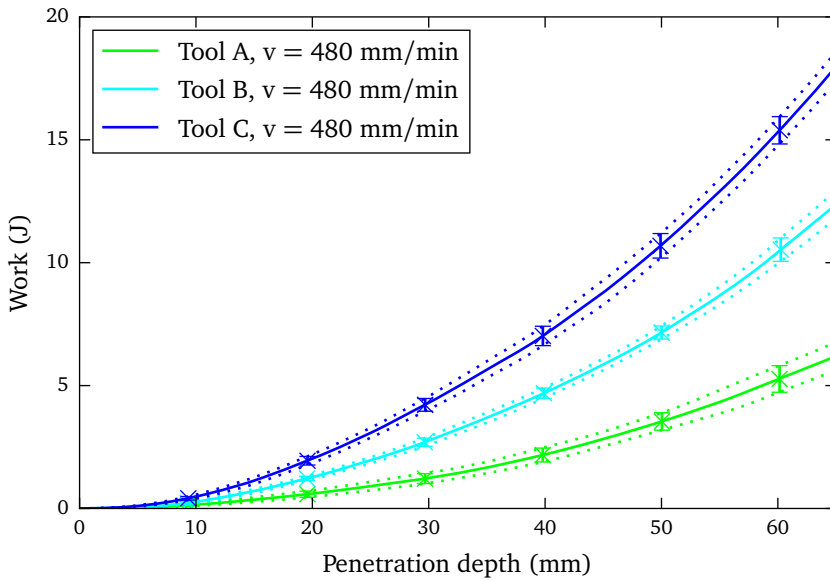

Figure 3.10: Effect of tool shape on penetration resistance.

Besides the tool shape also the penetration velocity was investigated. The penetration velocity did not show a significant influence on the penetration resistance (Figure 3.11) which is in agreement with Fowkes et al. (1973).

Iron ore pellets were also tested for the sensitivity to consolidation, however the effect on the penetration resistance was minimal. This experiment considered three different conditions: loose condition, vibrated condition and vibrated and compacted condition. In comparison, results for MAF concentrate can be viewed in Figure 3.12 and it can be noticed that the consolidation is of large influence on the penetration resistance. The most consolidated condition has a penetration resistance of more than four times that of the least consolidated condition. For grab unloading this means that the loading condition of the iron ore concentrate greatly affects the penetration behaviour of a grab and therefore the unloading capacity. This effect is absent for iron ore pellets due to their large, spherical shape.
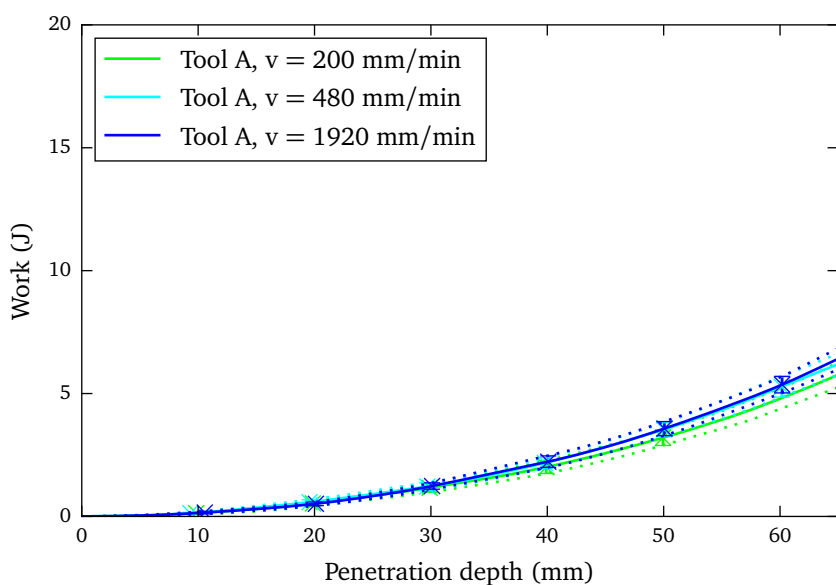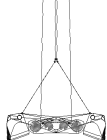
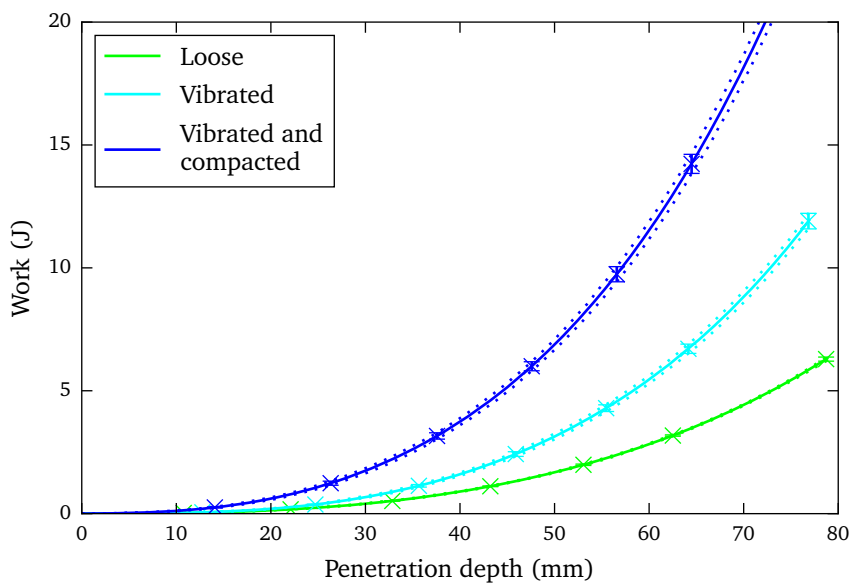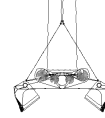Figure 3.11: Effect of penetration velocity on penetration resistance.

Figure 3.12: Effect of consolidation on the penetration resistance.

3.2.4 Flow Moisture Point Tests

As described in Section 3.1.1, moisture in the bulk material can suddenly affect the behaviour of the material through liquefaction, possibly triggered by vibrations. It is important to establish the flow moisture point of the tested materials to exclude materials that are sensitive to liquefaction. The flow moisture point (FMP) of a bulk material marks the moisture content at which the characteristics of the material become unstable. The FMP was determined using a penetration test, according to the standard described in the governing IMBSC code (International Maritime Organization, 2011). The transportable moisture limit (TML) is set to 90% of the FMP; this is the maximum amount of moisture in the bulk material still considered safe for transport. The IMBSC code also documents two other methods for testing the FMP, the Proctor-Fagerberg test and the flow table test. The penetration test was found to be the most conservative test in a comparison between three test methods in Appendix A.

Figure 3.13 shows the selected penetration test bolted to a vibration table. Materials were sieved and particles with a diameter of above 6.3 mm were excluded, as the test is not suitable for these large particles. The material was tampered in four layers and a pore pressure sensor was placed between the first and second layer. After the material was tampered, the cone was placed on top of the material and vibration of $2g$ started. The amount of penetration of the cone was measured: If penetration was more than 50 mm, the material has reached the FMP.
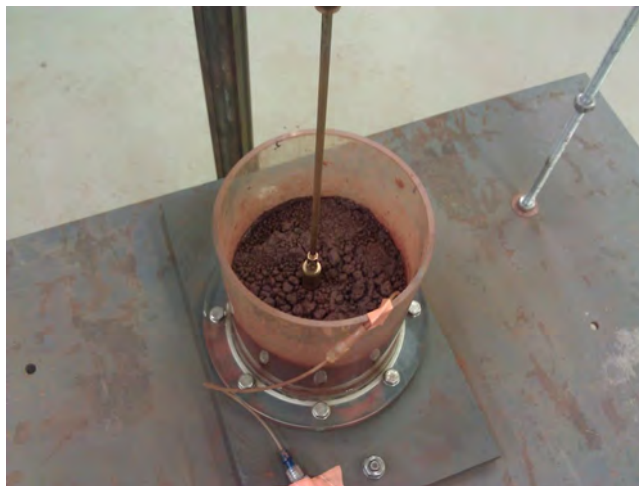

Figure 3.13: Flow moisture point test.

The flow moisture test was conducted for the three materials as well. After the vibration had been initiated, pore pressure increased and ores with a moisture content above FMP started to liquidate, allowing the cone to penetrate the material. The flow moisture point of Carajas ore was between 7.0% and 7.3% dry based as can be seen in

Figure 3.14. The FMP of SSFG was located between 7.0% and 7.2% dry based, scoring slightly lower values than Carajas ore. These moisture contents match the points where the bulk density starts increasing again with the moisture content.
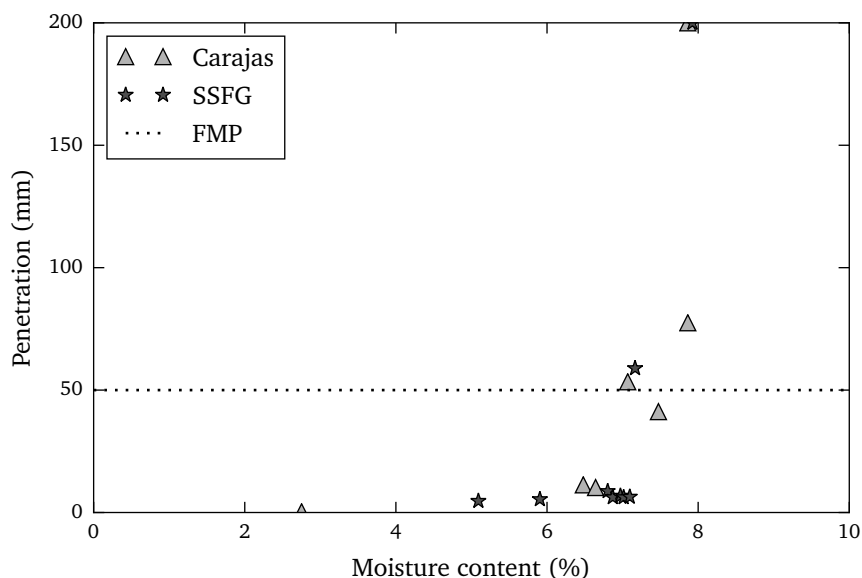

Figure 3.14: Flow moisture point penetration test for Carajas and SSFG ore.

As the Sishen ore did not show an increase in bulk density, it was expected that it would not liquidate. This has been confirmed since the flow moisture point was not found. This was verified by a penetration test using an excessive amount of water, submerging the ore. Even in this submerged state it was not possible to achieve penetration of more than 50 mm, due to the low number of fines present in Sishen ore. Therefore, it is unlikely that Sishen ore will liquidate. This also applies to iron ore pellets, which have an even smaller fines fraction.

3.2.5   Wall Friction and Rolling Resistance Tests

For bulk materials with a large median particle size such as iron ore pellets, a Jenike shear cell cannot be used to determine the wall friction coefficient. Large particles also tend to roll more, as their high mass increases the kinetic energy of the particles. Wall friction is an important factor in the closing of the grab, since it directly influences the grabbing resistance caused by the bulk material sliding along the inside and edges of the grab. Another characteristic that is taken into account is the rolling resistance of particles. The rolling resistance of particles affects the angle of repose, which in turn affects the filling process of a grab. Therefore both the wall friction coefficient and the
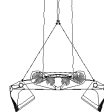
rolling resistance for larger particles are included as characterisation tests.

The wall friction coefficient φ_w quantifies the amount of friction between the bulk material and a wall. The wall friction coefficient is related to the wall friction angle according to Equation 3.2. The wall friction angle is the angle at which the frictional forces equal the gravitational forces of the body along the slope.

$$\tan(\theta) = \varphi_w \tag{3.2}$$

Figure 3.15 shows a schematic view of the apparatus used to measure the wall friction coefficient. A container with filled with particles is placed onto a steel slope. Rolling of the particles is prevented by blocking angular motion. During the experiment, the angle θ is slowly increased until the container with particles starts to slide downwards. At this point, the gravity forces from the container along the slope are larger than the friction can withstand, indicating that the wall friction angle has been reached. This procedure was repeated five times with different particles in the container.
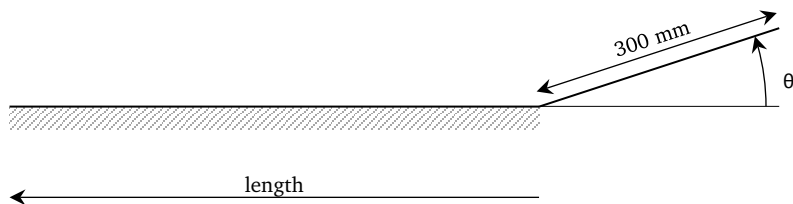

Figure 3.15: Set-up for measuring the wall friction and rolling friction coefficient.

A wall friction test was used to estimate the wall friction angle between iron ore pellets and steel. The wall friction angle between pellets and steel amounted to 22.5 degrees. Five measurements resulted in a 95% confidence interval of 0.5 degrees. The absence of rolling of the particles was confirmed by visual inspection, which was relatively easy due to the large particle diameter.

The rolling resistance was measured with the same set up of Figure 3.15. Particles were released at the top of the slope of 300 mm with a fixed angle $\theta = 14.7$ degrees and allowed to roll down the slope. For each particle, the total distance travelled was measured and this was repeated five times. Occasionally particles did not roll in a straight line but deviated from their trajectory in the final centimetres. These measurements were rejected as the distance measurements only considered the straight line distance. The rolling resistance test was conducted for 30 randomly selected iron ore pellets.
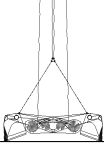
The rolling resistance test was also conducted with iron ore pellets and a steel surface. Pellets rolled down the slope and the distance covered was measured. The average rolling distance of a particle consisted of the complete slope and 22 centimetres of the flat surface. The high variation in the covered distance, likely to be caused by the variation in shapes, required the test to be repeated 150 times to achieve a 95% confidence interval of 1.5 centimetres. An interesting observation in this test was that larger particles tended to have a lower rolling resistance than smaller particles, though size is not a factor in the rolling resistance models of Chapter 4. This difference in resistance is probably not caused by the size or mass of the particles but instead due to the shape of the particles. Small and large particles showed surface deviations of roughly the same size, but due the size of the particles, a larger particle appeared to be more spherical, therefore a lower rolling resistance can be explained.

3.3 Selecting a Material to be Modelled

The previous sections have presented multiple experiments to characterize the iron ores. Based on the outcome of these experiments, one of the iron ores is selected for the material model fit for the simulation of the bulk material. Iron ore was chosen for the large number of shipments as well as the heavy and abrasive nature, making unloading a challenging task. In selecting one of the tested ores, several aspects need to be taken into account such as how the lab conditions can be related to the conditions of the validation test at a bulk terminal.

The two materials with a large fraction of fines, SSFG and Carajas ore, showed that changes in moisture content did affect the material characteristics. The bulk density was affected, however it did not affect the angle of repose until the ore was extremely moist with its moisture content above the transportable moisture limit (TML). It should be noted that both material behaved similar under the same moisture content, however the tested Carajas ore has a default moisture content of 6.3%, which is very close to its transportable moisture limit that lies between 6.3 and 6.6 percent, while SSFG has a lower content of 5.3% at a similar TML. This makes developing a material model for Carajas ore complex, as the material may liquidate temporarily during the experiments due to vibrations or the testing procedure.

The penetration test investigated the effect of the consolidation for iron ore fines and showed that the penetration resistance was greatly affected by consolidation of the material. In order to replicate grab unloading conditions in a material model, these conditions need to be quantified. However, it was not possible to link the tested consolidation conditions to the grab unloading conditions. Therefore, selecting a material with a negligible effect of consolidation such as iron ore pellets is preferred. Another benefit of selecting iron ore pellets is their larger size and spherical shape, which have advantages in a numerical simulation as can be read in Chapter 4.
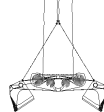
3.4 Conclusions

Iron ore concentrates and pellets have been tested extensively in this chapter and the pellets have been found the most suitable candidate for the material model. Pellets were preferred for their insensitivity to consolidation. Tests included density tests, angle of repose tests, penetration tests, flow moisture point tests, wall friction tests and rolling resistance tests. Particle density of pellets was measured at $4260\,\mathrm{kg/m^3}$ while bulk density was measured at $2135\,\mathrm{kg/m^3}$ after consolidation through vibration. Angle of repose of pellets have been measured at 26.0 and 40.8 degrees for a free cone method and a ledge method. Penetration resistance of pellets increased up to three times when using blunt tools while showing no effects of penetration rate or compaction. Wall friction angle was measured at 22.5 degrees while a rolling resistance test resulted in a average rolling distance of $22\,\mathrm{cm}$. These tests have produced all necessary data for calibrating a material model. This material model will be formulated in the next chapter and can then be used in co-simulation of grab and iron ore pellets.
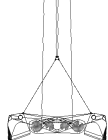
"Great things are done by a series of small things brought together."

Vincent van Gogh (1853 – 1890)

4

A Material Model for Iron Ore Pellets*

A material model of iron ore pellets is required to accurately predict the performance of a grab. This chapter establishes such a material model based on the iron ore pellets characteristics assessed in the previous chapter and the Discrete Element Method (DEM). The Discrete Element Method is a computational method that allows for the simulation of bulk materials, calculating each collision between particles according to contact properties of the material model. This chapter presents the calibration of the material model based on iron ore pellets characteristics, including the calibration tests themselves and their sensitivity to material model parameters. This is essential to the accuracy of the material model and as a consequence also essential to the accuracy of predicting grab performance.

The first section of this chapter describes the Discrete Element Method, a numerical method for particle based simulations. Section 4.2 presents the contact models that represent the collisions between particles, taking into account aspects such as contact forces, sliding and rolling resistance. Section 4.3 gives and overview of the material model parameters and the calibration approaches available. Section 4.4 investigates several calibration tests and their sensitivity to model parameters. These tests include a penetration tests, two angle of repose tests, a rolling friction test and a wall friction test, similar to the characterization tests of Chapter 3. In Section 4.5 the material model of iron ore pellets is calibrated based on the characteristics of iron ore pellets measured

---

*This chapter is partially based on Lommen et al. (2011, 2013)
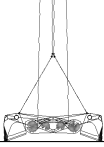
in the previous chapter. The result is a material model capturing the characteristics of iron ore pellets which can be used in a simulation of iron ore pellets.

4.1   Discrete Element Method

The Discrete Element Method (DEM) is a numerical method allowing for the simulation of granular materials. By considering particles as discrete elements, interactions with neighbouring particles and walls can be computed and the behaviour of the granular material can be simulated. Its development was initiated by Cundall and Strack (1979), which has started a branch of research and software development focussing on simulating bulk materials. A general DEM algorithm shown in Figure 4.1 consists of a loop containing four phases:
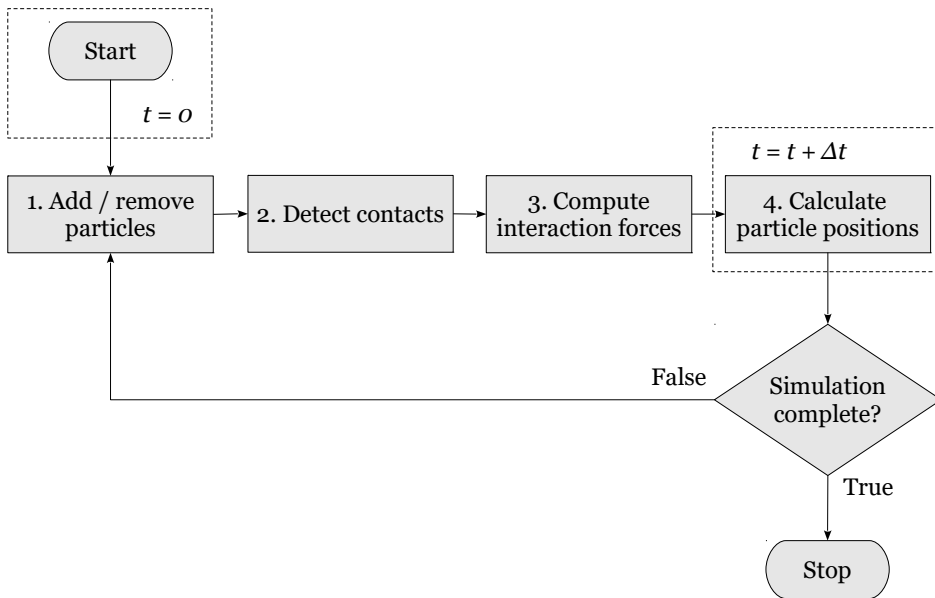

Figure 4.1: DEM algorithm.

1. Particles are added according to the settings of the particle generator. Particles outside the computational domain are removed from the simulation.

2. Contacts between particles and contacts between particles and equipment are detected with the help of a contact detection algorithm. Particles are modelled as rigid bodies and are allowed to overlap.
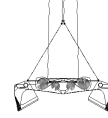
3. For each contact pair the interaction forces are computed based on the amount of overlap and the help of a contact model.

4. Particle movements are derived from the interaction forces and other forces acting on the particle during the small increment of time Δt, also called timestep. This results in new particle positions when the simulation advances to the next timestep.

After an iteration the current simulation time is compared to the configured stop time of the simulation. If the simulation has not reached the stop time, a new iteration of the loop is performed.

Adding particles to a simulation can be done through a particle generator. A particle generator can be instructed to generate a specified number of particles at a timestep, allowing for both filling a volume at once as well as continuous filling according to a specified rate. Particles can be created according to a particle size distribution, and their location can be set or they can be randomly placed in the simulation domain. Removing particles can be performed when a particle leaves the simulation domain or when a specified limit is exceeded, for example when a particle's velocity becomes unrealistically high and destabilizes the simulation.

The purpose of the contact detection algorithm is to detect all existing contacts between particles. This is done by dividing the simulation space into a grid of cells and checking for all grid cells if particles are in contact. Without the use of a grid, contact has to be checked between all particles, leading to an exponentially increasing detection time when the number of particle increases. The smaller the grid, the more efficient the contact detection becomes, since this reduces the number of contact checks of particle pairs not in contact, although memory requirements will increase. For further reading on contact detection algorithms the reader is referred to Munjiza (2004).

The computational costs of the detection algorithm depend on the complexity of the mathematical description of the surface of both particles. Contacts between simple spherical shapes can be detected fast, as the mathematical description of the surface of a sphere is also simple. An example of two spherical particles in contact is shown in Figure 4.2, here contact can be detected by checking whether Equation 4.1 is true.

$$\| \mathbf{x}_i - \mathbf{x}_j \| < R_i + R_j \tag{4.1}$$

Surface descriptions of multi-spheres are more complicated and therefore make detecting contacts computationally more expensive. Elements with sharp corners such as tetrahedrons or cubes require additional computational effort for determining the normal and shear direction of a contact pair (Hogue, 1998), further increasing the computational costs.
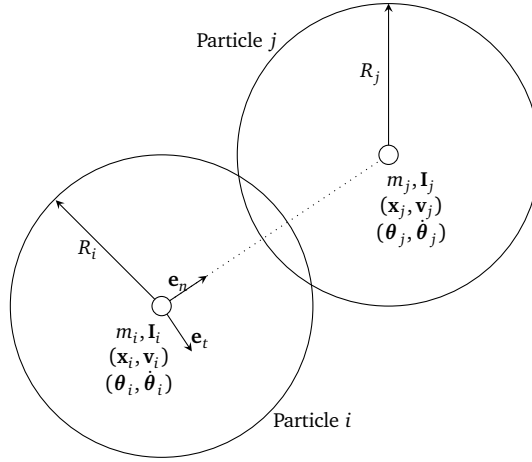
Figure 4.2: Two spherical particles i and j in contact. Each particle has a mass m, moments of inertia $\mathbf{I}$, a radius R, position $\mathbf{x}$, orientation $\boldsymbol{\theta}$ and velocities $\mathbf{v}$ and $\dot{\boldsymbol{\theta}}$ in three dimensional space. The unit vectors $\mathbf{e}_n$ and $\mathbf{e}_t$ are used to determine the normal and shear direction of the contact.

The overlap of contact pairs detected in the contact detection phase is used to compute the interaction forces of contact pairs. Overlap between particles can be in normal direction $\mathbf{e}_n$ as well as in tangential direction $\mathbf{e}_t$, representing the deformation of the particles. The larger the amount of overlap, the higher the amount of interaction force acting on both particles of the contact pair. Whether the interaction forces are proportional to the overlap depends on the formulation of the contact model.

For spherical particles the normal overlap δ_n can be computed by first determining the normal direction unit vector $\mathbf{e}_n$ (Equation 4.2). The normal overlap can then be calculated based on the difference between the distance between the spheres minus their combined radii (Equation 4.3). Next, the relative velocity vector $\mathbf{v}_{ij}$ at the contact point can be calculated with Equation 4.4, based on the velocities at the centre of masses $\mathbf{v}_i$ and $\mathbf{v}_j$ and the angular velocities $\dot{\boldsymbol{\theta}}_i$ and $\dot{\boldsymbol{\theta}}_j$. The relative normal velocity in the contact $\mathbf{v}_n$ can be computed by taken the inner product of $\mathbf{v}_{ij}$ and the normal direction vector $\mathbf{e}_n$ (Equation 4.5). The relative tangential velocity $\mathbf{v}_t$ can then be computed using Equation 4.6.

$$\mathbf{e}_n = \left(\mathbf{x}_i - \mathbf{x}_j \right) / \parallel \mathbf{x}_i - \mathbf{x}_j \parallel \tag{4.2}$$

$$\delta_n = \left(\mathbf{x}_i - \mathbf{x}_j \right) \cdot \mathbf{e}_n - \left(R_i + R_j \right) \tag{4.3}$$

$$\mathbf{v}_{ij} = \left(\mathbf{v}_i - \mathbf{v}_j \right) + \left(\dot{\boldsymbol{\theta}}_i \left(R_i - \frac{1}{2} \delta_n \right) + \dot{\boldsymbol{\theta}}_j \left(R_j - \frac{1}{2} \delta_n \right) \right) \tag{4.4}$$

$$\mathbf{v}_n = \mathbf{e}_n \left(\mathbf{v}_{ij} \cdot \mathbf{e}_n \right) \tag{4.5}$$

$$\mathbf{v}_t = \mathbf{v}_{ij} - \mathbf{v}_n \tag{4.6}$$

The tangential overlap $\boldsymbol{\delta}_t(t)$ at time t is calculated incrementally by adding the increment $\mathbf{v}_t \Delta t$ to the value of tangential overlap $\boldsymbol{\delta}_t$ of the previous timestep $t - \Delta t$ (Equation 4.7) rotated by a matrix O based on the transformation of $\mathbf{e}_n(t - \Delta t)$ to $\mathbf{e}_n(t)$.

$$\boldsymbol{\delta}_t(t) = O \boldsymbol{\delta}_t(t - \Delta t) + \mathbf{v}_t \Delta t \tag{4.7}$$

A *contact model* is used for calculating the contact forces based on a set of contact properties P such as overlap $\boldsymbol{\delta}$ and relative velocities $\mathbf{v}$. A general form of normal and tangential force contact models is given in Equation 4.8 and 4.9, and a more thorough description can be found in Section 4.2.

$$\mathbf{F}_n = f(P_n) \tag{4.8}$$

$$\mathbf{F}_t = f(P_t) \tag{4.9}$$

Various contact models exist, with the linear spring being the most commonly used contact model (Di Renzo and Di Maio, 2004). A popular, more detailed contact model consists of a normal contact based on Hertz (1882) and a tangential force calculation based on the work of Mindlin and Deresiewicz (1953). Usually a contact model consists of an elastic component and a damping component, resulting in a elastic force and a damping force in the contact. The contact model uses the overlap and various parameters to determine these interaction forces occurring in the contact of two particles.

The first step towards calculating the new particle positions is the computation of the net force $\Sigma \mathbf{F}_i$ acting on a particle i with Equation 4.10. All interaction forces from contacts with different particles are summarized and gravitational and other particle body forces are included. A similar procedure exist for computing the net torque $\Sigma \mathbf{T}_i$ on the particle i (Equation 4.11).

$$\Sigma \mathbf{F}_i = \sum (\mathbf{F}_n + \mathbf{F}_t) + m_i \mathbf{g} \tag{4.10}$$

$$\Sigma \mathbf{T}_i = \sum \mathbf{F}_t R_i + \sum \mathbf{T}_i \tag{4.11}$$

Newton and Euler equations (Equation 4.12 and 4.13) for each particle determine the accelerations $\ddot{\mathbf{x}}_i$ and angular accelerations $\dot{\boldsymbol{\theta}}_i$.

$$\ddot{\mathbf{x}}_i(t) = \frac{\Sigma \mathbf{F}_i}{m_i} \tag{4.12}$$

$$\ddot{\boldsymbol{\theta}}_i(t) = \frac{\Sigma \mathbf{T}_i}{I_i} \tag{4.13}$$

An integration scheme such as the forward difference scheme (Equation 4.14 and 4.15) can calculate the particle velocities and particle positions after time step Δt. Numerous integrations schemes suitable for DEM exist, competing on efficiency and accuracy, guidelines for selecting an appropriate integration scheme have been presented by Kruggel-Emden et al. (2008a)

$$\dot{\mathbf{x}}_i(t + \Delta t) = \dot{\mathbf{x}}_i(t) + \ddot{\mathbf{x}}_i(t)\Delta t$$
$$\mathbf{x}_i(t + \Delta t) = \mathbf{x}_i(t) + \dot{\mathbf{x}}_i(t)\Delta t \tag{4.14}$$
$$\dot{\boldsymbol{\theta}}_i(t + \Delta t) = \dot{\boldsymbol{\theta}}_i(t) + \ddot{\boldsymbol{\theta}}_i(t)\Delta t$$
$$\boldsymbol{\theta}_i(t + \Delta t) = \boldsymbol{\theta}_i(t) + \dot{\boldsymbol{\theta}}_i(t)\Delta t \tag{4.15}$$

The timestep Δt is the increment of time used to advance the simulation and needs to be chosen in such a way that computational costs are minimized while results are not affected. A common choice for the timestep is a fraction γ of the Rayleigh timestep Δt_R according to Equation 4.16. The Rayleigh timestep is the time needed for a shear wave to propagate through a solid particle (Ning, 1995) and depending on several particle properties described in Section 4.3. The fraction γ of the Rayleigh timestep commonly ranges from 0.2 to 0.4 for quasi-static particle simulations. The stability of DEM simulations coupled with MBD simulations will be discussed in more detail in Section 6.3, including the choice for the timestep Δt.

$$\Delta t_R = \pi R \sqrt{\frac{\rho}{G}} / (0.1631\nu + 0.8766) \tag{4.16}$$

4.2   Contact Models

Contact models calculate the contact forces based on the overlap of the contacting particles, as stated in Equation 4.8 and 4.8. The contact between two particles can be modelled with a set of springs, dashpots, frictional slider and a possible cohesion bond (Figure 4.3). Based on the overlap and the springs, dashpots, sliders and bonds in the contact model interaction forces are computed. By choosing the right coefficients and contact model, particle interaction can be accurately modelled.
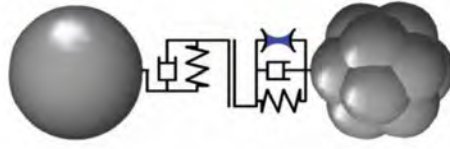
Figure 4.3: Contact between two particles modelled with springs, dashpots, friction slider and cohesion bond (Gröger and Katterfeld, 2007).

Cundall and Strack (1979) proposed a linear spring dashpot model where the contact force is proportional to the overlap of the contact pair. This linear model was preferred for its efficient linear computation, however nowadays the most common contact model is the Hertz-Mindlin model. This model produces similar macroscopic results, however its microscopic results are considered to be more accurate (Di Renzo and Di Maio, 2004), as it is based on the elastic theory of normal contact points of Hertz (1882) and the no-slip solution for the tangential contact proposed by Mindlin and Deresiewicz (1953).

The Hertz-Mindlin normal and tangential contact forces are a function of overlaps δ, velocities v and stiffness and damping coefficients (Equation 4.17 and 4.18). The damping component is based on the approach of Tsuji et al. (1992). Many studies have investigated the contact models describing the collisions between particles, for example Zhang and Vu-Quoc (2000) and Zhu et al. (2007). Extensive comparisons between contact models can be found in the work of Kruggel-Emden et al. (2007) and Kruggel-Emden et al. (2008b), including both normal and tangential models. Such comparisons will not be repeated in this study, instead the Hertz-Mindlin model is used.

$$\mathbf{F}_n = k_n \delta_n^{\frac{3}{2}} \mathbf{e}_n + c_n \mathbf{v}_n \sqrt{\frac{3}{2} k_n} \delta_n^{\frac{1}{4}} \tag{4.17}$$

$$\mathbf{F}_t = k_t \sqrt{\delta_n} \boldsymbol{\delta}_t + c_t \mathbf{v}_t \sqrt{k_t} \delta_n^{\frac{1}{4}} \tag{4.18}$$

k_n and k_t are the normal and tangential stiffness coefficients and c_n and c_t are the normal and tangential damping coefficients as defined in Equation 4.19 and 4.20.

$$k_n = \frac{4}{3} E^* \sqrt{R^*} \quad \text{and} \quad c_n = -2\sqrt{\frac{5}{6}} \beta \sqrt{m^*} \tag{4.19}$$

$$k_t = -8 G^* \sqrt{R^*} \quad \text{and} \quad c_t = -2\sqrt{\frac{5}{6}} \beta \sqrt{m^*} \tag{4.20}$$

These stiffness k and damping c coefficients are based on the properties of both colliding particles i and j. The equivalent Young's Modulus E^* and Shear Modulus G^*

of a contact can be in found in Equation 4.21 and 4.23. The equivalent radius R^* and mass m^* of a contact can be found in Equation 4.24 and 4.25. In case of a particle-wall interaction, the wall radius is $R_j = \infty$ and therefore $R^* = R_i$. For the equivalent mass in case of particle-wall contact, the wall mass is $m_j = \infty$ and therefore $m^* = m_i$.

$$\frac{1}{E^*} = \frac{\left(1 - v_i^2\right)}{E_i} + \frac{\left(1 - v_j^2\right)}{E_j} \tag{4.21}$$

$$E_i = 2G_i\left(1 + v_i\right) \tag{4.22}$$

$$\frac{1}{G^*} = \frac{\left(2 - v_i\right)}{G_i} + \frac{\left(2 - v_j\right)}{G_j} \tag{4.23}$$

$$\frac{1}{R^*} = \frac{1}{R_i} + \frac{1}{R_j} \tag{4.24}$$

$$m^* = \frac{m_i m_j}{m_i + m_j} \tag{4.25}$$

$$\beta = \frac{\ln C_R}{\sqrt{\ln^2 C_R + \pi^2}} \tag{4.26}$$

The damping coefficient β of Equation 4.26 is based on the coefficient of restitution C_R, which is defined as the ratio between the relative velocity of a particle before impact and the relative velocity of a particle after impact (Equation 4.27). A contact pair with $C_R = 1$ collides elastically, while pairs with $C_R = 0$ collide completely inelastic. It should be noted that this property depends on the damping behaviour of the contact and thus depends on both particles.

$$C_R = \frac{v_{\text{after collision}}}{v_{\text{before collision}}} \tag{4.27}$$

It can be observed that frictional coefficients do not influence the Hertz-Mindlin model, yet their influence is taken into account after applying the frictional slider and the rolling friction torque. The frictional slider is taken into account by limiting the tangential force $\mathbf{F}_t$ using the Coulomb friction law in Equation (4.28). When the limiting of the tangential force occurs, the tangential overlap $\boldsymbol{\delta}_t$ of Equation 4.7 is limited at the Coulomb friction force divided by the tangential stiffness with the help of Equation 4.29.

$$\|\mathbf{F}_t\| \leq \mu_s \|\mathbf{F}_n\| \tag{4.28}$$

$$\|\boldsymbol{\delta}_t\| \leq \frac{\mu_s \|\mathbf{F}_n\|}{k_t \sqrt{\delta_n}} \tag{4.29}$$

Rolling friction is accounted for by applying an additional torque $\mathbf{T}_r$ to both the
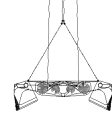
contacting particles, according to Equation 4.30. Here μ_r is defined as the tangent of the maximum angle of a slope where the torque of the rolling friction $\mathbf{T}_r$ counterbalances the torque generated by the gravity acting on the body.

$$T_{r,m} = -\mu_r R_i \left\| \mathbf{F}_n \right\| \qquad (4.30)$$

This torque can be implemented in several ways, Ai et al. (2010) compares four types of implementations and recommends model C for quasi-static simulations.

Model C rolling friction is an elastic-plastic spring-dashpot rolling friction model, where the amount of rolling friction torque $\mathbf{T}_r$ depends on the torque provided by the spring $\mathbf{T}_{r,k}$ and the dashpot $\mathbf{T}_{r,d}$ according to Equation 4.31.

$$\mathbf{T}_r = \mathbf{T}_{r,k} + \mathbf{T}_{r,d} \qquad (4.31)$$

The spring torque $\mathbf{T}_{r,k}$ depends on the rolling stiffness k_r of the contact and the incremental relative rotation between the two particles $\Delta\theta$ (Equation 4.32). The spring torque $\mathbf{T}_{r,k}$ is limited by Equation 4.33, this way the rolling friction is identical to Equation 4.30 when the rolling friction is fully mobilized.

$$\mathbf{T}_{r,k} = \mathbf{T}_{r,k}\left(t - \Delta t\right) - k_r \Delta\boldsymbol{\theta} \qquad (4.32)$$

$$\mathbf{T}_{r,k} = \begin{cases} \mathbf{T}_{r,k} & \left\| \mathbf{T}_{r,k} \right\| \leq -T_{r,m} \\ T_{r,m} \dfrac{\mathbf{T}_{r,k}}{\left\| \mathbf{T}_{r,k} \right\|} & \left\| \mathbf{T}_{r,k} \right\| > -T_{r,m} \end{cases} \qquad (4.33)$$

Following the suggestion of Wensrich and Katterfeld (2012), the rolling stiffness of Iwashita and Oda (1998) shown in Equation 4.34 is used and the viscous rolling damping torque is disabled. This removes the inelastic component as otherwise additional parameters would need to be calibrated, complicating the calibration process unnecessarily. The inelastic component will be reintroduced if it turns out to be essential to calibration of the material model.

$$k_r = k_t \sqrt{\delta_n} (R^*)^2 \qquad (4.34)$$

An alternative for the rolling friction models is the disabling of the rotation degrees of freedom of a particle (Bierwisch, 2009). He shows that although this seems unrealistic, it is possible to reproduce flow and static phenomena such as the angle of repose. Kessler and Prenner (2012) demonstrate this but also warn for unrealistic material accumulation due to the lack of roll-ability of the particles. Both the rolling model described above and the disabled rolling are considered when calibrating the material model.

4.3   Parameters of a Material Model

The behaviour of the contact model and therefore the simulated bulk material can be altered by changing the parameters of the contact model. These input parameters need to be configured in such a way that the simulated material behaviour reflects the material characteristics. Establishing adequate values for these parameters can be ensured through a process of calibration, where the input parameters are adjusted until a satisfactory material model has been developed.

Table 4.1 gives an overview of the most common input parameters that can be calibrated in a contact model, although these and their effect depend on the configuration and complexity of the contact model. The first three parameters G, ν and ρ are material properties, while the next three parameters C_R, μ_s and μ_r are interactions parameters which depend on both the materials involved in the contact. The static friction coefficient between wall and particles is designated as the wall friction coefficient ϕ_w, while the rolling friction coefficient between wall and particles is called ϕ_r. These are the input parameters that will be used in the iron ore pellets material model.

Property	Symbol	Unit
Shear Modulus	G	Pa
Poisson's ratio	ν	-
Particle density	ρ_p	kg/m³
Coefficient of restitution	C_R	-
Static Friction coefficient	μ_s	-
Rolling Friction coefficient	μ_r	-

Table 4.1: Input parameters.

The values for these input parameters can be based on different sources. Literature would be the most convenient way to determine these values, however literature values often cannot be applied directly into a simulation as the material and the contact model in literature are not identical to the material and used contact model. Another approach to acquire the values of input parameters is to measure these properties directly and independently, however this also presents difficulties. For example, measuring the stiffness of iron ore particles is complicated by the possible deformation of the testing equipment and the irregular shape of the particles (Paulick et al., 2014). Measuring the coefficient of restitution can be achieved with high-speed cameras (Grima and Wypych, 2010), although creating a reliable particle-particle collision proves to be hard. In order to achieve reliable results, it is considered best to determine the values by examining the material characteristics and calibrating the simulations to match
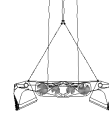
these characteristics.

Common tests to measure and calibrate the mechanical properties of bulk solids are triaxial tests and shear cells. It has been used to calibrate DEM parameters by various researchers (Härtl and Ooi (2008), Plassiard et al. (2009) and Tannant and Wang (2002)), which have calibrated friction and stiffness parameters. Another way to determine friction parameters is through an angle of repose test (Grima and Wypych, 2011; Katterfeld et al., 2013). A penetration test as calibration experiment has been used by Asaf et al. (2007). Pin on disk rotational testers can be used to estimate wear and sliding friction coefficients (Barrios et al., 2013).

Calibration is usually performed by trial and error, where the user will simulate until a match with the experiment can be produced. The influence of the relevant parameters is detected during a sensitivity analysis and this aids the user in estimating the material model parameters. Simulations using these estimated parameters are then compared to the experimental results and if necessary parameters are adjusted. Optimization techniques are not common, but are promising although they require intensive computational effort. Asaf et al. (2007) used the Nelder–Mead algorithm to minimize the area difference between real and simulation curves, however initial estimates of parameters needed to be close enough to the proper value of parameters. To determine the input parameters for the material model of iron ore pellets, calibration tests based on the experimental tests of Chapter 3 will be conducted.

4.4 Calibration Tests and Their Sensitivity to Model Parameters

In order to calibrate the material behaviour recorded with the experimental set-ups of Chapter 3, these tests need to be simulated with the Discrete Element Method. All parts significant to the material behaviour have to be modelled, this will make the experimental and the virtual set-up comparable and therefore the experimental and virtual material behaviour becomes comparable.

Particles are modelled according to the particle size distribution of Figure 3.3. This consists of generating spherical particles with an average particle radius R of 5.5 mm and a normalized standard deviation of 0.1. The choice for spherical particles follows from the average iron ore pellet shape and the fact that spherical elements are computationally the least expensive shape representation. Multi-spherical particles composed from multiple spheres can approximate the particle shape better, however this comes at additional computational costs which is too high for a co-simulation of roughly 77 m^3 of bulk material. The subject of computational costs of DEM simulations will be examined in more detail in Chapter 5, including the effects of increasing the particle size and lowering the stiffness coefficients.

The DEM software used in this research is EDEM®, a package developed by DEM-Solutions (DEM Solutions, 2014a). This program is equipped with several contact

models such as the Hertz-Mindlin model mentioned in Section 4.2. The software has been selected for its graphical interface, its coupling capabilities and the existing experience with this software at Delft University of Technology. The software package allows for the complete configuration of the model, including particle shape and CAD geometry import. It uses parallel processing on a workstation computer to shorten the computational time which makes it capable of simulating large scale particle processes.

Two contact models have been examined in the sensitivity analysis; the Hertz-Mindlin with angular movements restricted and the Hertz-Mindlin model with rolling model C. The rolling-restricted model has been selected as Bierwisch (2009) suggests that for spherical particles this can be useful. Moreover, the default rolling friction model of EDEM® is considered deficient by Ai et al. (2010) due to possible unbalanced torques of the contact. Because the rolling friction is dependent on the rotational velocity of a particle instead of the relative rotational contact velocity, it is possible that both particles of the contact have different rolling friction torques. As a consequence, the contact might not be in equilibrium and therefore the use of this rolling friction model should be avoided. The assessment of Ai et al. suggests that the rolling friction model C is the most capable model for pseudo-static processes, consequently this model is selected as well for the sensitivity analysis.

4.4.1   Bulk Density Test

For the bulk density test, a volume slightly larger than the set-up of Section 3.2.1 is filled with particles. Next, particles inside the space identical to the volume of the experiment are counted and their mass is summarized. This way the volume will be completely filled with particles, similar to the experimental bulk density test. Four different compaction methods are simulated: loose, vibrated, compacted and the combination of vibration and compaction, each method identical to the corresponding experimental method. The bulk density test examines the sensitivity of the input parameters on the bulk density at these four compaction levels.

Figure 4.4 shows that the relation between particle and bulk density is almost proportional, with the bulk density ranging between 0.57 and 0.59 times the particle density for the various compaction methods. Both contact models produced similar results. The different compacting methods only show marginal effects on the bulk density, for example vibrating the sample increased the bulk density with less than one and a half percent. Other input parameters showed negligible effects and therefore the bulk density has to be calibrated solely by selecting an appropriate particle density ρ_p. In order to achieve the bulk density of between 2067 kg/m³ and 2146 kg/m³ determined in the experiments, a particle density ρ_p near 3700 kg/m³ is required.
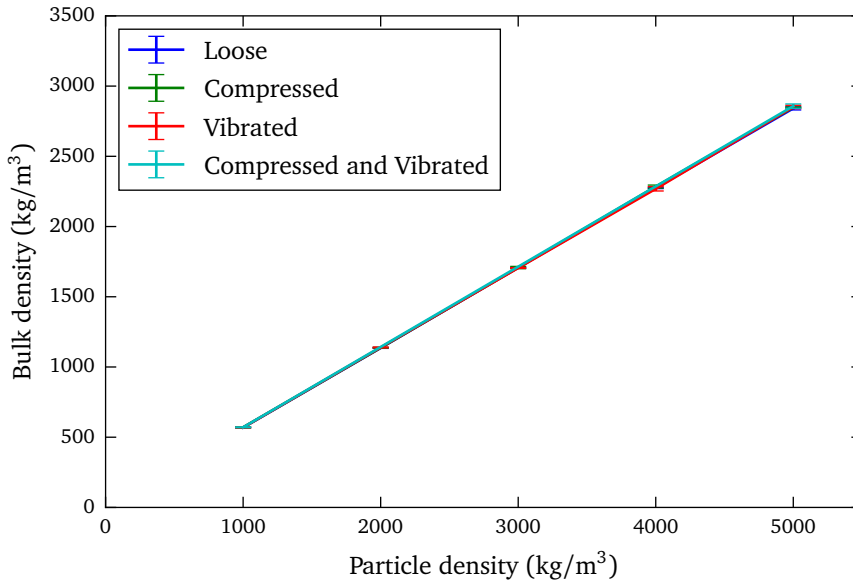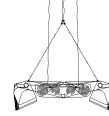
Figure 4.4: Bulk density.

4.4.2   Angle of Repose Tests

The two angle of repose tests are also modelled in EDEM®, displayed in Figure 4.5a. The ledge method test was randomly filled with particles at the initial timestep, which then fell down and settled until semi-steady state has been reached. Next, the flap of the box started to open and particles started moving in the direction of the opening in the box. Once particles had left the box they would continue falling down due to the effects of gravity until they left the computational domain. This simulation was allowed to continue until particles stopped flowing out of the box and the average particle velocity was approaching zero. Based on the remaining particles in the box the angle of repose was determined.

The free cone test has been simulated in a similar rectangular set-up, although the filling process differs. Instead of filling the volume at the start of the simulation and allowing them to settle before opening the ledge, the ledge is open and particles are generated continuously through the first two seconds. This method of creating an angle of repose resembles the free cone set-up as the flowing particles create a slope by settling down. The drop height in the simulation is comparable to the experimental drop height, making the kinetic energy in the system similar. A rectangular simulation set-up was preferred over a cylindrical set-up as the angle measurement technique of the ledge method could adapted for this set-up as well. No significant effect of the rectangular set-up was expected as possible wall effects were omitted from the results by excluding particles near the walls.

The angle of repose was measured by examining the positions of the particles in the box at the end of the simulation. The particle positions were binned into eight equally spaced horizontal layers n, excluding the particles close to the bottom, top or sides of the container. For each layer, the x and y coordinates of a point on the slope were determined. A linear curve then was fitted for the n points on the slope and the angle of repose could be determined from the slope of the fit (Figure 4.5b).

(a) Simulation set-up.   (b) Curve fit.
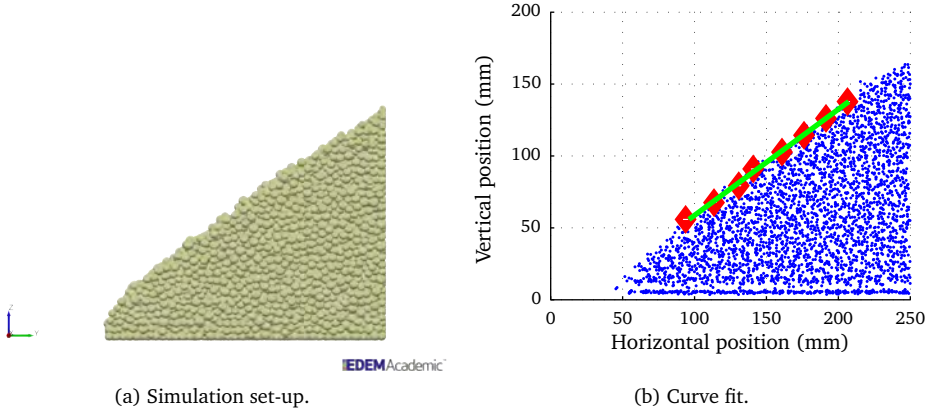
Figure 4.5: Angle of repose simulations.

A sensitivity analysis of the input parameters on the angle of repose revealed that the angle of repose is predominantly influenced by the two friction coefficients, both the static friction μ_s as well as the rolling friction coefficient μ_r. Figure 4.6 and 4.7 shows these effects for the rolling friction model C and it can be observed that higher friction coefficients relate to a higher angle of repose as has been reported by other researchers such as Wensrich and Katterfeld (2012). It should be noted that the influence of the friction coefficients is not similar for the ledge and the free cone tests, as the angle of repose is affected by the kinetic energy of the particles creating the heap. Obtaining both the experimental ledge angle of 41 degrees and the free cone angle of 27 degrees with the same combination of friction coefficients appears to be impossible, therefore a compromise needs to be made.

When rolling of particles has been made impossible, effects of the rolling friction coefficient no longer exist and the angle of repose depends solely on the static friction coefficient (Figure 4.8). Similar to the model with rolling, it appears to be impossible to obtain both experimental angles with the same input parameter μ_s and likewise a compromise regarding achieving both angles is required.

The effect of the stiffness coefficient on the angle of repose are insignificant when above a certain threshold value, this will be discussed in more detail in Section 5.1.3. The remaining coefficients showed negligible effects on the angle of repose and are therefore not of importance to the calibration of the angle of repose.
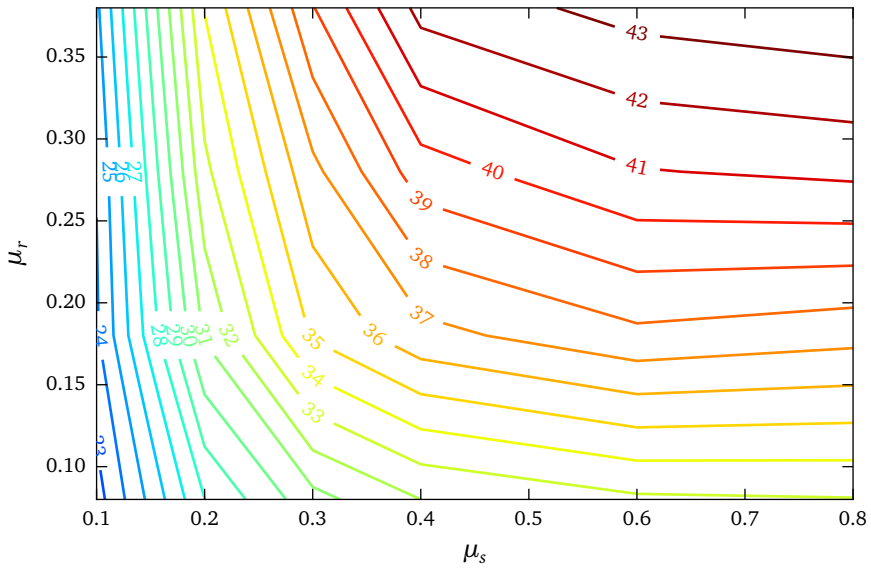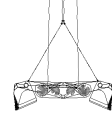
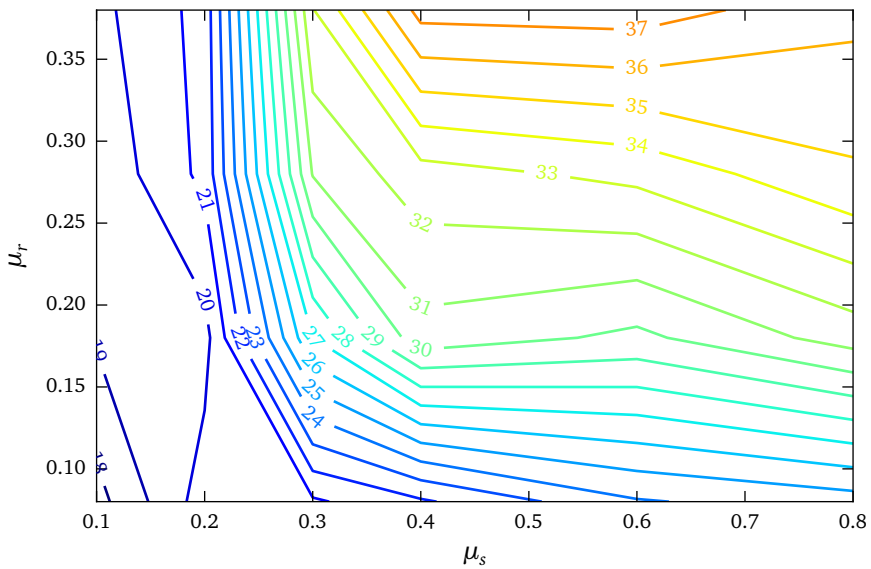Figure 4.6: Effect of friction coefficients μ_s and μ_r on the angle of the ledge method.

Figure 4.7: Effect of friction coefficients μ_s and μ_r on the angle of the free cone method.
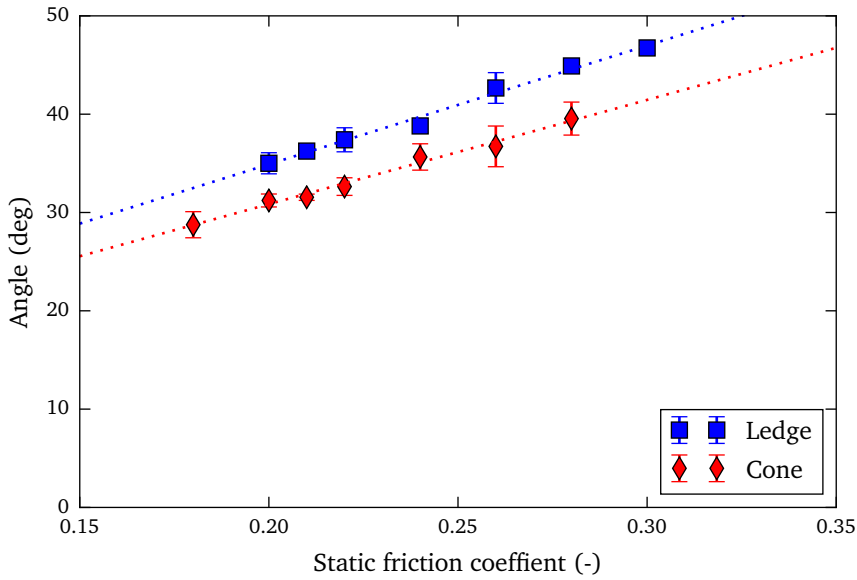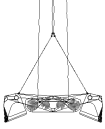
Figure 4.8: Angle of repose with no rolling restriction.

4.4.3   Penetration test

The penetration test of Section 3.2.3 is modelled as well in order to calibrate the penetration resistance of the material model to the penetration of iron ore pellets (Figure 4.9). Compared to the experimental set-up, the simulation set-up has some minor differences. Unlike in the experiments, the length of the container in the simulation is equal to the length of the tool, removing the insignificant particle-tool interaction at both ends of the tool. Periodic boundaries are introduced to prevent the aligning of particles along the wall, keeping the packing random and minimizing wall interference on the penetration process.

Prior to the penetration of bulk material, a container is randomly filled with particles with an average diameter of 11 mm and a normal distribution of 0.1, similar to the iron ore pellets of Section 3.1.2. Particles are generated in the first second of the simulation and fall down due to gravity. During the second second the container is vibrated to improve the packing of the particles. The particles are allowed to settle into semi-steady state until four seconds have passed. During this period the average particle velocity will decline rapidly until semi-steady state is achieved and ultimately the value of zero is approximated.
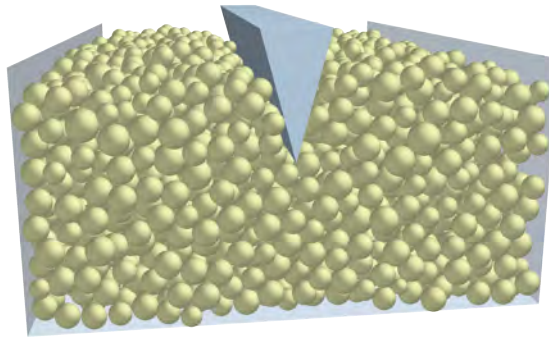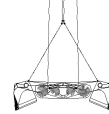
Figure 4.9: Simulation of the penetration test.

The tool starts moving towards the bulk material at $t = 4$ seconds, approaching the bulk material until the tool touches the first particle and penetration starts. The force-time data produced by the simulation is converted to the desired depth-force data. This is done using the same criterion as in the experiment: when a force of 0.5 N is registered, the depth is set to zero and based on the constant velocity of the tool the depth values are calculated. Data prior to the contact between tool and bulk material is truncated. As the simulation does not know how deep the tool has penetrated the material, simulation stops after 16 seconds. During post processing the depth-force data is integrated to obtain depth-work data similar to the penetration data of Chapter 3.

As an alternative to signal averaging by replicating simulations a number of times, the option of improving signal quality by increasing the tool length was investigated. By doubling the length of the tool of 200 mm to a length of 400 mm, the number of particles in contact with the tool was also doubled. Figure 4.10 shows data from 6 simulations performed with a 200 mm tool and data from 3 simulations with a 400 mm long tool divided by two. The data from the 200 mm simulations is much more scattered than the data from 400 mm measurements while the time needed to simulate both sets of data is identical. The reduced scatter of the 400 mm simulations leads to significantly smaller confidence intervals, confirming the higher accuracy of the larger tool. Therefore the larger tool is selected for calibrating the penetration resistance of the material model.
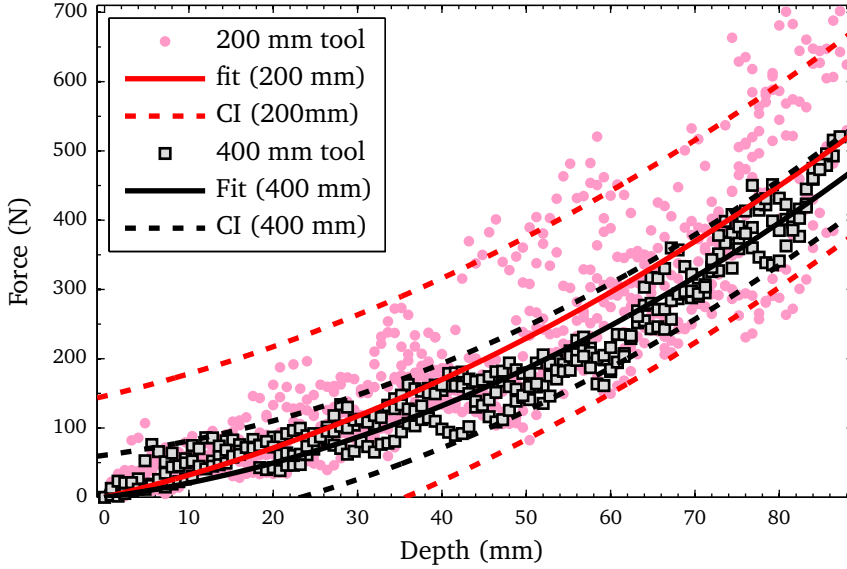
Figure 4.10: Variation in measurements between simulations of a 200 and 400 mm tool, both sets of simulations require the same amount of time.

A sensitivity analysis of the penetration tests using tool A from Figure 3.9 revealed that the resistance was affected by several input parameters: the friction coefficients μ_s, μ_r, ϕ_w and ϕ_r, and the particle density ρ_p (Figure 4.11). The sensitivity analysis is based on one simulation per configuration, as spotting the trends is considered more important than a high measurement accuracy. This allows to quickly discover the influence of input parameters, while establishing the accuracy of the measurements is saved for the calibration process. Figure 4.11 shows that the particle density ρ_p directly influences the penetration resistance, as the weight of the material to be pushed sideways becomes heavier as the particle density increases. Also the friction coefficients μ_s and μ_r affect the amount of material displaced due to the penetration and therefore affect the resistance as well. The wall friction coefficient ϕ_w and ϕ_r show a smaller effect as it is expected that an increased wall friction only increases friction along the tool and does not affect the amount of the material displaced. Hence these five input parameters (ρ_p, μ_s, μ_r, ϕ_w and ϕ_r) need to be considered when calibrating the penetration resistance of the material model.

4.4.4 Wall friction test and rolling friction test

The wall friction test of Section 3.2.5 is simulated by placing a single particle on a horizontal plane tilting with an angular velocity of 30 deg/s. The sliding angle is determined at the angle of the plane where particle velocity reaches the threshold

(a) Static friction coefficient μ_s.

(b) Rolling friction coefficient μ_r.

(c) Wall friction coefficient ϕ_w.

(d) Particle density ρ_p.
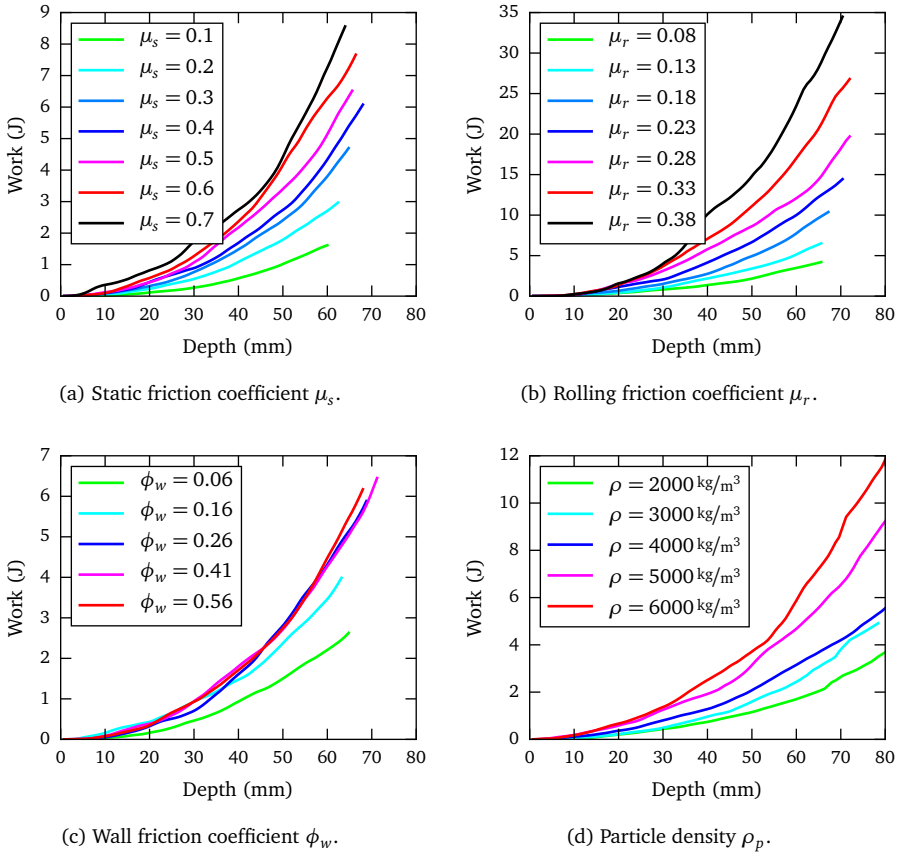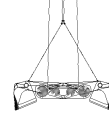
Figure 4.11: Sensitivity analysis of penetration resistance simulations.

value of $1.5\,\mathrm{mm/s}$ and the particle starts to slide. This threshold value is selected to exclude the particle movement due to the tilting of the plane. Rolling of particles is prohibited in this simulation , similar to the wall friction experiment.

Figure 4.12a depicts the relation between the wall friction coefficient ϕ_w, the wall friction angle and the sliding angle observed in this analysis. There appears to be a small difference between the wall friction angle and the sliding angle, and this difference is growing for larger wall friction coefficients. Other DEM input parameters did not show significant effects on the sliding angle. This means solely the wall friction coefficient can be used to calibrate the wall friction angle of the material model to the angle of 22.5 degrees found in the experiment. Ideally, a wall friction coefficient of 0.41 is selected, resulting in a match between sliding angles of the experiment and simulation.

(a) Wall friction test.   (b) Rolling friction test.
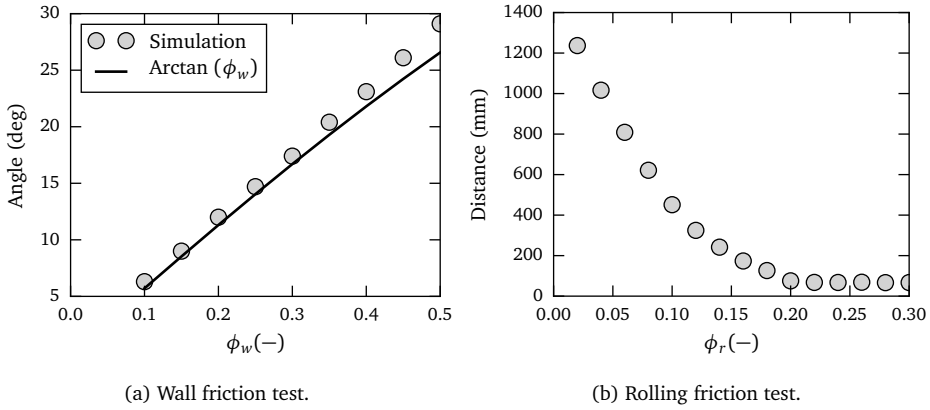
Figure 4.12: Wall friction and rolling friction test.

Simulations of the rolling friction test are conducted with the same slope as described in the previous chapter. Two particles, with $r = 8$ and $r = 13$ mm are placed next to each other on the top of the slope and allowed to roll downwards. The contact between particles and the surface has been modelled with the rolling friction model C described in Section 4.2. Both particles stopped at a similar distance, demonstrating that the particle size does not affect the rolling resistance. The sensitivity to the rolling resistance has been analysed for all input parameters.

As expected, the rolling friction coefficient is the most dominant variable on the rolling resistance. Figure 4.12b shows the relation between the rolling friction coefficient ϕ_r and the distance covered by the particles, where particles with a lower rolling friction coefficient cover a larger distance before stopping. The particle-surface sliding friction coefficient ϕ_w is considered to have a minor influence, affecting the distance by not more than 50 millimetres, while other parameters showed negligible influence. For approximating the distance of 22 cm found in the experiments, the rolling friction coefficient ϕ_r needs to be set around a value of 0.14.

When rolling of the particles is disabled, the rolling test transforms to a wall friction test, where particles with wall friction angle lower than the slope will start sliding. In this case, the rolling friction test can be omitted from the calibration process, as it does not provide extra information over the wall friction test.

4.5 Calibrating a Material Model for Iron Ore Pellets

The material model can now be calibrated to the experimental material behaviour of iron ore pellets after the sensitivities of the input parameters on the bulk material behaviour have been determined in the analysis of the previous section. As discussed in Section 4.3, the most common approach in calibrating the input parameters is through
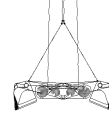
a process of trial and error, attempting to match all the characteristics of the behaviour. Calibration of the friction coefficients will be conducted for the two selected contact models, thus creating two material models for iron ore pellets. The two material models will share the calibrated values for the remaining input parameters.

For both models the calibration starts with selecting the particle density ρ_p. According to the analysis this is the only parameter affecting the bulk density of the material and should be chosen in such a way that the bulk density of material model reflects the bulk density of iron ore pellets. The analysis also revealed that the bulk densities of the three compacting levels were closer than observed in the experiment. Table 4.2 shows that in order to match the experimental bulk density of 2100 $^{kg}/_{m^3}$, the particle density needed to be been calibrated at 3700 $^{kg}/_{m^3}$, which results in a simulated bulk density of 2110 $^{kg}/_{m^3}$. The fact that the particle density in the material model does not match the particle density measured in the previous chapter is not of concern, as the particle density measurement considers the porosity of the particle, while DEM particles are models as solid spheres.

	Experiment	Simulation
Bulk density	2100 $^{kg}/_{m^3}$	2110 $^{kg}/_{m^3}$
Particle density	4260 $^{kg}/_{m^3}$	3700 $^{kg}/_{m^3}$

Table 4.2: Density values.

Stiffness coefficients are set to a high value which produce very small overlaps of the particles, thus limiting the effect of particle overlap on the bulk behaviour. This will be investigated further in the next chapter, where a study is made into the effects of reducing stiffness coefficients. The response to changes in the coefficient of restitution appeared to be limited for all of the conducted calibration tests. This is not strange, since the collision velocities are rather small in these tests as well as in the grabbing process, which limits the possible size of the damping component of the contact forces. The coefficient of restitution is set at $C_R = 0.6$, close to the estimation of 0.49 made by Barrios et al. (2013). The remaining friction coefficients will be calibrated for the two material models separately:

4.5.1 Without Rolling of Particles

First, the material model with the no-rolling restriction is be calibrated. Due to the lack of rolling of the particles in the model, the rolling friction test is not included in the calibration. It is not likely that this will have a significant effect on the accuracy of a coupled grab-iron ore pellets model, as the rolling of particles does not play a large role in grabbing bulk material. As the no-rolling contact model only has two variables, it will be challenging to find a single solution of μ_s and ϕ_w that can satisfy all six calibration tests (two angle of repose tests, 3 tools in the penetration test and

the wall friction test). The final set of input parameters are summarized in Table 4.3.

Property	Symbol	Value	Unit
Shear Modulus	G	1e10	Pa
Poisson's ratio	ν	0.3	-
Density	ρ	3700	kg/m^3
Coefficient of restitution	C_R	0.6	-
Static Friction	μ_s	0.21	-
Wall friction	ϕ_w	0.41	-

Table 4.3: Calibrated material model without rolling of particles.

The input parameters of the no-rolling material model approaches the iron ore pellets characteristics as follows:

- In the angle of repose sensitivity analysis, only a single input parameter (μ_s) showed an effect in the no-rolling model. While the experimental results showed a large difference of 14.8 degrees between de repose and ledge method (26.0 and 40.8 degrees), the maximum attainable difference in these simulations was not larger than 5 degrees. The value $\mu_s = 0.21$ results in an average of the simulated ledge and cone angles equal to the average of the experimental results, this way both angles are approximated equally well. This is considered acceptable because neither of the extreme angles are observed in grab behaviour, instead the heap forming inside the grab is the result of both processes. This resulted in the simulated angles of 31.5 and 36.4 degrees displayed in Figure 4.13. This approach will be validated together with overall validation of the co-simulation of grab and iron ore pellets.

(a) Angle of repose.   (b) Angle of movement.
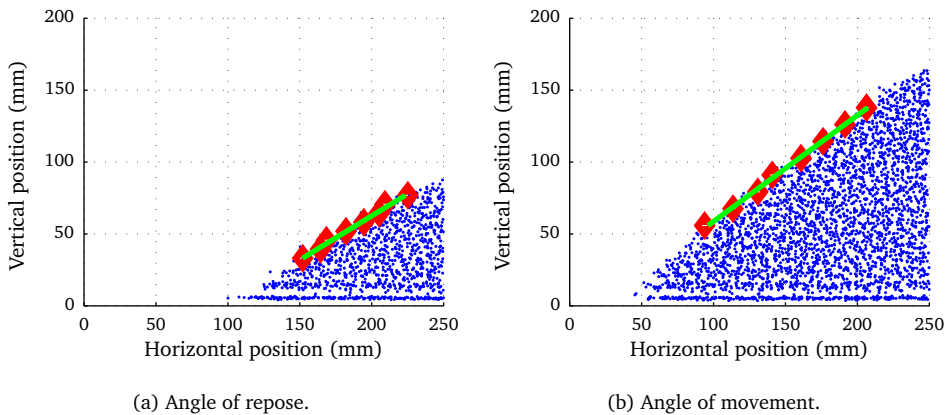
Figure 4.13: Calibrated angle of repose with the no rolling restriction.

- The sensitivity analysis of the wall friction test indicated that the wall friction coefficient ϕ_w should be in around 0.41 in order to to have a sliding angle within the confidence interval of the angle observed in the experiments of Section 3.2.5.

- The increase due to the different tools is approximated very well by the material model as displayed in Figure 4.14. It can be observed that the penetration tool C is less accurate and has a larger variation than the simulations using tool A and B, however the confidence interval of the prediction is still within range of the experimental results and therefore considered acceptable. The penetration simulations were not sensitive to a difference in penetration velocity , similar to the observations in the experiment (Lommen et al., 2011).
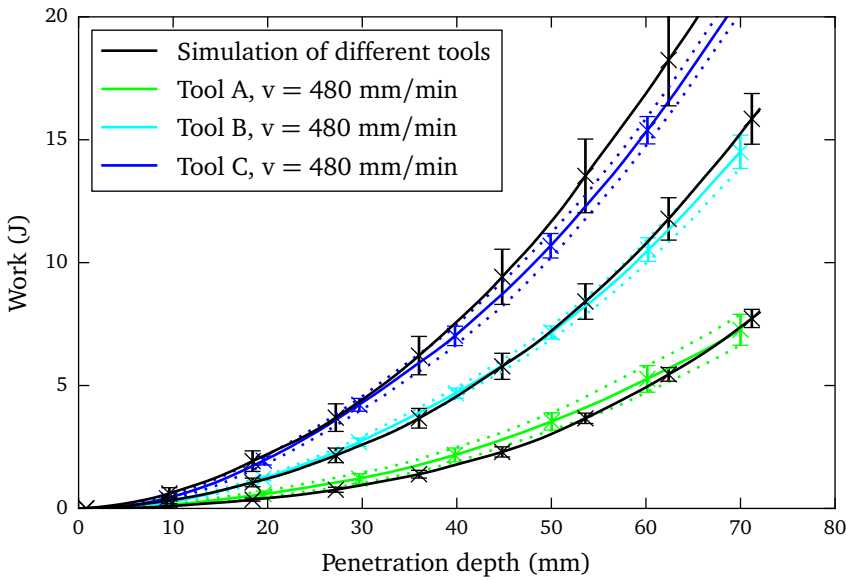
Figure 4.14: Calibrated penetration resistance with restricted rolling of particles.

4.5.2 Rolling of Particles Included

The second material model includes the rolling of particles and the rolling friction model presented in Section 4.2. Compared to the other contact model, two additional input parameters are present, being the rolling friction coefficients μ_r and ϕ_r. These two coefficients influence the rolling behaviour of interparticle contacts and contacts between particles and equipment.

The calibrated input parameters of the rolling material model are shown in Table 4.4.

Property	Symbol	Value	Unit
Shear Modulus	G	1e10	Pa
Poisson's ratio	ν	0.3	-
Density	ρ	3700	kg/m^3
Coefficient of restitution	C_R	0.6	-
Static Friction	μ_s	0.41	-
Rolling Friction	μ_r	0.145	-
Wall friction	ϕ_w	0.36	-
Rolling friction wall-particle	ϕ_r	0.13	-

Table 4.4: Calibrated material model with rolling of particles.

These input parameters result in the following behaviour:

- The simulated angle of repose are shown in Figure 4.13, being 26.5 degrees for the free cone method and 34.6 degrees for the ledge method. Compared to the rolling-restricted model, the difference between the two angles reduced with 3.1 degrees to 8.1 degrees, although this is still smaller than the difference experimental angles of 14.8 degrees.

(a) Angle of repose.

(b) Angle of movement.
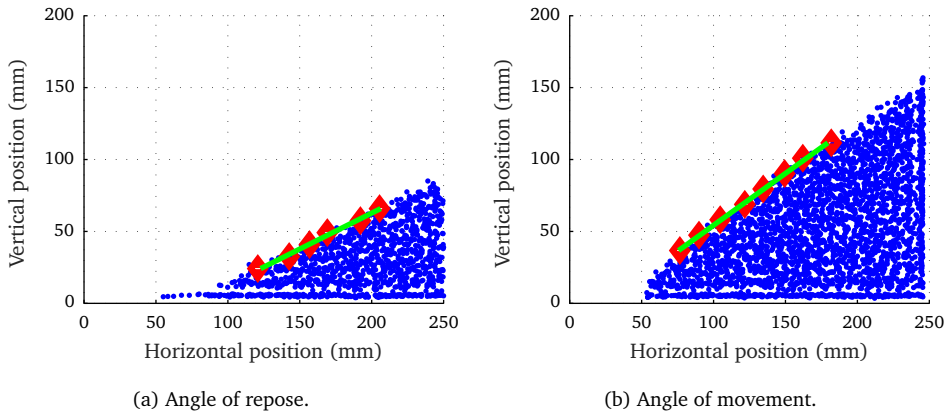
Figure 4.15: Calibrated angle of repose with rolling friction model.

- The wall friction coefficient $\phi_w = 0.36$ results in a sliding angle of 21 degrees, close to the experimental sliding angle of 22.5 degrees

- Particles in the simulation roll slightly further than the distance measured in the experiments, instead of the measured 22.5 cm the simulated distance is 10% higher.

- The simulated penetration behaviour compares very well to the experimental
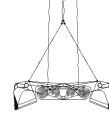
resistance (Figure 4.16). The increase in resistance for the blunter tools is predicted well and within the confidence intervals of the experiments.

Although not all experimental characteristics could be matched perfectly, these input parameters have been selected for the performance on the penetration test instead of achieving a good fit on the wall friction and rolling distance test. A perfect match on the wall test and rolling test requires higher friction coefficients, which would make achieving a good fit on the penetration test impossible. A good fit on the penetration test is considered more important due to its close resemblance to the penetration of a grab, therefore this test was prioritised over the wall and rolling test.
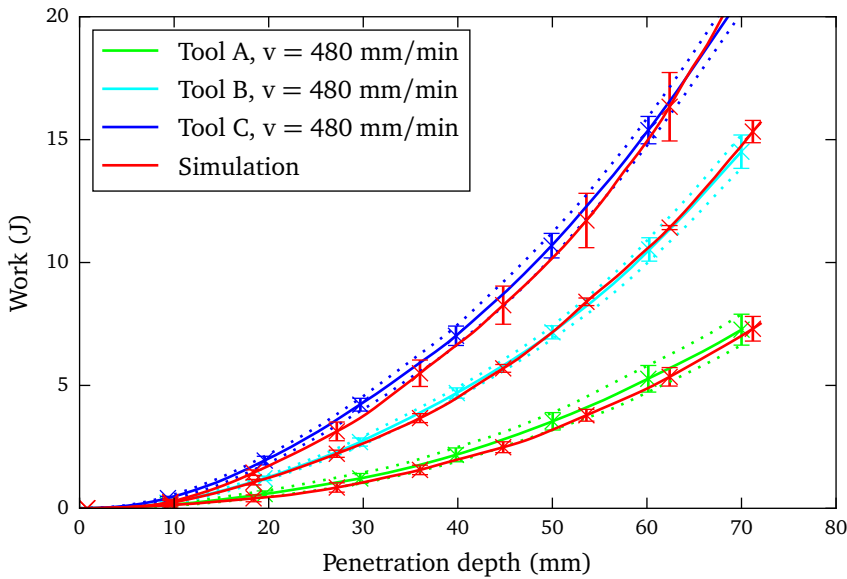
Figure 4.16: Calibrated penetration resistance with with rolling friction model.

4.6 Conclusions

This chapter has presented a material model for iron ore pellets suitable for a Discrete Element Method simulation. The selected DEM contact models calculate normal forces based on the Hertz contact theory and uses a tangential solution based on the work of Mindlin and Deresiewicz. Two material models have been calibrated, one using the rolling friction solution of Iwashita and Oda (1998), the other prohibits rolling motion of particles, following the suggestion of Bierwisch (2009). Both models have been calibrated to the material characteristics of Chapter 3.

A complete match between the material models and all the characteristics was not found, making it necessary to prioritize characteristics. The penetration characterist-

ics are approximated very well by the both material models, this is also considered important for grab simulation and therefore prioritized. Bulk density is also approximated well, although compaction effects are much smaller than those observed in the experiments. Largest challenge in the calibration was attaining the same difference between the angle of movement and the angle of repose in the simulation, which could not be reached. The experimental difference amounted to fourteen degrees, while the simulation that approached these angles best resulted in a difference of five degrees in the no-rolling model and eight degrees in the rolling model. Although not a complete match, the material models are considered to be calibrated and ready to be tested in the validation.

The material models developed in this chapter are based on the characteristics of iron ore pellets and can be applied to simulate material behaviour using the Discrete Element Method. Techniques for optimizing the computational costs of this material model will be presented in the next chapter, and as a result large scale simulations of iron ore pellets can be performed promptly.
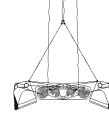
5

Computational Costs of Large Scale Simulations[*]

This chapter focuses on reducing the computational costs of large scale Discrete Element Method (DEM) simulations, as a large scale co-simulation of a grab requires $77\,\mathrm{m}^3$ of iron ore pellets, making the computational costs prohibitive. The objective of this chapter is to investigate two techniques, the first technique focussing on increasing the critical timestep size of a simulation, while the second technique is focussing on reducing the number of elements in the simulation. It is crucial that these techniques do not alter the behaviour of the simulated bulk material and accordingly the accuracy of the material model.

Section 5.1 investigates increasing the critical timestep by means of reducing the stiffness of the contacts. A lower stiffness leads to less abrupt collisions and increases the duration of the contact, which allows for a larger timestep. In this section the role of contact stiffness for a single contact is examined as well as the bulk behaviour. Reducing the number of elements is achieved through coarse graining and presented in Section 5.2. Coarse graining relies on increasing the size of particles in the simulation and thus the number of elements is reduced. This section presents a coarse graining scheme and investigates the equivalent behaviour of the coarse material.

---

[*]This chapter is partially based on Lommen et al. (2012a, 2014)

5.1   Effects of Stiffness Reduction on Bulk Behaviour

Users applying the Discrete Element Method (DEM) on large scale industrial processes involving hundreds of thousands of particles are constantly on the lookout for ways to decrease computing time. Even with the strong increase of computational power in the last decades, large scale simulations still require considerable effort to complete. For example, a full scale grab simulation needs an estimated 8.3 years to complete using the required $77\,\text{m}^3$ of pellet sized elements with a stiffness of $G = 16\,\text{GPa}$ found by Barrios et al. (2013). These computational costs have been estimated for a 2014 workstation hexa core PC, and elements with a particle density of $4000\,\text{kg/m}^3$.

One of the possibilities to speed up DEM simulations is a particle stiffness reduction as stated by Malone and Xu (2008). By making particles less stiff, also called softer, a larger timestep can be used (Equation 4.16). This results in less iterations per second of simulation time and therefore shortens the computing time. As a result, the computational costs can be lowered with a factor of $\sqrt{10}$ when the stiffness of particles is reduced with a factor of 10. In case of a grab simulation, this stiffness reduction would decrease the computational effort from 8.3 years to 2.5 years.

Stiffness of contacts has been identified as an important parameter in DEM simulations by Huang et al. (2008); Masson and Martinez (2000), however, other researchers have showed that a stiffness reduction did not affect results (Härtl and Ooi, 2008). The study of Malone and Xu (2008) summarized that lower values of stiffness have benefited users without significantly altering results. In an overview of DEM predictions, Cleary (2010) states that "Long experience has shown that average overlaps of 0.1–0.5% are required to ensure that the flow behaviour is not dependent on the spring stiffness.". Yet the pitfalls of a large reduction are still unclear, possibly influencing simulation results and invalidating predictions made by DEM.

This section investigates and quantifies the effects of particle stiffness on bulk material behaviour. It assesses to what extent a lower stiffness still results in accurate predictions while computing costs of DEM simulations are lowered. This is achieved by observing the behaviour of a contact pair together with the bulk behaviour. The bulk behaviour is examined by a tri-axial compression test, angle of repose tests, and a penetration test, each test studying a different particle process. Only particle processes involving an average of four contacts per particle or more are considered, as these processes are likely to benefit most of a decrease in computing costs. In all these tests, the effects of reducing particle stiffness on simulation results are studied in the pursuit of lower computing costs. Effects on the stability of a co-simulation of Discrete Element Method and MultiBody Dynamics is investigated in Section 6.3.

5.1.1   Single Contact

Before the influence of particle stiffness on an assembly of particles is investigated, a single contact pair is analysed, since this is the building block of all bulk material
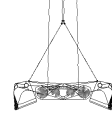
handling processes. This is done by examining the effect of stiffness on the interaction forces and particle displacements of particle-wall contacts (Figure 5.1). Because interaction forces and particle displacements are both dependent on the contact model, the Hertz-Mindlin model of Section 4.2 has been selected. By lowering the shear modulus G, the effective Young's modulus will be lowered as well, resulting in reduced stiffness constants k_n and k_t (Equation 4.19, 4.20, 4.21, 4.22 and 4.23).

v = 1 ms^{-1}
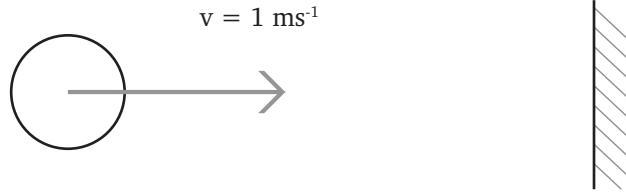
Figure 5.1: Particle - wall contact.

The contact behaviour is also depending on the momentum of the colliding particles, determined by the mass of the particles m and the relative velocity Δv. The momentum of the particles should therefore be considered when reducing the particle stiffness. According to Malone and Xu (2008), the momentum can be taken into account by inspecting the amount of overlap δ_n between the particles. Users who want to translate the amount of stiffness reduction feasible for their model should compare the normal overlaps δ_n instead of the stiffness or shear modulus, since this does not take into account differences in the process and particle properties.

The single contact simulations are performed with a shear modulus varying between 1e4 and 1e11 Pa. The upper value is based on the shear modulus of steel, which equals 80 GPa. The lower bound is chosen at 1e4 to investigate a possible stiffness reduction of factor 1e7. Spherical particles are modelled in three different sizes in order to study the effect of kinetic energy: a diameter of 4, 8 and 16 mm. Particles approached the wall with a velocity of 1 m/s while gravity is excluded and other particle parameters are constant at $\nu = 0.25$, $\rho = 1500$ kg/m³ and $C_R = 0.5$.

Figure 5.2a and 5.2b show the effect of stiffness on the contact time and average elastic contact force of a single contact. It can be observed that when the stiffness of the particle is reduced the average contact force decreases. At the same time, the contact time increases in order to keep the collision energy constant. The higher mass of larger particles and therefore higher kinetic energy leads to larger contact forces, suggesting that the kinetic energy of the colliding bodies influences the effect of stiffness reduction. When examining the average normal overlap during the contacts displayed in Table 5.1, it can be noted that the percentage of the particle radius consumed by the normal overlap increases for the stiffer particles and that a reduction from 1e10 to 1e8 already exceeds the 0.1–0.5% limit stated by Cleary (2010). This implies that stiffness is a parameter of importance during impact collisions, and will affect simulation results if

(a) Average normal elastic force.

(b) Average time of contact.
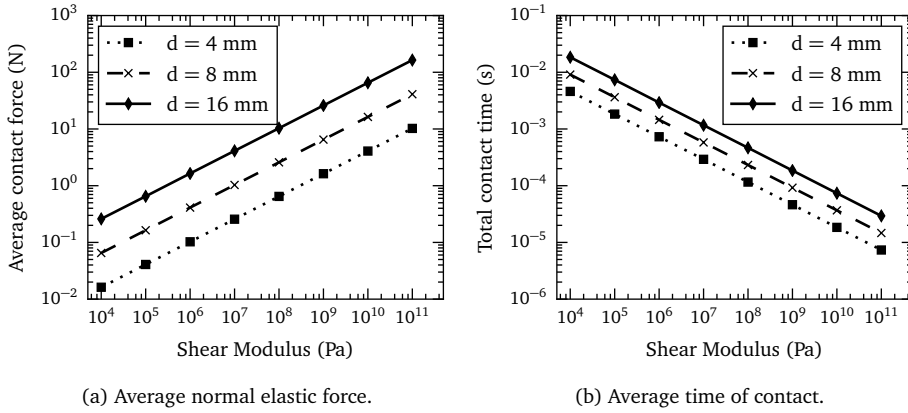
Figure 5.2: Single contact characteristics.

a substantial number of collisions with a large relative velocity of $1 \, \text{m/s}$ are present in the system.

d \ G	1e4	1e5	1e6	1e7	1e8	1e9	1e10	1e11
4	34.9	13.9	5.55	2.20	0.880	0.350	0.139	0.0553
8	35.1	14.0	5.56	2.21	0.877	0.350	0.139	0.0554
16	35.0	13.9	5.55	2.21	0.876	0.350	0.139	0.0554

Table 5.1: Percentage of normal overlap compared to the particle radius ($100\delta_n/R_i$).

5.1.2   Bulk Compression Test

The effects of contact stiffness on the packing of particles and the bulk modulus are studied with the bulk compression test shown in Figure 5.3. This test investigates whether changes in particle stiffness affect the energy dissipation of an assembly in particles. Ideally, energy dissipation should remain constant when particle stiffnessess are reduced.

The test consists of a square floorplate with sides of $0.3 \, \text{m}$, where contacts between this floorplate and the particles used the same properties as interparticle contacts. Both X and Y direction boundaries are periodic, allowing particles to exit on one side only to enter on the opposing side. The bulk compression test is performed with 18,000 particles, modelled with a Poisson's ratio of 0.25, coefficient of restitution C_R of 0.5, a coulomb friction coefficient μ_s of 0.5 and a rolling friction coefficient μ_r of 0.04. These values are selected to match the properties used during the single contact tests. The effect of the normal stiffness was studied using different shear moduli, ranging from 1e4 Pa to 1e11 Pa.
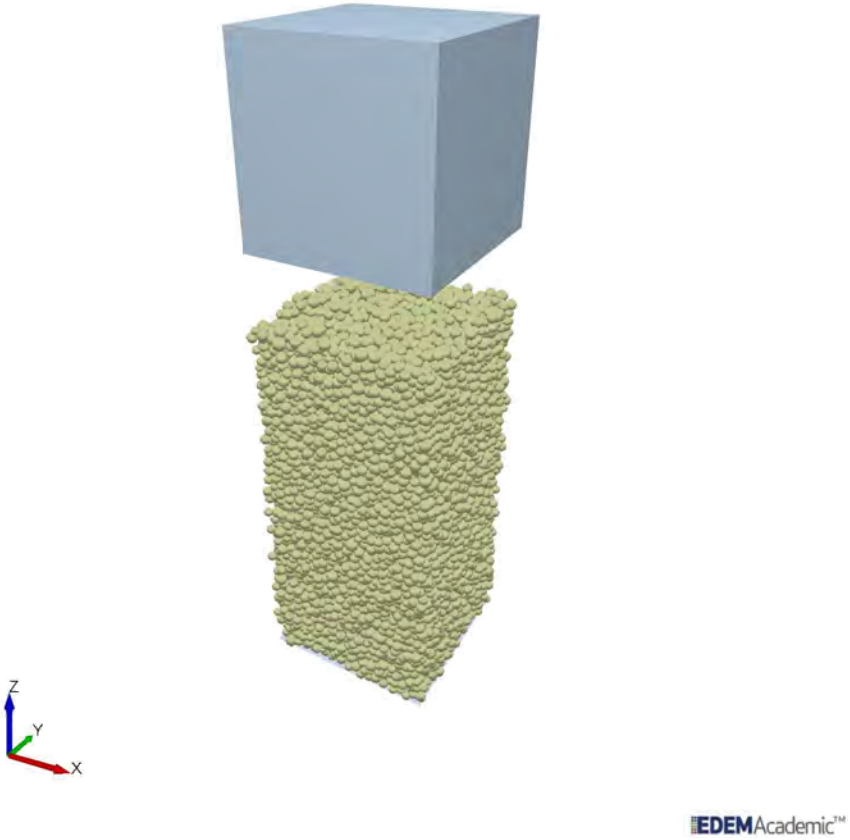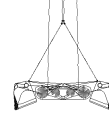
Figure 5.3: Bulk compression rig during compression.

The simulation set-up is filled with particles using a dynamic particle generator with a rate of 20,000 particles per second and particles are allowed to settle. Next, a cube with a mass of 50 kg is dropped on the particles from a height of 0.2 m above the top surface of the bulk material and a gravitational constant of 9.81 m/s². After releasing the cube its velocity was limited to 1 m/s and its trajectory was measured.

At the moment the mass m_c of 50 kg touched the bulk material, the bulk material started to act as a spring-damper. Based on the measured motion of the mass displayed in Figure 5.4a, the characteristics of the system can be derived, such as the bulk stiffness k_b and bulk restitution coefficient. The bulk stiffness is computed by determining the eigenfrequency of the motion f_n and taking the mass of the cube m_c into account according to Equation 5.1. Figure 5.4b shows a linear relation between the shear modulus of the particles and the bulk stiffness. A simulation using a shear modulus of 1e4 Pa turned out to be impossible as the contacts of the bulk material were unable to generate sufficient force to reverse the direction of the mass and normal overlaps

would exceed the particle radius. It can be observed from Figure 5.4b that changes in the particle stiffness proportionally affect the bulk stiffness. Consequently, particle stiffness is not a feasible speed-up strategy for simulations where the eigenfrequency or stiffness of the bulk material is considered important.

$$k_b = (2\pi f_n)^2 m_c \tag{5.1}$$

(a) Motion of the mass ($G = 1e8\,\text{Pa}$).
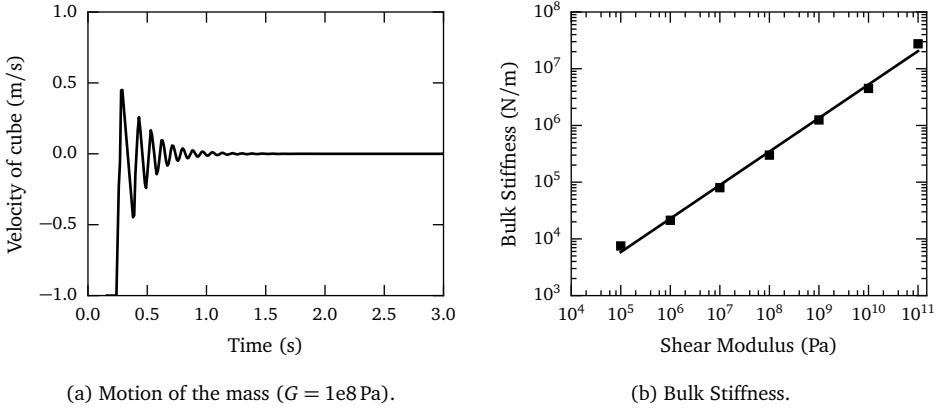
(b) Bulk Stiffness.

Figure 5.4: Bulk stiffness response.

Damping behaviour was studied by examining the first six collisions between the block and the particles. By measuring the velocities before and after each collision, a coefficient of restitution C_R for the bulk material was derived with the help of Equation 2.8. The coefficients of restitution for all shear moduli are displayed in Figure 5.5 and it can be observed that most bulk restitution coefficients are higher than the particle restitution coefficient $C_R = 0.5$. At the first collision, simulations with a high stiffness (1e9 Pa and higher) showed a bulk restitution coefficient of < 0.4, while the low stiffness simulations (1e7 Pa and less) reported much higher values. This indicates that there is a threshold in stiffness reduction where bulk damping behaviour is changed.

Soft bulk material showed significantly less damping than the stiff material resulting in coefficients of restitution of up to 0.9 as well as smaller differences between the six collisions. These differences could still be acceptable if this lack of damping could be compensated by decreasing the particle restitution coefficient. However, when the particle restitution coefficient is reduced to 0.01 this results in a bulk restitution of 0.7, suggesting that it is impossible to create high damping bulk materials with soft particles.

In order to avoid large changes in damping behaviour, the stiffness reduction should remain above the threshold of $G = 1e9\,\text{Pa}$, when normal overlaps amount to 0.33%. Simulations with higher normals overlaps, such as 1% and 10% occurring at the lower
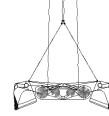
stiffness of 1e8 Pa and 1e6 Pa, should be avoided to prevent large changes in the energy dissipation of the bulk material. This is in agreement with the 0.1–0.5% limit stated by Cleary (2010). In short, a reduction in particle stiffness does not affect the simulation of energy dissipation of the bulk material as long as normal overlaps stay above 0.33% and can be considered to reduce computational costs of the simulation.
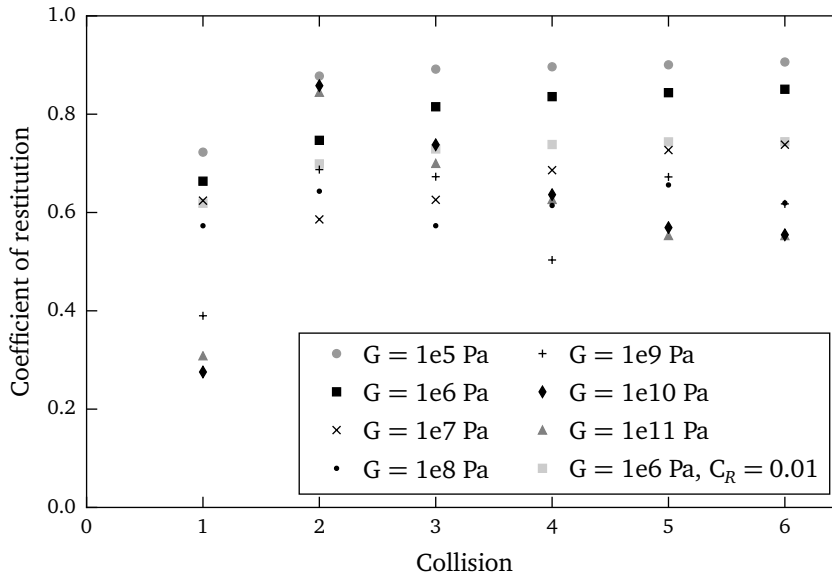
Figure 5.5: Restitution coefficient of bulk material.

5.1.3 Angle of Repose Test

An angle of repose test is examined to investigate the shearing behaviour of an assembly of soft particles. A set-up is modelled according to Figure 5.6 while the depth of the chambers is set to 160 mm. Particles are modelled according to the properties displayed in Table 5.2, selected to match the properties of glass beads. After filling the upper chamber, both side panels are lowered with a lowering speed of 10 mm/s, gradually enlarging the opening to five times the particle size. This allowed the particles to enter the lower chamber, leaving a pile in the upper chamber. The angles of the pile are computed by using the particle positions and a linear curve fit to the surface of the slope similar to the method described in Section 4.4.2.

d	4 mm	C_R	0.9
ν	0.22	μ_s	0.5
ρ	2470 kg/m³	μ_r	0.01

Table 5.2: Particle properties of angle of repose set-up.
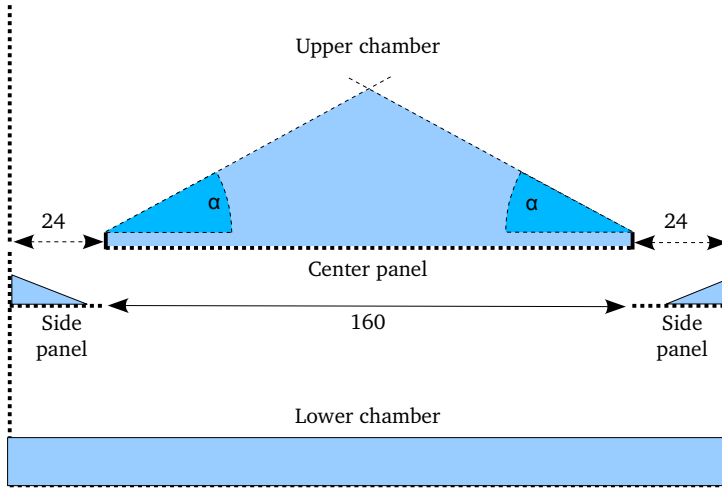
Figure 5.6: Angle of repose set-up.

The first effects on the angle of repose start to show in Figure 5.7 when a shear modulus of smaller than 1e7 Pa is used. Different shear moduli between 1e7 and 1e11 Pa appear to have no influence on the angle of repose. When the bulk density of the angle of repose test is examined, an increase can be detected at the same moment the angle decreases. At the moment the angle of repose and bulk density changes the average of the normal overlaps of the contacts is 0.34% of the particle radius, and this value can be considered as a limit for the maximum allowed softness of particles, which is in agreement with the experience of Cleary (2010). The overlap value was confirmed in a second series of angle of reposes test simulations using a particle density of 7800 ^{kg}/$_{m^3}$ instead of 2470 ^{kg}/$_{m^3}$. This means that changing the stiffness from the 1e11 to 1e7 Pa can decrease computing time up to a factor of 100 without significantly altering the shearing behaviour of the bulk material.
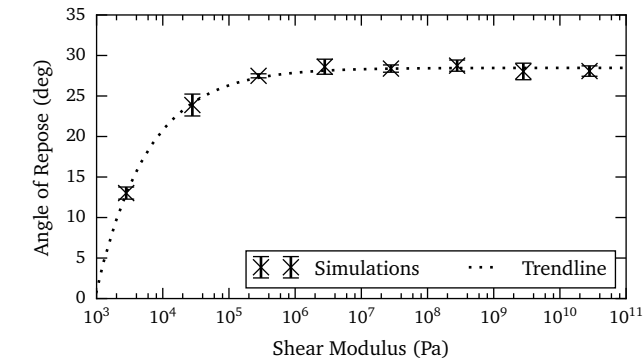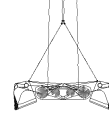
(a) Angle of repose.
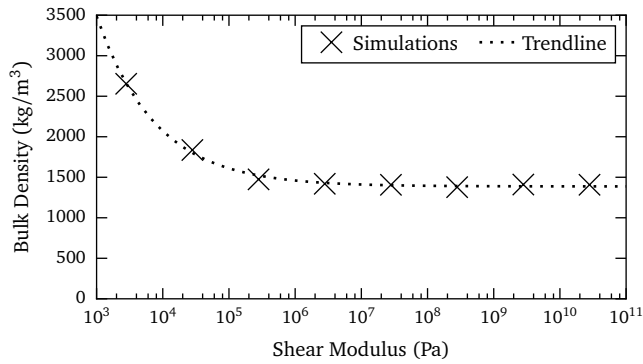
(b) Bulk density.
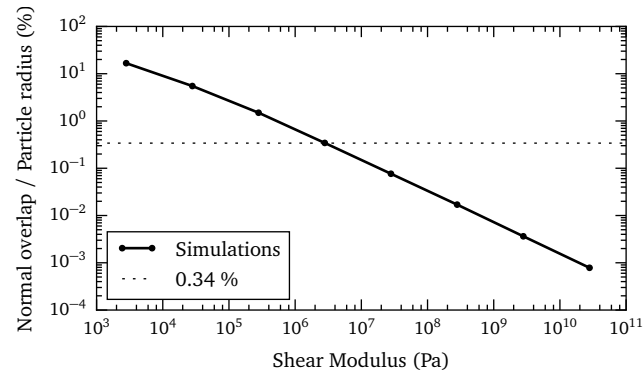
(c) Normal overlap.

Figure 5.7: Effect on angle of repose and bulk density.

5.1.4   Penetration Test

The purpose of the penetration test is to investigate the effect of the stiffness of single particle-tool contacts on the total acting force on the tool. In this penetration test a tool penetrates a bed of particles using a constant velocity while measuring the required force. The test consists of a box filled with particles according to the parameters in Lommen et al. (2011), displayed in Table 5.3. Simulations are repeated 10 times for shear moduli between 1e5 Pa and 1e10 Pa. Rolling of particles is prohibited in order to reduce the effect of the spherical particle shape. The penetration test uses the procedure described in Section 4.4.3, tool A of Figure 3.9 and a penetration rate of 8 mm/s for the investigation on particle stiffness and material-equipment interaction.

G	1e8 Pa		C_R	0.6
ν	0.2		μ_s	$0.5-1.5$
ρ	3500 kg/m³		ϕ_w	$0.5-1.5$
d	15 mm		particles	5000

Table 5.3: Particle properties of penetration test.

Lowering the stiffness resulted in a lower penetration resistance, as can be seen in Figure 5.8. Simulations using a shear modulus of 1e8 Pa or higher, having normal overlaps of 0.3% or smaller, did not show large differences in average resistance. Normal overlap for the other simulations ranged from 0.013% for 1e10 Pa to 8% for 1e5 Pa. For soft particles, the confidence interval of the mean turned out to be much smaller than for stiff particles. This is likely related to the difference between the average and maximum contact force. In case of stiff particles, a few particles contributed greatly to the penetration resistance, even up to 30% of the total force for a single particle. For softer particles the maximum contact force is much closer to the average contact force, this reduces the variation between simulations and overall resistance. The decrease in penetration resistance can however be compensated by increasing coulomb friction, although this might affect other aspects of a simulation such a the angle of repose described in Section 4.4.2. The results show that reducing particle stiffness while considering the 0.3% limit does not affect penetration behaviour and can therefore be employed as a strategy to reduce computational costs.

Particle stiffness reductions have been investigated as a strategy to reduce computational costs of a DEM simulation without compromising results. The stiffness reductions directly affected the collision behaviour of a single contact pair and the stiffness response of an assembly of particles and should be avoided in simulations where these aspects are considered important. Other aspects such as the energy dissipation, the shearing behaviour, bulk density and penetration resistance showed negligible impact as long as normal overlaps remain below 0.3%. For simulations that rely on these aspects, a particle stiffness reduction can therefore be applied to reduce computational costs.
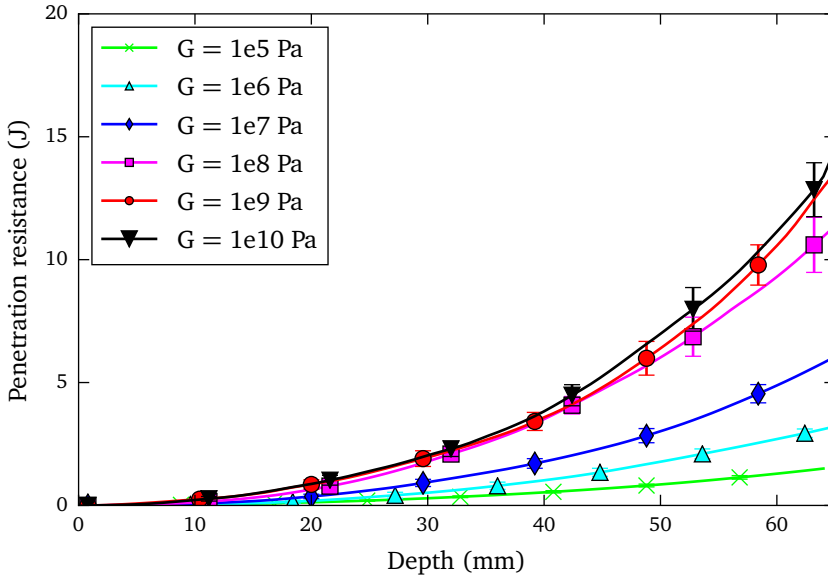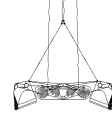
Figure 5.8: Penetration resistance.

When a particle stiffness reduction is contemplated for a full scale grab simulation, these findings need to be taken into account. A full scale grab simulation with iron ore pellets primarily relies on an accurate calculation of the penetration and cutting behaviour of the grab, as well as the shearing behaviour and the bulk density of the material. Because these aspects are insensitive to particle stiffness reduction with regard to the stated 0.3% limit, it is not necessary to use the iron ore pellet stiffness of $G = 16\,$GPa determined by Barrios et al. (2013). Instead, stiffness can be reduced to $G = 300\,$MPa resulting in a lowering of computational costs of 8.3 years with a factor of 7.3 to 1.14 years or approximately 10^4 hours.

5.2 Coarse Graining

Coarse graining is a technique where the original particles with radius R are substituted by larger, coarser grains with radius R'. The coarse grain radius R' can be expressed as a multiplication of the original grain radius R and a scaling factor s as shown in Equation 5.2. For example the use of scaling factor $s = 2$ results in particles twice the original size. The accent $'$ will be used for other parameters as well, and denotes these parameters at the coarse scale.

$$R' = sR \tag{5.2}$$

The main advantage of coarse graining is reducing the number of elements in a simulation which in turn lowers the computational costs. Another benefit of using larger

grains is that the critical timestep increases as well, reducing the number of iterations required to complete a simulation. Coarse graining allows for large scale simulation containing large volumes of particles while keeping computational expenses affordable, however the effects of coarse graining on the accuracy still need to be assessed carefully.

Figure 5.9 shows that the computational costs of a single simulation of the required $77\,m^3$ of bulk material for grab operation are decreasing for coarser element sizes. These cost have been determined for a 2014 workstation hexa core PC and elements with a particle density of $4000\,{}^{kg}/_{m^3}$ and a shear modulus of $300\,MPa$. It can be seen that the computational costs are approximately 10^4 hours for elements with the same size as the pellets of the material model, which is considered impractical for virtual prototyping of grabs. In fact, a computing time of 24 hours or less is desired for simulating a large number of grab design variations. To achieve these desired reduction in computation costs, applying the coarse graining technique needs to explored.
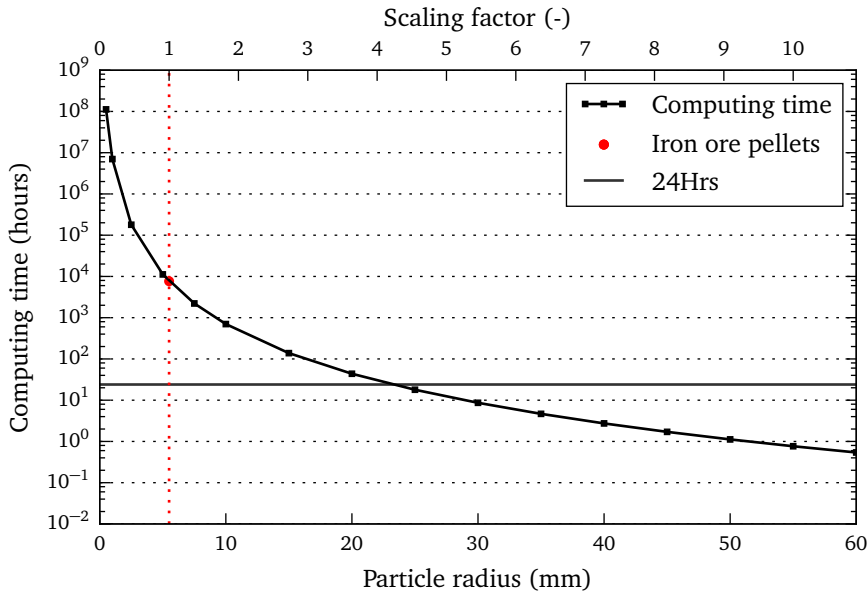
Figure 5.9: Effect of particle size on computing time.

Coarse graining has been researched by several researchers, although their findings are not always in agreement. For example, Baars (1996) writes that the average grain size only affects on the micro scale and "has absolutely no influence on the macro behaviour.", while the publication of Achmus and Abdel-Rahman (2003) states that "a remarkable scale effect exists" and that "the parameters of the model have to adapted by means of a new calibration procedure if the scaling factor is changed.".

A promising approach for coarse graining of Bierwisch et al. (2009) is based on the idea that the system with the scaled grain size should incorporate the same energy
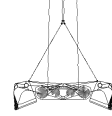
density as the original system with unscaled grains. As the potential energy density is independent of the grain radius if void ratio and particle density are constant, it is required that particle density of the scaled system ρ'_p is identical to the particle density of the original system ρ_p (Equation 5.3). According to Bierwisch et al., the proposed scaling system does not affect the volume fraction, therefore the potential energy density of the scaled system is comparable to the original system.

$$\rho_p = \rho'_p \tag{5.3}$$

Consequently, the mass of the coarse grained particles are scaled according to Equation 5.4, while the moment of inertia can be found in Equation 5.5.

$$
\begin{aligned}
m' &= \frac{4}{3}\pi R'^3 \rho' \\
&= s^3 m
\end{aligned}
\tag{5.4}
$$

$$
\begin{aligned}
I' &= \frac{2}{3}m' R'^2 \\
&= s^5 I
\end{aligned}
\tag{5.5}
$$

In order to create similarity for the kinetic energy density as well, the particle velocities should be the same as in the original system. This means that coarse graining should not affect the accelerations and decelerations of the system.

A system of coarse grained particles is assumed to move equally as the original system of particles (Equation 5.6), implying that the velocity of the coarse grained particle is equal to the average of the group of original particles it is representing (Sakai and Koshizuka, 2009). This satisfies the demand for a similar kinetic energy density displayed in Equation 5.7.

$$v' = v \tag{5.6}$$

$$\frac{1}{2}m'v'^2 = s^3 \frac{1}{2}mv^2 \tag{5.7}$$

The contact stiffness and damping need to be scaled accurately as well, in order to maintain the same energy losses experienced in inelastic collisions. Figure 5.10 shows the spring-damper system in normal direction of a group of original particles as well as the coarse grain with $s = 2$. As the coarse grain doubles in size, eight of the original particles are replaced by the coarse grain. In order to conserve the character of the contact, the stiffness k'_n and damping c'_n of the coarse grained particle needs to be the same as the equivalent stiffness k_{eq} and damping c_{eq} of the group of original particles.

(a) Coarse grain   (b) Original system
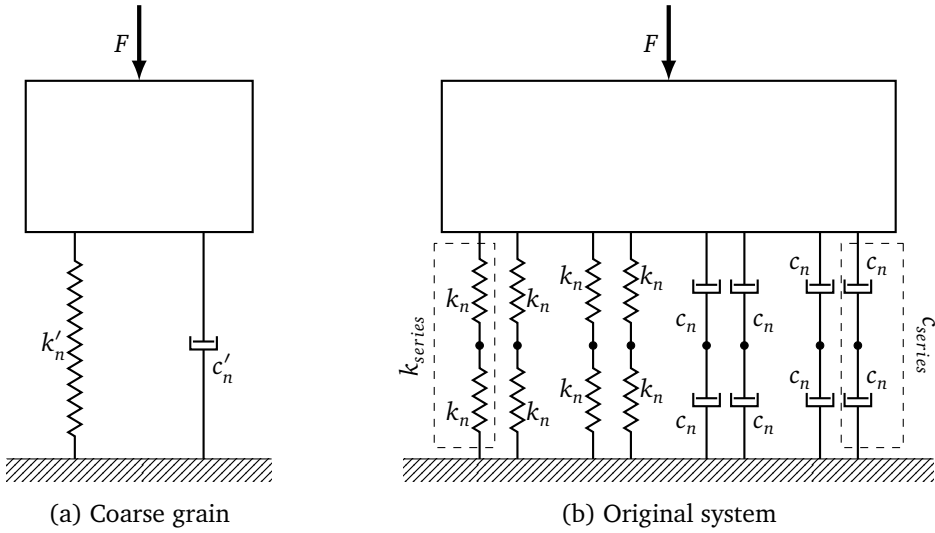
Figure 5.10: A coarse grain contact of $s = 2$ and the equivalent contact of original group of particles.

The equivalent stiffness of the original system k_{eq} consists of s^2 pairs of original springs and can be derived according to Equation 5.8. First step is determining the stiffness k_{series} of each of the four pairs. This can be done based on $\delta_{series} = s\delta_n$ and the definition of k_n in Equation 4.19:

$$
\begin{aligned}
k_{eq} &= s^2 k_{series} \\
&= s^2 \frac{\frac{1}{4} F_k}{\delta_{series}^{1.5}} \\
&= s^2 \frac{\frac{1}{4} F_k}{(s\delta_n)^{1.5}} \\
&= s^2 \frac{k_n}{s^{1.5}} \\
&= \sqrt{s} k_n
\end{aligned}
\tag{5.8}
$$

When the same equivalent Young's modulus is maintained for the coarse system (Equation 5.9),

$$E'^* = E^* \tag{5.9}$$

the stiffness of the coarse system k'_n in Equation 5.10 is equal to the equivalent stiffness of the original system k_{eq}. For the tangential stiffness k_t, the same scaling factor can be acquired. Therefore, the contact stiffness is identical to the equivalent stiffness of
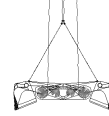
the original system.

$$
\begin{aligned}
k'_n &= \frac{4}{3} E'^* \sqrt{R'^*} \\
&= \sqrt{s}\frac{4}{3} E^* \sqrt{R^*} \\
&= \sqrt{s}\, k_n \\
&= k_{eq}
\end{aligned} \tag{5.10}
$$

Equation 5.11 shows that the equivalent damping coefficient c_{eq} can be obtained by computing the damping of the s^2 series of springs. The damping of each series of springs c_{series} can be determined based on the definition of c_n in Equation 4.19, $\delta_{series} = s\delta_n$ and the scaling factors for v_n (Equation 5.6) and k_n (Equation 5.10).

$$
\begin{aligned}
c_{eq} &= s^2 c_{series} \\
&= s^2 \frac{\frac{1}{4}F_d}{v_{series}\sqrt{k_{series}\delta_{series}^{1.5}}} \\
&= s^2 \frac{\frac{1}{4}F_d}{v_n\sqrt{\frac{k_n}{s^{1.5}}(s\delta_n)^{1.5}}} \\
&= s^2 \frac{\frac{1}{4}F_d}{\sqrt{s}v_n\sqrt{k_n(\delta_n)^{1.5}}} \\
&= s^2 \frac{c_n}{\sqrt{s}} \\
&= s^{1.5} c_n
\end{aligned} \tag{5.11}
$$

Equation 5.12 then shows that the damping coefficient c'_n of the coarse grain is identical to the equivalent damping c_{eq}. For the tangential damping c_t the same scaling factor can be calculated. This confirms that the energy losses due to inelastic collisions are the same for the original and the coarse grained system.

$$
\begin{aligned}
c'_n &= 2\sqrt{\frac{5}{6}}\beta\sqrt{m'^*} \\
&= s^{1.5}2\sqrt{\frac{5}{6}}\beta\sqrt{m^*} \\
&= s^{1.5} c_n \\
&= c_{eq}
\end{aligned} \tag{5.12}
$$

Normal contact forces acting on the particles in the coarse grained system are estimated to be s^3 times larger than in the original system (Bierwisch, 2009). This means that the entire group of original particles are all considered to be in the same collision as the coarse grained particle.

The tangential force F'_t in the coarse grained system computed using the same static

friction coefficient μ_s, as shown in Equation 5.13.

$$
\begin{aligned}
F_t' &= \mu_s F_n' \\
&= \mu_s s^3 F_n
\end{aligned}
\tag{5.13}
$$

For the contact model with rolling motions also the rotational energy of the coarse grained system needs to be comparable as the original system (Equation 5.14). When rotation is considered, both the original particles and the coarse grain rotate around their respective centre of mass. Rotation around other particles is only taken into account when this leads to a rotational velocity $\dot{\theta}$. By ensuring rotational energy is similar, the coarse grain system can be compared to the original system.

$$
\frac{1}{2} I' \dot{\theta}'^2 = s^3 \frac{1}{2} I \dot{\theta}^2
\tag{5.14}
$$

The torques on the coarse grains depend on the contact forces and the radius of the particle, and accordingly the torque is s^4 times higher the original torque. This is also true for the rolling friction torque. Equation 5.15 shows the rotational velocity of the coarse grained particle $\ddot{\theta}'$ when the coarse grain's torque and moment of inertia (Equation 5.5) are taken into account. The resulting angular velocity of the coarse grain satisfies Equation 5.14, confirming that the coarse grain has the same rotational energy as the group of original particles and consequently similarity between original and coarse system is achieved.

$$
\begin{aligned}
\ddot{\theta}' &= \frac{T'}{I'} \\
&= \frac{F_t' R' + \mu_r F_n' R'}{I'} \\
&= \frac{s^3 F_t s R + \mu_r s^3 F_n s R}{s^5 I} \\
&= \frac{1}{s} \ddot{\theta}
\end{aligned}
\tag{5.15}
$$

This shows that the coarse grain system has the same energy components as the original system. These identical components consist of the potential energy, the kinetic energy, the dissipation of energy through damping and the rotational energy. The following subsections focus on testing this coarse graining scheme. The coarse graining is assessed with an angle of repose test, a wall interaction and a penetration test. The effect of coarse graining on the accuracy and stability of a co-simulation of DEM and MBD is assessed in Section 6.2.1 and 6.3.

5.2.1   Angle of Repose

Angle of repose simulations were performed to investigate the effect of coarse graining on the simulated shearing behaviour. Figure 5.11a shows the angle of repose of particles

with a diameter of 7.5 mm and coarse grains with $s = 2$ and $s = 4$, all without rolling. It can be observed that the angles produced are comparable, although for very gentle angles the coarse grains with $d = 30$ mm show a steeper angle than the original system. It is possible that this is an effect of the limited number of elements in the coarse grain simulations, disturbing the accuracy of the angle measurements. The results with the material model with rolling motions are shown in Figure 5.11b, where it can be observed that the scaling factor did not significantly affect the outcome of the simulations. These results demonstrate that the proposed coarse graining scheme is able to predict shearing behaviour of particles regardless of the chosen scale.

(a) No-rolling material model.

(b) Rolling particles.
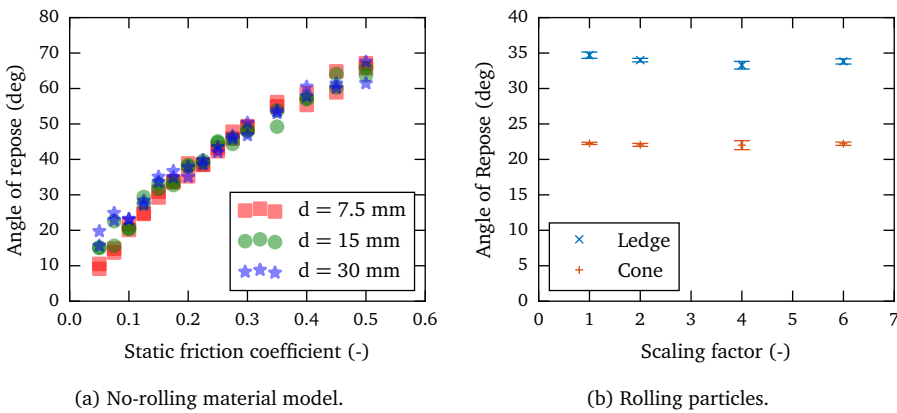
Figure 5.11: Coarse graining of angle of repose.

5.2.2 Penetration Resistance

The effect of coarse graining was also investigated in a penetration tests. The penetration test is similar to the penetration tests described in the previous chapters, however there are some differences. The test uses tool shape C of Figure 3.9, a penetration rate of 100 mm/s and a maximum penetration depth of 300 mm in order to approximate grab penetration more closely. The penetration test has been modelled in such a way that the resistance of the tip and shaft is measured separately. The tip is defined as the part of the tool where the cross is still expanding until it reaches the maximum width of 40 mm.

The penetration resistance of the calibrated particles ($s = 1$) and four coarser materials is shown in Figure 5.12. It can be observed that the resistance on the tip becomes higher when the grains become larger, averaging an additional 16 % for each step in grain size. Splitting of the bulk material into two parts to slide along the shaft is significantly harder for coarser grains. It is likely that the assumption that the coarse grain moves in a similar way as the original system no longer holds during penetration. Splitting of the bulk materials depends on the available voids between the particles,

pushing particles to either side of the tip. As the number of voids reduces as the grain size increases, finding a path through the bulk material becomes more challenging and requires more movement underneath the tool. In short, resistance gains as grain size increases, due to the direct dependence of the penetration process on the particle size and consequently the number of voids.

(a) On the tip.   (b) On the shaft.
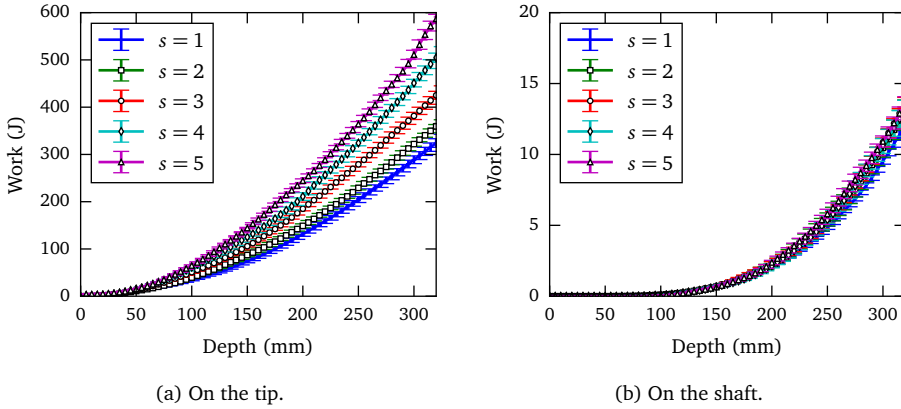
Figure 5.12: Effect of coarse graining on the penetration resistance.

The resistance on the shaft is much lower than the tip and does not show such a strong effect as the tip. The small difference between the original system and the coarser systems is possibly caused by the shaft area close to the tip that experiences slightly higher compressive forces due to the additional particle movements required for splitting the coarser systems. All the other contacts between the bulk material and the shaft are scaled without affecting the resistance, confirming the coarse graining scheme except for tip forces.

As the reduction of the computational expenses is essential for the application of virtual prototyping of grabs, ways of mitigating the effects on the splitting the bulk material have been investigated. Since the coarse grains behave adequately in the angle of repose test and for the shaft friction, a solution that incorporates changing behaviour in these tests is ruled out. This leads to a solution that changes the contact behaviour of the tip, for example assigning different contact properties to the tip-particle contacts.

The tip-particle contacts can be altered in several ways, for example in their stiffness, damping and sliding behaviour. Lowering the stiffness of the particle-tip contacts would mean that overlap would become higher than the recommended value of Section 5.1 and compresses the bulk material, resulting in undesired local density concentrations around the tip. Also the transfer of a contact from the tip to the shaft would lead to problems since a jump in stiffness would result in undesired jumps in overlap. Damping of the contacts did not show any effect in the sensitivity analysis of the previous chapter since contact velocities are low and are therefore not expected to aid in reducing the

penetration resistance. Adjusting the sliding coefficient of the tip is in fact the most promising solution, reducing the additional friction forces caused by the additional travel of the coarse grains to normal proportions. Consequently, the sliding behaviour of the tip-particle contacts is selected to resolve the increase in tip forces caused by the coarse graining scheme.

Influencing the penetration by lowering the wall friction coefficient of the tip is investigated by assigning a different value to the tip while the wall friction coefficient of the shaft remains unaffected. Figure 5.13 shows that for coarse grains with $s = 4$ the wall friction needs to be reduced to $\phi'_w = 0.05$ in order to achieve the same the penetration characteristics as the original system. It appears that the limit for coarse graining of penetration is reached at $s = 5$, since the wall friction cannot be reduced further and it is no longer possible to compensate for the coarser grains. For the material model with rolling motions both tip friction coefficients ϕ'_w and ϕ'_r have been adjusted. Figure 5.14 shows that the material model including rolling needs more compensation, resulting in an upper limit of $s = 3$ for the coarse graining of the penetration. By applying reduced tip-particle friction coefficients both material models can be coarse grained while maintaining the penetration characteristics of the original system.

(a) $s = 4$ (b) $s = 5$
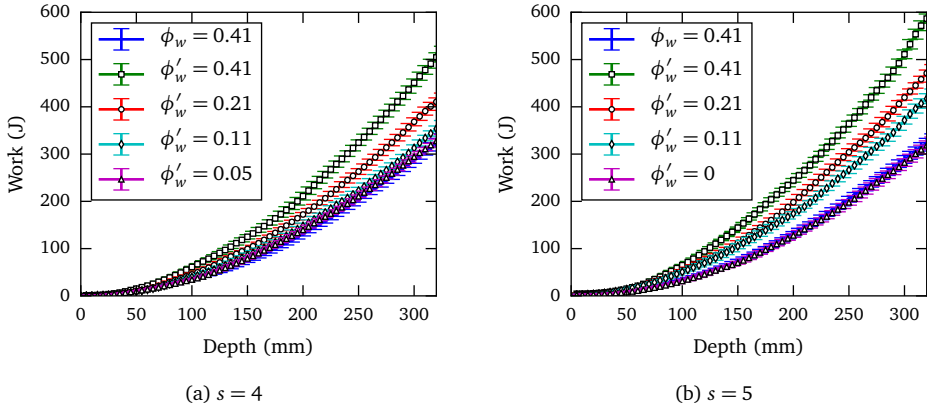
Figure 5.13: Penetration resistance with adjusted tip friction coefficient.

The coarse graining scheme leads to a considerable reduction in computational costs and cuts simulation time of a large scale grab. For the material model excluding rolling, the maximum scaling factor of $s = 5$ reduced the computing time from an estimated 10^4 hours to just under 18 hours. The material model including rolling can be coarse grained with $s = 3$, resulting in a computing time of five days. With the help of these reductions, the coarse grain material model can now be used to complete full scale grab simulations within days instead of years without significant consequences.
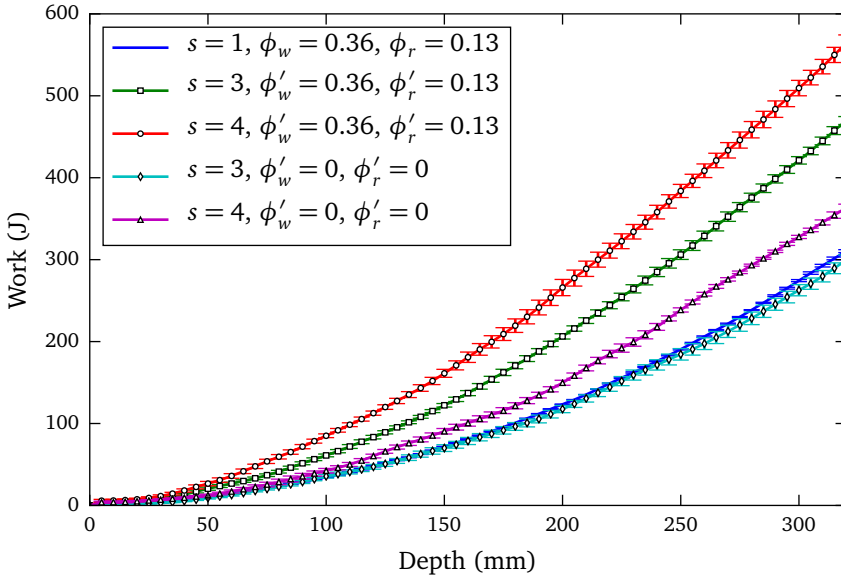
Figure 5.14: Penetration resistance for coarse grain rolling material model.

5.3 Conclusions

This chapter has investigated two methods for reducing the computational costs of a large scale DEM simulation: particle stiffness reduction and coarse graining. Both methods have been found to speed up computational time while maintaining simulation accuracy. For a large scale grab simulation this provided a reduction in computational time from an estimated 8.3 years to 18 hours, while the calibrated behaviour of the material model was preserved.

It has shown that a particle stiffness reduction can lead to a speed up as well as result in undesired effects and therefore should be treated with care. The stiffness reductions directly affected the collision behaviour of a single contact pair and the stiffness response of an assembly of particles and should be avoided in simulations where these aspects are considered important. Other aspects such as the energy dissipation, the shearing behaviour, bulk density and penetration resistance showed negligible impact as long as normal overlaps remain below 0.3% of the particle radius. This observed value is comparable with the 0.1–0.5% limit experienced by Cleary (2010). Reducing particle stiffness to the stated 0.3% limit offers considerable savings in computational expenses for DEM models concerning these aspects, such as an iron ore pellet grab simulation. In case of the iron ore pellets grab, the particle stiffness reduction resulted in cost reduction factor of 7.3, while the calibrated behaviour of the material model is not affected.

The coarse graining technique demonstrates that a group of particles can be replaced by a single, coarse particle as long as the particle process is not inherently dependent on the grain size. The coarse grain system contains identical amounts of potential, kinetic, rotational and dissipated energy as the original system. This was confirmed in simulations of the angle of repose, where the shearing behaviour of coarse grains matched the behaviour of the material model. Sliding resistance on the shaft of the penetration tool was also constant for the tested grain sizes. However, coarse graining of the penetration resulted in an increase in resistance on the tip of 16% when grain size doubled. This increase caused by the coarser grain could be compensated by lowering the sliding friction of the penetrating tip which would bring the resistance back to normal levels. The coarse graining technique resulted in a reduction of 10^4 hours to just under 18 hours for the iron ore pellet grab simulation while the calibrated behaviour including penetration resistance remained constant.

In conclusion, the findings establish that both techniques can help users to simulate large scale DEM simulations without affecting results. Both the large scale material model and the grab model can now be coupled into a co-simulation. How these two models can be coupled together is presented in the next chapter, this is the last step in creating a large scale co-simulation of a grab and iron ore pellets.

6

Developing a Co-simulation of an Equipment and Material Model

This chapter shows how the Discrete Element Method (DEM) and Multibody Dynamics (MBD) can be coupled, which is a requisite for coupling the grab model with the material models. It establishes a method for verifying the coupling through series of simple tests with known analytical solutions, proving the correctness of the coupling program. This chapter examines the robustness of the coupling, presenting a guideline for obtaining stable results.

Section 6.1 documents the coupling for both directions, from DEM to MBD and from MBD to DEM, Section 6.2 demonstrates that the proposed method of coupling is capable of achieving accurate results by examining a selection of scenarios of coupled models where the co-simulation is compared to an analytical solution. Section 6.3 examines the stability of the co-simulation and offers an approach to selecting a feasible timestep as well as a suitable communication interval.

6.1 Coupling of an Equipment Model and a Material Model

For a co-simulation of both particulate material and equipment, three software components are required as displayed in Figure 6.1. The first component is the discrete element

method for simulation of particle behaviour and forces acting on the equipment. These loads are sent to the multibody dynamics component which consists of a mechanism of multiple bodies connected to each other through cables, joints and contacts. The load on the mechanism affects the position of its bodies and these new positions are sent back to the DEM program. The coupling consists of sending the position of the selected bodies from the dynamic model to the particle model, and sending the load data of the selected bodies from the particle model to the dynamic model. A coupling server, the third software component, is employed to communicate with the two simulation packages, sending input to them and asking for output from them.
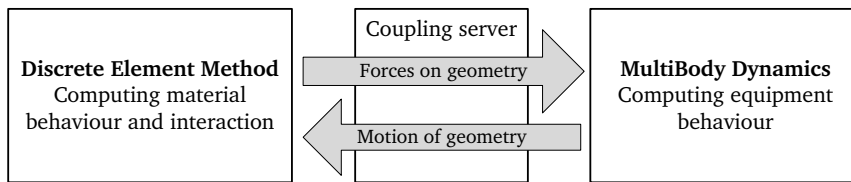
Figure 6.1: Co-simulation of an equipment and particle model.

The DEM software component used in this research is EDEM®, a package developed by DEM Solutions (2014a). The program can be accessed through the graphical user interface or through the extended Application Programming Interface (API). As the data exchange needs to occur at regular intervals, a coupling without user intervention through the API is highly preferable as this will eliminate the need for the user to manually couple the programs. By writing C++ user defined libraries, users can add their own programming to the DEM software. The API offers possibilities for user defined contact models, particle body forces, particle generators and multibody dynamics coupling.

The MultiBody Dynamics (MBD) software component used in this research is Adams®, a package developed by MSC Software (2014). The program can collaborate with other programs through the Adams/Controls package. Previously the only programs able to connect with the Adams®/Controls package were MSC Software's EASY5® and Matlab® from the Mathworks Inc., but recently this list has expanded to the Adams® external interface and the Functional Mock-up Language. The Adams® external interface offers programmers access to Adams®/Solver through a collection of functions in C and exchange information when desired.

Published research on coupling DEM and MBD programs has been limited so far. The works conducted by Yoon et al. (2011, 2012) and Park et al. (2012) investigated the inclusion of particles in a MBD package, focussing on the use of the computer's graphical processing unit to perform to calculations. A general purpose approach for coupling with Adams® has been written by Elliott (2000), and offers several handles
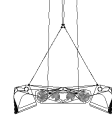
how to accomplish a robust and accurate coupling with an external interface. Coetzee et al. (2010) has modelled a dragline bucket where the DEM code PFC uses an external component that calculates the motion of the dragline bucket. A coupling written for EDEM® and Adams® by ESTEQ (2008) has been used in the earlier stages of this research. This coupling uses MSC. Software's EASY5® to communicate with Adams® and is restricted to outdated versions of EDEM. This made it impossible to use recent versions of the EDEM® program and to simulate batches of co-simulations. Therefore, a light coupling server has been developed that could interact with the recent versions of both packages without the need to configure EASY5® for each co-simulation.

This coupling server software component is a self-written program which interacts with the DEM and MBD components. The coupling server couples the selected MBD bodies and the selected DEM geometries, sticking the two models together and behaving as glue between the two models. As both DEM and MBD do not simulate at the same speed and do not advance with the same timestep, the coupling server has to coordinate the exchange of data and the schedule required. For example, a stand-alone DEM simulation advances with a timestep of 1e-6 seconds, while a stand-alone MBD simulation prefers to simulate with a timestep of 1e-2 seconds or more. Running both codes at the same timestep is undesirable, as this will increase the computational costs for the faster simulation and in addition increase computational costs due to the overhead of the coupling. Instead, the two simulations communicate at a communication interval $n\Delta t$, which is for practical reasons a multiple n of the smallest timestep Δt. The coupling server works for both directions, coupling the load data from DEM to MBD and the position data from MBD to DEM and is explained in the following subsections.

6.1.1 From DEM to MBD

The main purpose of linking the bulk material simulation to the equipment simulation is to perform the equipment simulation with loads caused by the bulk material. Starting point is a vector with the position and trajectory $\mathbf{x}(t)$ of a coupled body during a communication interval $n\Delta t$. This vector contains the position, orientation and velocities of the geometry. With this data of the geometry the DEM simulation checks whether particles are in contact with the body during the communication interval and calculates the corresponding load data $\mathbf{F}(t)$ in Equation 6.1:

$$\mathbf{x}(t) \rightarrow \boxed{\text{DEM}} \rightarrow \mathbf{F}(t) \tag{6.1}$$

The load data $\mathbf{F}$ of each coupled body consists of six components: both forces F and torques T in three directions. The forces and moments are oriented in the directions of the global coordinate system and around the body's centre of mass. At each communication interval $n\Delta t$, the load data $\mathbf{F}$ is requested from the DEM simulation for all the bodies to be coupled.

However, the load data $\mathbf{F}(t)$ cannot be applied directly in the MBD simulation as this value is not necessarily constant during the communication interval $n\Delta t$. If the

load calculated in DEM increases every timestep Δt as shown in Figure 6.2 the correct value to be communicated with MBD is denoted by the grey area. Unfortunately the dynamics calculation uses the communicated value without regard for its history during the communication interval, which in this case leads to an overestimation displayed by the Error area. The communicated value should therefore be somewhere between $F(t - n\Delta t)$ and $F(t)$.
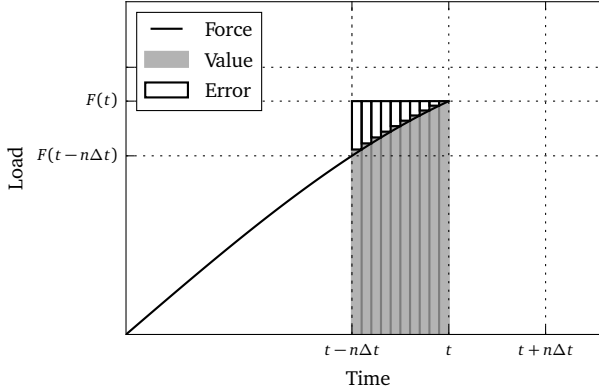
Figure 6.2: Force averaging in DEM.

This can be resolved by averaging the force during the last n timesteps that took place since the previous communication time in Equation 6.2:

$$\bar{F}(t) = \frac{1}{n} \sum F(t) + F(t - \Delta t) + F(t - 2\Delta t) + \ldots + F(t - n\Delta t) \qquad (6.2)$$

where $\bar{F}(t)$ is the average force at time t during the communication interval $n\Delta t$. This average force is computed by starting at zero and at each timestep adding the particular force data. This operation is performed for all coupled bodies and all of their components according to Equation 6.3:

$$\mathbf{F}(t) \rightarrow \boxed{\text{Force averaging}} \rightarrow \bar{\mathbf{F}}(t) \qquad (6.3)$$

The Adams® solver requests the inputs to the solver to be given at the same time as the outputs. This means that if the the load data $\bar{\mathbf{F}}$ of time t is fed to the solver, it would return the accompanying positions and velocities of the bodies at time t. Unfortunately the positions and velocities at time t were the starting point of Equation 6.1. In fact, at the next communication between MBD and DEM the position data at time $t + n\Delta t$ is required. In order to have the MBD solver deliver this, it requires load data at $t + n\Delta t$.

To achieve the load data $\bar{\mathbf{F}}(t + n\Delta t)$ the available load data $\bar{\mathbf{F}}(t)$ has to be extra-

polated (Elliott, 2000) in Equation 6.4:
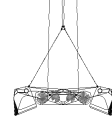
$$\bar{\mathbf{F}}(t) \rightarrow \boxed{\text{Force extrapolation}} \rightarrow \bar{\mathbf{F}}(t + n\Delta t) \tag{6.4}$$

The load data is extrapolated to $t + n\Delta t$ by finding a quadratic solution based on the last three available load data points as displayed in Figure 6.3. First step is finding a quadratic solution displayed in Equation 6.5 which fits the three data points:

$$\bar{F}(t) = c_1 t^2 + c_2 t + c_3 \tag{6.5}$$
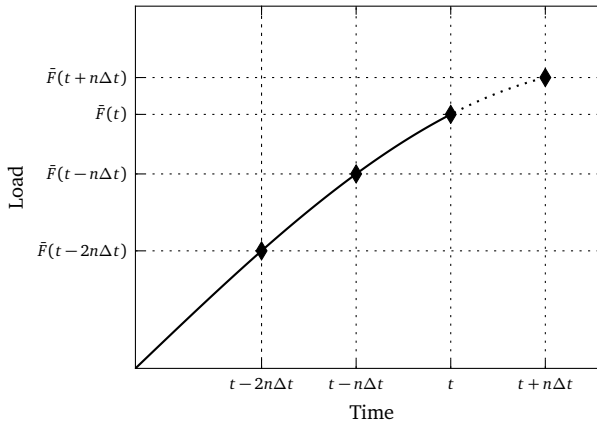
Figure 6.3: Force extrapolation required for MBD solver.

The solution is found by applying Cramer's Rule (Cramer, 1750) to the system of linear equations in Equation 6.6.

$$T_C \mathbf{c} = \bar{\mathbf{F}}_\mathbf{C} = \begin{bmatrix} t^2 & t & 1 \\ (t-n\Delta t)^2 & t-1n\Delta t & 1 \\ (t-2n\Delta t)^2 & t-2n\Delta t & 1 \end{bmatrix} \begin{bmatrix} c_1 \\ c_2 \\ c_3 \end{bmatrix} = \begin{bmatrix} \bar{F}(t) \\ \bar{F}(t-n\Delta t) \\ \bar{F}(t-2n\Delta t) \end{bmatrix} \tag{6.6}$$

According to Cramer the three coefficients c_1, c_2 and c_3 can be defined (Equation 6.7) in terms of determinants defined in Equations 6.8, 6.9, 6.10 and 6.11.

$$c_1 = \frac{\det(C_1)}{\det(T_C)}, c_2 = \frac{\det(C_2)}{\det(T_C)}, c_3 = \frac{\det(C_3)}{\det(T_C)} \tag{6.7}$$

$$\det(C_1) = \begin{vmatrix} \bar{f}(t) & t & 1 \\ \bar{f}(t-n\Delta t) & t-n\Delta t & 1 \\ \bar{f}(t-2n\Delta t) & t-2n\Delta t & 1 \end{vmatrix} \tag{6.8}$$

$$\det(C_2) = \begin{vmatrix} t^2 & \bar{f}(t) & 1 \\ (t-n\Delta t)^2 & \bar{f}(t-n\Delta t) & 1 \\ (t-2n\Delta t)^2 & \bar{f}(t-2n\Delta t) & 1 \end{vmatrix} \tag{6.9}$$

$$\det(C_3) = \begin{vmatrix} t^2 & t & \bar{f}(t) \\ (t-n\Delta t)^2 & t-n\Delta t & \bar{f}(t-n\Delta t) \\ (t-2n\Delta t)^2 & t-2n\Delta t & \bar{f}(t-2n\Delta t) \end{vmatrix} \tag{6.10}$$

$$\det(T_C) = \begin{vmatrix} t^2 & t & 1 \\ (t-n\Delta t)^2 & t-n\Delta t & 1 \\ (t-2n\Delta t)^2 & t-2n\Delta t & 1 \end{vmatrix} \tag{6.11}$$

The three coefficient of Equation 6.7 can then be applied in Equation 6.5 to extrapolate the load data $\bar{F}$ to $t + n\Delta t$ as shown in Equation 6.12:

$$\bar{F}(t+n\Delta t) = c_1(t+n\Delta t)^2 + c_2(t+n\Delta t) + c_3 \tag{6.12}$$

This operation is performed for all force and moment components for each body at each communication interval.

Another benefit of the extrapolation of load data is that is works similar to a smoothing operation. This will prevent the DEM simulation of feeding erratic forces to the MBD solver which could jeopardize the stability of the co-simulation. The stability of a co-simulation will be discussed in more detail in section 6.3.

6.1.2   From MBD to DEM

The Multibody Dynamics solver calculates the movement of the mechanism based on the external loads from DEM and the mechanism modelled in Adams® (Equation 6.13). The movements of the coupled bodies from the MBD solver are required for the next iteration of the coupling in in EDEM®.

$$\mathbf{F}(t+n\Delta t) \rightarrow \boxed{\text{MBD}} \rightarrow \mathbf{x}(t+n\Delta t) \tag{6.13}$$

In a way, the multibody dynamics solver is always ahead of the discrete element simulation as it uses extrapolated loads to compute the position data. Before the outputs from the MBD solver can be applied in the DEM package coordinate transformation is necessary (Equation 6.14). Two differences between the codes have to be resolved for a successful co-simulation: position versus translation and Euler angles versus
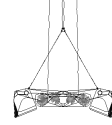
orientation matrix:

$$\mathbf{x}(t + n\Delta t) \rightarrow \boxed{\text{Coordinate transformation}} \rightarrow \mathbf{x}(t + n\Delta t) \quad (6.14)$$

Adams® uses the absolute position of a body x while EDEM® uses the translation Δx of the body with the original position x_0 of the body as origin. These differences can simply be overcome by applying Equation 6.15:

$$\Delta x = x - x_0 \quad (6.15)$$

Adams® uses a 3-1-3 body rotation sequence (Kane et al., 1983) and the transformation from Euler angles ψ, θ and ϕ to a rotation matrix O can be achieved by Equation 6.16:

$$O = \begin{bmatrix} \cos(\psi)\cos(\phi) - \sin(\psi)\cos(\theta)\sin(\phi) & -\sin(\psi)\cos(\phi) - \cos(\psi)\cos(\theta)\sin(\phi) & \sin(\theta)\sin(\phi) \\ \cos(\psi)\sin(\phi) + \sin(\psi)\cos(\theta)\cos(\phi) & -\sin(\psi)\sin(\phi) + \cos(\psi)\cos(\theta)\cos(\phi) & -\sin(\theta)\cos(\phi) \\ \sin(\psi)\sin(\theta) & \sin(\psi)\sin(\theta)\cos(\psi)\sin(\phi) & \cos(\theta) \end{bmatrix} \quad (6.16)$$

By default both programs define the orientation around the current centre of mass.

At this point, the geometry data at $t + n\Delta t$ is sent to DEM program. This includes the position, velocity, orientation and angular velocity of each coupled body. While the position and orientation are needed for correct positioning of the coupled body, this is not true for the velocities. These are used for the calculation of contact forces according to the definition of the Hertz Mindlin contact model discussed in Section 4.2.

The EDEM® software automatically interpolates the geometry data for all the DEM timesteps between t and $t + n\Delta t$ according to the linear interpolation of the SLERP algorithm (Shoemake, 1985). The difference between the non-linear movement and the linear interpolation of the SLERP algorithm should be considered when selecting a suitable communication time $n\Delta t$. For example, a circular motion during the time $n\Delta t$ will be interpreted as a straight line, therefore n should be chosen in such a way that this effect can be ignored.

6.2 Verification of the Coupling

The coupling of the two codes discussed in the previous section is verified in this section. The verification process is performed with four different tests, starting with a simple test and gradually increasing the complexity. At each simulation experiment, the simulation results are compared to the analytical solution. Without such a verification it will remain unclear whether the implemented coupling can produce accurate results.

The four tests have been selected to test the implemented coupling step by step, with each test focussing on additional aspects:

1. The first test examines whether the implemented coupling can accurately predict the contact of a single particle colliding with a wall of a coupled body. Also this test

examines if the coupling server is interfacing correctly with Adams®. Adams® is given a known load of particle collisions and has to return the corresponding behaviour of the body. This test is limited to translations only.

2. Aim of the second test is to verify that the coupling server interfaces correctly with EDEM®. EDEM® will be given a known motion for a body and has to return the corresponding load data to the coupling server. The given motion consists of both translations and rotations.

3. The third test verifies that the two-way coupling works for a scenario limited to translational forces and movements.

4. The final test of the coupling of Discrete Element Method and Multibody Dynamics Method verifies that the two-way coupling works for a scenario including rotations and moments.

The agreement between the co-simulation results and the analytical results is evaluated according to the coefficient of determination R^2 described by Weisberg (2005). Because both results are based on the same mathematical problem a very high coefficient of determination is to be expected. Correlation should exceed 0.99, demanding high accuracy while allowing for numerical scatter in the co-simulation.

6.2.1   Particle - Wall Collision

The first test of the verification process is a simple test where particles are shot at and collide with a geometry. Instead of using two particles in DEM, one of them has been replaced with a body whose behaviour is calculated with MBD. Aim of this test is to investigate whether a simple collision between particle and geometry can be computed correctly. In this first scenario, displayed in Figure 6.4, a single particle was generated and collided with the cube, which only has translational degrees of freedom.

Figure 6.4: Particle - cube collision test.

The particle has a radius of 10 mm, a coefficient of restitution of 0.5 and an initial velocity of $u_p = 2\,\mathrm{m/s}$. The cube was at rest at the start of the scenario and has a mass m_c of 10 kg. Different particle masses m_p were used in this test, ranging from 0.01 kg to 10 kg. During the simulation where gravitational forces are absent, the particles collided with the cube, transferring their energy according to Equations 6.17 and 6.18:

$$v_c = \frac{m_p u_p + m_c u_c + m_p C_R(u_p - u_c)}{m_p + m_c} \tag{6.17}$$
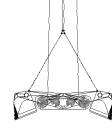
$$v_p = \frac{m_p u_p + m_c u_c + m_c C_R(u_c - u_p)}{m_p + m_c} \tag{6.18}$$

where v_p is the velocity after collision, u_p the initial velocity and m_p the mass of the particle and v_c, u_c and m_c for the cube. Simulations have been performed with a timestep of 5e-6 seconds.

Table 6.1 shows the velocities of the colliding bodies after the collision as well as the error according to Equation 6.19.

$$\text{Error} = 100 \left(\frac{v_{\text{Simulation}}}{v_{\text{Theory}}} - 1 \right) \tag{6.19}$$

It can be observed that the test particles of 100 times lighter showed acceptable agreement. However, simulations using heavier particles with a particle/cube ratio of 5 and 1 did not show good agreement with theory. This is presumably caused by the calculation of the particle/wall contact in EDEM®. The built-in contact models all assume that the mass of the wall or body is equal to 1e8 kg (Arumugan, 2014), while in fact it should be significantly less. This affects the value of the equivalent mass (Equation 4.25) which in turn affects the calculation of the damping force (Equation 4.17 and 4.18). To reduce this error to an acceptable level, users should limit the geometry to particle mass ratios to at least 100 to 1 or use a customized contactmodel that does not assume the mass of the geometry. Simulations with high coefficients of restitution C_R will be affected less as the damping component of the contact force is smaller.

m_p	$\frac{m_c}{m_p}$	Theory		Simulation		Error (%)	
		v_p	v_c	v_p	v_c	p	c
0.01 kg	1000	-9.97e-1	3.00e-3	-9.98e-1	3.02e-3	0.141	0.672
0.02 kg	500	-9.94e-1	5.99e-3	-9.95e-1	6.03e-3	0.130	0.642
0.1 kg	100	-9.70e-1	2.97e-2	-9.74e-2	2.94e-2	0.365	0.783
1 kg	10	-7.27e-1	2.72e-1	-7.56e-1	2.75e-1	4.31	0.943
2 kg	5	-5.00e-1	5.00e-1	-5.54e-1	-5.10e-1	10.8	2.09
10 kg	1	5.00e-1	1.50e0	3.87e-1	1.62e0	22.7	7.84

Table 6.1: Particle - geometry collisions with $u_p = 2\,\text{m/s}$ and $m_c = 10\,\text{kg}$.

Next, the single particle is replaced by a stream of particles, each with a mass of 0.01 kg and hitting the cube with their own initial speed of $2\,\text{m/s}$ minus the current speed of the cube. Particles are created at a rate of 200 particles per minute. Due to the incoming momentum of the particles, the cube starts accelerating, although the rate of acceleration decreases due to the increasing distance between the starting point of the particles and the position of the cube, requiring the particles to travel longer before they collide with the cube. Figure 6.5 shows the velocity and displacement of the cube calculated by the co-simulation as well as theoretical calculations based

on Equation 6.17. It can be observed that the agreement between co-simulation and theory is very good as the coefficients of determination R^2 exceed 0.999. This proves that the collision between particle and body is computed correctly.

(a) Velocity of the cube.

(b) Position of the cube.
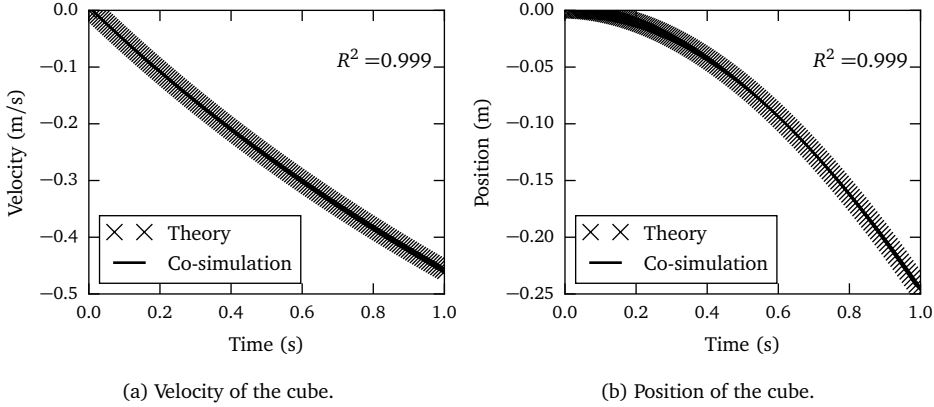
Figure 6.5: A stream of particles hitting the cube, causing it to accelerate.

6.2.2   Motorized Rotating Pendulum

The second test of the verification process used a box filled with particles connected to a pendulum, rotating at a constant angular velocity. Aim of this test is to assure that the coupling server correctly updates the position of the body in EDEM® and whether the load calculated in EDEM® corresponds with the theoretical approach. This will be achieved by comparing the forces acting on the joint of the pendulum predicted by the simulation to the gravitational and centrifugal forces of the box with particles. As the interaction forces do not affect the motion of pendulum the forces on the joint and the torque required for the rotation can be calculated by Equations 6.20, 6.21 and 6.22:

$$F_x = -m\omega^2 r \cos\theta \tag{6.20}$$

$$F_y = m\omega^2 r \sin\theta + mg \tag{6.21}$$

$$T_z = F_x r \sin\theta - F_y r \cos\theta \tag{6.22}$$

$$m = \Sigma m_p + m_c \tag{6.23}$$

In this test the pendulum has a mass m according to Equation 6.23, consisting of Σm_p of 236.6 kg and m_c of 10 kg. The pendulum has a horizontal starting position and rotates counter-clockwise at a constant angular velocity ω of 72 deg/s. The radius r of the pendulum is 1.5 m and gravity is acting at 9.81 m/s². Figure 6.6a shows the simulation of the motorized pendulum.
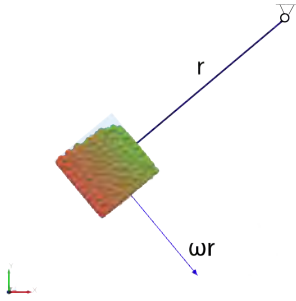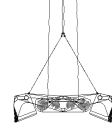
(a) Box with particles moving in a circular motion.
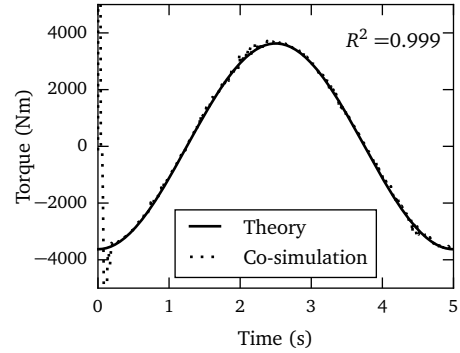
(b) Torque required for the circular motion.

Figure 6.6: Motorized pendulum.

Figure 6.6b shows the torque required for rotating the particle box at the prescribed angular velocity. First, the box in the simulation needs to be accelerated to the prescribed angular velocity which results in a mismatch during the first 0.25 seconds as Equation 6.20 and 6.21 assume constant velocity. For the remainder of test, it can be seen that the predictions of the co-simulation match very well with the theoretical approach based on Equation 6.22, resulting in a coefficient of determination of 0.999. This confirms that the coupling server and EDEM® calculate the expected load output well while given a known input, both for translational movements as well as rotational movements.

6.2.3 Translating Spring Damper System

The third test of the verification process uses a box of particles connected to a translational spring damper system. Aim of this test is to investigate whether the coupling server and MBD process the load input correctly and if it results in the desired response of the system. This test is again limited to translational forces and movements. The response of the spring damper system can be described according to Equation 6.23 and 6.24:

$$m\frac{d^2x}{dt^2} + c_d\frac{dx}{dt} + kx = mg \qquad (6.24)$$

The box has a mass of 100 kg and the particles have a mass of 261.8 kg while the spring has a constant k of 5000 N/m, preloaded at 100 N and the damper has a damping coefficient c_d of 500 Ns/m. The particles have a coefficient of restitution C_R of 1 in order to exclude damping from the particles.

(a) Velocity of the box.   (b) Position of the box.
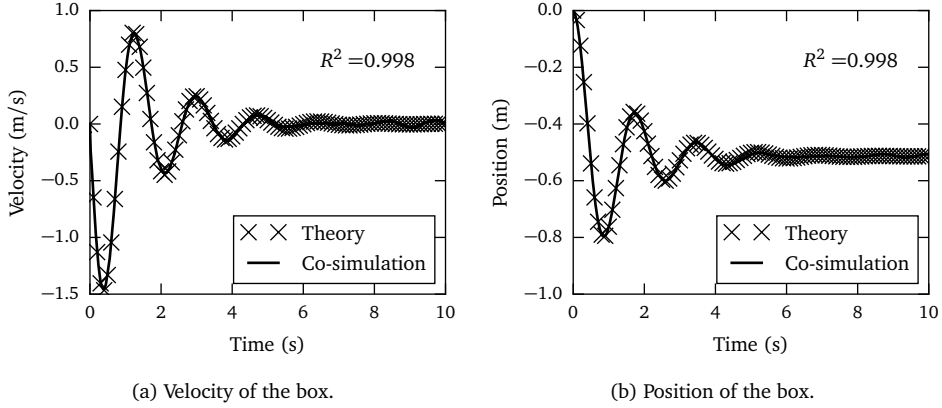
Figure 6.7: System response predicted by the co-simulation compared to the system response according to Equation 6.24.

Figure 6.7 shows the velocity and position of the box of particles during the simulation. Due to weight of the particles and the box, the box drops down in search for a new equilibrium. Due to the damper present in the system, the velocity is reduced, damping the system and gradually slowing down the box. It can also be observed from Figure 6.7 that the response predicted by the co-simulation correlates well with the response following from Equation 6.24, resulting in a determination coefficient of 0.998. This proves that the coupling server and MBD software Adams® properly transform the translational forces of the particles to translational movements of the mechanism.

6.2.4   Torsional Spring Damper System

The final test of the coupling of Discrete Element Method and Multibody Dynamics Method is performed by confirming the response of a torsional spring and damper system. Aim of this test is to verify that the MBD software Adams® and DEM software EDEM® are coupled correctly to the coupling server, both for translations and rotations. The motor of the pendulum example in Section 6.2.2 has been replaced by a torsional spring with a stiffness κ of 40 Nm/deg and a torsional damper C_d of 20 Nms/deg. The system can then by described by Equations 6.23 and 6.25:

$$\frac{d^2\theta}{dt^2}I + \frac{d\theta}{dt}C_d + \kappa\theta = mgr\cos\theta \tag{6.25}$$

where I is the moment of inertia and the load on the system is determined by the mass of the box $m_c = 50$ kg, the total particle mass $\Sigma m_p = 266.4$ kg and the angle of the pendulum θ. The initial position of the pendulum is horizontal.

(a) Angular velocity.   (b) Rotation.
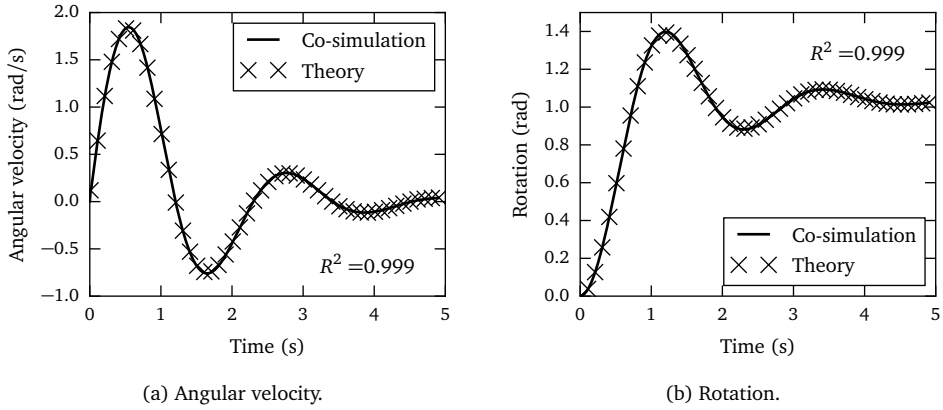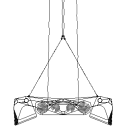
Figure 6.8: Response of system calculated by a coupled simulation compared to the equation of motion in Equation 6.25.

In Figure 6.8 the angular velocity and rotation of the pendulum are shown. Due to the weight of the box with particles, the pendulum started accelerating. The torsional spring prevents the pendulum from reaching vertical position while the torsional damper reduces the angular velocity. When the outcome of the simulation is compared to the equation of motion it becomes clear that the coupling of DEM and MBD produces very accurate results with a determination coefficient of 0.999.

This final test concludes the verification process of the coupling method described in Section 6.1. This proves that the developed coupling of DEM and MBD works as expected and is capable of accurately simulating systems where particles and mechanisms interact.

6.3 Coupling Stability

Besides an accurate co-simulation of DEM and MBD also a robust coupling is desired. Without robustness, simulations will fail or produce considerable errors. Both the solvers of the DEM and MBD have their own preferences for achieving a stable simulation with the lowest possible computational costs. However, when the two solvers are coupled in a co-simulation, these preferences sometimes conflict and need to be resolved. This section focuses on the stability of a co-simulation and aims to provide users with a guideline for robust and stable co-simulations while minimizing computational costs .

6.3.1   Stability of DEM

The stability of a DEM simulation is determined by the size of the timestep Δt or Δt_{DEM}, which is the stepsize the simulation uses to advance through time (Equation 4.14). It is essential that these timesteps are not too large, as contacts need to be detected in time in order to calculate the interaction forces correctly. If the selected timestep is too large, overlap between the particles might be aggravated, causing a disproportional response from the contact model as described in Chapter 4. This response consists of interaction forces which are too large and leads to a large acceleration of the particle, therefore resulting in a large displacement during a timestep. It is likely that the next contacts of the particle will also be disproportional, initiating a chain reaction of unstable contacts which will result in the explosions of particles, a scenario well known by DEM users.

Choosing a stable timestep size is a topic of interest for many DEM users, as a very conservative estimate of the timestep will raise computational costs significantly. One of the available guidelines of choosing a suitable timestep is the definition of the Rayleigh timestep shown in Equation 6.26 (Ning, 1995). This is the amount of time required for the propagation of a surface wave through a particle and has proven to be a useful tool for estimating a suitable timestep.

$$\Delta t_R = \pi R \sqrt{\frac{\rho}{G}} \frac{1}{(0.1631\,\nu + 0.8766)} \tag{6.26}$$

Users are recommended to take a fraction γ_R of the Rayleigh timestep Δt_R of 20% for systems with high coordination numbers (=>4) and up to 40% for lower coordination numbers (DEM Solutions, 2014b).

Another guideline for determining the critical timestep is based on the eigenfrequency ω of a single particle (O Sullivan and Bray, 2004) shown in Equation 6.27. Here, a safety factor γ_ω of 0.8 is commonly taken into account to ensure a stable integration.

$$\Delta t_\omega = 2 \sqrt{\frac{m}{k_n}} \tag{6.27}$$

The value for Δt_ω is usually smaller than Rayleigh critical timestep Δt_R, as pointed out by Yade-DEM (2015). For example the critical timestep Δt_ω for the particles of the material model is 20% of Δt_R, while for the large scale model this ratio increases to 31%. It can be concluded that the critical timestep based on the eigenfrequency Δt_ω is slightly more conservative than the Rayleigh critical timestep Δt_R when the safety factors γ_R and γ_ω are taken into account. In case of simulation scenarios where particles collide at high velocities, smaller timesteps should be taken to avoid disproportional response of the contact model.
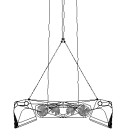
6.3.2 Stability of MBD

The solver of a MBD simulation works completely different from the DEM simulation. As opposed to solving the governing equations in discrete timesteps in the DEM, the Adams®/Solver solves governing equations of the model in continuous time. Adams® default solver GSTIFF uses backward differentiation formulas and fixed coefficients for prediction and correction, based on the work of Gear (1971). It is a variable step size integrator, which means means that the internal MBD simulation time does not advance at constant intervals, as it actually can slow down and reverse if the corrector has trouble converging.

Stability of the results is guaranteed by the correcter of the solver that monitors the error in the solution and checks if this is smaller that the specified corrector error tolerance. The corrector can force the solver to reduce its stepsize or repeat the previous steps at a smaller interval. It can be helpful to use the modified corrector instead of the original in models that have discontinuities in their force functions, for example when interacting with DEM. The modified correct only applies error control on a limited set of variables such as the displacements and is less strict on the prediction errors of the load data from DEM. The complete implementation of the corrector can be found in the Solver's manual (MSC Software, 2013).

Other variants of the GSTIFF solver are the WSTIFF solver (van Bokhoven, 1975) which uses variable coefficients instead of the GSTIFF's constant coefficients based on the assumption that the timestep does not change. Each time the timestep changes, the GSTIFF solver introduces a small error, while the WSTIFF solver prevents this. This makes WSTIFF is a more suitable solver for simulations with discontinuous forces such as contacts or interaction with other discrete functions such as the DEM.

6.3.3 Stability of Co-simulation

The two different solvers approaches causes some challenges when it comes to combining MBD and DEM. Elliott (2000) demonstrates several examples where the co-simulation results are not computed accurately, due to combination of a continuous MBD solver and a external discrete solver. The MBD solver selects its own timestep, and only requires the error tolerance to be configured. However, each time a communication takes place, a timestep is forced in the MBD solver. The maximum MBD timestep Δt_{MBD} therefore depends on the DEM timestep Δt_{DEM} and the communication interval n (Equation 6.28):

$$\Delta t_{\text{MBD}} \leq n \Delta t_{\text{DEM}} \tag{6.28}$$

The stability of the coupling is investigated by examining co-simulations of the spring-damper system from Section 6.2.3. Table 6.2 presents the accuracy and costs of co-simulations using different DEM timesteps Δt_{DEM} and communication intervals n. It shows three coefficients of determination: for the position x, velocity v and force F acting on the geometry. Most important is the accuracy of the position of the geometry,

as an inaccurate position can lead to missed contacts and false contact forces. Accurate simulations have been marked grey when the correlation between the simulation and the analytic solution is above 0.99.

When the interval is chosen too large the computed velocity starts to deviate from the analytical solutions. This is shown in Figure 6.9 when $\Delta t_{\text{DEM}} = 1e-4$ and $n = 25$. This is undesirable as the geometry velocity is part of the contact interaction force calculation and therefore an error can propagate through the system (Equation 4.8). The determination coefficient of load data on the geometry is less high compared to the position and the velocity of the geometry. This is mainly caused by the discrete nature of the particle contacts and often compensated at the next communication interval. For example, when the interaction force is exaggerated this triggers larger than accurate acceleration of the geometry, while at the next communication the contact force is likely to be underestimated due to the aggravated displacement of the geometry during the interval. However, this behaviour tends to escalate into instability the more iterative steps are taken as the coupling is in fact too loose.

(a) Position.   (b) Velocity.   (c) Force.
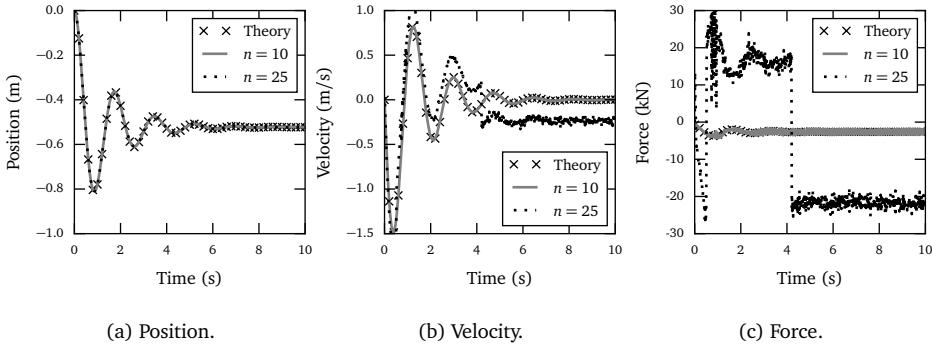
Figure 6.9: Example of unstable coupling: the communication interval is too large. $\Delta t_{DEM} = 1e-4$ s.

When the interval is chosen too small and the MBD solver is forced to have a very small timestep Δt_{MBD}, the accuracy of the solution is affected as well (Equation 6.28). Figure 6.10 shows an example where a small DEM timestep $\Delta t_{\text{DEM}} = 1e-5$ s is chosen in combination with a communication interval of $n = 1$, here the computed solution starts to differ from the analytical solution. By forcing the MBD simulations to use a very small timestep, numerical scatter is amplified, resulting in the so called *pinging* of the mechanism. The pinging can be observed from the erratic curve of the velocity and position of the geometry in Figure 6.10. The proposed force extrapolation of Section 6.1.1 reduces this problem as it also acts as a smoothing operator, although it obviously does not eliminate this problem.

(a) Position. (b) Velocity. (c) Force.
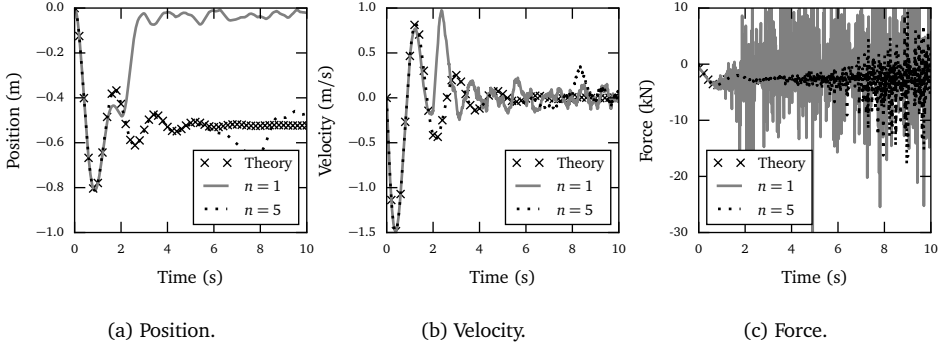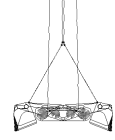
Figure 6.10: Another example of unstable coupling: pinging of the MBD solver because the communication timestep is too small. $\Delta t_{\text{DEM}} = 1e-5\,\text{s}$.

$t_s = \Delta t_{\text{DEM}}(s)$	$\Delta t_{\text{MBD}}(s)$	$n = \frac{\Delta t_{\text{MBD}}}{\Delta t_{\text{DEM}}}(-)$	$t_{\text{total}}(h:\min:s)$	R^2 of x	R^2 of v	R^2 of F
1e-5	1e-5	1	4:03:43	0.09660	0.58219	0.00185
	5e-5	5	0:53:54	0.85019	0.96361	0.02700
	1e-4	10	0:36:29	0.99985	0.99995	0.68607
	2.5e-4	25	0:28:06	0.99999	0.99998	0.99117
	5e-4	50	0:25:29	0.99999	0.99998	0.99559
	1e-3	100	0:23:53	0.99998	0.99985	0.19334
	1e-2	1000	0:02:23	0.35532	0.02900	0.00065
1e-4	1e-4	1	0:15:08	0.99973	0.99992	0.71259
	5e-4	5	0:05:10	0.99999	0.99998	0.99687
	1e-3	10	0:03:57	0.99998	0.99992	0.39737
	2.5e-3	25	0:03:07	0.99992	0.72059	0.02915
	5e-3	50	0:02:35	0.97173	0.47166	0.00438
	1e-2	100	0:00:22	0.35368	0.03011	0.00070
	1e-1	1000	0:00:22	0.02381	0.00002	0.00004

Table 6.2: Effect of different timestep and communication interval. $\Delta t_R = 5.21e-4\,\text{s}$.

The computational costs of a co-simulation also depend on the selection of the communication interval n. The critical timestep of the MBD solver is usually much larger than the DEM. Simply connecting both software components with $n = 1$ can be undesirable, since this requires both components to run at the same speed and may result in additional computational costs while accuracy does not improve. It can be observed from Table 6.2 that co-simulations with a communication interval $n = 1$ dramatically increases computational costs with a factor of up to eight, because at each DEM timestep the two software components communicate with each other. As the communication interval increases the computational costs decrease as the MBD solver is not forced to use very small increments. Simulations with a DEM timestep of 1e-4 s and an interval of 100 or more have even lower computational costs, however their

low costs are due to instability of the co-simulation, causing all the particles to leave the computational domain which affects the computational costs dramatically.

A guideline for achieving a stable and efficient co-simulation is shown in Figure 6.11 and consists of the following steps:

- For the DEM a stable timestep has to be determined, based on the Rayleigh critical timestep Δt_R or the eigenfrequency critical timestep Δt_ω. This needs to consider particle masses, stiffness and impact velocities characteristic for the simulation. A safety factor γ needs to be taken into account, however, a very conservative factor will lead to an unnecessary increase in computational costs.

- The MBD solver needs to be chosen based on the presence of contacts in the simulation and the nature of the interaction between particles and equipment. If the interaction is intermittent or contacts are causing abrupt events in the simulation, the WSTIFF solver is recommended. The corrector and its error tolerance need to reflect the nature of the simulation. If the simulated system contain discontinuities such as contacts that are high impact collisions between geometry and particles, the modified corrector can be used since it is less strict on force prediction errors.

- The communication interval n needs to be chosen in such as way that the DEM code is provided with sufficient updates of the geometry's position in order to prevent a disproportional response from the contact model. A value of $n = 5$ can be selected as initial value. For simulations with a small Δt_{DEM} and a large geometry mass a higher value for n can be helpful to prevent forcing the MBD solver to use small timesteps, reducing the risk of pinging.

- The stability of the co-simulation can be tested by experimenting with the communication interval n. By examining co-simulations with different intervals the quality of the results can be assessed. A communication interval that is too large can be recognized by comparing the velocity profiles of the geometries to the derivative of the position data. An interval that is too small can be identified by examining the forces acting on the geometry. If these forces are extremely erratic, it is likely that the MBD will have difficulties in successfully computing the accompanying velocities and displacements.

- If the co-simulation is found to lack stability, its settings needs to be reconfigured. A first step in achieving a more robust solution is to alter the communication interval, depending on the evaluation. If changing the communication interval does not produce the desired effect, the MBD solver needs to be reconfigured. As a last resort, since this has the largest impact on the computational costs, the DEM timestep can be lowered.
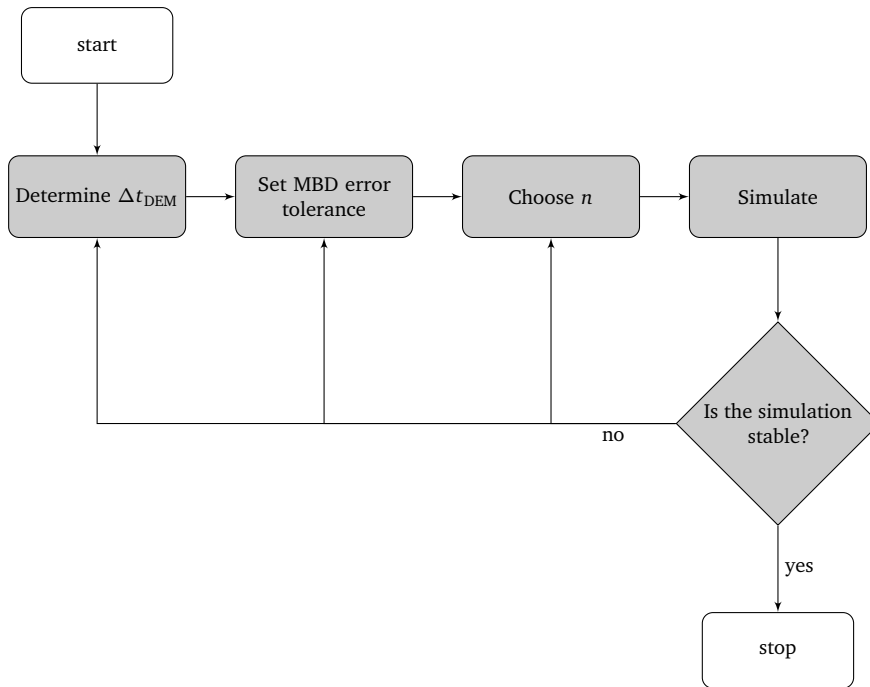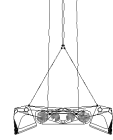
Figure 6.11: Achieving a stable co-simulation.

6.4 Conclusions

This chapter shows how a Discrete Element Method model (DEM) can be successfully coupled with a Multi Body Dynamics (MBD) model into a co-simulation. By exchanging load and position data, both models can cooperate and together compute the interaction between bulk material and handling equipment. The two computational methods have been coupled in two ways, which consists of the coupling the load data on the geometry from DEM to MBD and the position data from MBD to DEM.

The coupling has been tested thoroughly in several scenarios, starting with a simple scenario of a single collision between particle and geometry and concluding with a complex scenario combining translation and rotation. All tests clearly demonstrated that the coupling is successful in predicting particle-equipment interaction.

A guideline has been developed for achieving a stable and efficient co-simulation. The robustness of the coupling has been assessed, demonstrating cases where the coupling is too tight as well as the effects of a coupling that is too loose. When the proposed guideline for a stable co-simulation is adopted, this coupling technique is ready for a simulation of iron ore pellets and a scissors grab.

The coupling of this chapter can now be combined with the developed MBD model of a grab and large scale iron ore pellet DEM material models into a co-simulation. How

accurate this co-simulation performs in predicting grab performance is investigated in the validation in the next chapter, establishing the accuracy of all the components of the co-simulation.

"The final test of a theory is its capacity to solve the problems which originated it."

George Dantzig (1914 – 2015)

7

Validating a Large Scale Coupled Model of a Scissors Grab and Iron Ore Pellets

This chapter validates a co-simulation in which the grab model is coupled with the large scale material model. At this point, it is unclear to what extent a coupled grab model and material model is able to predict the performance observed in practice. By comparing its predicted results to the outcome of physical, large scale experiments conducted on a bulk terminal, the accuracy of the model will be assessed.

Section 7.1 discusses the experimental tests on a bulk terminal, focussing on the data acquisition of the measurements. Section 7.2 describes the coupling of the scissors grab model and the iron ore pellets model and the configuration of the co-simulation. The results of the experiments are compared to the predictions of the coupled model in Section 7.3 which will determine the merit of the developed grab co-simulation.

7.1 Validation Test on Terminal

In order to determine the accuracy of the coupled models, validation tests have been performed, consisting of full scale tests with a scissors grab on a bulk terminal. These tests were conducted on a bulk terminal in the Netherlands using the same iron ore pellets of Chapter 3 and a scissors grab designed for iron ores of Chapter 2. In these full scale tests the closing process of a scissors grab in iron ore pellets is monitored, as

displayed in Figure 7.1. By comparing the measured behaviour during closing with the predicted behaviour, the developed co-simulation can be validated.

Figure 7.1: Validation experiments on bulk terminal.

The accuracy of the coupled model can be assessed by comparing the following aspects of the virtual grab behaviour to the real world behaviour:

- The predicted mass should approximate the final mass of iron ore pellets in the grab after closing has completed and hoisted away of the surface of the bulk material. Besides the final value, also the increase in cable forces during closing needs to be evaluated.

- The motion of the virtual grab should compare to the closing trajectory of the scissors grab in iron ore pellets. Most important is the vertical movement of the main hinge as result of the resistance encountered by the knives, forcing the main hinge point upwards in the closing stage.

The co-simulation and the experimental results are compared using the coefficient of determination described by Weisberg (2005). A coefficient of determination of $R^2 > 0.8$ is considered to be sufficient during closing, similar to the requirement for the MBD model in Chapter 2. Section 6.3 determined that the R^2 of geometry positions is higher than geometry forces, therefore in this validation the requirement for geometry positions is increased to $R^2 > 0.9$. This means that less than 20% and respectively 10% of the variance can be attributed to unknown variables such as modelling errors,

measurement errors and variability caused by the manual operation and swinging of the grab, irregularities in the bulk material surface and other external factors.

The surface shape of the bulk material is expected to influence the grab behaviour significantly and therefore included as a variable in this validation. Experiments were conducted with two different surfaces of the bulk material:

1. A flat surface was tested in three measurements. This type of surface likely results in a symmetric closing process and can be created in the simulation environment with relative ease. Creating a flat surface in the experiments was slightly more challenging in the experiments as can be observed in Figure 7.1.

2. Asymmetric closing was investigated in the experiment where the grab was lowered into the side of the heap. The sloped surface causes one bucket to penetrate at a lower height that the other.

The measurement fluctuations are determined by repeatedly grabbing the bulk material. Because the surface conditions and grab operation vary with each measurement, results may also vary with each measurement. For example, measurement fluctuation is introduced by the crane driver, who manually operates the grab. The fluctuations are investigated by conducting a series of eight measurements consisting of grabbing the material, hoisting and releasing it above the grabbed area. The surface of these fluctuation tests would sit between the heap surface and the flat surface.

The following data is collected in the experiment to compare to the load and the motion of the grab in the co-simulation:

- Cable forces derived from the load sensor in the boom of the crane.

- Winch velocities and torques through the winch drive's sensors.

- Grab position through video analysis.

The data is acquired and processed according to the following subsections.

7.1.1 Load Data

The load data allows for the measuring of the load in the cables and can therefore be used to assess the quantity of bulk material grabbed. The load sensor is located in the boom of the crane and is connected to one closing cable and one hoisting cable and by doubling the signal the total load on the crane can be evaluated. By measuring only two of the four cables there could be a difference between the measured loads and the actual loads, although this difference should be small as the grab is completely symmetrical and equipped with a load balancer.

Figure 7.2 shows the loads measured for the eight fluctuation measurements. It can be observed that the quality of the signal is not very high due to the maximum measuring frequency of 2 Hz, especially when compared with the 1 Hz eigenfrequency

of the cables. During lowering, denoted by "L", the load consists of the empty grab of 15 ton and the weight of the cables. The time is defined at zero when the grab touches the surface of the bulk material. Because the grab is now resting (R) on the bulk material, the load is reduced to the weight of the cables. When closing (C) starts, the load starts to increase and when time reaches six seconds, the closing of the grab pauses at roughly 90% closed. At this point, the grab is hoisted (H) until the grab is suspended (S) in the air.
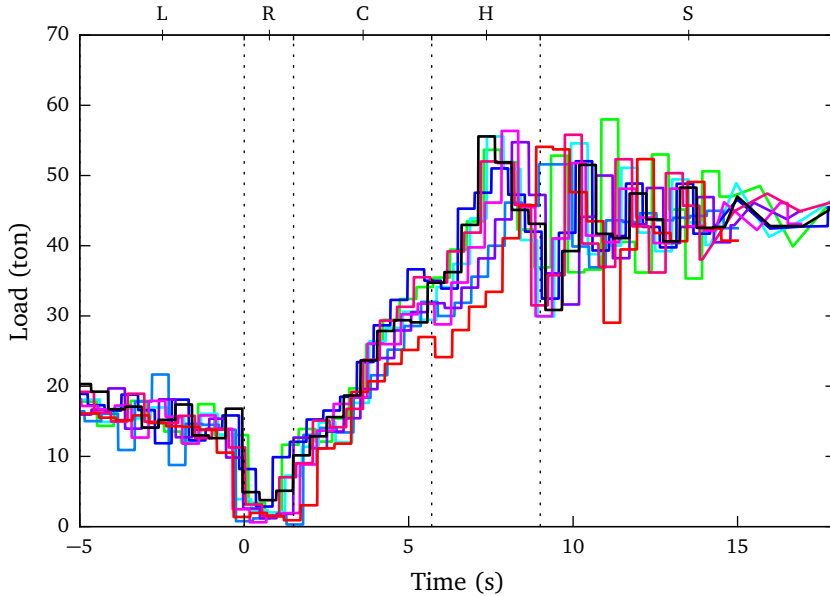
Figure 7.2: Load data during the eight fluctuation measurements, which consists of lowering (L), resting on the surface (R), closing (C), hoisting (H) and suspended from the crane (S).

7.1.2   Winch Data

The velocities, frequencies and torques of the winch drives were also recorded, using the drives' sensors. Each drive is connected through a gearbox to a drum with two cables, respectively two closing cables or two hoisting cables. The torque required to open or close the grab includes the moment of inertia of the gearbox and the drive itself. The winch velocities and torques are recorded with a the maximum measuring frequency of 100 Hz.

Figure 7.3 shows the recorded winch velocities and torques during the eight fluctuation measurements. Concerning the winch velocities it can be concluded that closing occurs with little variation between measurements, although the lowering and hoisting movements shows more variation. This means that the effect of the manual crane
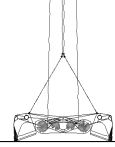
operation is small during the closing of the grab.

(a) Closing winch velocity.

(b) Hoisting winch velocity.
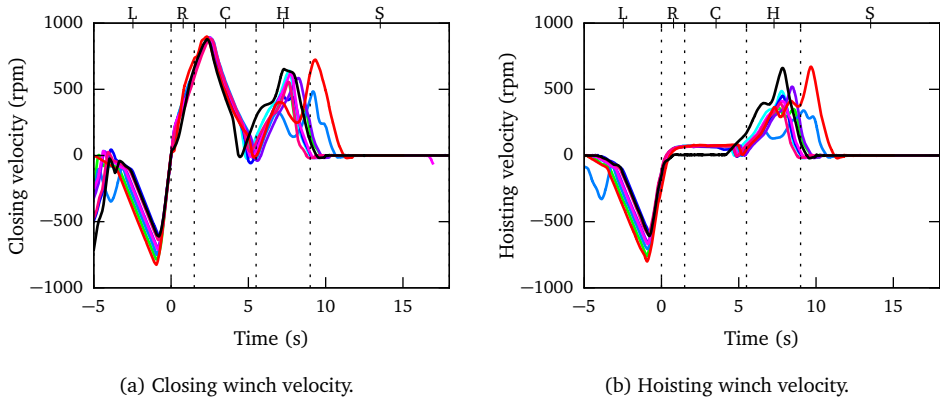
Figure 7.3: Winch velocities during eight grab cycles. These cycles consist of lowering (L), resting on the surface (R), closing (C), hoisting (H) and suspended from the crane (S).

Winch torques during the first part of closing fluctuate considerable more (Figure 7.4, likely caused by differences in cable slack. When the winch acceleration changes direction at $t = 3\,s$ (Figure 7.3a), abrupt changes can be seen in the torque diagrams (Figure 7.4) while cable forces continue to rise (Figure 7.2). This means that the momentum of the drive and gearbox have a large effect on the required torque and interferes with the assessment of grab performance.

(a) Closing winch torque.

(b) Hoisting winch torque.
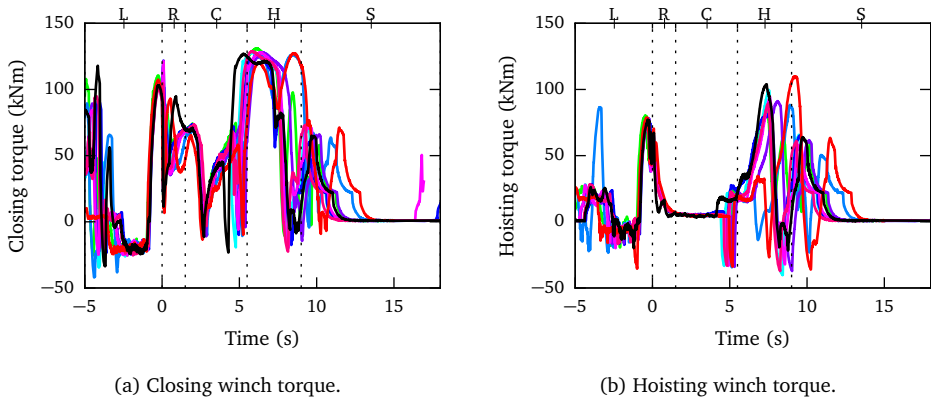
Figure 7.4: Winch torques during eight grab cycles. These cycles consist of lowering (L), resting on the surface (R), closing (C), hoisting (H) and suspended from the crane (S).

7.1.3   Position Data

The position and velocity of the grab were measured by analysing video captures of the closing process. The grab has been marked at three different locations, shown in Figure 7.1. Two markers were placed on the buckets and a large marker was placed on the main hinge of the grab. Video was captured in Full HD resolution at 25 frames per second. This proved to be sufficient in tracking the motions of the three markers. The origin was set to the main hinge point marker when the grab was resting at the surface of the bulk material as shown by the axes in Figure 7.5. For the tracking of the markers, the automatic tracking software Tracker (Brown) was used. Grab movements were captured in 2D because a side view for a second camera could not be obtained at the terminal. Measuring the position of the grab with accelerometers and a data-acquisition system mounted on the grab was considered unfeasible.
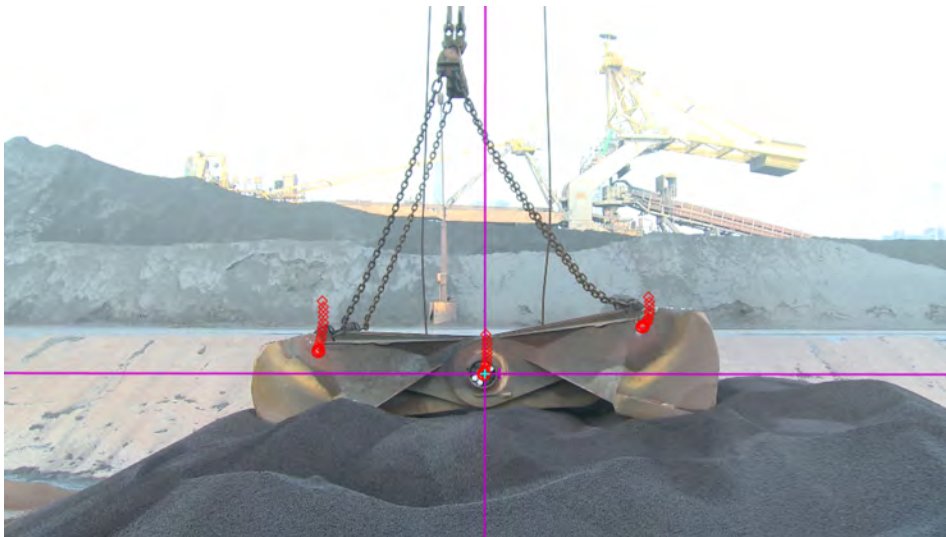
Figure 7.5: Origin and tracking of markers during the experiment.

Figure 7.6 shows the positions of the markers on the main hinge point, the left bucket and the right bucket. During closing the main hinge point is pushed upwards while the markers on the buckets are slightly moving towards the bulk material. It appears that the trajectories during closing vary a little, likely caused by a variation in bulk material surface which results in a variation in closing resistance.

The accuracy of the position data can be assessed by examining the distance between the bucket markers to the main hinge point marker. This distance should be constant, since the bucket marker and the main hinge marker are on the same body. However, the measured distance in Figure 7.7 shows an increase of up to 8%, depending on the opening angle and the height of the grab. This error should be taken into account when comparing the experiments to the coupled models' predictions in Section 7.3.
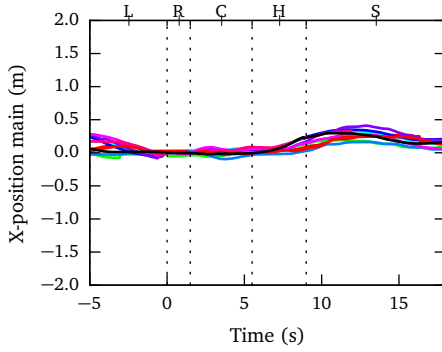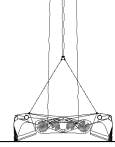
(a) Horizontal position of main hinge point.
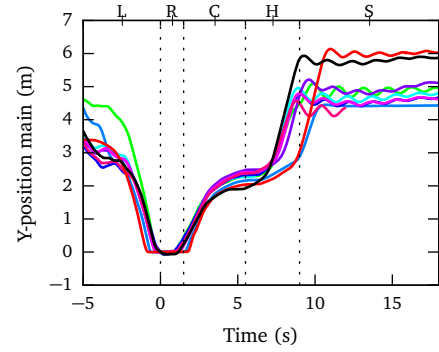
(b) Vertical position of main hinge point.
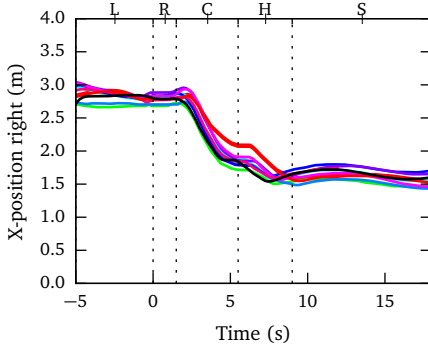
(c) Horizontal position of right marker.
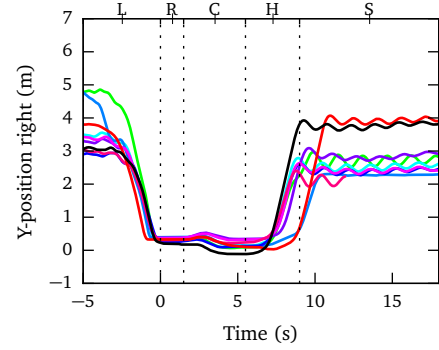
(d) Vertical position of right marker.
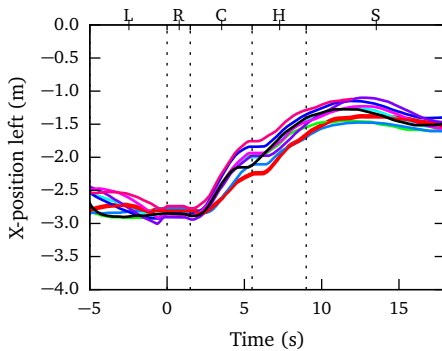
(e) Horizontal position of left marker.
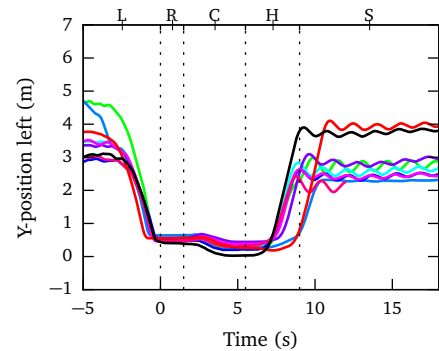
(f) Vertical position of left marker.

Figure 7.6: Horizontal (X) and vertical (Y) position of the three markers measured in a series of eight experiments. Each experiment consists of lowering of the grab (L), resting on the surface (R), closing (C), hoisting (H) and suspended from the crane (S).
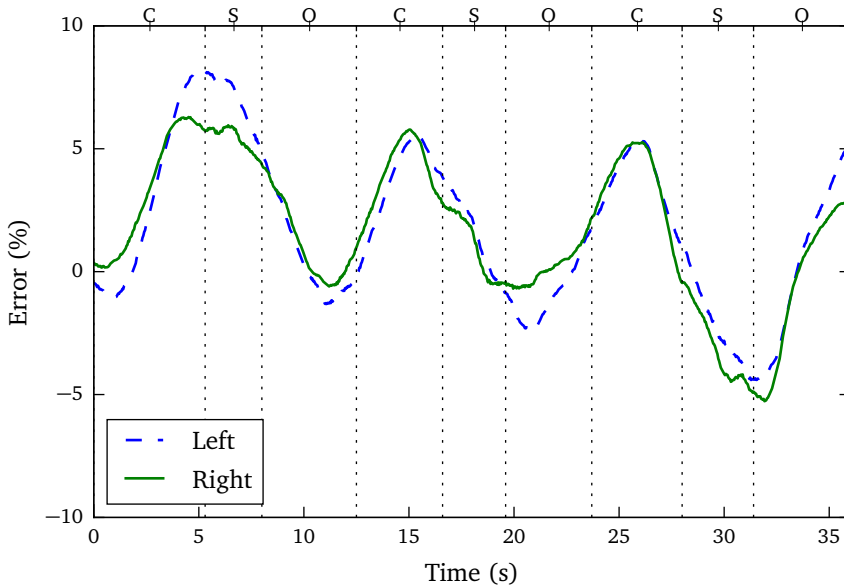
Figure 7.7: Error in distance between bucket marker and main hinge marker during closing (C), opening (O) and suspending (S).

7.2　Configuration of the Co-simulation

The scissors grab model of Chapter 2 and the iron pellet model of Chapters 3, 4 and 5 can now be combined using the co-simulation technique of Chapter 6. Both models have been calibrated and tested and are ready for a co-simulation. Figure 7.8 contains the coupled models, where the left side of the figure shows the multibody dynamics simulation and the right hand side of the figure shows the discrete element simulation. These two simulations interact with each other using the coupling technique of the previous chapter.

7.2.1　Configuration of Multibody and Coupling

Two bodies of the scissors grab are coupled, being the two buckets as these bodies interact with the bulk material. The cables, chains, disks and suspension are not modelled in the DEM software and are only present in the multibody dynamics model because they do not interact with the particles. The buckets are imported into EDEM® where their surfaces are meshed. All the interaction forces between the surface elements and the particles are transformed into a force vector and a moment vector acting around the centre of mass of the bucket. These forces and moments are then communicated to the multibody dynamics model where they act on markers located in the centre of

mass of the coupled bodies.
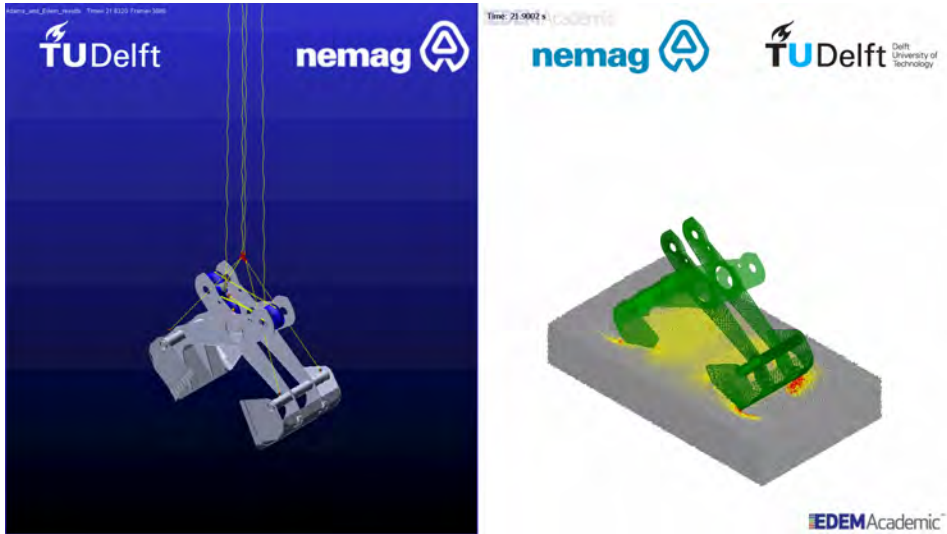
Figure 7.8: Co-simulation of a scissors grab, consisting of the MBD model (left) and the DEM model (right).

Particles are generated two seconds before the grab is expected to be in contact with the bulk material. The two seconds allow for the particles to settle completely while unnecessary computational costs are avoided. Another reduction in costs is achieved by simulating the first 15 seconds only in the MBD solver as there are no particles to be simulated yet, which means that there is no input from DEM for the MBD solver. This reduces the computational time with a factor of 100, as the overhead from the coupling is no longer required and the MBD solver can use much larger timesteps without compromising the stability of the results.

7.2.2 Configuration of DEM Domain Size

For an adequate simulation it is not required to simulate the large, completely filled cargo hold of a bulk carrier, instead a surface of bulk material with a certain depth can be used. Smaller domains require less elements to create a surface of bulk material, resulting in lower computational costs. This section determines the minimum dimensions of the volume of bulk material, both the length and width of the surface as well as the depth of the bulk material.

A grab simulation with a very large domain size has been simulated as a null measurement and compared to simulations with a reduced domain size. These smaller domain simulations should meet the following constraints:

- The domain should be long enough so that it does not affect the penetration of

the bulk material. The span of the grab when completely opened approximates seven meters. A surface length of nine meters was found to be sufficient for an unaffected penetration, as the high compressive forces due to the penetration were mitigated well within this distance. Figure 7.9 shows the very large domain compared to the reduced domain size.

(a) Very large domain.	(b) Reduced domain.
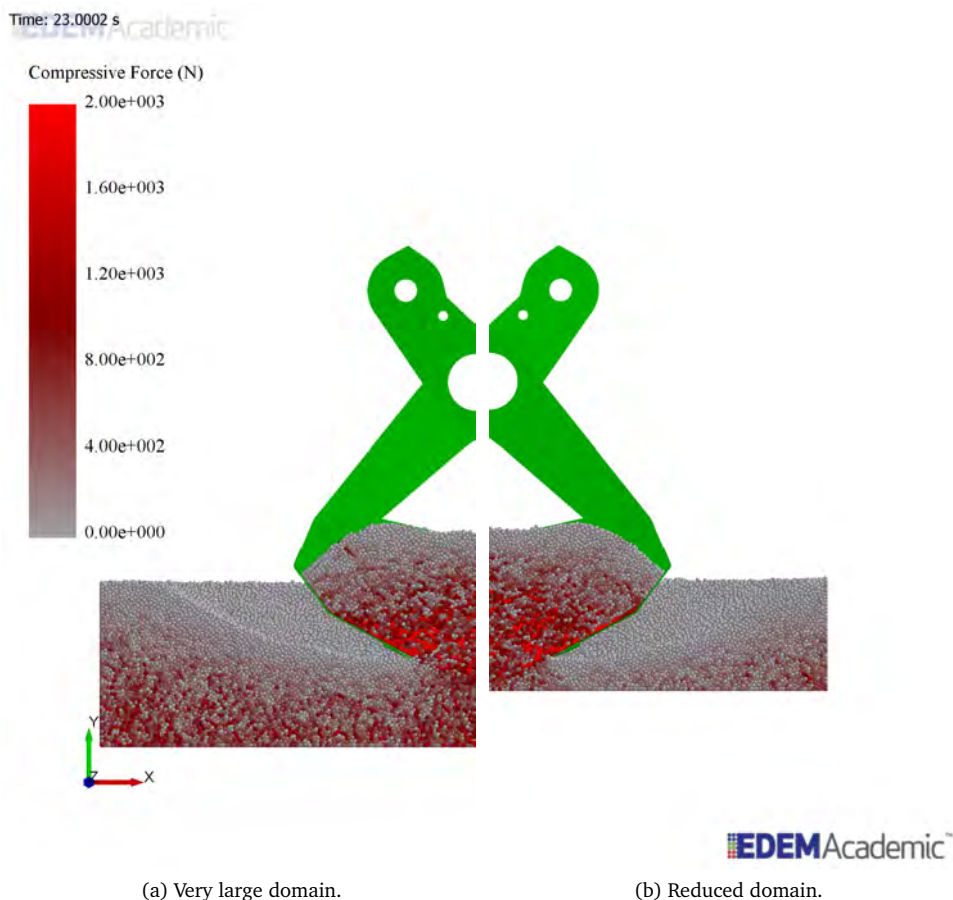
Figure 7.9: Front view at $t = 23\,\mathrm{s}$ of bulk material surrounding grab during closing. The size of the domain in this figure has a surface length of $9\,\mathrm{m}$, a distance of $1\,\mathrm{m}$ between knife and bottom and a surface width of $10\,\mathrm{m}$.

- The height of the bulk material should be large enough so that it does not affect the cutting process of the bulk material during closing. During the closing of the grab the knives of the buckets travel downwards as well as towards each other. A distance of 1 meter between the lowest point of the trajectory of the knifes and the bottom of the domain was maintained to ensure wall effects from the
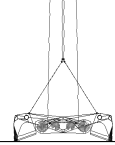
bottom where negligible, which was confirmed by examining the compressive forces in this area as shown in Figure 7.9. Enlarging this distance did not result in significant changes in the closing process, demonstrating that the bottom effects are negligible when a layer of one meter is taken into account.

- The domain should be wide enough so that it does not affect the cutting process as well as the spillage between the two buckets. The side view in Figure 7.10 shows a simulation with a width of 10 m, which shows that the disturbance of the surface is limited to half of the original domain. Thus, a domain of 5 m is needed to prevent the domain boundary from affecting the simulation outcome.
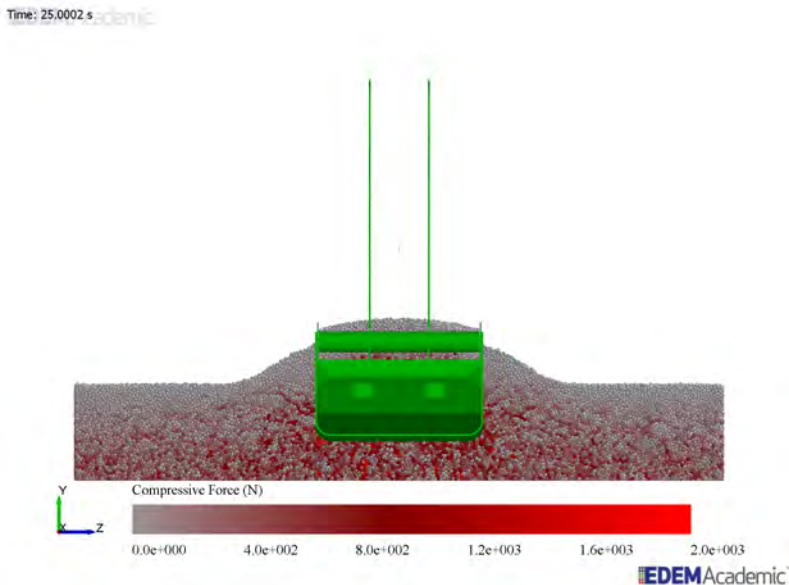
Figure 7.10: Side view at $t = 25$ s bulk material surrounding grab during closing. The size of the domain in this figure has a surface length of 9 m, a distance of 1 m between knife and bottom and a surface width of 10 m.

7.3 Validation Results

This section compares the prediction of the configured co-simulation with the tests conducted on the terminal. Three terminal measurements are simulated, each using the measured crane operation and a flat surface. In addition, a sloped surface is examined to investigate to what extent the validity of the coupled model can be expanded to sloped surfaces. First the flat surface is examined, followed by the sloped surface, both

using the large scale $s = 5$ no rolling material model calibrated in Section 4.5.1 and coarse grained in Section 5.2. After these surfaces, the effect of coarse graining is examined as well as the benefit of using the rolling-C material model (Section 4.5.2).

7.3.1 Flat Surface

The flat surface experiment has been conducted three times, and have resulted in a mass of iron ore pellets displayed in Table 7.1, averaging to a 27.8 ton per cycle. These experiments have each been simulated with the no-rolling material model, resulting in an average load of 27.5 ton. The small differences in outcome can be explained through the variation in the bulk material surface, operating characteristics and numerical scatter. This section compares experiment 3 and simulation 3 in more detail as these showed the largest difference in grabbed material, while figures for the other two comparisons can be found in Appendix B.

	mass (ton)			mass (ton)
Experiment 1	27.2		Simulation 1	28.1
Experiment 2	27.9		Simulation 2	27.8
Experiment 3	28.3		Simulation 3	26.6
Average	27.8		Average	27.5

Table 7.1: Grabbed material in experiments and simulation.

Figure 7.11 shows the comparison of the measured load on the crane in simulation and experiment. The co-simulation predicts the increasing load during closing (C) due to the grabbing of material quite well, with a coefficient of determination of 0.928, which exceeds the required 0.8. During hoisting (H) a peak is visible in experimental signal at approximately $t = 26\,s$ which is not shown by the co-simulation, likely caused by a slight difference in cable slack between model and experiment. During suspension (S) it can be noted that the co-simulation damps out quicker than the experiment. Apart from these differences, this comparison demonstrates that the whole loading process of the grab can be accurately predicted.

The winches of the crane control the motion of the grab and in order to maintain the assigned winch velocities, torque is required. Figure 7.12 shows the torque of the closing and hoisting winch during a grab cycle. When the grab opens and lowers (L), agreement is off during the first nine seconds. In the experiment, the grab starts opened while in the simulation the grab starts closed, resulting in additional closing torques to open the grab. For the hoisting winch, the brake is activated in the experiment while the simulation lacks a winch brake, as discussed in Section 2.4. The predicted closing winch torques have a correlation coefficient of 0.838 in the closing stage (C), approximating the experiment sufficiently. In the hoisting stage a deviation can be noticed, which is caused by a slightly shifted equilibrium between closing and hoisting cables. However, when both the closing and winch torques are combined a hoisting
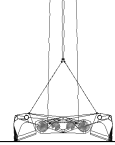
correlation of 0.809 is achieved. These result confirm that the forces required for closing and hoisting a grab with iron ore pellets are correctly predicted.
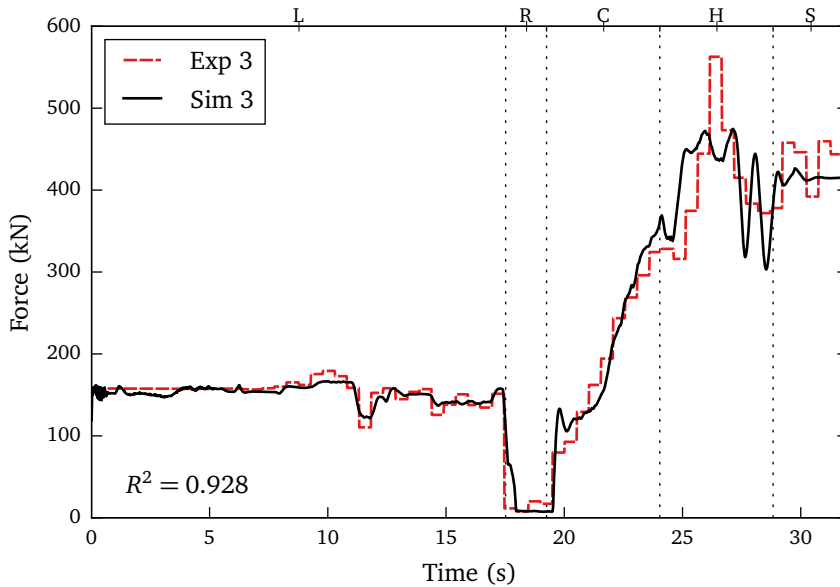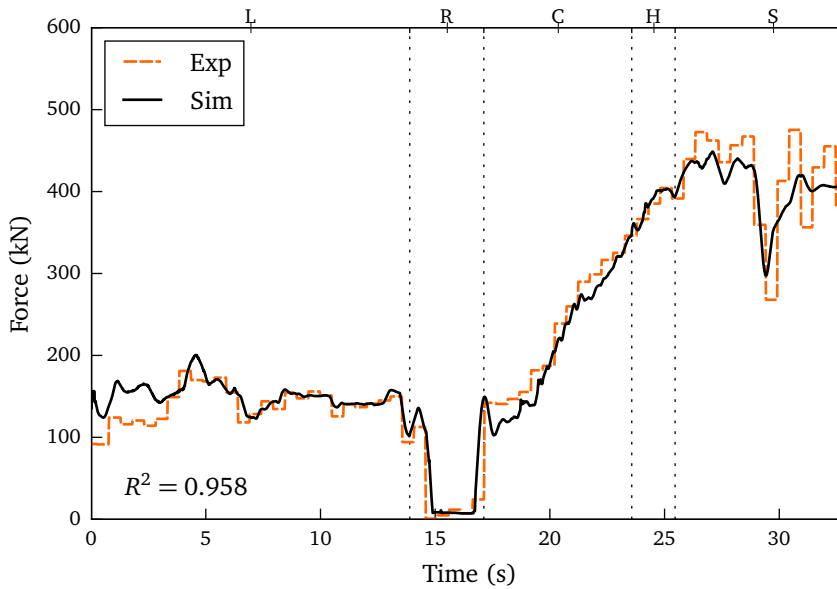

Figure 7.11: Load comparison between simulation 3 and experiment 3 with a flat surface. Grab operation consists of lowering of the grab (L), resting on the surface (R), closing (C), hoisting (H) and being suspended from the crane (S).


(a) Closing winch torque.

(b) Hoisting winch torque.
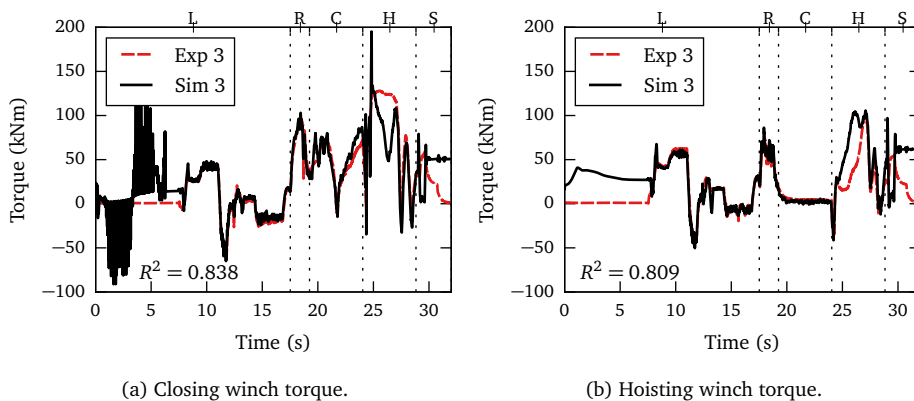
Figure 7.12: Closing and hoisting torque during simulation 3 and experiment 3 with a flat surface. Grab operation consists of lowering of the grab (L), resting on the surface (R), closing (C), hoisting (H) and being suspended from the crane (S).
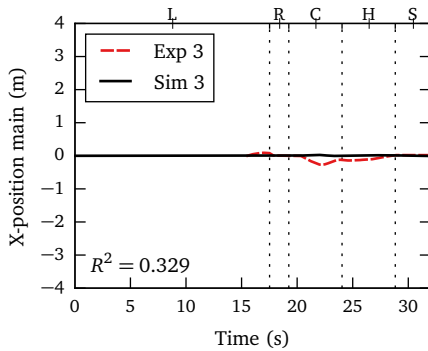
(a) Horizontal position of main hinge point.
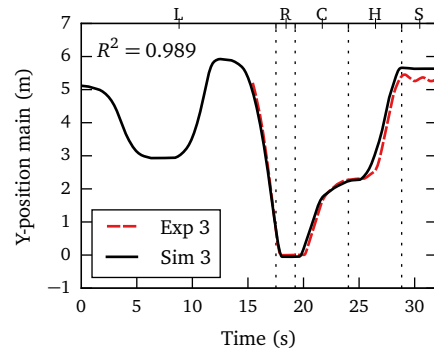
(b) Vertical position of main hinge point.
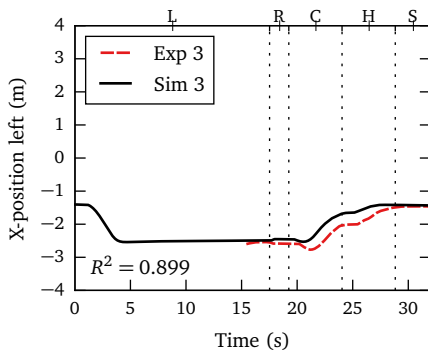
(c) Horizontal position of left marker.
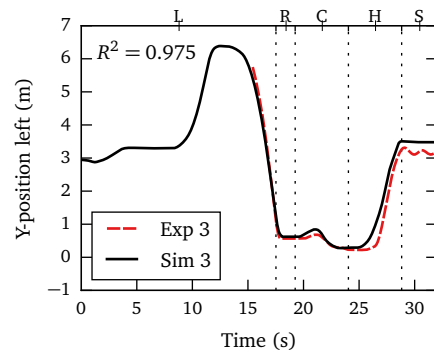
(d) Vertical position of left marker.
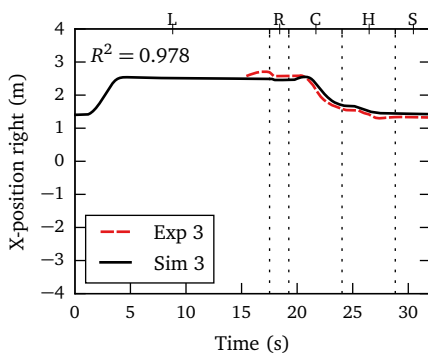
(e) Horizontal position of right marker.
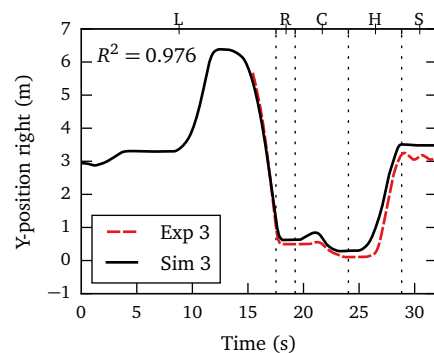
(f) Vertical position of right marker.

Figure 7.13: Comparison between simulating and video-tracking of the three applied markers on the grab, on flat surface experiment 3. Grab operation consists of lowering of the grab (L), resting on the surface (R), closing (C), hoisting (H) and being suspended from the crane (S).
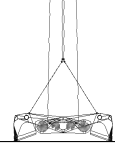
Figure 7.13 shows the position of the markers in the simulation and experiment. The vertical movement of the virtual main hinge point can easily be matched to the position of the markers during the experiment. The vertical movement of the buckets show also similar good vertical match with correlation coefficients exceeding 0.975, well above the desired $R^2 > 0.9$. During hoisting (H) the error of the match grows, perhaps an effect of the video measurement error of Section 7.1.3. The small horizontal movement of the main hinge point in the experiment is very likely the result of a slightly asymmetric surface, which was not present in the co-simulation. This horizontal displacement is also visible in the horizontal position of the left and right markers, both shifted to the left. Overall, the dynamics of the grab during closing are predicted very well, except for the horizontal shift likely caused by the irregular bulk surface.

The confidence interval of the simulation determines how many times a simulation needs to be repeated for achieving a reliable mean value. Ideally, this confidence value is as small and certain as possible, however this would require a large number of replications for each simulation. For the grab simulation, a 95% confidence interval is considered adequate and a maximum interval size of 5% is used. The simulation of experiment 3 is performed three times to see whether these conditions can be met.

Figure 7.14 shows the confidence intervals that occur when the flat simulation is performed three times. It can be seen that the load has a small confidence interval with a maximum of 9 ton, amounting to 2.2% of the load signal, below the desired 5%. The torques show a larger confidence, especially in the first seconds of the simulations. This is likely caused by the less than optimal opening of the grab, causing lots of erratic angular accelerations to maintain the prescribed angular velocity. During closing and hoisting the interval is much smaller and amounts to approximately 6% of the torque signal. This value exceeds the desired 6%, although this is not considered a large problem as the increase in cable forces can be monitored with the load sensor as well.

(a) Load.

(b) Torques.
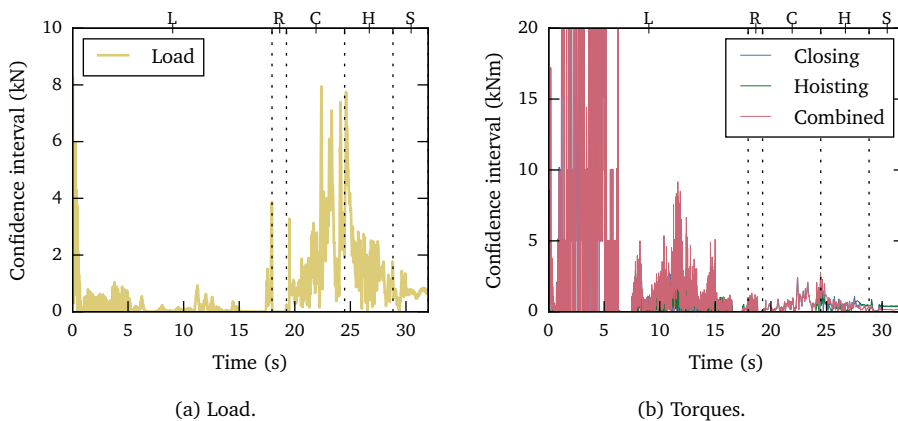
Figure 7.14: Confidence intervals of three simulations.

The variation of marker positions between the three flat simulations in Figure 7.15 approximates to 0.01 m during closing, which is quite small considering the particle size of $R = 0.0275$ m in these simulations. Thus, for reaching the desired confidence intervals, a sample of size of three is sufficient for the load and position of the grab.

(a) Horizontal position.   (b) Vertical position.
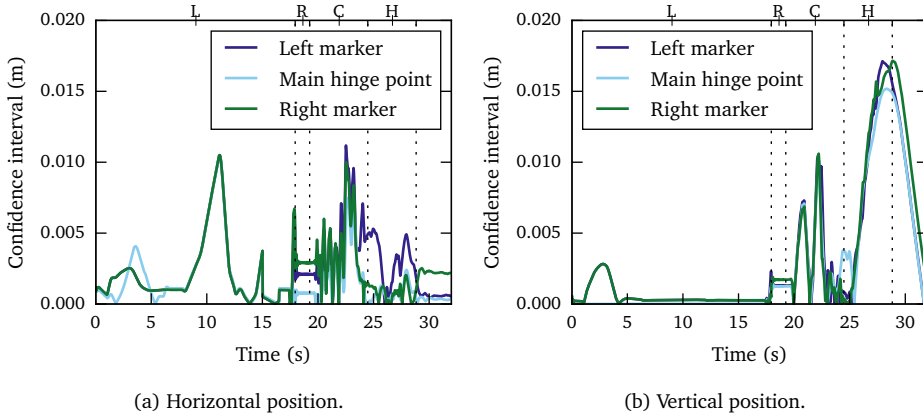
Figure 7.15: Confidence intervals of the grab simulated position.

7.3.2 Sloped Surface

After validating the coupled model on flat surfaces, a sloped surface is simulated to investigate whether the validation can be expanded. Figure 7.16 shows a screenshot taken from the sloped experiment, showing that the grab has penetrated the pile of iron ore pellets at an angle of 28 degrees. Compared to the measurements on the flat surface, which grabbed an average of 27.8 ton, the sloped surface measurement grabbed less at 26.4 ton. The co-simulation predicted a load of 25.7 ton and was able to predict the loading of the grab on the sloped surface better than the flat surface, as can be concluded from Figure 7.17. A possible explanation for the improved results is the absence of fluctuations on the sloped surface in the experiment. The sloped surface signals correlate with a $R^2 = 0.958$, well above the desired 0.8 and therefore the load validation can be expanded to sloped surfaces.

(a) In the simulation.
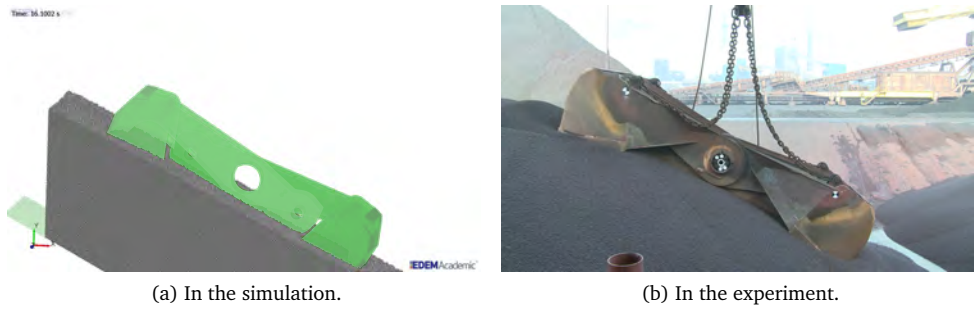
(b) In the experiment.

Figure 7.16: Grab on sloped surface of 28 degrees.

Figure 7.17: Load comparison between simulation and experiment with a sloped surface. Grab operation consists of lowering of the grab (L), resting on the surface (R), closing (C), hoisting (H) and being suspended from the crane (S).

Torques on the closing winches are also predicted well as can be observed from Figure 7.18. During the closing phase, a correlation coefficient of 0.927 is achieved, demonstrating the accuracy of the coupled models in a more challenging asymmetric surface. Correlation for the hoisting winch is affected by the shifted equilibrium of the cables in the suspended phase shown in Figure 7.18b, caused by the absence of a balancing mechanism in the co-simulation.

(a) Closing winch torque.   (b) Hoisting winch torque.
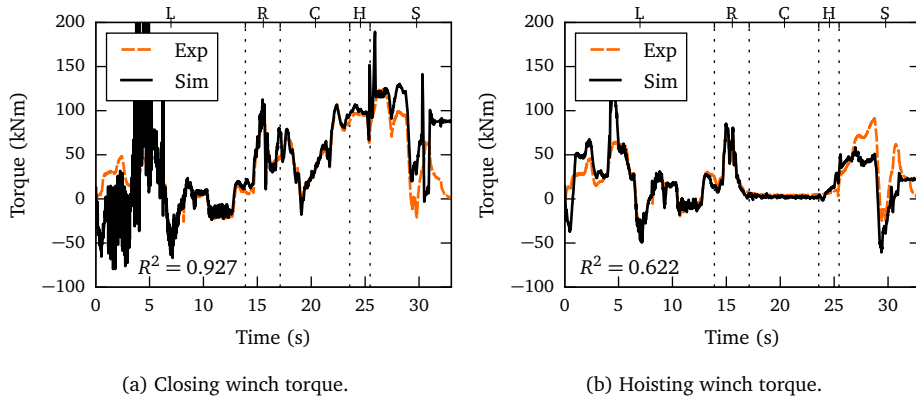
Figure 7.18: Closing and hoisting torque during simulation and experiment with a sloped surface. Grab operation consists of lowering of the grab (L), resting on the surface (R), closing (C), hoisting (H) and being suspended from the crane (S).

The motion analysis and the position data of the markers in Figure 7.19 show a clear difference from the flat closing situations. Most obvious is the difference in vertical position between the left and the right marker, a direct effect of the sloped surface. Another aspect is the horizontal movement of the main hinge point, which was marginal in the flat situation. Overall, correlation of the position data is good, although slightly less than in the flat situations. It appears the grab in the experiment shows a little bit more downward motion during closing. One probable cause is that the video measurement error discussed in Section 7.1.3 was more prevalent in the sloped situation, possibly a result from not being able to record from a full frontal view in the sloped situation.

7.3.3   Effect of Coarse Graining

Chapter 5 presented a general coarse graining approach and an adapted approach for penetration processes, which consists of adapted wall friction coefficients for the tip of the knives. However, assigning different coefficients to the same geometry is not possible and therefore the bucket geometry in EDEM® is split into two parts: the knife and the remaining part of the bucket. This split is also performed in Adams®, which leads to four coupled bodies: two buckets and two knives. In Adams® the knives are connected to the buckets with a fixed joint, resulting in the same motions for bucket and knife while loads are combined.
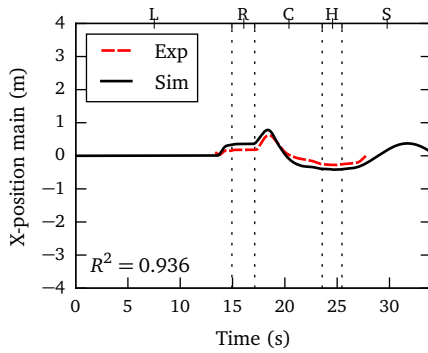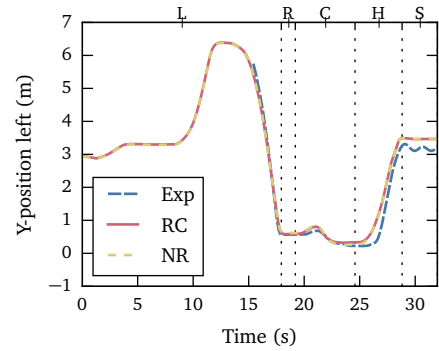
(a) Horizontal position of main hinge point.
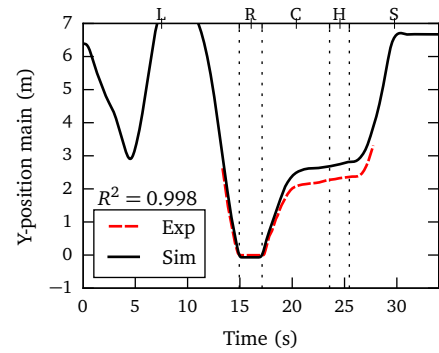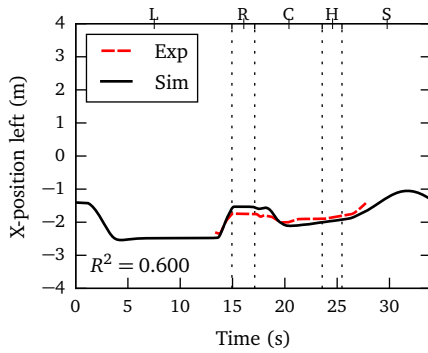
(b) Vertical position of main hinge point.

(c) Horizontal position of left marker.
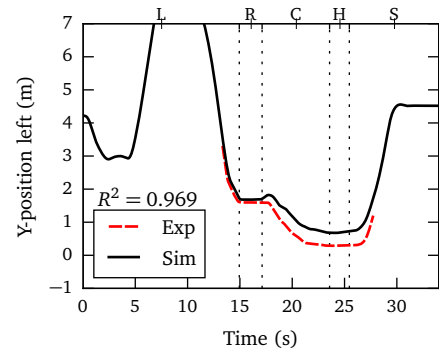
(d) Vertical position of left marker.
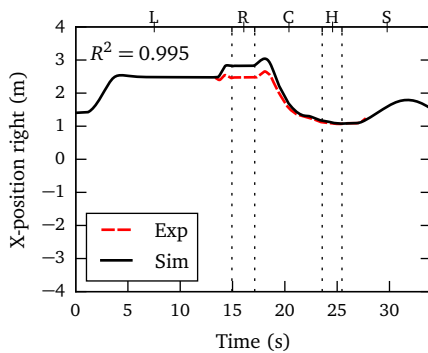
(e) Horizontal position of right marker.
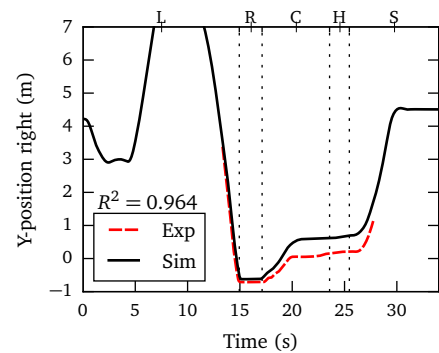
(f) Vertical position of right marker.

Figure 7.19: Comparison between simulating and video-tracking of the three applied markers on the grab, at a sloped surface. Grab operation consists of lowering of the grab (L), resting on the surface (R), closing (C), hoisting (H) and being suspended from the crane (S).

Figure 7.20 shows the effect of coarse graining on the filling of the grab, with and without compensation for the penetration behaviour. Clearly, the increase in grain size results in a decline in the mass of material grabbed when there is no compensation for the increase in penetration resistance. When the compensation discussed in Section 5.2.2 is taken into account this effect disappears and the predicted amount becomes independent on the selected particle scale. This independence demonstrates that the adapted coarse graining technique can be used in large scale grab simulations to save considerable amounts of computation effort without compromising results.
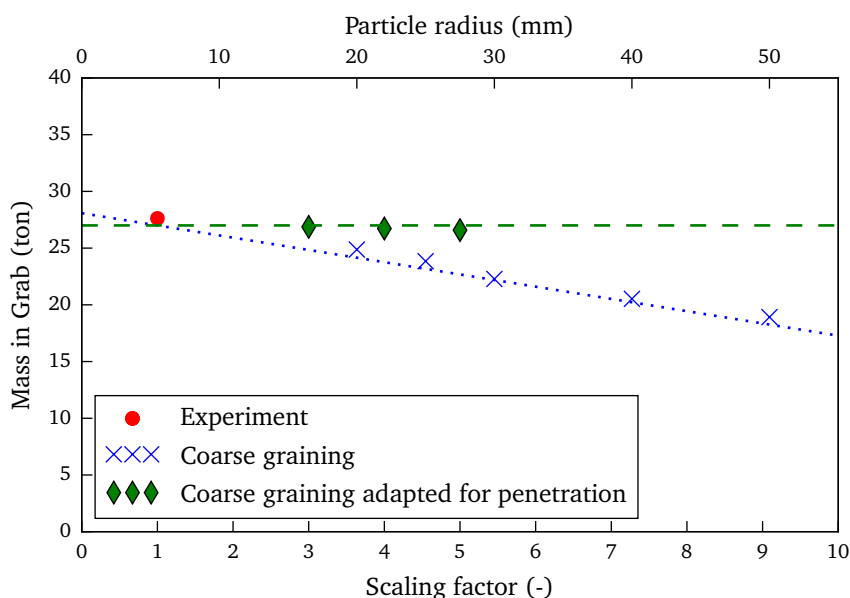
Figure 7.20: Effect of coarse graining on the grabbed amount of iron ore pellets. Two approaches are tested, the general approach of Section 5.2 and an adapted approach for penetration processes of Section 5.2.2.

7.3.4   Effect of Rolling Particles

Two material models have been calibrated in Chapter 4 to the properties of iron ore pellets and have been coarse grained in Chapter 5. The preceding validation simulations have all been performed with the no-rolling model (NR), which has proved itself capable of predicting iron ore pellet behaviour interacting with a grab. The second material model, the more complex rolling-C model (RC), is investigated here and compared to the experiment and the no-rolling model. The rolling-C model includes rolling of particles, allowing for a better calibration of the bulk material characteristics and is therefore expected to outperform the no-rolling material model.

The maximum grain size for the rolling-C model has been determined at $s = 3$ in
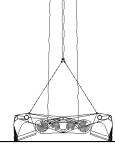
Section 5.2.2, which is lower than $s = 5$ for the no-rolling model. As a result, a co-simulation with $77\,\text{m}^3$ requires 4.6 times more particles, increasing the computational costs. Hence, only the flat surface experiment 3 is examined in the validation of the rolling-C model.

Figure 7.21 shows the load prediction of the rolling and no-rolling models with $s = 3$ compared to experiment 3. It can be seen that the curve predicted by the rolling-C model does not differ much from the no-rolling model and results in similar end values. During the final stage of closing, the rolling-C models predicts the experimental value more closely, resulting in a $R^2 = 0.941$ compared to a $R^2 = 0.925$ for the no-rolling model. Regarding the torque prediction in Figure 7.22, the rolling-C model shows similar behaviour, resulting in comparable coefficients of correlation given in Table 7.2.
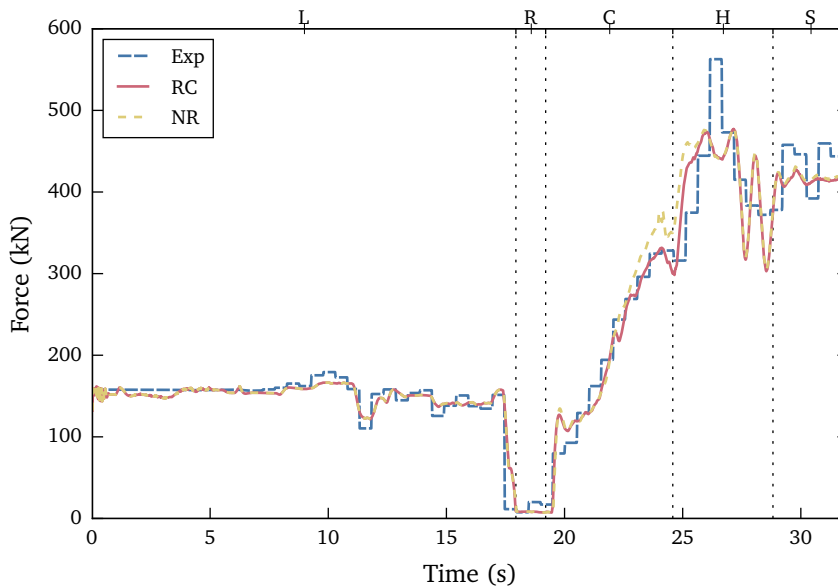
Figure 7.21: Load comparison between experiment 3, no-rolling (NR) material model and the rolling C material model (RC). Grab operation consists of lowering of the grab (L), resting on the surface (R), closing (C), hoisting (H) and being suspended from the crane (S).

The position of the markers and the main hinge point of the grab during simulation are shown in Figure 7.23. It can be observed that there are no large differences in the simulated positions of the two material models, indicating that the motion of the grab during closing is almost identical. This absence of large differences can be confirmed when the coefficients of determination for the positions are examined in Table 7.2, showing negligible benefit. Regarding the low R^2 for the horizontal position of the main hinge marker, all horizontal movement of this marker in the experiment can be

attributed to fluctuations in the bulk surface which are not present in the simulation (Figure 7.23a). As a result, the coefficient of determination between zero and random fluctuations is not high.

(a) Closing winch torque.　　　　　　　　(b) Hoisting winch torque.
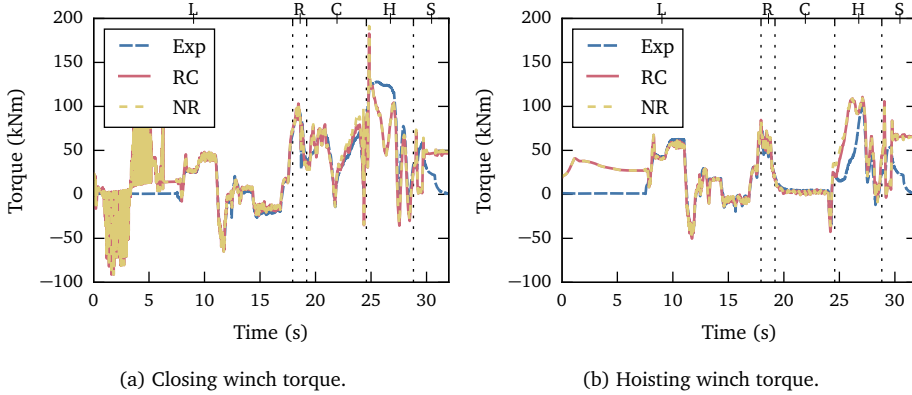
Figure 7.22: Closing and hoisting torque of the no-rolling (NR) and the rolling friction C (RC) material models compared to experiment 3. Grab operation consists of lowering of the grab (L), resting on the surface (R), closing (C), hoisting (H) and being suspended from the crane (S).

	RC, $s = 3$	NR, $s = 3$	NR, $s = 5$
Load	0.941	0.925	0.928
Closing	0.881	0.819	0.838
Hoisting	0.813	0.781	0.809
Main-x	0.117	0.010	0.329
Main-y	0.990	0.989	0.989
Left-x	0.913	0.901	0.899
Left-y	0.977	0.976	0.975
Right-x	0.982	0.982	0.978
Right-y	0.978	0.976	0.976

Table 7.2: Coefficients of determination R^2 for no-rolling (NR) and rolling-C (RC) material models.
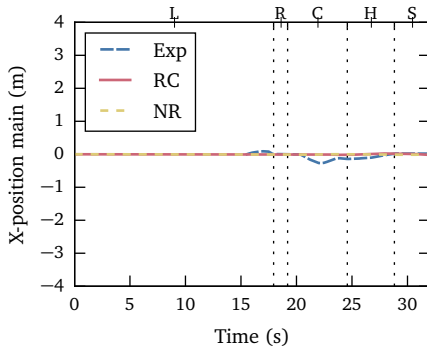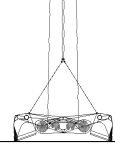
(a) Horizontal position of main hinge point.
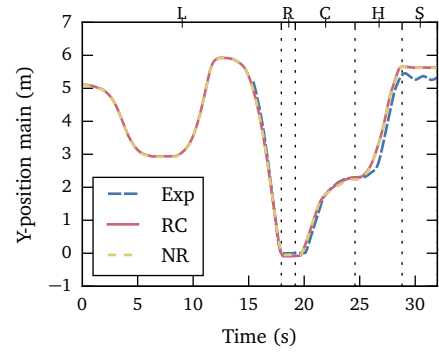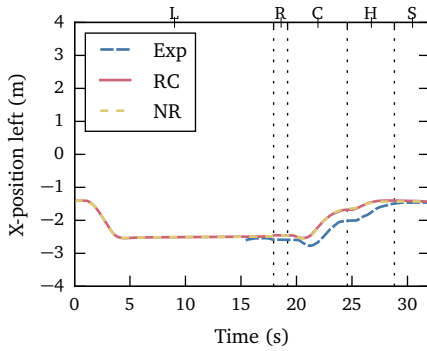
(b) Vertical position of main hinge point.

(c) Horizontal position of left marker.

(d) Vertical position of left marker.
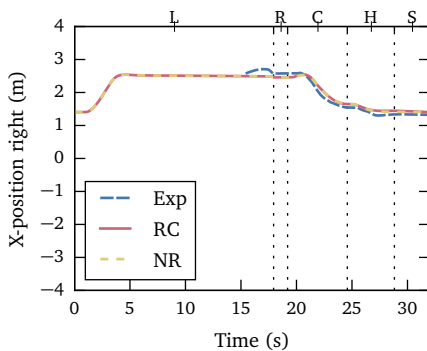
(e) Horizontal position of right marker.
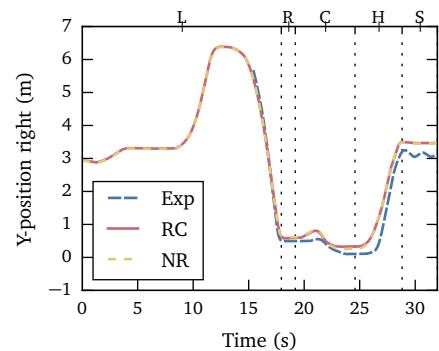
(f) Vertical position of right marker.

Figure 7.23: Comparison between the no-rolling and rolling-C material models (NR & RC) and video-tracking of the three applied markers on the grab, on flat surface experiment 3. Grab operation consists of lowering of the grab (L), resting on the surface (R), closing (C), hoisting (H) and being suspended from the crane (S).

The rolling-C model was expected to show an improved correlation to the experiment, however benefits of using such a model are minimal. Improvements are less than the confidence interval of the no-rolling $s = 5$ material model, while correlation improved marginally. Thus, simulations of a grab can be performed with the less expensive no-rolling model without compromising accuracy.

7.4   Conclusions

This chapter has convincingly validated and established the accuracy of the co-simulation of coupled grab and material model. Predictions made by the coupled models matched the outcome of bulk terminal measurements excellently, both in flat and sloped situations. Crane loads were predicted at an average of 27.5 ton while experiments showed an average filling of a grab at 27.8 ton. Coefficients of determination for the load data exceeded 0.922 on a flat surface and even 0.958 on a sloped surface. Vertical motion of the grab during closing has been predicted, achieving $R^2 > 0.975$ for flat surface and 0.964 for the sloped surface. The observed comparisons validate that the developed coupled models are capable of predicting grab performance.

In addition, the coarse graining of Chapter 5 and the two calibrated material models of Chapter 4 have been evaluated for a large scale grab simulation. Grab simulations using scaled particle sizes showed comparable results, when applying the coarse graining scheme and the adapted approach derived from an isolated small scale penetration simulation. Regarding the material models, the more complex material model including rolling friction according to Iwashita and Oda (1998) did not offer significant improvement in grab prediction over the other material model where rolling motion is restricted and substantial computational costs are saved. In brief, similar grab behaviour has been predicted, independent of the selected grain size or material models.

Overall, the validation presented in this chapter demonstrates the approach of this thesis. It presents a virtual grab model interacting with virtual iron ore pellets, with behaviour similar to their physical counterparts. This validation leads to the final step presented in the next chapter: implementing and applying the validated models in the grab design process, clearing the way for new advances in grab performance.

8

Virtual Prototyping of Grabs

This chapter aims at demonstrating the virtual prototyping of grabs using the validated model. Several key performance indicators will be defined, allowing for a fast and clear comparison between grab prototypes. By investigating the effects of grab design variables, it becomes possible to link design changes to an increase in performance. These increases will be combined into a new virtual grab prototype, opening a new approach for developing high-performance grab unloaders for bulk materials.

The key performance indicators for evaluating grab performance are defined in the first section, including the grab trajectory. Section 8.2 investigates the effects of a selection of four grab variables on the key performance indicators. These effects are combined in Section 8.3, resulting in an improved grab prototype.

8.1 Key Performance Indicators of a Grab

In the previous chapter, the behaviour of a grab has been quantified by examining the load, torque and motion of the grab during closing. These data were convenient to measure with the use of the sensors present in the crane and an analysis of captured video recordings and offered a satisfactory basis for validation the behaviour of the virtual grab. However, a wider range of data is available or can be extracted from the co-simulation. When evaluating prototypes, additional data of the simulation can therefore be used in quantifying and understanding the performance of a virtual prototype.
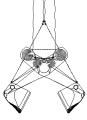
The performance of a grab can be examined in many ways, for example by examining the mass of the material in the bucket, the stress network of the compressed particles (Figure 8.1a) or the relative sliding wear (Figure 8.1b) based on Archard (1953). Although each simulation is very rich in results, analysing and comparing prototypes can become an intensive task. Consequently, a summary of grab performance is desired for a rapid evaluation of a prototype.

(a) Average normal contact force.   (b) Relative wear on buckets.
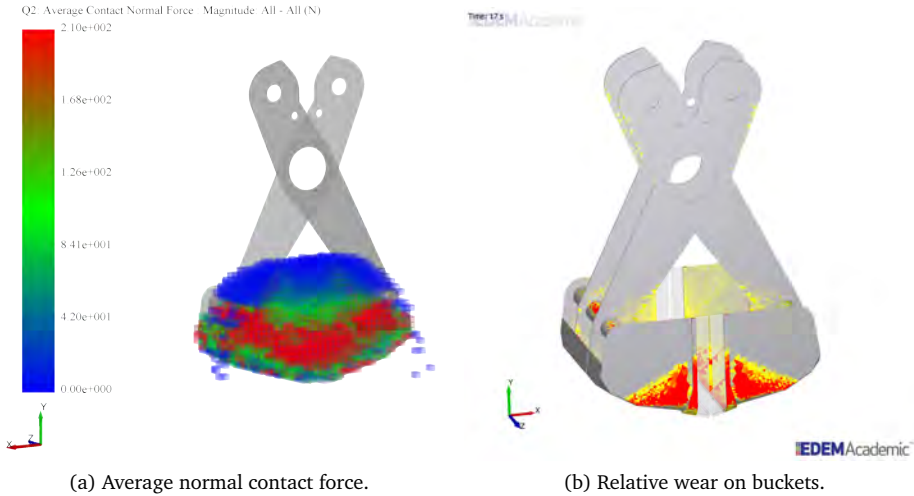
Figure 8.1: Detailed analysis of grab performance.

In order to capture the performance of a virtual grab prototype quickly, six Key Performance Indicators (KPIs) have been defined. These KPIs allow for a quick and quantitative comparison between prototypes, giving engineers the possibility to detect trends and select the best prototype for a selected number of scenarios. These KPIs focus solely on different aspects of the performance of a prototype, operating costs, production or other engineering aspects such as strength, stiffness or fatigue are not taken into account. This section presents the definitions of the following indicators:

- Mass indicator Ψ_{mass},

- Grab efficiency indicator $\Psi_{grab\,efficiency}$,

- Volume indicator Ψ_{volume},

- Spillage indicator $m_{spillage}$,

- Closing resistance indicator $\Psi_{closing\,resistance}$,

- Closing time indicator $\Psi_{closing\,time}$.
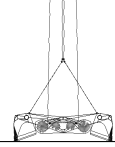
8.1.1 Mass Indicator

Grab unloading systems are usually evaluated by comparing the hoisted mass to the hoisting capacity of the grab crane. Obviously the combined mass of grab and material needs to be below the hoisting capacity of the crane (Equation 2.1), however the performance of a grab focusses on the ratio between steel and grabbed iron ore. Ideally, the entire hoisting capacity is used for hoisting bulk material during each cycle, however, a grab needs its mass for penetrating the material, as well as its structural strength and being able to maintain a long lifespan.

The mass indicator Ψ_{mass} compares the amount of grabbed material to the weight of the grab by means of Equation 8.1,

$$\Psi_{\text{mass}} = \frac{m_{\text{DWT}} + m_{\text{spillage}}}{m_{\text{grab}}} \tag{8.1}$$

where m_{grab} is the mass of the grab, m_{DWT} is the mass of the bulk material inside the grab and m_{spillage} is the mass of the bulk material spilled over the sides of the grab after closing. Spilled material is taken into account here to focus on the effectiveness of the grabbing process, without possible influences of a limiting bucket capacity. As a result, the prototypes are here assessed on their grabbing performance and not whether the bucket is sufficiently large. The reference grab has an average Ψ_{payload} of 1.874 with a 95% confidence interval of 0.002 based on three simulations.

8.1.2 Grab Efficiency Indicator

The grab efficiency indicator $\Psi_{\text{grab efficiency}}$ indicates the efficiency of the closing. During closing the grab moves through the bulk material, displacing the particles that are inside the closing trajectory of Figure 8.2. Ideally, all the material inside the closing trajectory ends up being picked up by the grab and no effort is wasted on material that leaks between the two knives during closing.

The grab efficiency is defined according to Equation 8.2 as the ratio between the bulk material that has been grabbed, consisting of the material inside m_{DWT} and the mass spilled over the sides m_{spillage} and the bulk material inside the closing path $m_{\text{closingpath}}$.

$$\Psi_{\text{grab efficiency}} = \frac{m_{\text{DWT}} + m_{\text{spillage}}}{m_{\text{closingpath}}} \tag{8.2}$$

The bulk material $m_{\text{closingpath}}$ is calculated by computing the enclosed area $A_{\text{closingpath}}$ based on the closing trajectory and multiplying by the width of the grab w and bulk density in situ ρ_{insitu} as shown in Equation 8.3. The bulk density ρ_{insitu} of the untouched bulk material is measured before penetration occurs by counting the mass of the particles present in a defined volume underneath the surface of the bulk material.

$$m_{\text{closingpath}} = A_{\text{closingpath}} w \rho_{\text{insitu}} \tag{8.3}$$
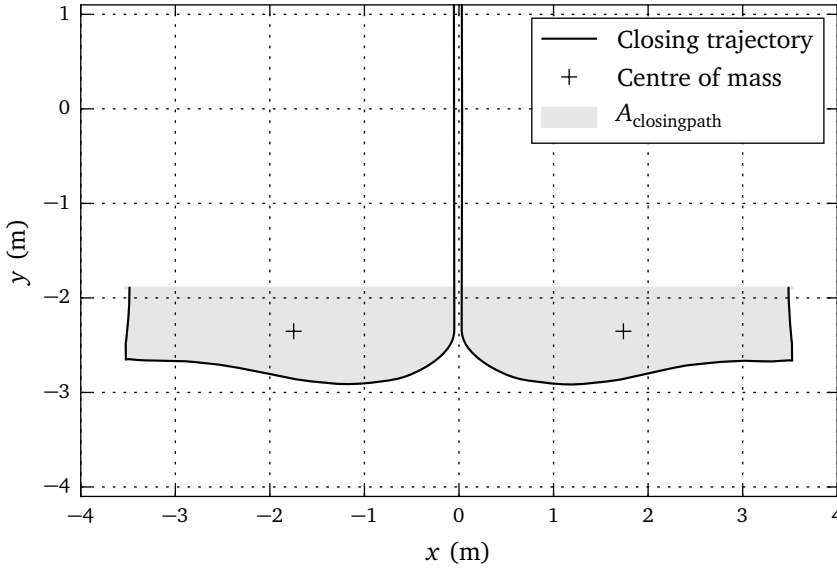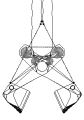
Figure 8.2: Closing trajectory of a grab.

The reference grab has an average $\Psi_{\text{grab efficiency}}$ of 0.904 with a 95% confidence interval of 0.011 based on three simulations.

8.1.3   Volume Indicator

Whether or not the grab performance matches the bucket volume needs to be evaluated as well. If the bucket volume is higher than the volume of the grabbed material it means that steel and therefore mass is waisted on the bucket.

The volume indicator compares the volume of the grabbed material to the volume definition of the grab with the help of Equation 8.4:

$$\Psi_{\text{volume}} = \frac{V_{\text{DWT}}}{V_{\text{grab}}} = \frac{m_{\text{DWT}}}{\rho_{\text{ingrab}} V_{\text{grab}}} \tag{8.4}$$

The volume of the grabbed material considers both the volume occupied by particles as well as the volume of the voids. Calculation of the volume is performed by extracting the total mass of the particles m_{DWT} and dividing this by the bulk density in the grab ρ_{ingrab}. This bulk density ρ_{ingrab} is measured by examining the mass of particles inside a control volume of cubic meter inside the grab, and is slightly higher than ρ_{insitu} due to compression of the material. The maximum capacity of the grab V_{grab} is defined as the volume displayed in Figure 8.3. This volume V_{grab} consists of the volume inside the buckets combined with the volume on top, calculated with an angle of 33 degrees as

observed in practice. A value of $\Psi_{\text{volume}} < 1$ indicates that the grab is not completely filled and has room for more material. The reference grab has an average Ψ_{volume} of 1.014 with a 95% confidence interval of 0.001 based on three simulations.

Figure 8.3: Definition of maximum capacity of grab V_{grab}.

8.1.4 Spillage Indicator

The spillage indicator Ψ_{spillage} of Equation 8.5 shows the level of spillage of the grab which happens if the bucket volume of the grab is smaller than its digging capacity. Material spilled means that the grab is outperforming its bucket.

$$\Psi_{\text{spillage}} = \frac{m_{\text{DWT}}}{m_{\text{DWT}} + m_{\text{spillage}}} \tag{8.5}$$

A value of $\Psi_{\text{spillage}} = 1$ indicates that no material has been spilled from the grab. The reference grab has an average Ψ_{spillage} of 0.991 with a 95% confidence interval of 0.001 based on three simulations.

When Equation 8.1 is multiplied with Equation 8.5, the payload of the grab unloader system can be determined in Equation 8.6. Instead of examining the payload of the system Ψ_{payload}, this chapter uses Ψ_{mass} and Ψ_{spillage} as these distinguish the grabbing performance from the holding performance.

$$\Psi_{\text{payload}} = \Psi_{\text{mass}}\Psi_{\text{spillage}} \tag{8.6}$$

8.1.5 Closing Resistance Indicator

The closing resistance indicator $\Psi_{\text{closing resistance}}$ evaluates the energy required for closing the grab while grabbing material. This value is useful for finding the closing path and grab design that requires the least amount of energy. This KPI is defined according to Equation 8.7:
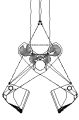
$$\Psi_{\text{closing resistance}} = \frac{W_{\text{closing}}}{m_{\text{closingpath}}} \qquad (8.7)$$

where $m_{\text{closingpath}}$ is given in Equation 8.3 and W_{closing} is the work of the grab on the bulk material during closing of the grab according to Equation 8.8. This equation consists of the sum of the closing forces F_{closing} over the travelled distance Δx.

$$W_{\text{closing}} = \Sigma F_{\text{closing}} \Delta x \qquad (8.8)$$

The reference grab has an average $\Psi_{\text{closing resistance}}$ of 43.3 kJ/ton with a 95% confidence interval of 0.15 kJ/ton based on three simulations. In comparison, hoisting energy for a grab filled with material and a height difference of 1 m requires 16 kJ/ton.

8.1.6   Closing Time Indicator

The closing time indicator analyses the time it takes to complete the grabbing of the material. This is important as a reduction in closing time will result in a reduction of cycle time, therefore increasing the hourly capacity of a grab unloader. The closing time indicator is defined as:

$$\Psi_{\text{closing time}} = t_{\text{exit}} - t_{\text{start}}$$

Here is t_{start} defined as the time at which the closing commences and the horizontal movement of the knives start, while t_{exit} identifies the time at which the tip of the grab knives have met each other and no leakage can occur anymore. The reference grab has an average $\Psi_{\text{closing time}}$ of 3.97 s with a 95% confidence interval of 0.02 s based on three simulations.

8.2   Single Parameter Variations

This section aims at demonstrating the effects of grab parameter changes on the performance of a grab, quantified by the KPIs defined in the previous section. By studying the variation of a single grab parameter, its effects on grabbed mass, efficiency and spillage should become visible. This should confirm the value of the KPIs for evaluating grab performance, and improve the understanding of the relations between grab parameters and grab performance.

The performance of a grab unloader depends on many design variables and customer preferences. Grab unloader operators select a suitable grab based on their preferences on unit price, operating costs and unloading capacity. The scope of this thesis is limited to the performance of grab designs, and assessing all possible variables and preferences is also considered out of the scope of this research and very elaborative. For example, the bucket of a grab can be designed in many ways, from varying key dimensions such
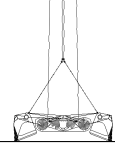
as grab width up to subtle variations concerning the shape of the knives. Likewise, the grab mechanism consisting of the cables and pulleys on the grab can be varied in numerous ways as well, such as in existing grab types described in Chapter 2 or new grab concepts to be invented.

Therefore, four parameters of a scissors grab have been selected as a demonstration of studying isolated parameter variations, while all other parameters were kept constant. These parameters are: the mass of a grab m, the width of a grab w, the length of a grab l, and the height of a grab h. The parameters are displayed in Figure 8.4 and are varied according to Table 8.1 up to 80% and 120% of the original value. In the first set displayed in Table 8.1a, the mass is varied while the w, l and h dimensions are kept constant and thus the volume of the bucket remains constant as well. In the three other sets, the volume is affected by the change in either w, l and h, while the mass of the prototype is constant. Changes in KPIs are considered significant when the new KPI lies outside the confidence intervals mentioned in the previous section. By isolating these dimensions one by one, their influence on the KPI will become clear, allowing for a smart selection of virtual prototypes to be tested.

| m | 0.8 | 0.9 | 1.0 | 1.1 | 1.2 |

(a) Mass.

| w | 0.8 | 0.9 | 1.0 | 1.1 | 1.2 |

(b) Width.

| l | 0.8 | 0.9 | 1.0 | 1.1 | 1.2 |

(c) Length.

| h | 0.8 | 0.9 | 1.0 | 1.1 | 1.2 |

(d) Height.

Table 8.1: Scaled parameter variations.
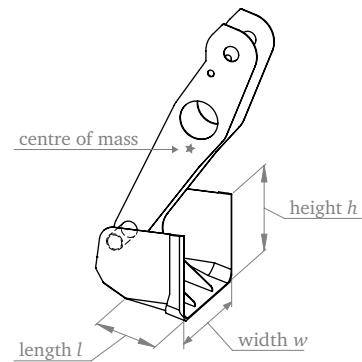
Figure 8.4: Grab parameters width w, length l and height h. The mass m is equally distributed around the centre of mass.

For operating the virtual prototypes a virtual grab operator has been developed based on the operator characteristics measured on bulk terminal. The virtual operator opens the grab, lowers the grab towards the bulk material surface with a rate of $1.6\,\mathrm{m/s}$ until contact has been made and the grab penetrates the bulk material. Closing winch direction is then reversed, resulting in the closing in the grab. In practice, the hoisting winch aids in hoisting the grab due to the limited strength of the closing winch and cables. This does not require consideration in the virtual environment, where the hoisting of the grab can be achieved completely by the closing winch and cables.
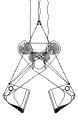
8.2.1   Mass of a Grab

The grab mass affects the strength and stiffness of a grab and determines the mass ratio. The closing path of grabs with a different mass is shown in Figure 8.5, where it can be observed that the changes in mass mostly affect the initial penetration. Heavier grabs penetrate deeper than lighter grabs and this results in a larger volume of material grabbed.
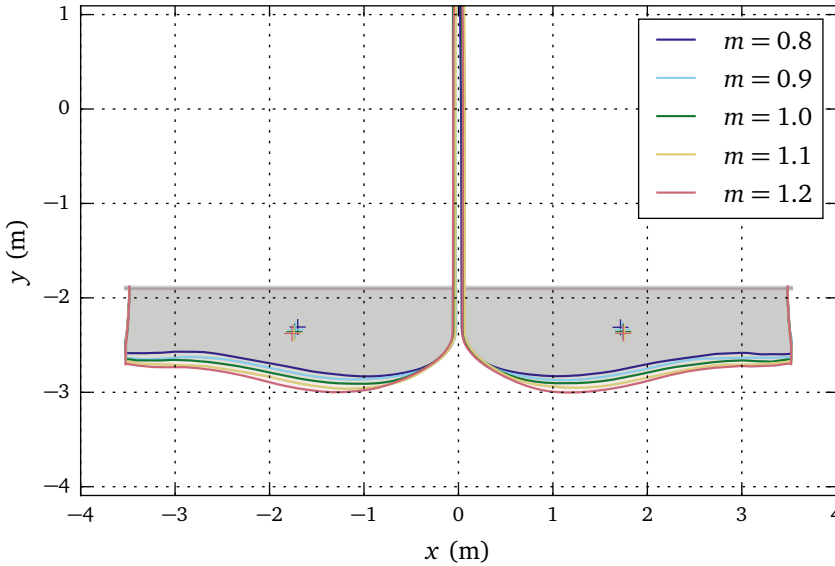
Figure 8.5: Closing trajectory for grabs with varying mass.

The effects the changes in mass and penetration causes on the key performance indicators can be seen in Figure 8.6. The mass indicator in Figure 8.6a shows that the heavier grabs negatively impact the mass ratio, favouring lighter grabs, although the mass is also required for the strength and stiffness of the bucket. The grab efficiency indicator in Figure 8.6b reveals that the additional material in the deeper closing paths of heavier grabs also results in a lower grab efficiency. The heavy grabs lose part of the additional material during the closing of the buckets, with large amounts of material leaking between the two knives. In short, these heavy grabs are less efficient when it comes to transferring the material inside the closing path to the inside of their buckets.

The capacity of these grab prototypes remains unaffected because the dimensions of the grab (l, w, h) are kept constant. As the amount of material grabbed becomes less for the lighter grabs, the volume indicator reduces. This indicates that the grab is not filled completely. For a heavier grab, overfilling results in a higher volume indicator and a lower spillage indicator (Figure 8.6d). The low spillage indicator indicates that the grab is overfilling, spilling excessive material from the buckets.
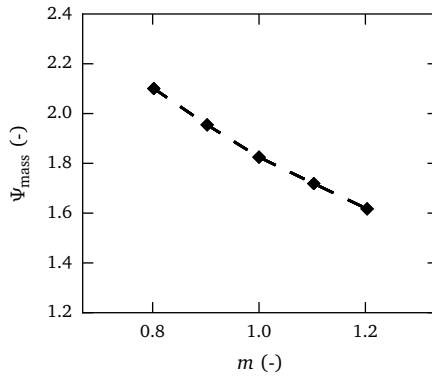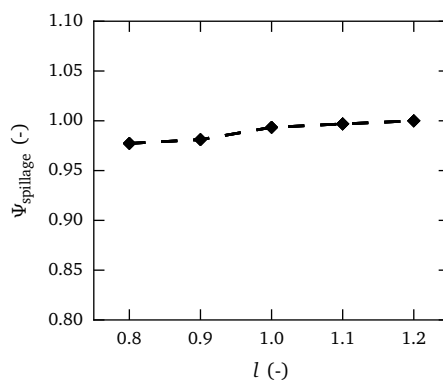
(a) Mass indicator.
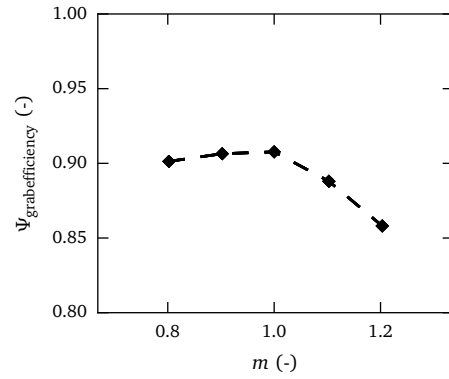
(b) Grab efficiency indicator.
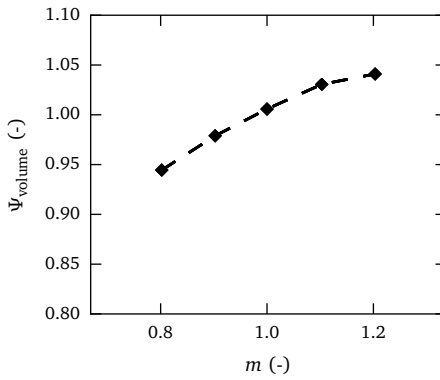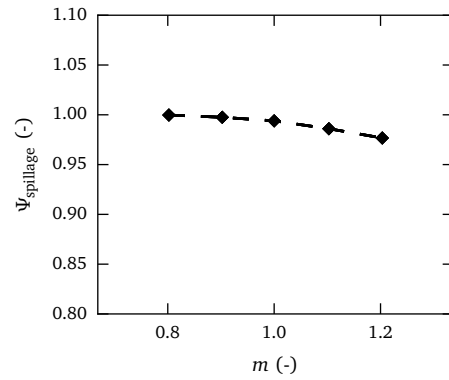
(c) Volume indicator.

(d) Spillage indicator.
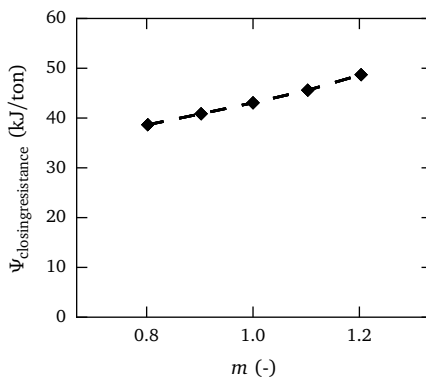
(e) Closing resistance indicator.
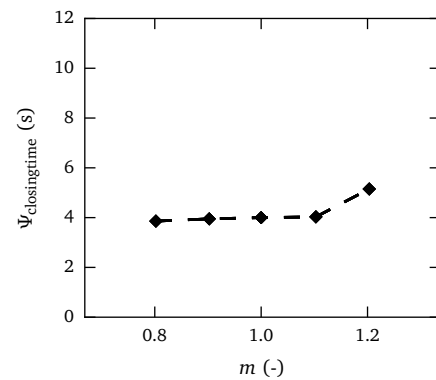
(f) Closing time indicator.

Figure 8.6: Effects of grab mass m. The grab with the original mass m_{grab} has $m = 1$.

8.2.2   Width of a Grab

Grab designers often use the width of the grab w in order to adapt a grab to a specific bulk material. For example, although coal and iron ore differ significantly in bulk properties, grabs with the same target load for these material share the same dimensions, except for the width of the grab. When only the grab width is varied to achieve a specified volume, this may result in the choice for a sub-optimal width of the grab.

Figure 8.7 shows the closing trajectories of grabs of a different width and the same mass. It can be observed that the width only affects the initial penetration due to the changes in mass per meter of knife. For example, wider grabs such as the $w = 1.2$ have a lower pressure on their knives, and this results in a slightly lower penetration. Due to the fact that length of the side knives remained constant, the effect on the penetration is smaller than the results from the change in mass.
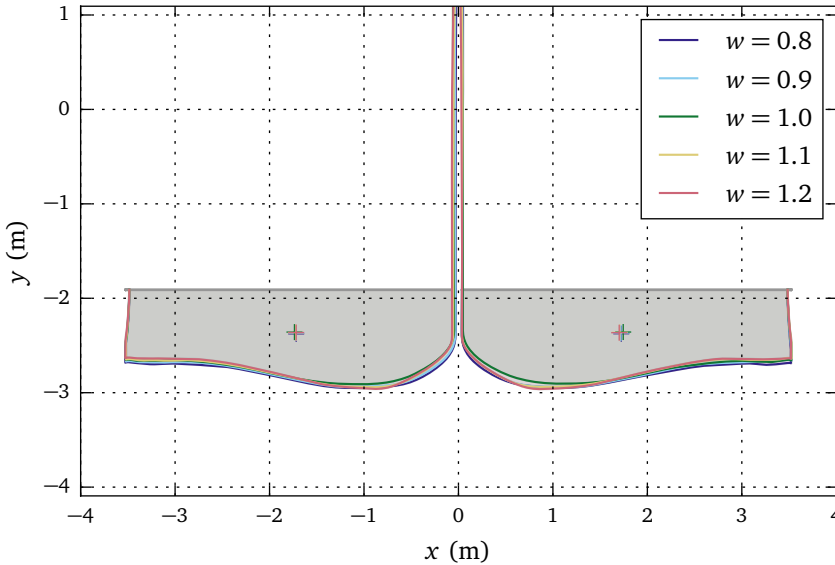
Figure 8.7: Effect of grab width on closing trajectory.

The key performance indicators in Figure 8.8 show that the wider grabs are able to grab more material (Figure 8.8a) with a higher efficiency (Figure 8.8b). The smaller grabs benefit from the deeper penetration and small volume, while the large grabs benefit from the increase in grab efficiency, both increasing the volume indicator as shown in Figure 8.8c. Closing resistance reduces for the wider grabs, since much more volume of material can be excavated while only the bottom knife's resistance increases due the larger width. The time required for closing in Figure 8.8f also shows a slight increase due to the extra material that has been grabbed.
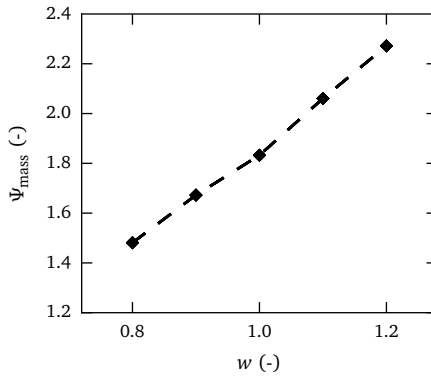
(a) Mass indicator.
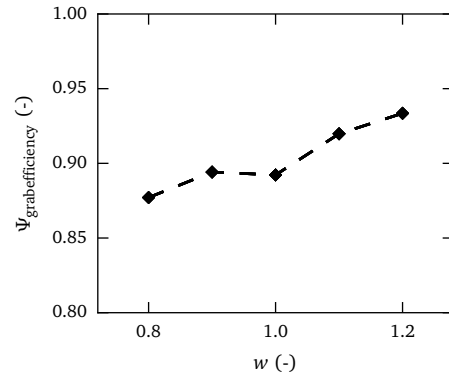
(b) Grab efficiency indicator.
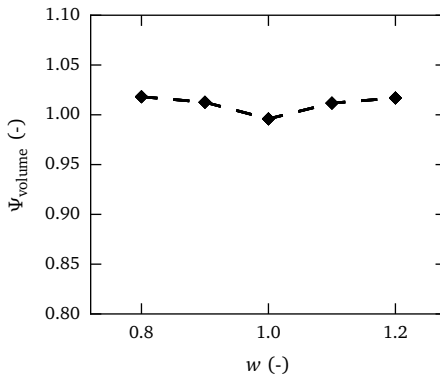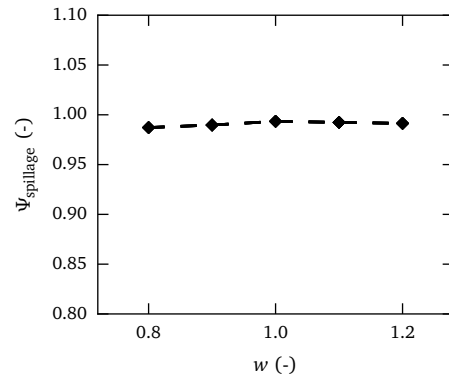
(c) Volume indicator.

(d) Spillage indicator.
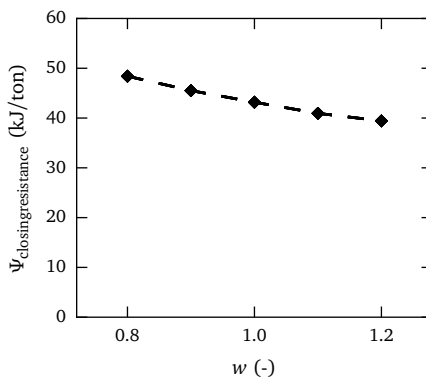
(e) Closing resistance indicator.
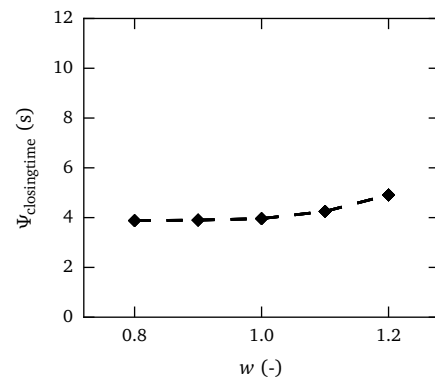
(f) Closing time indicator.

Figure 8.8: Effects of grab width *w*.

8.2.3   Length of a Grab

The length of the bucket is constructed using multiple segments and therefore depends on multiple dimensions. The first segment, which starts at the knives, is the largest length dimension and is therefore selected to study the effect of the length while the mass is kept constant. By changing this dimension l, the complete back of the bucket will either shift away or towards the knives (Figure 8.4).

Figure 8.9 shows that the closing trajectories of grabs with a different length are similar in the first meters of closing and start to differ considerably. Shorter grabs reach their back and the main bucket beam earlier (Figure 2.10), which forces them out of the bulk material. On the other hand, larger grabs have more space in the back and can therefore maintain a more horizontal closing trajectory. Due to this longer closing path, the larger grabs are able to touch much more material than the shorter grabs, as the enclosed area of the trajectory increases.
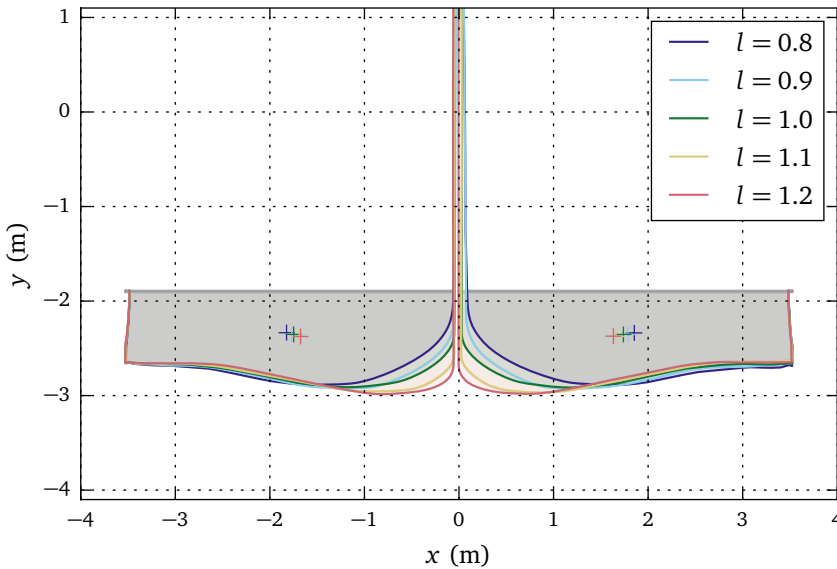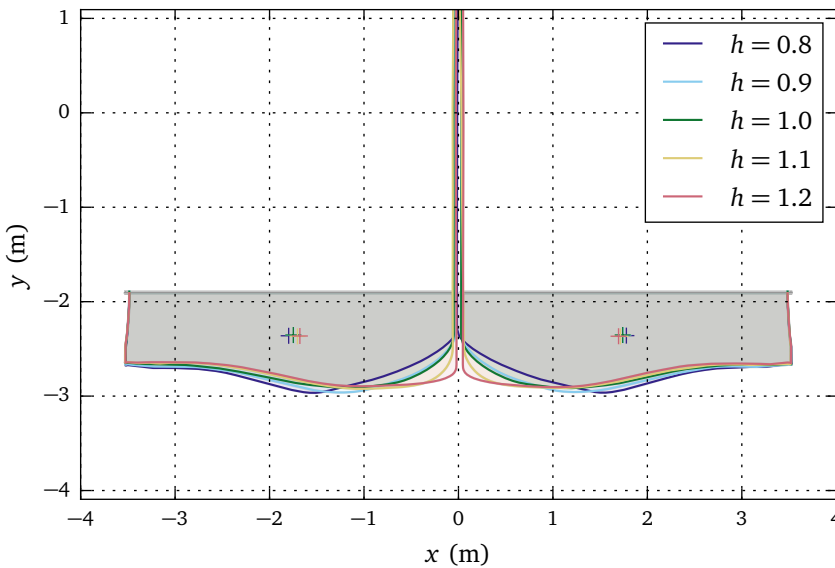

Figure 8.9: Trajectories for grabs with different lengths.

The increase in touched material combined with a higher efficiency (Figure 8.10b) leads to an improved mass indicator seen in Figure 8.10a. Even though the capacity of the shorter grabs is also smaller, additional spillage is limited (Figure 8.10d), although the larger grabs do show a drop in volume (Figure 8.10c), indicating these grabs are not completely filled. Closing resistance is reduced for the larger grabs (Figure 8.10e), while closing time is also reduced since the opposing knives reach each other in an earlier stage of the closing trajectory.
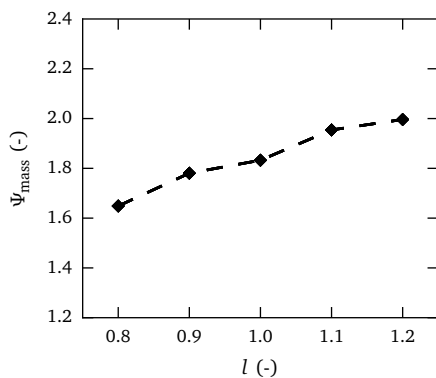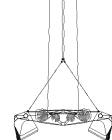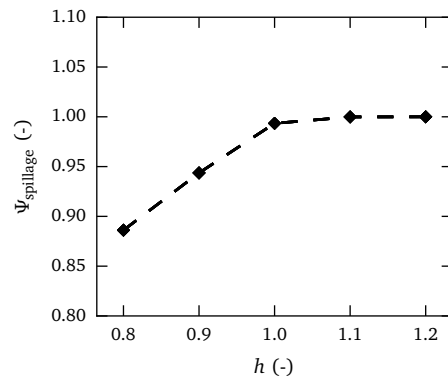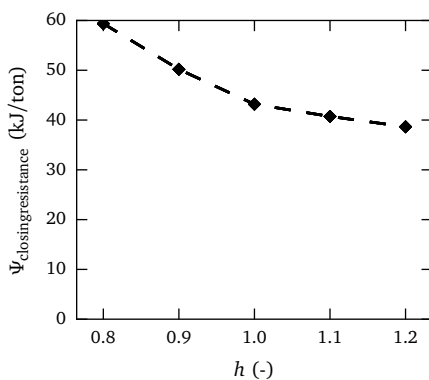
(a) Mass indicator.
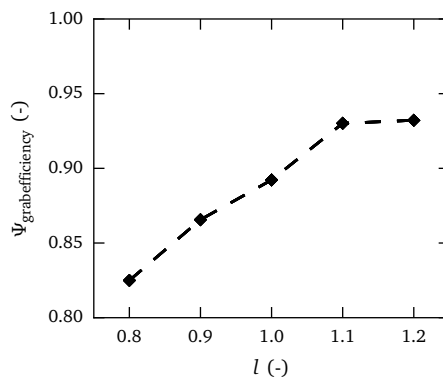
(b) Grab efficiency indicator.
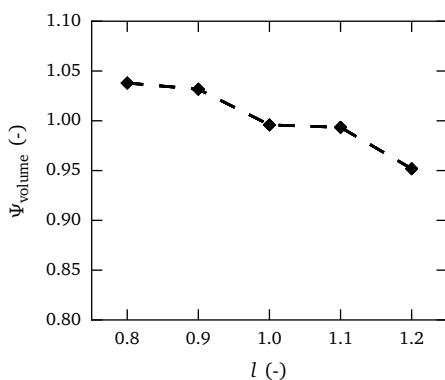
(c) Volume indicator.

(d) Spillage indicator.
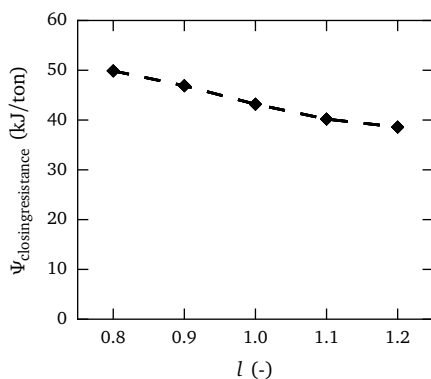
(e) Closing resistance indicator.
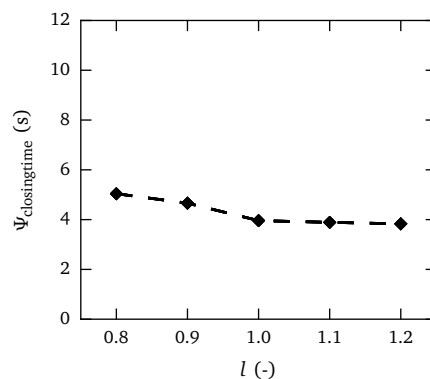
(f) Closing time indicator.

Figure 8.10: Effects of grab length.
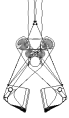
8.2.4 Height of a Grab

The height of a grab is defined as the distance between the edge of the bucket and the lowest point of the knives. Changing the height of a grab influences mostly the capacity of the grab, as increasing the height results in an increase of bucket volume while decreasing reverses this effect. The footprint is unaffected and consequently the initial penetration is expected to remain unaffected as well as the mass is kept constant.

Figure 8.11 shows the effect of different bucket heights on the closing trajectory of a grab. The differences in closing trajectory are likely caused by the affected position of the beam in the bucket required for the grab's strength (Figure 2.10). For grabs with a lower height, the beam is positioned lower, consequently material reaches the main bucket beams earlier and forces the grabs out of the bulk material. Grabs with a larger height show an opposite effect as they are able to maintain their horizontal closing path longer, resulting in an increase in the mass indicator and the grab efficiency (Figure 8.12a and 8.12b).

Figure 8.11: Trajectories for grabs height.

Changing the grab height also changes the bucket volume and therefore a clear effect can be seen in the volume and spillage indicator (Figure 8.12c and 8.12d). Grabs with a small height have a bucket volume that is much lower than the grabbed volume, resulting in reaching the maximum for the volume indicator and spillage of up to eight percent. The large spillages and limited bucket volume for the smaller grabs result in a higher closing resistance per ton, shown in Figure 8.12e.
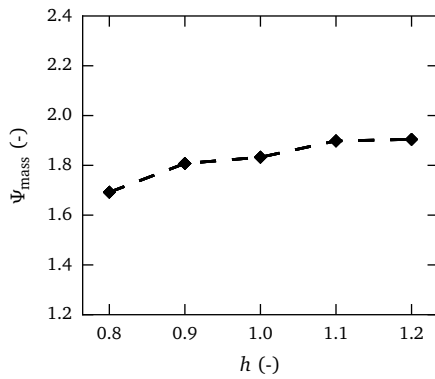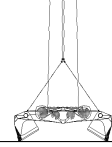
(a) Mass indicator.
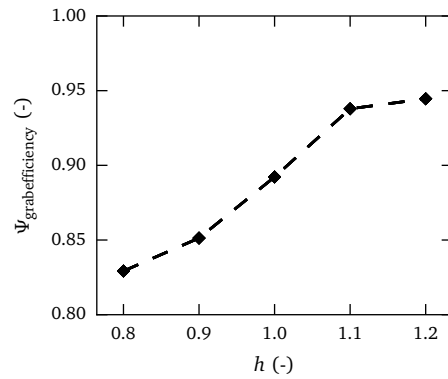
(b) Grab efficiency indicator.
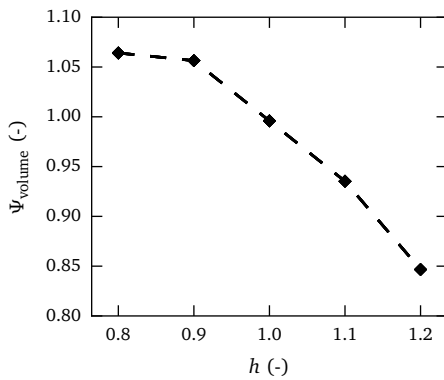
(c) Volume indicator.

(d) Spillage indicator.

(e) Closing resistance indicator.
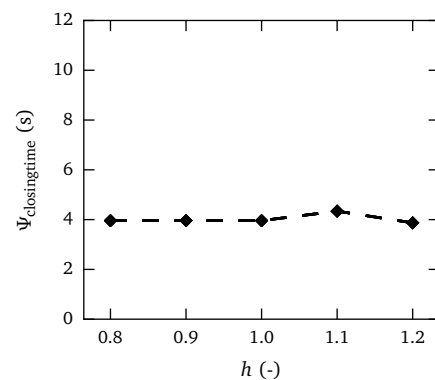
(f) Closing time indicator.

Figure 8.12: Effects of grab height h.
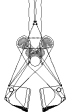
This demonstration has presented the effects of four grab parameter variations on the behaviour and performance of a grab. It was shown that the KPIs defined in Section 8.1 offer a clear and quantitative method of evaluating the effects of these grab parameter variations. Relations between isolated grab parameters and performance indicators such as mass, grabbing efficiency and spillage were detected effortlessly, which enhances the understanding of a grab interacting with iron ore pellets.

Comparing the closing trajectory of the prototypes provides additional insight in the interaction between grab and iron ore pellets. Clearly visible was the connection between the penetration of the grab and the grabbing performance. In addition, the position of the main bucket beam apparently affected the closing trajectory significantly, serving as a capacity limiter of a grab. When changing the length or height of a scissors grab bucket this should be taken into account. These four variations have demonstrated that the performance of a grab can be assessed with the help of the key performance indicators and the closing trajectory.

8.3   Improving Grabs through Virtual Prototyping

Although studying the effects of grab parameters contributes much to the understanding of the grab closing process, these parameters variations are quite limited examples of virtual grab prototyping. In developing a new prototype there is no need to restrict to a single variable, also combinations can be investigated.

Eighteen virtual prototypes have been designed, each having a different combination of length, width and height dimension. These prototypes have an equal bucket volume indicated in Figure 8.3, identical to the volume of the reference grab. Table 8.2 shows the dimensions of 18 grab prototypes and one reference grab ($l = 1$, $w = 1$ and $h = 1$). The maximum variation of the dimensions is set at 20% compared to the reference grab to keep changes compatible to the strength and stiffness of the prototypes. Mass of the prototypes is calculated by adding the difference in bucket material mass to the reference grab, as shown in Table 8.3.

w / l	0.8	0.9	1.0	1.1	1.2
0.8	-	-	1.16	1.056	0.98
0.9	-	1.18	1.07	0.98	0.91
1.0	1.23	1.10	1.00	0.91	0.84
1.1	1.16	1.04	0.94	0.86	-
1.2	1.10	0.98	0.88	-	-

Table 8.2: Height of the virtual prototypes.
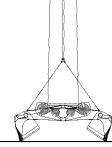
| l \ w	0.8	0.9	1.0	1.1	1.2
0.8	-	-	0.986	0.987	0.989
0.9	-	0.995	0.993	0.993	0.995
1.0	1.008	1.002	1.000	1.000	1.005
1.1	1.016	1.010	1.007	1.010	-
1.2	1.023	1.017	1.015	-	-

Table 8.3: Mass of the virtual prototypes.

The performance of the prototypes is shown in Figure 8.13 and several observations can be made. In general the mass performance of the prototypes with a large length exceeds those with less length (Figure 8.13a), similar to the observations in Section 8.2.3. Likewise, prototypes with a larger width exceed those with less width, similar to Section 8.2.2. Although all prototypes share the same bucket volume, a look at Figure 8.13c and 8.13d tells that several prototypes with $\Psi_{volume} < 1$ and $\Psi_{spillage} = 1$ cannot fill this volume, underperforming compared to the reference grab.

Large changes in $\Psi_{closing\ time}$ are not predicted as expected, as all prototypes use the type and dimensions of the closing mechanism. The closing resistance indicator $\Psi_{closing\ resistance}$ slightly favours wider grabs, as the side knives of these grabs experience less resistance. The grab efficiency indicator $\Psi_{closing\ resistance}$ shows that some prototypes have a higher efficiency in moving touched material into their buckets, influenced by the combined effects of changing length, width, height and mass.

The prototypes with $\Psi_{volume} > 1.014$ show a clear improvement in grabbed material as the grabbed material exceeds the bucket volume identical to that of the reference grab. For example, the grab with $l = 1.0$ and $w = 1.2$ has $\Psi_{volume} = 1.084$, which means it has 6.9% more material in its buckets. In addition, spillage of this prototype changes from $\Psi_{spillage} = 0.991$ to 0.904, spilling 8.8% more material compared to the reference grab, indicating the grab is outperforming its bucket. This leads to the new prototype grabbing 2.155 times its own mass instead of $\Psi_{mass} = 1.874$, an impressive increase in grabbed material of 15.0% (Figure 8.13a). As a result, the payload of the grab unloader system improves from 1.868 to 1.948, an increase of 4.2%, strongly limited by the size of the buckets. When the size of the buckets is matched to the grabbing performance and thus spillage is prevented, a prototype with an attractive payload ratio increase of 15.0% should be possible.

Chapter 7 validated the coupled model and established the accuracy of its predictions, which should be taken into account when interpreting these results. Overall, determination coefficients exceeded 0.9, meaning that less than 10% of the variation in the compared signals was attributed to influences not captured by the model. It would be sensible to take into account a similar 10% variation for the results achieved in this chapter.
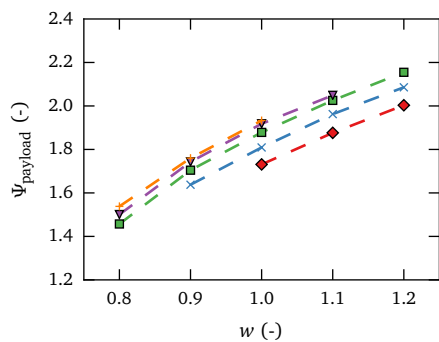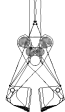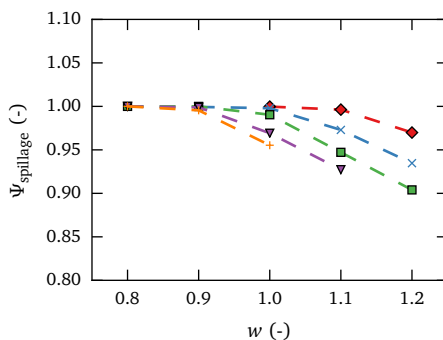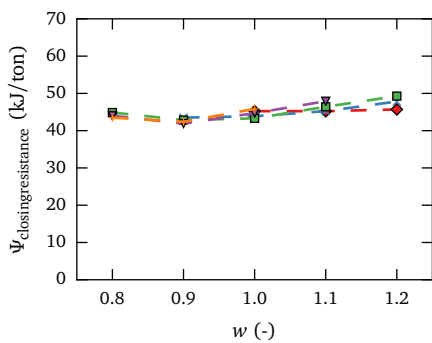
(a) mass indicator.
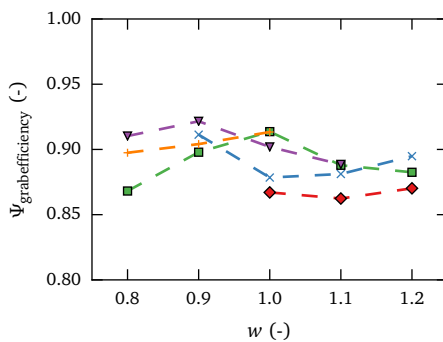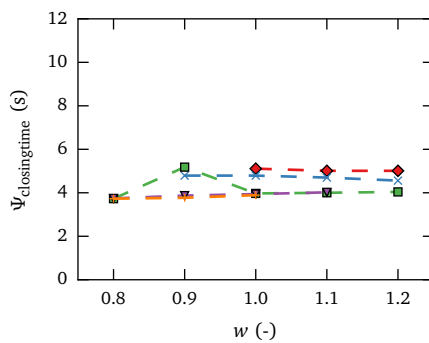
(b) Grab efficiency indicator.
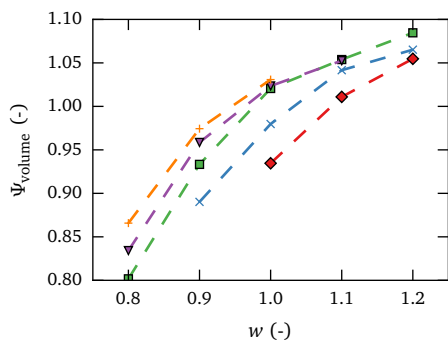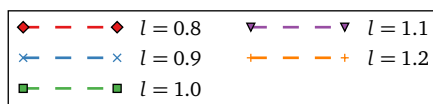
(c) Volume indicator.

(d) Spillage indicator.

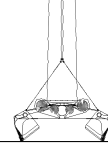(e) Closing resistance indicator.

(f) Closing time indicator.

(g) Legend.

Figure 8.13: The performance of the virtual grab prototypes.

Although these prototypes are not immediately ready for production and might require additional engineering, these results demonstrate that virtual prototyping can lead to significant potential improvements of grab designs. Possibly even larger gains in grab performance can be achieved when all grab design variables are included in an optimization study of grab performance.

8.4   Conclusions

This chapter has demonstrated that an improved grab design can be achieved through virtual prototyping using the validated co-simulation of grab and iron ore pellets. In a comparison of selected grab prototypes, performance increases in grabbed material of up to 15 percent have been achieved. Larger improvements should be feasible when the prototype design variables are extended to all possible parameters, including the closing mechanism of the grab.

Moreover, this demonstration has shown that grab performance can be evaluated in three distinct ways. Prototypes can be compared fast and clearly with the help of six key performance indicators, where changes in mass, grabbing efficiency and spillage are easily detected. More insight into the interaction between prototype and material is achieved in a graphical comparison of closing trajectories of the prototypes. Lastly, a prototype can also be analysed in detail, for example by studying stress concentrations on the buckets, aiding in preventing heavy localised wear on the buckets. With the help of these grab analysis tools, virtual prototypes of grabs can be analysed thoroughly and swiftly.

Overall, this chapter shows that if virtual prototyping is implemented in the design process of grabs, significant gains can be achieved. According to the preferences of grab customers, engineers can develop prototypes and test these in the virtual environment, establishing a fast and affordable alternative to the building and testing of physical prototypes. This thesis can now be concluded in the next chapter, along with some recommendations for further improvements.
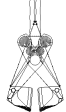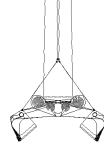
"And I want to know
The same thing
Everyone wants to know
How's it going to end?"

Tom Waits, (1949 – present)

9

Conclusions and Recommendations

This chapter concludes this thesis with the main findings on the research objective and provides recommendations for future work. The main objective of this thesis was to investigate whether a co-simulation of MultiBody Dynamics (MBD) and Discrete Element Method (DEM) models can establish a reliable and accurate environment for the virtual prototyping of grabs for iron ore.

9.1 Conclusions

The main findings regarding the research objective of this thesis are:

- **Model validation.** Chapter 7 has convincingly validated and established the accuracy of the co-simulation of coupled grab and material model. Predictions made by the coupled models matched the outcome of bulk terminal measurements excellently, both in flat and sloped situations. Crane loads were predicted at an average of 27.5 ton while experiments showed an average filling of a grab at 27.8 ton. Coefficients of determination for the load data exceeded 0.922 on a flat surface and even 0.958 on a sloped surface. Vertical motion of the grab during closing has been predicted, achieving $R^2 > 0.975$ for flat surface and 0.964 for the sloped surface. The observed comparisons validate that the developed coupled models are capable of predicting grab performance.

- **Benefits of virtual prototyping.** Chapter 8 has demonstrated that an improved grab can be achieved through virtual prototyping using the validated co-simulation of grab and iron ore pellets. In a limited comparison of grab prototypes, performance increases in grabbed material of up to 15 percent were observed. Larger improvements should be feasible when the prototype design variables are extended to all possible parameters, including the closing mechanism of the grab.

- **Analysis of prototypes.** Moreover, Chapter 8 has shown that virtual grab performance can be evaluated in three distinct ways. Prototypes can be compared fast and clearly with the help of six key performance indicators, where differences in payload, grabbing efficiency and spillage are easily detected. More insight into the interaction between prototype and material is achieved in a graphical comparison of grab closing trajectories of the prototypes. Lastly, a prototype can also be analysed in detail, for example by studying stress concentrations on the buckets, aiding in preventing heavy localised wear on the buckets. With the help of these grab analysis tools, virtual prototypes of grabs can be analysed thoroughly and swiftly.

The main findings regarding developing the validated model are:

- **Grab model.** Chapter 2 has shown that MultiBody Dynamics is a suitable method for simulation the behaviour of a scissors grab. The developed model was compared to an analytical solution as well as measurements conducted with an empty scissors grab on a bulk terminal. The closing cable forces of the model matched with the analytical solution showing an increasing an increasing closing cable force for larger a opening angle of the grab. In the comparison with measurements on the bulk terminal, closing winch torques were predicted with an R^2 of 0.91, demonstrating the accuracy of the model. In brief, these comparisons confirm that MultiBody Dynamics can predict the behaviour of complex mechanisms such as a grab.

- **Bulk Materials.** Iron ore concentrates and pellets have been tested extensively in Chapter 3 and the pellets have been found the most suitable candidate for the material model. Pellets were preferred for their insensitivity to consolidation. Tests included density tests, angle of repose tests, penetration tests, flow moisture point tests, wall friction tests and rolling resistance tests. Particle density of pellets was measured at $4260 \, ^{kg}/_{m^3}$ while bulk density was measured at $2135 \, ^{kg}/_{m^3}$ after consolidation through vibration. Angle of repose of pellets have been measured at 26.0 and 40.8 degrees for a free cone method and a ledge method. Penetration resistance of pellets increased up to three times when using blunt tools while showing no effects for penetration rate or compaction. Wall friction angle was measured at 22.5 degrees while a rolling resistance test resulted in a average
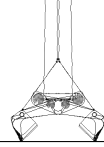
rolling distance of 22 cm. These tests have produced all necessary data for calibrating a material model.

- **Material model.** Chapter 4 has presented two material models for iron ore pellets suitable for a Discrete Element Method simulation. One using the rolling friction solution of Iwashita and Oda (1998), the other prohibits rolling motion of particles, following the suggestion of Bierwisch (2009). Both models calculate normal forces based on the Hertz contact theory and use a tangential solution based on the work of Mindlin and Deresiewicz. The more complex material model including rolling friction did not offer significant improvement in grab prediction over the other material model where rolling motion is restricted and substantial computational costs are saved.

- **Calibration of material model.** Furthermore, Chapter 4 showed that a complete match between the material models and all the measured characteristics was not found, making it necessary to prioritize characteristics. Penetration characteristics are approximated very well by the both material models, this is also considered important for grab simulation and therefore prioritized. Bulk density is also approximated well, although compaction effects are much smaller than those observed in the experiments. Largest challenge in the calibration was attaining the same difference between the angle of movement and the angle of repose in the simulation, which was not found. The experimental difference amounted to fourteen degrees, while the simulation that approached these angles best resulted in a difference of five degrees in the no-rolling model and eight degrees in the rolling model.

- **Particle stiffness reduction.** Chapter 5 has shown that a particle stiffness reduction can result in undesired effects and therefore should be treated with care. The stiffness reductions directly affected the collision behaviour of a single contact pair and the stiffness response of an assembly of particles and should be avoided in simulations where these aspects are considered important. Other aspects such as the energy dissipation, the shearing behaviour, bulk density and penetration resistance showed negligible impact as long as normal overlaps remain below 0.3% of the particle radius. This observed value is comparable with the 0.1–0.5% limit experienced by Cleary (2010). Reducing particle stiffness to the stated 0.3% limit offers considerable savings in computational expenses for DEM models concerning these aspects, such as an iron ore pellet grab simulation. In case of the iron ore pellets grab, the particle stiffness reduction resulted in cost reduction factor of 7.3, while the calibrated behaviour of the material model is not affected.

- **Coarse graining.** In addition, Chapter 5 has shown that computational costs can be reduced by replacing a group of particles by a single, coarse particle as long as the particle process is not inherently dependent on the grain size. The coarse grain system contains identical amounts of potential, kinetic, rotational and

dissipated energy as the original system. This has been confirmed in simulations of the angle of repose, where the shearing behaviour of coarse grains matched the behaviour of the material model. Sliding resistance on the shaft of the penetration tool was also constant for the tested grain sizes. However, coarse graining of the penetration resulted in an increase in resistance on the tip of 16% when grain size doubled. This increase caused by the coarser grain can be compensated by lowering the sliding friction of the penetrating tip which brings the resistance back to normal levels. The coarse graining technique resulted in a reduction of 10^4 hours to just under 18 hours for the iron ore pellet grab simulation while the calibrated behaviour including penetration resistance remained constant. Grab simulations using scaled particle sizes showed comparable results, when applying the coarse graining scheme and the adapted approach derived from an isolated small scale penetration simulation. In brief, similar grab behaviour has been predicted, independent of the selected grain size.

- **Coupling.** Chapter 6 shows how a Discrete Element Method model (DEM) can be successfully coupled with a Multi Body Dynamics (MBD) model into a co-simulation. The coupling has been tested thoroughly in several scenarios, starting with a simple scenario of a single collision between particle and geometry and concluding with a complex scenario combining translation and rotation. Each test clearly demonstrated that a co-simulation of DEM and MBD is successful in predicting particle-equipment interaction.

In conclusion, this thesis has shown how a reliable and accurate co-simulation of Multibody Dynamics scissors grab and Discrete Element Method models of iron pellets can be developed. Coupling these models has resulted in the possibility of virtual prototyping of grabs for iron ore, focussing on rapid assessment of the performance of virtual prototypes. Instead of the traditional ways of evaluating grab performance, virtual prototyping can now be used as an accurate and affordable alternative.

9.2   Recommendations

In the first place, the virtual prototyping of grabs presented in this thesis should be implemented in the grab design process for iron ore pellets. Evidently, the limited set of design variables explored in this thesis should be extended to incorporate all possible grab prototypes. However, some challenging issues remain that can still benefit from future research:

- The current model assesses the performance of a given prototype. It would be nice to see the assessment expand to a strength and stiffness evaluation. An indication of the costs related to the production of a prototype would also be welcome. Also a validated, quantitative wear prediction is helpful in evaluating prototypes.

- When these topics are addressed in the evaluation of the virtual prototypes, it should be investigated if an optimization algorithm can be developed for the design of grabs. In this optimization costs should be minimized and performance maximized while sufficing stiffness, strength and wear requirements.

This thesis has developed a model for scissors grabs and iron ore pellets, which were selected for their free flowing behaviour and lack of sensitivity to consolidation and moisture. However, also other products are handled by grab unloaders, often non-free flowing or cohesive; consequently, the next challenge is to develop the model further to be able to predict grab interaction with other materials. This should include new materials such as wood chips, wood pellets and biocoal. When calibrating these new material models, the following items can be investigated:

- Other contact models and particle shapes should be investigated to incorporate the differences in characteristics of these materials.

- For calibrating these new material models, an automatic calibration algorithm can be adopted instead of the manual approach used in this thesis. Such an algorithm could greatly reduce the time required for an engineer or scientist to calibrate a new material model. However, this thesis has shown that not all material characteristics can be matched, this should be taken into account when implementing such an algorithm.

- The new material models should be evaluated for other bulk handling processes as well, such as belt conveying, chute transfers and feeder mechanisms.
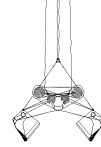
Bibliography

Aberkrom, P., 1982a. Grijpers voor de overslag van stortgoed: theoretische benadering en praktijkgegevens. Doctoraalopdracht TT.913, TU Delft, Delft.

Aberkrom, P., 1982b. Het ontwerp van een 50-tons vork-schaargrijper. Doctoraalopdracht TT.952, TU Delft, Delft.

Aberkrom, P., Aberkrom, P., Oct. 1988. Optimizing the Handling of Bulk Solids by Means of Grabs. Bulk Solids Handling 8 (5), 551–558. URL http://trid.trb.org/view.aspx?id=262723

Achmus, M., Abdel-Rahman, K., 2003. The influence of up-scaling on the results of particle method calculations of non-cohesive soils. In: Proceedings of 1st International PFC Symposium on Numerical Modelling in Micromechanics via Particle Methods. Balkema, Lisse, The Netherlands, pp. 183–187.

Ai, J., Chen, J., Rotter, J., Ooi, J., Jan. 2010. Assessment of rolling resistance models in discrete element simulations. Powder Technology 206 (3), 269–282.

Alting, A., 1967. Greifer fur neuere Massengutumschlaganlagen. Fordern und Heben 17 (2), 87–91.

Archard, J. F., Aug. 1953. Contact and Rubbing of Flat Surfaces. Journal of Applied Physics 24, 981–988. URL http://adsabs.harvard.edu/abs/1953JAP....24..981A

Arumugan, S., Feb. 2014. multibody coupling [ref:_00d205mcp._500d0z0iti:ref]. In e-mail.

Asaf, Z., Rubinstein, D., Shmulevich, I., Jan. 2007. Determination of discrete element model parameters required for soil tillage. Soil and Tillage Research 92 (1-2), 227–242. URL http://www.sciencedirect.com/science/article/B6TC6-4JVSWGD-1/2/3062571bb2c613af5821a10a1fef9a2a

Ayers, P., Perumpral, J., 1982. Moisture and Density Effects on Cone Index. Transactions of the American Society of Agricultural Engineers 25 (5), 1169–1172.

Baars, S. v., 1996. Discrete Element Analysis of Granular Materials. PhD Thesis, Delft University of Technology, Delft, The Netherlands. URL http://resolver.tudelft.nl/uuid: bc642899-842e-4593-88ef-9aa1afcc5e41

Bardet, J. P., Huang, Q., Jul. 1993. Rotational stiffness of cylindrical particle contacts. In: Proceedings of the Second International Conference on Micromechanics of Granular Media. Balkema, Rotterdam, The Netherlands, Birmingham, United Kingdom, pp. 39–43.

Barrios, G. K. P., de Carvalho, R. M., Kwade, A., Tavares, L. M., Nov. 2013. Contact parameter estimation for DEM simulation of iron ore pellet handling. Powder Technology 248, 84–93. URL http://www.sciencedirect.com/science/article/pii/ S0032591013000910

Bauerschlag, D., 1979. Untersuchungen zum Füllverhalten von Motorgreifern. PhD Thesis, Leibniz Universität Hannover, Hannover.

Bierwisch, C., Kraft, T., Riedel, H., Moseler, M., Jan. 2009. Three-dimensional discrete element models for the granular statics and dynamics of powders in cavity filling. Journal of the Mechanics and Physics of Solids 57 (1), 10–31. URL http://www. sciencedirect.com/science/article/pii/S0022509608001750

Bierwisch, C. S., Sep. 2009. Numerical simulations of granular flow and filling. PhD Thesis, University of Freiburg, Freiburg. URL http://www.freidok.uni-freiburg.de/ volltexte/6498/

Blas, J., Oct. 2009. Iron ore pricing emerges from stone age. The Financial Times. URL http://web.archive.org/web/20110322231042/http://www.ft.com/cms/s/0/ b0580bf6-c220-11de-be3a-00144feab49a,s01=1.html#axzz3RvbB8O36

Blundell, M., Harty, D., 2015. Chapter 3 - Multibody Systems Simulation Software. In: Blundell, M., Harty, D. (Eds.), The Multibody Systems Approach to Vehicle Dynamics (Second Edition). Butterworth-Heinemann, Oxford, pp. 87–184. URL http://www.sciencedirect.com/science/article/pii/B9780080994253000030

Brans, T., 2000. Simulation of a four rope grab. Computeropdracht 2000.TT.5331, TU Delft, Delft.

Briggs, A., Oct. 1973. Bucket assembly for use in a material handling apparatus. U.S. Classification 212/81; International Classification B66C1/62, B66C3/00, B66C13/22, B66C3/16, B66C3/14, B66C3/18, B66C3/12, B66C13/32; Cooperative Classification B66C3/125; European Classification B66C3/12B. Patent Number: US3767060A, United States. URL http://www.google.com/patents/US3767060
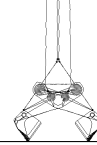
Brouwer, R., 1986. Vorschaargrijper. Doctoraalopdracht 86.TT.2076, TU Delft, Delft.

Brown, D., 2015. Tracker Video Analysis and Modeling Tool. URL http://physlets.org/tracker/

CASAR Drahtseilwerk Saar GmbH, ???? Product Specifications Stratoplast. URL http://www.casar.de/

Champion, V., 1989. Bulk Handling, Grabbing attention. Cargo Systems 1989 (May), 91–93.

Cleary, P. W., Apr. 2010. DEM prediction of industrial and geophysical particle flows. Particuology 8 (2), 106–118. URL http://www.sciencedirect.com/science/article/pii/S1674200109001308

Coetzee, C., Els, D., Dymond, G., Feb. 2010. Discrete element parameter calibration and the modelling of dragline bucket filling. Journal of Terramechanics 47 (1), 33–44. URL http://www.sciencedirect.com/science/article/B6V56-4W4JXPX-1/2/316eaccba7cf7aa27b42f464127f4de3

Conrad, S., 1969. Über die Inhaltsbemessung von Selbstgreifern für Massengüter. Deutsche Hebe- und Fördertechnik 13 (9), 615–617.

Cramer, G., 1750. Introduction à l'analyse des lignes courbes algébriques. chez les frères Cramer et C. Philibert.

Cundall, P. A., Strack, O. D. L., 1979. Discrete Numerical Model for Granular Assemblies. Geotechnique 29 (1), 47–65.

DEM Solutions, 2014a. EDEM.

DEM Solutions, 2014b. EDEM 2.6 User Guide.

Di Renzo, A., Di Maio, F. P., Feb. 2004. Comparison of contact-force models for the simulation of collisions in DEM-based granular flow codes. Chemical Engineering Science 59 (3), 525–541. URL http://www.sciencedirect.com/science/article/pii/S0009250903005414

Dietrich, G., 1969. Der Einfluss der Korngrösse des Schüttgutes auf die Füllmasse von Zweischalengreifern. PhD Thesis, TU Dresden, Dresden, Germany.

Dietrich, G., 1971a. Einfluss bestimmter Greifer- und Schuttgutparameter auf die Masse des gegriffenen Guts - Teil I. Hebezeuge und Fordermittel 11 (3), 75–77.

Dietrich, G., 1971b. Einfluss bestimmter Greifer- und Schuttgutparameter auf die Masse des gegriffenen Guts - Teil II. Hebezeuge und Fordermittel 11 (4), 105–107.

Dietrich, G., 1971c. Einfluss bestimmter Greifer- und Schuttgutparameter auf die Masse des gegriffenen Guts - Teil III. Hebezeuge und Fordermittel 11 (5), 137–141.

Drenth, K., Cool, T., Sep. 2000. Transport Science for Operations Management, 1st Edition. Thomas Cool Consultancy & Econometrics.

Duran, J., 2000. Sands, Powders and Grains: An introduction to the Physics of Granular Materials. Partially ordered systems. Springer, New York.

Elliott, A., 2000. A Highly Efficient, General-Purpose Approach for Co-Simulation with ADAMS®. In: Proceedings of the 15th European ADAMS Users' Conference. Rome, Italy. URL http://web.mscsoftware.com/support/library/conf/adams/euro/2000/euro00_day1.cfm

ESTEQ, 2008. ADAMS-EDEM Coupling.

FAG Germany, 2012. FAG Germany | Products & Services | Spherical roller bearings. URL http://www.fag.de/content.fag.de/en/products_services/rotativ_products/spherical_roller_bearings/spherical_roller_bearings.jsp

Feng, C., Yu, A., Sep. 1998. Effect of liquid addition on the packing of mono-sized coarse spheres. Powder Technology 99 (1), 22–28. URL http://linkinghub.elsevier.com/retrieve/pii/S0032591098000862

Feyrer, K., Mar. 2007. Wire Ropes: Tension, Endurance, Reliability. Springer.

F.M. Dekking, C. Kraaikamp, H.P. Lopuhaä, L.E. Meester, 2004. Probability and Statistics for the 21st Century. Delft University of Technology.

Fowkes, R., Frisque, D., Pariseau, W., 1973. Materials handling research: penetration of selected granular materials by wedge-shaped tools. U.S. Bureau of Mines, Washington, D.C.

Gale, G. W., Jul. 1892. Well-excavator. Cooperative Classification B66C3/12. Patent Number: US479149A, United States. URL http://www.google.com/patents/US479149

Gear, C., 1971. The Simultaneous Numerical Solution of Differential - Algebraic Equations. IEEE Transactions on Circuit Theory CT- 18 (1), 89–95. URL http://slac.stanford.edu/cgi-wrap/getdoc/slac-pub-0723.pdf

Gebhardt, R., 1972. Resistance to the Penetration of Cutters into Bulk Goods with Medium or Coarse Grain Size. Wissenschaftliche Zeitschrift der Technischen Unversitat Dresden 21 (6), 1109–1116.

Gower, G. L., Oct. 1967. A History of Dredging. In: Proceedings of Dredging Symposium. London, United Kingdom, pp. 3–11. URL http://z-telford-01.ingenta.com/content/chapter/d1967c.44777.0002
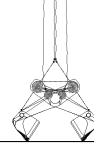
Grima, A., Wypych, P., Jun. 2010. Discrete element simulation of a conveyor impact-plate transfer: calibration, validation and scale-up. Australian Bulk Handling Review May/June 2010 (May/June 2010), 64–72.

Grima, A., Wypych, P., Apr. 2011. Development and validation of calibration methods for discrete element modelling. Granular Matter 13 (2), 127–132.

Gröger, T., Katterfeld, A., 2007. Application of the discrete element method in materials handling. Bulk Solids Handling 27 (1), 17–22.

Grootveld, R., 1977. Modern grab design and operation: the scissors grab. In: Proceedings of the 1st International Bulk Handling and Transport Conference. Vol. 1. Rotterdam, Netherlands.

Gustafsson, G., Häggblad, H.-Å., Knutsson, S., Aug. 2009. Experimental characterization of constitutive data of iron ore pellets. Powder Technology 194 (1-2), 67–74. URL http://www.sciencedirect.com/science/article/pii/S0032591009002204

Härtl, J., Ooi, J., Jun. 2008. Experiments and simulations of direct shear tests: porosity, contact friction and bulk friction. Granular Matter 10 (4), 263–271. URL http://dx.doi.org/10.1007/s10035-008-0085-3

Hellkotter, W., 1975. Zweischalengreifer neuer bauart. Fordern und Heben 25 (5), 370–372.

Hertz, H., 1882. Ueber die Berührung fester elastischer Körper. Journal Fur Die Reine Und Angewandte Mathematik 1882 (92), 156–171.

Hinkley, J., Waters, A., O'Dea, D., Listster, J., 1994. Voidage of ferrous sinter beds: new measurement technique and dependence on feed characteristics. International Journal of Mineral Processing 41, 53–69.

Hogue, C., 1998. Shape representation and contact detection for discrete element simulations of arbitrary eometries. Engineering Computations (Swansea, Wales) 15 (2-3), 374–390.

Huang, H., Tutumluer, E., Hashash, Y., Ghaboussi, J., Aug. 2008. Contact stiffness affecting discrete element modelling of unbound aggregate granular assemblies. In: Advances in Transportation Geotechnics. CRC Press, pp. 167–172.

International Maritime Organization, 2011. International Maritime Solid Bulk Cargoes Code. URL http://www.imo.org/en/OurWork/Safety/Regulations/Pages/BulkCarriers.aspx

International Steel Statistics Bureau, Jan. 2015. Global Overview. URL http://www.issb.co.uk/global.html

Iwashita, K., Oda, M., 1998. Rolling Resistance at Contacts in Simulation of Shear Band Development by DEM. Journal of Engineering Mechanics 124 (3), 285–292. URL http://ascelibrary.org/doi/abs/10.1061/%28ASCE%290733-9399%281998% 29124%3A3%28285%29

Iwashita, K., Oda, M., 1999. Mechanics of Granular Materials: An Introduction. CRC Press, Rotterdam.

Janssen, H., 1895. Versuche über Getreidedruck in Silozellen. Zeitschrift der Vereines Deutscher Ingenieure 39 (35), 1045–1049.

Janszen, W., 1967. Grijpers. Literature Assignment TT.180, TU Delft, Delft.

Jiang, M. J., Yu, H.-S., Harris, D., 2006. Discrete element modelling of deep penetration in granular soils. International Journal for Numerical and Analytical Methods in Geomechanics 30 (4), 335–361. URL http://dx.doi.org/10.1002/nag.473

Kane, T. R., Likins, P. W., Levinson, D. A., 1983. Spacecraft Dynamics. McGraw Hill. URL http://ecommons.library.cornell.edu/handle/1813/637

Katterfeld, A., Donohue, T., Ilic, D., Wensrich, C., Jul. 2013. On the calibration of DEM parameters for the simulation of bulk materials under dynamic conditions. In: Conference Proceedings of the 11th International Congress on Bulk Materials Storage, Handling and Transportation. The University of Newcastle, Australia.

Kessler, F., Prenner, M., Oct. 2012. Investigation into Bulk Material Parameters for Discrete Element Simulation. In: Conference Proceedings of the XX International Conference on Material Handling, Constructions and Logistics. University of Belgrade, Faculty of Mechanical Engineering, Belgrade, Serbia, pp. 25–39.

Kim, K., Prezzi, M., Salgado, R., Lee, W., 2008. Effect of penetration rate on cone penetration resistance in saturated clayey soils. Journal of Geotechnical and Geoenvironmental Engineering 134 (8), 1142–1153. URL http://www.scopus.com/inward/record.url?eid=2-s2.0-48449084032& partnerID=40&md5=5468adff65d710b147addcfc7a7c995b

Kinshofer GmbH, Apr. 2011. English: Motor grab for gantry cranes with double HPXdrive cylinderless grab drive unit by Kinshofer GmbH in Germany. URL https://commons.wikimedia.org/wiki/File:KinshoferGmbH_motor_grab_for_ gantry_cranes.jpg

Kirincic, J., 1983. Increase of the bulk cargo unloading rate by means of the technical improvement of grab unloaders. PORTS & HARBORS 28 (1), 11–15.

Kruggel-Emden, H., Simsek, E., Rickelt, S., Wirtz, S., Scherer, V., Feb. 2007. Review and extension of normal force models for the Discrete Element Method. Powder
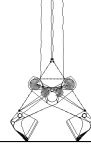
Technology 171 (3), 157–173. URL http://www.sciencedirect.com/science/article/pii/S0032591006004360

Kruggel-Emden, H., Sturm, M., Wirtz, S., Scherer, V., Oct. 2008a. Selection of an appropriate time integration scheme for the discrete element method (DEM). Computers & Chemical Engineering 32 (10), 2263–2279. URL http://www.sciencedirect.com/science/article/B6TFT-4R53RCD-1/2/daaa36c527191b4ae5e72f2014892d97

Kruggel-Emden, H., Wirtz, S., Scherer, V., Mar. 2008b. A study on tangential force laws applicable to the discrete element method (DEM) for materials with viscoelastic or plastic behavior. Chemical Engineering Science 63 (6), 1523–1541. URL http://www.sciencedirect.com/science/article/pii/S0009250907008767

Langerholc, M., Česnik, M., Slavič, J., Boltežar, M., Mar. 2012. Experimental validation of a complex, large-scale, rigid-body mechanism. Engineering Structures 36, 220–227. URL http://www.sciencedirect.com/science/article/pii/S0141029611004962

Laue, J., 1997. Stability of heaps of iron ore concentrate. In: Proceedings of the 7th International Offshore and Polar Engineering Conference. Vol. 1. Honolulu, United States of America, pp. 921–927.

Leikert, F., 1963. Bewegungsrichtung und Nutzkraft am Zweischalenstangengreifer. Deutsche Hebe- und Foerdertechnik 9 (3), 33–38.

Lommen, S., Schott, D., Lodewijks, G., Sep. 2012a. DEM speedup: Stiffness effects on bulk material behavior. In: Proceedings of the 07th International Conference for Conveying and Handling of Particulate Solids. Friedrichshafen, Germany, p. 7.

Lommen, S., Schott, D., Lodewijks, G., Oct. 2012b. Developing a DEM model of a Grab. In: Conference Proceedings of BulkSolids Europe 2012. Vogel Business Media, Berlin, Germany.

Lommen, S., Schott, D., Lodewijks, G., 2012c. Multibody dynamics model of a scissors grab for co-simulation with discrete element method. FME Transactions 40 (4), 177–180.

Lommen, S., Schott, D., Lodewijks, G., Sep. 2012d. Validation of a multibody dynamics model of a scissors grab for DEM modelling. In: Proceedings of the 20th International Conference on Material Handling, Constructions and Logisitics. Belgrade, Serbia, pp. 61–65.

Lommen, S., Schott, D., Lodewijks, G., Jul. 2013. Validation of a co-simulation of a Grab using Discrete Element Method and Multibody Dynamics Models. In: Conference Proceedings of the 11th International Congress on Bulk Materials Storage, Handling and Transportation. The University of Newcastle, Australia.

Lommen, S., Schott, D., Lodewijks, G., Feb. 2014. DEM speedup: Stiffness effects on behavior of bulk material. Particuology 12, 107–112. URL http://www.sciencedirect.com/science/article/pii/S1674200113001387

Lommen, S., Schott, D., Rahman, M., Lodewijks, G., Sep. 2011. The Penetration of Iron Ore Pellets: Calibrating discrete element parameters using penetration tests. In: Proceedings of the 11th Particulate System Analysis Conference. Edinburgh, United Kingdom, p. 5. URL www.psa2011.com

Maitland, C., Apr. 2012. Vinalines Queen Sinks, 22 Seafarers Lost at Sea. URL http://gcaptain.com/hazardous-cargo-sinking/

Malone, K. F., Xu, B. H., Dec. 2008. Determination of contact parameters for discrete element method simulations of granular systems. Particuology 6 (6), 521–528. URL http://www.sciencedirect.com/science/article/B8JJD-4TY91CT-6/2/1880f078cea26ab4632e406f5fa0146c

marinelink.com, Jan. 2013. World's Largest Grab Unloader Operational. URL http://www.marinelink.com/news/operational-unloader350624.aspx

Masson, S., Martinez, J., Apr. 2000. Effect of particle mechanical properties on silo flow and stresses from distinct element simulations. Powder Technology 109 (1–3), 164–178. URL http://www.sciencedirect.com/science/article/pii/S003259109900234X

Mbele, P., Mar. 2012. Pelletizing of Sishen concentrate. Journal of the Southern African Institute of Mining and Metallurgy 112 (3), 221–228. URL http://www.scielo.org.za/scielo.php?script=sci_abstract&pid=S0038-223X2012000300013&lng=en&nrm=iso&tlng=en

Meijaard, J. P., Oct. 1991. Dynamics of mechanical systems: algorithms for a numerical investigation of the behaviour of non-linear discrete models. Dissertation, TU Delft, Delft University of Technology. URL http://repository.tudelft.nl/view/ir/uuid%3Aa03f8a62-4168-46cd-b58a-67418fb99c1d/

Meijers, P., Jan. 1997. Dynamica 3-A: Lecture Notes wb1303. URL http://repository.tudelft.nl/view/ir/uuid%3A401b88f5-a1d7-46a2-a08a-850ad66e28b8/

Miedema, S., Becker, S., 1993. The Use of Modeling and Simulation in the Dredging Industry, in Particular the Closing Process of Clamshell Dredges. In: Conference Proceedings of the CEDA Dredging Days. CEDA, Amsterdam, The Netherlands, p. 26.

Miedema, S., Becker, S., de Jong, P., Wittekoek, S., 1992. On the Closing Process of Clamshell Dredges in Water Saturated Sand. In: Conference Proceedings of WODCON XIII. Vol. 30. WODA, Bombay, India.
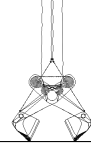
Miedema, S. A., Sep. 1987. Berekening van de snijkrachten bij het snijden van volledig met water verzadigd zand: Basistheorie en toepassingen voor 3-dimensionale mesbewegingen met periodiek variërende snelheden voor, bij het baggeren gebruikelijke, snijdende ontgravingsmiddelen. Delft University of Technology. URL http://resolver.tudelft.nl/uuid:aaa1487d-3d4d-4242-9a4d-e0f2c2723c9d

Miedema, S. A., 2008. A Sensitivity Analysis of the Production of Clamshells. WEDA Journal of Dredging Engineering 9 (1), 19. URL https://www.westerndredging.org/index.php/information/weda-journal

Miedema, S. A., Vlasblom, W., Nov. 2006. The Closing Process of Clamshell Dredges in Water-Saturated Sand. In: Conference Proceedings of the CEDA African Section: Dredging Days. CEDA, Tangiers, Morocco, p. 24.

Mindlin, R., Deresiewicz, H., 1953. Elastic Spheres in Contact Under Varying Oblique Forces. J. Appl. Mech 75, 327–344.

Miszewski, A., Lommen, S., Schott, D., Lodewijks, G., Sep. 2012. Effect of Moisture Content on the Angle of Repose of Iron Ore. In: Proceedings of the 07th International Conference for Conveying and Handling of Particulate Solids. Friedrichshafen, Germany, p. 9.

MSC Software, 2013. ADAMS 2013.2 Solver User Manual. URL https://simcompanion.mscsoftware.com/infocenter/index?page=content&id=DOC10407&cat=2013_ADAMS_DOCS&actp=LIST&showDraft=false

MSC Software, 2014. ADAMS 2013.2. URL http://www.mscsoftware.com/product/adams

Mukherji, B., Jan. 2014. India Imposes 5% Tax on Export of Iron Ore Pellets. Wall Street Journal. URL http://www.wsj.com/articles/SB10001424052702304007504579348021724107090

Munjiza, A., 2004. The combined finite-discrete element method. John Wiley & Sons Ltd.

Muthuswamy, M., Tordesillas, A., Sep. 2006. How do interparticle contact friction, packing density and degree of polydispersity affect force propagation in particulate assemblies? Journal of Statistical Mechanics: Theory and Experiment 2006 (09), P09003–P09003. URL http://iopscience.iop.org/1742-5468/2006/09/P09003

Nemag B.V, Feb. 1969. Grijper met twee, via paren plaatvormige draagarmen, onderling scharnierbaar verbonden bakken. Patent Number: 6711272, Netherlands.

Nieman, G., 1935. Neue erkentnisse im Greiferbau. Zeitschrift des Vereines Deutscher Ingenieure 79 (10), 325–328.

Ning, Z., 1995. Elasto-plastic impact of fine particles and fragmentation of small agglomerates. PhD Thesis, Aston University, Birmingham, United Kingdom. URL http://eprints.aston.ac.uk/14260/

Ninnelt, A., 1924. Uber Kraft und Arbeitsverteilung an Greifern, besonderes an Motorgreifern. Ziemsen Verlag, Wittenberg.

O Sullivan, C., Bray, J., 2004. Selecting a suitable time step for discrete element simulations that use the central difference time integration scheme. Engineering Computations 21 (2/3/4), 278–303.

Park, J., Yoo, W., Park, H., Aug. 2004. Matching of Flexible Multibody Dynamic Simulation and Experiment of a Hydraulic Excavator. In: Proceedings of the Second Asian Conference on Multibody Dynamics. Seoul, Korea, pp. 459–463.

Park, J.-S., Yoon, J.-S., Choi, J.-H., Rhim, S.-S., Apr. 2012. Co-simulation of MultiBody Dynamics and Plenteous Sphere of Contacted Particles Using NVIDIA GPGPU. Transactions of the Korean Society of Mechanical Engineers A 36 (4), 465–474. URL http://koreascience.or.kr/journal/view.jsp?kj=DHGGCI&py=2012&vnc=v36n4&sp=465

Paulick, M., Morgeneyer, M., Kwade, A., Dec. 2014. A new method for the determination of particle contact stiffness. Granular Matter 17 (1), 83–93. URL http://link.springer.com/article/10.1007/s10035-014-0537-x

Pfahl, W., 1912. Kräfteverteilung und Greifen bei Selbstgreifern. Schade, Berlin.

Plassiard, J.-P., Belheine, N., Donzé, F.-V., Oct. 2009. A spherical discrete element model: calibration procedure and incremental response. Granular Matter 11 (5), 293–306. URL http://dx.doi.org/10.1007/s10035-009-0130-x

Priestman, S., 1946. Grabs. Priestman Bros LtD, Hull & London.

Pronk, J., 1999. Ontwerpen van grijpers voor stortgoed. Ontwerpopdracht 99.3.TT5149, TU Delft, Delft, The Netherlands.

Rhodes, M., Mar. 2008. Introduction to Particle Technology. John Wiley & Sons, Ltd, Chichester, UK. URL http://www3.interscience.wiley.com/cgi-bin/bookhome/117932420?CRETRY=1&SRETRY=0

Sakai, M., Koshizuka, S., Feb. 2009. Large-scale discrete element modeling in pneumatic conveying. Chemical Engineering Science 64 (3), 533–539. URL http://www.sciencedirect.com/science/article/pii/S0009250908005228

Scheffler, M., Feyrer, K., Matthias, K., 1998. Fördermaschinen; Hebezeuge, Aufzüge, Flurförderzeuge. Fördertechnik und Baumaschinen. Vieweg, Braunschweig.

Sepling, M., 1985. Continuous Bulk Unloader Versus Grab Unloader: A Comparison of Ship Unloading Systems. Bulk Solids Handling 5 (1), 21–26.

Shoemake, K., 1985. Animating Rotation with Quaternion Curves. In: Proceedings of the 12th Annual Conference on Computer Graphics and Interactive Techniques. SIGGRAPH '85. ACM, New York, NY, USA, pp. 245–254. URL http://doi.acm.org/10.1145/325334.325242

Sohn, H., Moreland, C., 1968. The Effect of Particle Size Distribution on Packing Density. The Canadian Journal of Chemical Engineering 46, 162–167.

Spanke, M., 2000. Comparison of different types of ship unloaders with focus on continuous unloading technology. Bulk Solids Handling 20 (4), 494–498.

Standish, N., Yu, a. B., He, Q., Nov. 1991. An experimental study of the packing of a coal heap. Powder Technology 68 (2), 187–193. URL http://linkinghub.elsevier.com/retrieve/pii/0032591091801275

Strominski, B., Jul. 2007. Deutsch: Terex-Fuchs MHL 360 beim Tag der Offenen Tür zum 50. Jubiläum des Baggerherstellers Terex-Fuchs in Bad Schönborn. URL https://commons.wikimedia.org/wiki/File:Terex-Fuchs_MHL_360_hoch.jpg

Tannant, D., Wang, C., 2002. Numerical and experimental study of wedge penetration into oil sands. Canadian Institute of Mining and Metallurgy Bulletin 95 (1064), 65–68. URL https://www.cim.org/

Tauber, B. A., 1967. Grejfernye Mechanizmy: Teorija, rasčet i konstrukcii. Izd. Mašinostroenie.

Tauber, T., 1959. The effect of the design of a cable grab on its scooping capacity. Russian Engineering Journal 39 (8), 30–34.

Thomas, R., 2002. Not much action to grab. International Bulk Journal 2002 (MAY), 43–47.

Torke, H., 1962. Untersuchungen uber Fullvorgang bei Versuchen im Sand. Deutsche Hebe und Fordertechnik 1962 (8), 43–58.

Tsuji, Y., Tanaka, T., Ishida, T., Sep. 1992. Lagrangian numerical simulation of plug flow of cohesionless particles in a horizontal pipe. Powder Technology 71 (3), 239–250. URL http://www.sciencedirect.com/science/article/B6TH9-440YYC9-G8/2/bdd2486d4d7c776850ec281cd1660fa0

van Bokhoven, W., Feb. 1975. Linear implicit differentiation formulas of variable step and order. IEEE Transactions on Circuits and Systems 22 (2), 109–115.

Verheul, C., 1996. TKC Toolkit.

Verhoeven, C., 1949. Over grijpers voor de verhandeling van stortgoed. In: Haventechniek: voordrachten gehouden tijdens en studies ingezonden ter gelegenheid van het

Eerste Internationaal Congres over Haventechniek gehouden te Antwerpen van 16 tot 19 Juni 1949 bij de viering van het vierde lustrum. Vlaamse Ingenieursvereniging, Antwerpen.

Vermeer, B., Jan. 2011. Analysis of the increased maximum load occurences of bulk cranes. Master thesis 2011.TEL.7654, TU Delft, Delft, The Netherlands.

Vermeer, B., Schuurmans, R., Schott, D., Lodewijks, G., Oct. 2012. Analysis of the increased maximum load occurences of bulk cranes. In: Conference Proceedings of BulkSolids Europe 2012. Vogel Business Media, Berlin, Germany.

Vrančić, F., 1615. Machinae novae (New machines). self published, Venice.

Weisberg, S., Apr. 2005. Applied Linear Regression. John Wiley & Sons.

Wensrich, C., Katterfeld, A., Feb. 2012. Rolling friction as a technique for modelling particle shape in DEM. Powder Technology 217, 409–417. URL http://www.sciencedirect.com/science/article/pii/S0032591011006000

Whittaker, E. T., 1970. A Treatise on the Analytical Dynamics of Particles and Rigid Bodies: With an Introduction to the Problem of Three Bodies. CUP Archive.

Wiek, L., Oct. 1986. Staalkabels: Geometrie en levensduur. URL http://resolver.tudelft.nl/uuid:8dcf5ff2-23b0-45e3-8e77-a13bda8accb6

Wilkinson, H. N., Jun. 1963. Research into the Design of Grabs by Tests on Models. Proceedings of the Institution of Mechanical Engineers 178 (1), 831–843. URL http://pme.sagepub.com/content/178/1/831

Wittekoek, S., 1991a. The determination of the closing process of clamshell dredges in water saturated sand. Tech. Rep. 90.3.GV.2771, Delft University of Technology, Delft, The Netherlands.

Wittekoek, S., 1991b. The development of an improved clamshell. Tech. Rep. 90.3.GV.2858, Delft University of Technology, Delft, The Netherlands.

Wittekoek, S., 1991c. The validation of a calculation method for the simulation of the closing process of clamshell grabs for dredging purposes. Tech. Rep. 90.3.GV.2829, Delft University of Technology, Delft, The Netherlands.

Wittenburg, J., Nov. 2007. Dynamics of Multibody Systems, 2nd Edition. Springer, Berlin ; New York.

World Coal Association, Jan. 2015. Coal Market & Transportation. URL http://www.worldcoal.org/coal/market-amp-transportation/

Xu, J., Zou, R., Yu, a. B., Oct. 2006. Quantification of the mechanisms governing the packing of iron ore fines. Powder Technology 169 (2), 99–107. URL http://linkinghub.elsevier.com/retrieve/pii/S0032591006003147

Yade-DEM, May 2015. DEM background. URL https://yade-dem.org/doc/formulation. html#equation-eq-dtcr-particle-stiffness

Yoo, W., Kim, K., Kim, H., Sohn, J., 2007. Developments of multibody system dynamics: Computer simulations and experiments. Multibody System Dynamics 18 (1), 35–58.

Yoon, J., Park, J., Ahn, C., Choi, J., 2011. Cosimulation of MBD (multi body dynamics) and dem of many spheres using GPU technology. In: Proceedings of Particle-Based Methods II - Fundamentals and Applications. International Center for Numerical Methods in Engineering, Barcelona, Spain, pp. 778–785.

Yoon, J. S., Choi, J. H., Rhim, S., Koo, J. C., Apr. 2012. Particle Dynamics Integration to Multibody Dynamics Using Graphics Processing Unit. Advanced Science Letters 8 (1), 366–370.

Yu, A., Standish, N., Lu, L., Feb. 1995. Coal agglomeration and its effect on bulk density. Powder Technology 82 (2), 177–189. URL http://linkinghub.elsevier.com/retrieve/ pii/0032591094029128

Zemmrich, G., 1965. Einseil-, Motor- und Hydraulikgreifer. Fördern und Heben 1965 (3), 126–130.

Zhang, X., Vu-Quoc, L., Feb. 2000. Simulation of chute flow of soybeans using an improved tangential force-displacement model. Mechanics of Materials 32 (2), 115–129. URL http://www.sciencedirect.com/science/article/B6TX6-3YB4D3C-4/ 2/ccf5197fa42fad45a894eaa5f9e6679a

Zhu, H. P., Zhou, Z. Y., Yang, R. Y., Yu, A. B., 2007. Discrete particle simulation of particulate systems: Theoretical developments. Chemical Engineering Science 62 (13), 3378–3396.

A

Flow Moisture Point Tests

This appendix compares the tests described in the International Maritime Solid Bulk Cargoes Code (IMSBC) of the International Maritime Organization (2011) to determine the flow moisture point (FMP) of a bulk material. The flow moisture point is defined as the level of moisture content where a bulk material is showing signs of liquefaction, and the material starts to behave as a continuum material instead of a discrete material. The FMP depends on the level of compaction and vibration of the sample, which should match with transport conditions. In order to maintain material characteristics and therefore ensure safety during transport of bulk materials, the moisture content should not exceed the transport moisture limit (TML), which is defined as a fraction of the FMP.

The International Maritime Solid Bulk Cargoes Code describes three laboratory test procedures currently in use to determine the FMP and TML: a flow table test, the Proctor-Fagerberg test and a penetration test. The iron ore from the Carajas region described in Chapter 3 will be used to investigate differences between the tests.

A.1   Flow Table Test

The flow table test consists of using a flow table to determine whether a tampered sample of bulk material has achieved flow state. The flow state is determined by observing whether plastic deformation of the sample occurs. Plastic deformation occurs when the sample stops cracking, starts to stick to the table and leave sliding

marks, and increases in diameter. The test has been performed for Carajas samples with increasing moisture content, Figure A.1 shows the increase in diameter of the prepared samples. During the experiments, it was observed that measurements conducted with a moisture content of 6.6% up to 7.2% dry based still showed signs of cracking the sample, which indicate that a flow state has not been developed yet. At a moisture content of 7.4% dry based, an average increase of 1.3 mm was measured, the sample started to stick to the table and left sliding marks when pushed off the table. At this moisture content, the sample is considered to have achieved flow state, therefore the flow moisture point according to the flow table test is at 7.4% dry based. The TML is defined at 90% of the FMP measured by the flow table, resulting in a TML of 6.7% dry based.
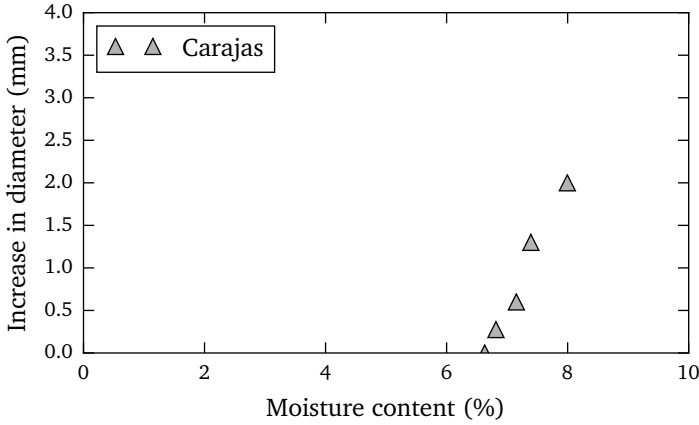
Figure A.1: Flow table results.

A.2   Proctor-Fagerberg Test

The Proctor Fagerberg test is a test similar to the Proctor ISO test, however it uses a different level of tamping. The Fagerberg test prepares the sample by tamping five layers of material with a hammer weight of 350 g, while the ISO uses test three layers of material and hammer weight of 2500 g. Both the ISO and the Fagerberg test conditions have been examined. Figure A.2 shows the relation between the void ratio of the Carajas ore and the net water content using the particle density of 4.89 $^{ton}/_{m^3}$ measured in Section 3.2.1. Here V_v is the volume of the voids in the sample, V_p the volume of particles and V_w the volume of water in the sample. It can be observed that the TML is approached at a net water content of 0.37, which occurs at a moisture content of 7.6% dry based. The tamping prescribed by the ISO specification is much higher and therefore 70% saturation is reached at the lower moisture content of 6.8% dry based.
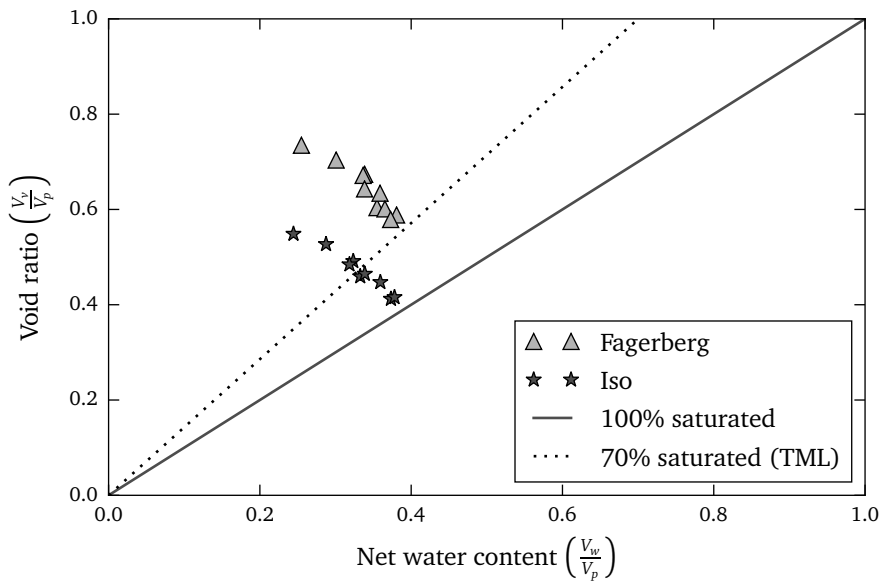
Figure A.2: Proctor-Fagerberg test results.

A.3   Penetration Test

Figure A.3 shows the selected penetration test bolted to a vibration table. The material was tampered in four layers and a pore pressure sensor was placed between the first and second layer. After the material was tampered, the cone was placed on top of the material and vibration of $2g$ started. The amount of penetration of the cone was measured: If penetration was more than $50\,\text{mm}$, the material has reached the FMP.
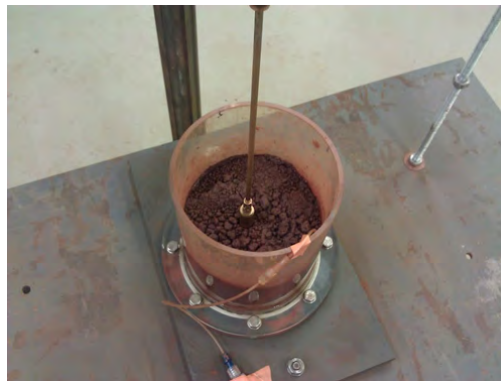
Figure A.3: Penetration test.

After the vibration had been initiated, pore pressure increased and ores with a moisture content above FMP started to liquidate, allowing the cone to penetrate the material. The flow moisture point of Carajas ore was between 7.0% and 7.3% dry based as can be seen in Figure A.4. The TML is defined as 90% of the FMP measured by the penetration table, resulting in a TML between 6.3% and 6.6% dry based.
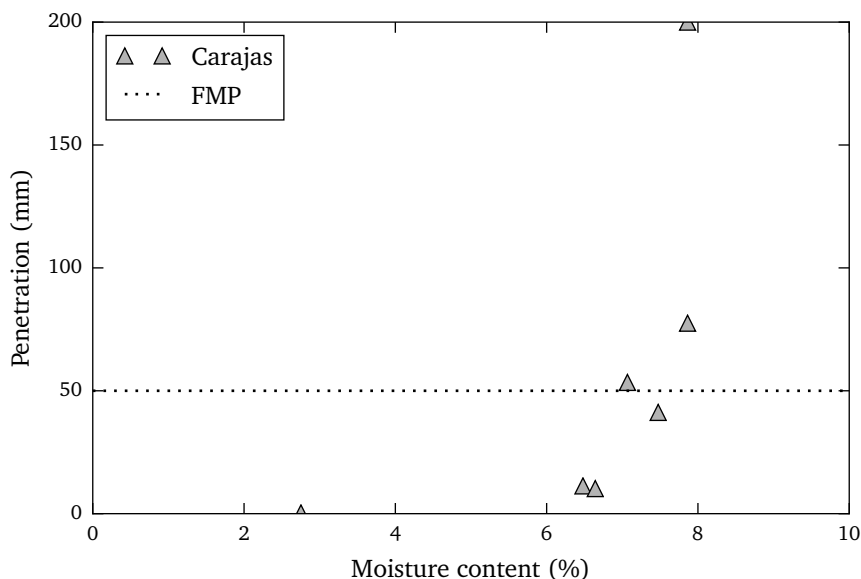
Figure A.4: Flow moisture point penetration test for Carajas ore.

A.4   Conclusions

When the findings of the three test are compared it can be noted that the penetration test and flow table test produces similar results, caused by the same amount of tamping applied in these tests. Of the two tests, the penetration test is the preferred test, as it is more conservative and focuses on a quantitative assessment of the flow state. The proctor test uses a lighter level of compaction, resulting in a higher TML. The ISO compaction produces similar results to the flow table and penetration tests and seems to be more suitable for determining the TML of iron ore fines.
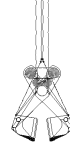
B

Validation Results of Flat Surfaces

In this appendix the validation results for the additional two flat surfaces are shown. The flat surface experiment has been conducted three times, and have resulted in quantities of iron ore pellets displayed in Table B.1, averaging to a 27.8 ton per cycle. These experiments have each been simulated, resulting in an average load of 27.5 ton. The small differences in outcome can be explained through the variation in the bulk material surface, operating characteristics and numerical scatter. Experiment 3 and simulation 3 have been compared in detail in Chapter 7, while figures for the other two comparisons can be found here.

	mass (ton)
Experiment 1	27.2
Experiment 2	27.9
Experiment 3	28.3
Average	27.8

	mass (ton)
Simulation 1	28.1
Simulation 2	27.8
Simulation 3	26.6
Average	27.5

Table B.1: Grabbed material in experiments and simulation

B.1   Flat Surface Experiment 1
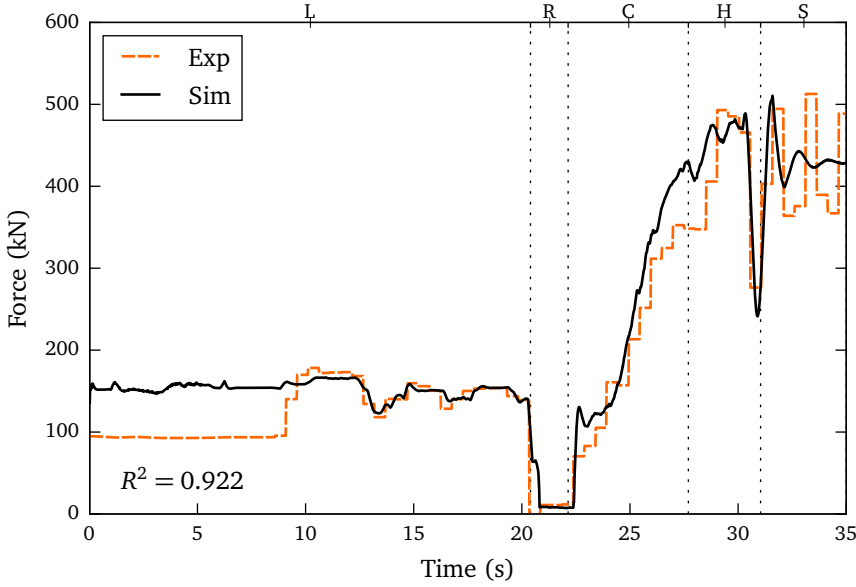
Figure B.1: Load comparison between simulation and experiment with a flat surface. Grab operation consists of lowering of the grab (L), resting on the surface (R), closing (C), hoisting (H) and being suspended from the crane (S).


(a) Closing winch torque.

(b) Hoisting winch torque.

Figure B.2: Closing and hoisting torque during simulation and experiment with a flat surface. Grab operation consists of lowering of the grab (L), resting on the surface (R), closing (C), hoisting (H) and being suspended from the crane (S).
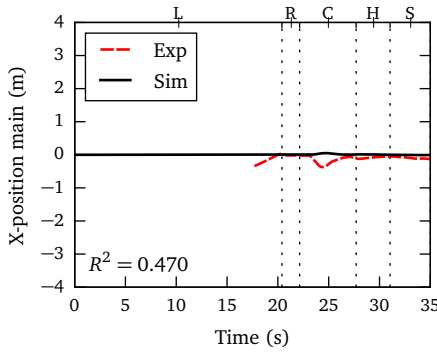
(a) Horizontal position of main hinge point.
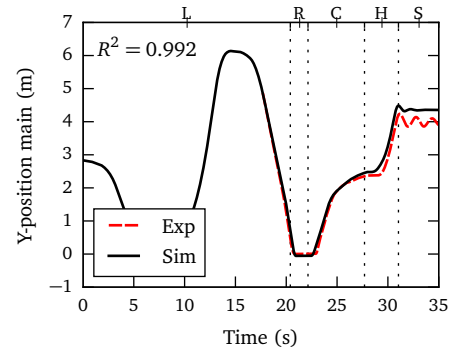
(b) Vertical position of main hinge point.
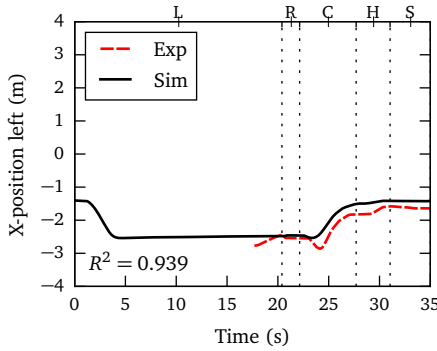
(c) Horizontal position of left marker.
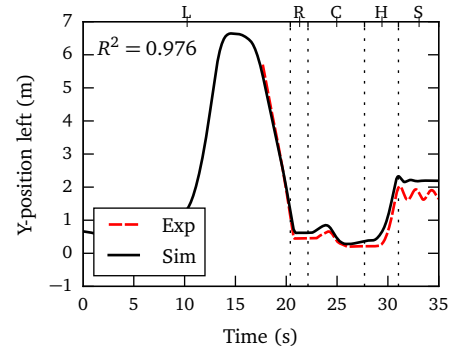
(d) Vertical position of left marker.
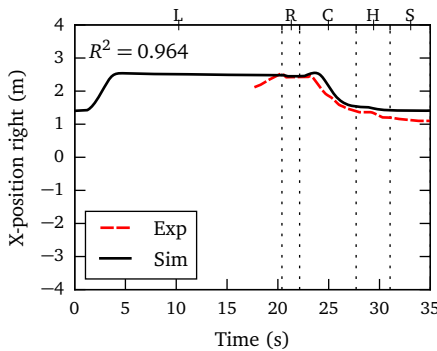
(e) Horizontal position of right marker.
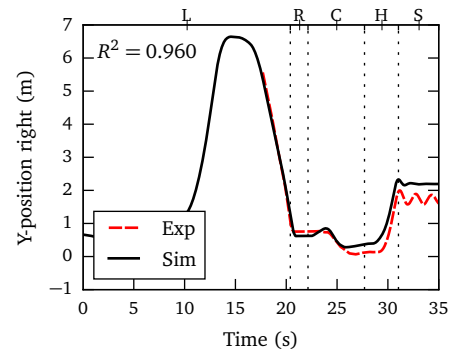
(f) Vertical position of right marker.

Figure B.3: Comparison between simulating and video-tracking of the three applied markers on the grab, on a flat surface. Grab operation consists of lowering of the grab (L), resting on the surface (R), closing (C), hoisting (H) and being suspended from the crane (S).

B.2 Flat Surface Experiment 2
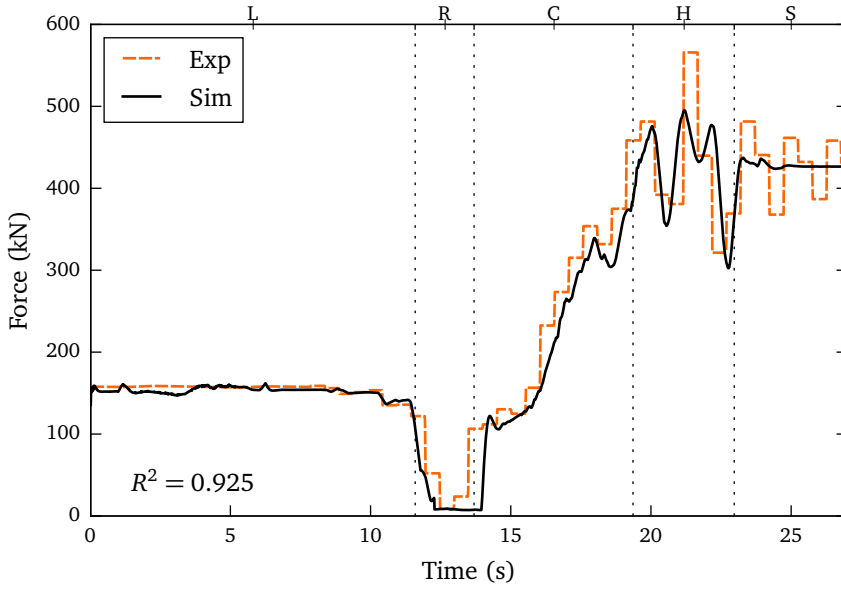
Figure B.4: Load comparison between simulation and experiment with a flat surface. Grab operation consists of lowering of the grab (L), resting on the surface (R), closing (C), hoisting (H) and being suspended from the crane (S).

(a) Closing winch torque.

(b) Hoisting winch torque.
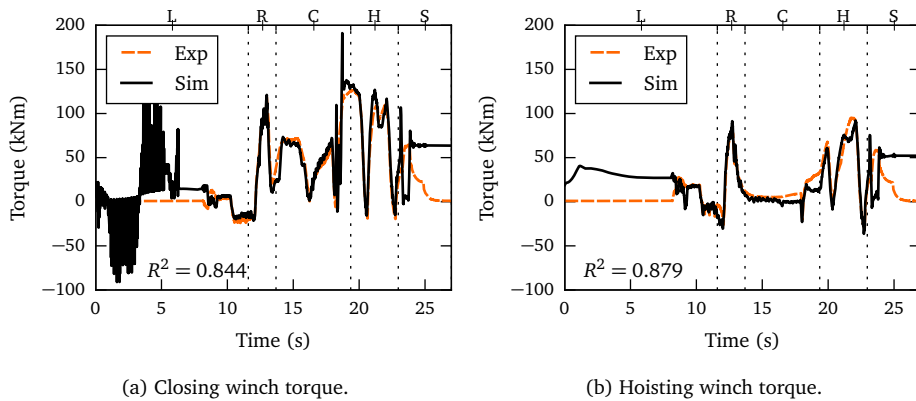
Figure B.5: Closing and hoisting torque during simulation and experiment with a flat surface. Grab operation consists of lowering of the grab (L), resting on the surface (R), closing (C), hoisting (H) and being suspended from the crane (S).
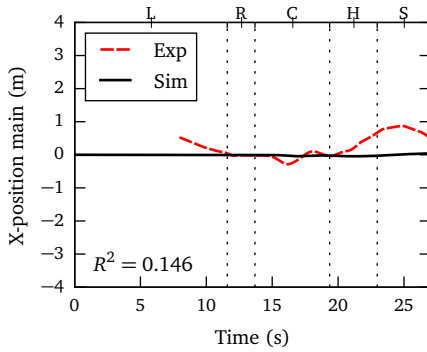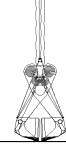
(a) Horizontal position of main hinge point.
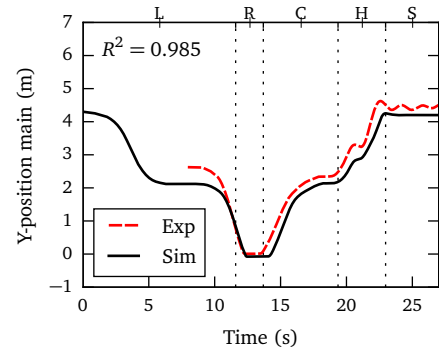
(b) Vertical position of main hinge point.
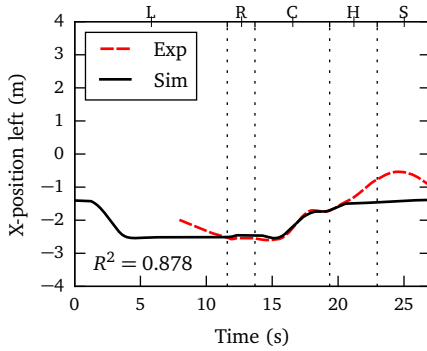
(c) Horizontal position of left marker.
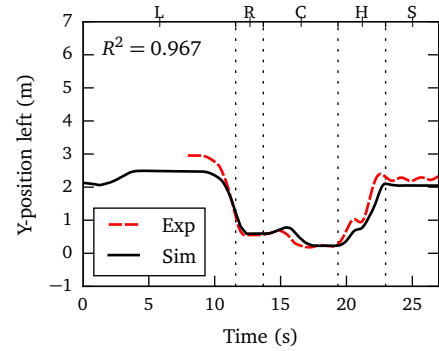
(d) Vertical position of left marker.
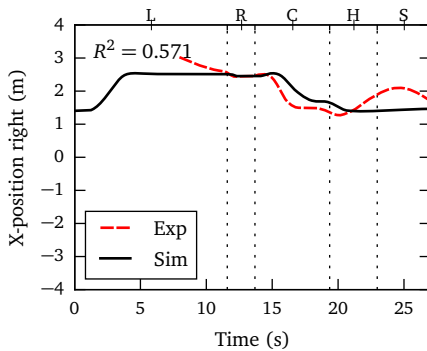
(e) Horizontal position of right marker.
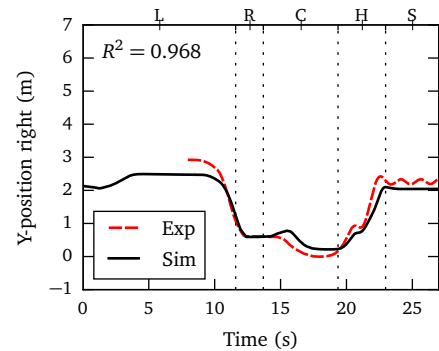
(f) Vertical position of right marker.

Figure B.6: Comparison between simulating and video-tracking of the three applied markers on the grab, on a flat surface. Grab operation consists of lowering of the grab (L), resting on the surface (R), closing (C), hoisting (H) and being suspended from the crane (S).

C

Verification of Rolling Friction Model C

The implementation of the rolling friction model has been verified by comparing the outcome of reference cases to the outcome published in Ai et al. (2010) and Wensrich and Katterfeld (2012). This appendix presents the outcome of these tests, thus verifying the implementation of the model.

- The work of Wensrich and Katterfeld (2012) presents a single particle reference test which includes the rolling friction the solution used in this dissertation, which is based on the rolling stiffness of a Iwashita and Oda (1998) (Equation 4.34) and the absence of a damping term $\mathbf{T}_{r,d}$ (Equation 4.31). Also included is a solution using the rolling stiffness of Bardet and Huang (1993) and a damping term $\mathbf{T}_{r,d}$ for the rolling friction torque $\mathbf{T}_r$ of Equation 4.31. This test will verify the rolling friction solution of a single particle used in this dissertation.

- The work of Ai et al. (2010) presents a multiple particle test, also using the rolling stiffness k_r and a damping term $\mathbf{T}_{r,d}$ based on the work of Bardet and Huang (1993). By including this test, the implemented rolling friction torque of an assembly of contact pairs can be verified.

The rolling stiffness of Bardet and Huang (1993) is displayed in Equation C.1. Here J_i is a dimensionless coefficient which varies to 0.25 and 0.5. Bardet and Huang found J_i to be close to 0.5 in their tests of hard rubber cylinders on a flat surface.

$$k_r = 2J_i R^* \|\mathbf{F}_n\| \qquad\qquad (C.1)$$

The damping term is based on Equation C.2 and is only active when the rolling torque $\mathbf{T_{r,k}}$ is not fully mobilized. It is not expected that the rolling damping dissipates much energy, however it helps to stabilize particles and prevent oscillation (Ai et al., 2010).

$$\mathbf{T}_{r,d} = \begin{cases} -C_r \left(\dot{\boldsymbol{\theta}}_i - \dot{\boldsymbol{\theta}}_j \right) & \left\| \mathbf{T_{r,k}} \right\| < -T_{r,m} \\ 0 & \left\| \mathbf{T_{r,k}} \right\| = -T_{r,m} \end{cases} \tag{C.2}$$

The damping term $\mathbf{T}_{r,d}$ is dependent on the relative rotation velocity $\dot{\boldsymbol{\theta}}_i - \dot{\boldsymbol{\theta}}_j$ and the rolling damping coefficient C_r show in Equation C.3, which is defined as a proportion η_r of the critical damping $2\sqrt{I^* k_r}$, with I^* being the equivalent moment of inertia (Equation C.4).

$$C_r = \eta_r 2\sqrt{I^* k_r} \tag{C.3}$$

$$I^* = 1 \bigg/ \left(\frac{1}{I_i + m_i R_i^2} + \frac{1}{I_j + m_j R_j^2} \right) \tag{C.4}$$

C.1   Single Particle Test of Wensrich and Katterfeld

The single particle test of Wensrich and Katterfeld (2012) consists of a particle rolling on a plate with an initial velocity of $150\,\mathrm{mm/s}$. The exact test conditions have been copied and the rolling friction model of this thesis (Iwashita and Oda, 1998) and Bardet and Huang have been applied to the contact between particle and plate.

Figure C.1 shows the rolling friction torque and the angular velocity of the particle. When compared to Figure 2 of Wensrich and Katterfeld (2012) it can be concluded that these are in excellent agreement.

(a) Rolling friction torque.   (b) Angular velocity.
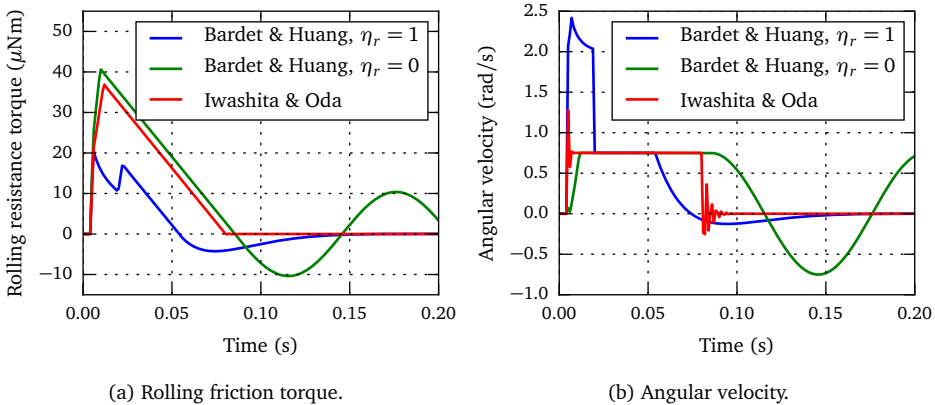
Figure C.1: Simulation results of single particle test.
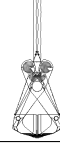
C.2 Multiple Particle Test of Ai et al.

The multiple particle test of Ai et al. (2010) involves a stack of particles arranged in a specified pattern. The test conditions and particle properties of this test have been copied and the rolling friction model of Bardet and Huang (1993) has been applied. At the beginning of the simulation the assembly of particles collapses and a heap of particles is formed. Figure C.2 shows the resulting heap after 10 seconds of simulation for two different timesteps. When compared to Figure 14 in Ai et al. (2010) it can be concluded that the implementation is in agreement and that the rolling friction model is capable of generating a static pile.

(a) $\Delta t = 5\mathrm{e} - 6\,\mathrm{s}$.   (b) $\Delta t = 1\mathrm{e} - 6\,\mathrm{s}$.
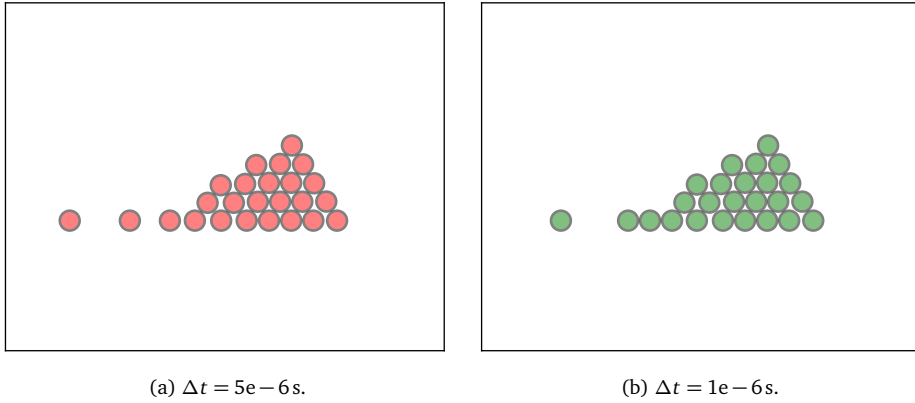
Figure C.2: Simulation results of multiple particle test.

C.3 Conclusions

This appendix has shown that the rolling friction solution used in this thesis has been implemented correctly. The rolling behaviour of a single particle matched to the reference test of Wensrich and Katterfeld, including a rolling friction solution of Bardet and Huang not used in this thesis. Rolling behaviour of an assembly of particles has been matched as well, demonstrating that the contact torques are balanced and therefore correctly implemented.
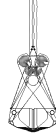
Nomenclature

In this dissertation the following symbols have been used:

Symbol	Unit	Description
A	m^2	Area
B		Set of implicit equations to be solved in a Multibody Dynamics analysis
Δt	s	Timestep. A small increment of time that a simulation uses to advance through time
Δt_{DEM}	s	Timestep for DEM simulation
Δt_{MBD}	s	Timestep for MBD simulation
k	N/m	Stiffness coefficient
k_n	N/m$^{1.5}$	Normal stiffness coefficient
k_r	Nm	Rolling stiffness coefficient
k_t	N/m$^{1.5}$	Tangential stiffness coefficient
c_d	Ns/m	Damping coefficient
c_n	Ns/m	Normal damping coefficient
c_t	Ns/m	Tangential damping coefficient
$\mathbf{e}$	—	Unit vector between particles during contact.
G	Pa	Shear Modulus
g	m/s^2	Gravitational constant
l	m	Length
m	kg	Mass
M	—	Grab mechanism ratio
n	—	Number of Δt_{DEM} that fit in Δt_{MBD}
r	m	Radius
s	—	Coarse graining factor

Symbol	Unit	Description
x	m	Position in a Cartesian system
y	—	Variables to be solved for in a Multibody Dynamics Analysis
x	m	Vector containing the x, y and z position of a coupled body
F	N	Force
F	N	Vector containing forces in x, y and z direction
M	—	Mechanism ratio
T	Nm	Torque
I	kgm^2	Moment of Inertia
R	m	Particle radius
O		Rotation matrix
α	rad	Angle
δ	m	Contact overlap / elongation
ρ	kg/m³	Density
ν	—	Poisson's Ratio
ψ	rad	Angle
θ	rad	Angle. (opening angle)
ϕ	rad	Angle
γ	—	Fraction of Rayleigh timestep
κ	Nm/deg	Torsional stiffness
C_d	Nms/deg	Torsional damping coefficient
C_R	—	Coefficient of restitution
C_r	—	Rolling damping coefficient
c_d	Ns/m	Damping coefficient
ω	rad/sec	Rotational speed
r	m	Radius
u	m/s	Initial velocity
v	m/s	Velocity

Acknowledgements